NANYANG
TECHNOLOGICAL
UNIVERSITY

MEMBRANE DISTILLATION: MODULE DESIGN AND MODELING

YANG XING

SCHOOL OF CIVIL AND ENVIRONMENTAL ENGINEERING

NANYANG TECHNOLOGICAL UNIVERSITY

2012

MEMBRANE DISTILLATION: MODULE DESIGN AND MODELING YANG XING 2012

MEMBRANE DISTILLATION: MODULE DESIGN AND MODELING

YANG XING

YANG XING

School of Civil and Environmental Engineering

A thesis submitted to the Nanyang Technological University
in fulfillment of the requirements for the degree of Doctor of Philosophy

2012

ACKNOWLEDGEMENTS

I would like to express the most sincere gratitude to my supervisors, Associate Professor ***Wang Rong*** and Professor ***Anthony G. Fane***, for their tireless guidance, timely encouragement and valuable advice throughout the past three years. The perfect combination of their respective expertise on membrane materials/characteristics (Prof. Wang) and process engineering/energy perspectives (Prof. Fane) has given me a profound understanding on the membrane technology, which of course has greatly intrigued my interest and driven the progress of my research. It is lucky for me to work with both of them—their exceptional intelligence and academic integrity have given me substantial influence, for now and forever.

I would like to thank Prof. W.B. Krantz for his brilliant advice on communication and technical writing skills, which are beneficial for my whole life. It is always a pleasant experience conversing with Prof. Krantz, not only because of the sparkling inspirations he has given me, but also his optimistic nature that has an enormous influence on me.

My sincere acknowledgement goes to School of Civil & Environmental Engineering (CEE) and Singapore Membrane Technology Center (SMTC) for scholarship and Siemens Water Technology (SWT) for funding the project and membrane supply. Special thanks are due to Bhindo and Shuhui (Final Year Project students) and Shi Lei for their helps and support on process operations, membrane characterization and membrane surface modification; and my former colleague Dr. Yuhui for his kind advice on Computational Fluid Dynamics (CFD) modeling, without which I would not be able to make tremendous progress within such a short period of time.

Many thanks to my friends and staff from Singapore Membrane Technology Centre (SMTC), Guizi, Chen Lin, Wei Jing, Vera, Saren, Zhang Yuan, Guangzhi, Amir, Thengi, Saeid, Chunheng, Lu Yinghong, Lauren, Shuwen, Liao Yuan, Chou Shuren,

Ziggy, Filicia, Jingsong, etc. for their sharing of knowledge and making my research life more enjoyable, and also the technicians in Environmental Lab 1&2—especially Aidil and Chew Wang, for their kind support on equipment and consumable purchase. Without their patient help, I would not be able to conduct my research work. Also, I would like to show my appreciation to the membrane suppliers for the hollow fiber membranes and their precious advice. Without their support, I would not be able to commence this thesis study.

Lastly, I would like to thank my dearest parents and family for giving me unlimited support and bearing with my nagging miseries whenever frustrations/difficulties were met—words would be too pale to express my gratitude and love. Also, to those good friends (Alek, David, Aisha, Veras, Ria, Yiyi, Kei, Liujian, etc.) that I met outside SMTC lab during my three-year stay in Singapore—thanks for all the priceless fun and kind encouragement, and sorry for forcing you (i.e., Alek) to review my boring scientific papers once in a while—I would never make it without any of you, who have made me a more optimistic and stronger person.

PUBLICATIONS AND PRESENTATIONS

In Journals

- **Xing Yang,** Rong Wang, Lei Shi, Anthony G. Fane, Marcin Debowski, Performance improvement of PVDF hollow fiber-based membrane distillation process, Journal of Membrane of Science, 369 (1-2) (2011) 437-447
- **Xing Yang**, Rong Wang, Anthony G. Fane, Novel designs for improving the performance of hollow fiber membrane distillation modules, Journal of Membrane of Science, 384 (1-2) (2011) 52-62
- **Xing Yang**, Hui Yu, Rong Wang, Anthony G. Fane, Analysis on the effect of turbulence promoters in hollow fiber membrane distillation module via computational fluid dynamic (CFD) simulations, Journal of Membrane of Science, 415 - 416 (2012), 758-769.
- **Xing Yang**, Hui Yu, Rong Wang, Anthony G. Fane, A computational fluid dynamic (CFD) modeling study on microstructured fiber designs for membrane distillation applications, Journal of Membrane of Science, in press.
- **Xing Yang**, Rong Wang, Anthony G. Fane, Chuyang Tang, I.G. Wenten, Membrane Module Design and Dynamic Shear-Induced Techniques to Enhance Liquid Separation by Hollow Fiber Modules: A Review, submitted to Water Treatment and Desalination.
- Hui Yu, **Xing Yang**, Rong Wang, Anthony G. Fane, Numerical simulation of heat and mass transfer in direct membrane distillation in a hollow fiber module with laminar flow, Journal of Membrane of Science, 384 (1-2) (2011) 107-116
- Hui Yu, **Xing Yang**, Rong Wang, Anthony G. Fane, Analysis of heat and mass transfer by CFD for performance enhancement in direct contact membrane distillation, Journal of Membrane of Science, 405- 406 (2012) 38- 47
- Guizi Chen, **Xing Yang**, Rong Wang, Anthony G. Fane, Performance

enhancement and scaling control with gas bubbling in a direct contact membrane distillation, Desalination, in press.

- Guoqiang Guan, Rong Wang, Filicia Wicaksana, **Xing Yang**, Anthony G. Fane. Analysis of membrane distillation crystallization system for high salinity brine treatment with zero discharge using Aspen flowsheet simulation, submitted to Industry and Chemical Engineering Research, 2012.
- Guoqiang Guan, Rong Wang, **Xing Yang**, Anthony G. Fane. Simulations of energy consumption in direct contact and vacuum membrane distillation processes for brine treatment, to be submitted.

At International Conferences

- **Xing Yang**, Rong Wang, Anthony G. Fane, Evaluation of Three Hydrophobic Hollow Fiber Membranes for MD Application (oral presentation), Membrane Society of Australasia (MSA) student symposium, Feb.18-21, 2010, Wallongong, Australia.

- A.G. Fane, Rong Wang, Chuyang Tang, and **Xing Yang**, Membrane Distillation and Forward Osmosis: Advances in Membranes, Modules, and Applications, IDA World Congress, Sept. 4 – 9, 2011, Perth, Western Australia.

- **Xing Yang**, Rong Wang, Anthony G. Fane, Membrane distillation: hollow fiber module design and Computational Fluid Dynamics (CFD) modeling, Northern American Membrane Society (NAMS) conference, June 9-12, 2012, New Orleans, USA.

- **Xing Yang**, Hui Yu, Rong Wang, Anthony G. Fane, Membrane distillation: hollow fiber module design and Computational Fluid Dynamics (CFD) modeling, Singapore International Water Week (SIWW), July 1-5, 2012, Singapore.

TABLE OF CONTENTS

ABSTRACT

Membrane distillation (MD) is an emerging technology for seawater desalination that is traditionally accomplished by conventional separation processes such as thermal distillation or reverse osmosis. It is potentially cost effective as it is feasible to utilize low-grade waste heat and/or alternative renewable energy sources. However, the industrialization of MD is impeded by several technical challenges which include the membrane pore-wetting problem, low permeability, and concentration/temperature polarization effect, etc.

This thesis provides a comprehensive review on the state-of-the-art of MD technology with focuses on some areas that need to be further investigated or strengthened, such as novel membranes and improved membrane module design with the aid of mathematical modeling, which may offer strategies to address the challenges.

A preliminary study of the performance improvement of the hollow fiber-based direct contact membrane distillation (DCMD) system has been conducted. The original hydrophobic polyvinylidene fluoride (PVDF) hollow fiber and two modified membranes (unmodified, plasma modified and chemically modified) were used and compared. It was found that modified membranes presented better hydrophobicity while maintaining similar structural properties and less vulnerability to pore wetting, thus resulting in more sustainable long-term performance. Single fiber tests in combination with heat transfer analysis showed that a critical length *Lc* existed to assure sufficient driving force along the fiber to maintain a high MD efficiency. In addition, the over MD coefficient decreased with increasing packing density.

As a continuation, five types of modified hollow fiber module configurations with structured-straight fibers, curly fibers, central-tubing for feeding, spacer-wrapped and spacer-knitted fibers, have been designed and constructed. Their module performances were evaluated based on permeation flux experiments, fluid dynamics studies, and tracer-response tests for flow distribution as well as process heat transfer analysis in a DCMD system. The fluxes of the modified designs showed low sensitivity to the feed flow velocity, the modules with undulating membrane surfaces (curly and spacer-knitted fibers) were able to achieve more than 300% flux improvement in the laminar flow regime. The heat transfer analysis emphasizes the advantage of the modules with undulating membrane surface for enhancing permeation flux and mitigating temperature polarization (TP).

To further reveal the fundamentals of the heat-transfer process and module performance, a resistance-in-series model was used to analyze local heat-transfer resistances in DCMD and well-verified mathematical models (less than 5 % error) were developed for computational fluid dynamics (CFD) simulations. With the aid of two dimensional numerical simulations, nine modified hollow fiber modules with various turbulence promoters were designed and modeled to investigate their potential in improving heat transfer and module performance for a liquid-boundary layer dominant DCMD process. The feed heat-transfer coefficient h_f of the modified modules generally showed much slower decreasing trends along the fiber length compared to the original (unmodified) module. The temperature polarization coefficient (*TPC*) and mass flux distribution curves of the modified modules with annular baffles and floating round spacers presented increasing trends and gained an optimal improvement of 57% and 74%, respectively. Also, configurations with appropriate attached quad spacers or floating round spacers achieved a good compromise between enhanced permeation fluxes and modest hydraulic energy consumption (*HECs*).

A connection of membrane fabrication and process engineering was speculated via the concept of microstructured hollow fiber designs, which was introduced to facilitate MD applications. Hollow fibers with ten different geometries were used to make MD modules, and a series of three dimensional CFD simulations were carried out to investigate their capability of depolarizing the buildup of liquid boundary layers, and thus improving water productivity. The results of heat-transfer coefficients, average *TPC* and mass flux N_m showed that the gear-shaped fiber module had the most encouraging improvement over the original design, followed by the wavy designs 07 and 08. It was also found that a high water production could be obtained using wavy fiber modules with an increased membrane area by surface corrugations. However, these geometries might possibly cause high *HEC*.

Keywords: direct contact membrane distillation, hollow fiber membrane characteristics, module design, hydrodynamics, performance enhancement, computational fluid dynamics (CFD) simulation.

LIST OF SYMBOLS

A	effective membrane area, m^2
A_s	membrane area of a single fiber, m^2
a	membrane permeation constant
B	geometric factor determined by pore structure
b	shape parameter of the wavy arch on the membrane surface
b_v	friction of permeability arising from viscous effects, $0 < b < 1$ (= 0, for Knudsen diffusion; = 1, for Poiseuille flow)
C	membrane distillation coefficient, kg m^{-2} h^{-1} kPa^{-1}
C_b	bulk concentration of salt solution, kg m^{-3} or wt %
C_m	salt concentration at the membrane surface, kg m^{-3} or wt %
$C(t)$	temporal tracer concentration at the effluent, mol·m^{-3}
c_p	specific heat capacity of material, J kg^{-1} K^{-1}
c_0	pulse injection tracer concentration at the feed entrance, mol·m^{-3}
d_h	hydraulic diameter, m
d_i	inner diameter of the hollow fiber, μm
d_o	outer diameter of the hollow fiber, μm
d_s	housing diameter of the module, mm
D	diffusion coefficient of the solute through the membrane, m^2·s^{-1}
D_s	diffusion coefficient of the solute in shell side, m^2·s^{-1}
D_t	diffusion coefficient of the solute in tube side, m^2·s^{-1}
E_t	tensile modulus, MPa
ΔF	overall driving force of the mass transfer

g	acceleration of gravity, $\mathrm{m\cdot s^{-2}}$
Gz	Graetz number
H	effective heat-transfer coefficient based on the temperature difference across the entire membrane, $\mathrm{W\cdot m^{-2}\cdot K^{-1}}$
ΔH_T	latent heat of vaporization of water at temperature T, $\mathrm{J\cdot kg^{-1}}$
h	local heat-transfer coefficient of fluids and membrane, $\mathrm{W\cdot m^{-2}\cdot K^{-1}}$
h_f	feed-side local heat-transfer coefficient, $\mathrm{W\cdot m^{-2}\cdot K^{-1}}$
h_p	permeate-side local heat-transfer coefficient, $\mathrm{W\cdot m^{-2}\cdot K^{-1}}$
K	permeability of the porous membrane, $\mathrm{kg\cdot m^{-1}\cdot h^{-1}\cdot kPa^{-1}}$
k	overall mass transfer coefficient, $\mathrm{m\cdot s^{-1}}$
k_{shell}	local mass transfer coefficient in shell side, $\mathrm{m\cdot s^{-1}}$
k_{tube}	local mass transfer coefficient in tube side, $\mathrm{m\cdot s^{-1}}$
k_m	local mass transfer coefficient across membrane, $\mathrm{m\cdot s^{-1}}$
L	effective fiber length, mm
L_b	dimension of a gear with a square shape, mm
L_C	critical fiber length, mm
Lx	interval between two corrugated waves on the membrane surface, mm
Ly	vertical distance between an internal and the membrane outer surface, mm
M	molecular weight of component, $\mathrm{kg\cdot mol^{-1}}$
m	mass of the permeate, kg
n	number of fibers
N_m	vapor flux, $\mathrm{kg\cdot m^{-2}\cdot h^{-1}}$
Nu	Nusselt number

P	saturated vapor pressure, Pa
P_1	partial pressure of the vapor at the membrane surfaces on the feed, kPa
P_2	partial pressure of the vapor at the permeate side, kPa
ΔP	applied pressure of the process, Pa
P_c	power consumption of the circulation pump, kW
ΔP_{fluid}	pressure drop along the module length in the shell side, Pa
$\Delta P_{interface}$	pressure drop on the membrane surface, kPa
P_{liquid}	hydrostatic pressure on the membrane surface of the feed side, kPa
Pr	Prandtl number, $\frac{c_p\mu}{\lambda}$
P_{vapor}	partial pressure in the membrane pores, kPa
Q	heat-transfer rate through the liquid film, W
q	heat flux, $\mathrm{W\ m^{-2}}$
q_{MD}	transmembrane latent heat flux, $\mathrm{W\ m^{-2}}$
q_{HL}	conductive heat loss, $\mathrm{W\ m^{-2}}$
R	gas constant, 8.314 $\mathrm{J\ mol^{-1}\ K^{-1}}$
R_{mi}, R_{mo}	inner, outer radii of hollow fiber, m
r_{max}	maximum pore size, μm
r_{mean}	mean pore size, μm
Re	Reynolds number, $\frac{d_h v\rho}{\mu}$
S_h	source term of energy transport equation, $\mathrm{J\ m^{-3}\ s^{-1}}$,

$$S_h = \begin{cases} \dfrac{q_{MD}}{\delta r} \cdot \dfrac{R_{mo}}{R_{mi}} & \text{for } r = R_{mi} \\ -\dfrac{q_{MD}}{\delta r} & \text{for } r = R_{mo} \\ 0 & \text{otherwise} \end{cases}$$

Sc	Schmidt number, $\dfrac{\mu}{\rho D}$
Sh	Sherwood number, $\dfrac{k\, d_h}{D}$
ΔT	bulk temperature difference, K
T_f	bulk temperature of the feed, K
T_p	bulk temperature of the permeate, K
Δt	time interval, h
$\bar{t}$	theoretical residence time of the vessel V/V_0, s
t_m	mean residence time, s
V	volumetric flow rate of the fluid, m^3 s^{-1}
V_0	volume of an empty module
v	fluid recirculated velocity, m s^{-1}
u	normalized velocity of feed or permeate, m s^{-1}
x, r	axial, radial directions in cylindrical coordinate, m
Δx	cross-sectional dimension of the wavy arch in *x* direction, mm
Δy	cross-sectional dimension of the wavy arch in *r* direction, mm

Greek letters

α	interval angle between two neighboring gears on the cross section of the fiber
α_1, β_1	constants in Sh_{shell} correlation
δ_b	strain at break, %
δ_m	membrane thickness, μm

δ_r	grid scale in the *r* direction, m
δ_{tf}	thickness of the thermal boundary layer at the feed side, μm
δ_{tp}	thickness of the thermal boundary layer at the permeate side, μm
δ_x	thickness of the concentration boundary layer, μm
σ^2	variance, s^2
${\sigma_\theta}^2$	dimensionless variance
η	pump efficiency, %
η_h	energy efficiency
ϕ	module packing density, %
μ	viscosity of the fluids, Pa s^{-1}
ρ	fluid density, kg m^{-3}
τ	tortuosity of the membrane matrix
θ	dimensionless time
$\bar{\bar{\tau}}$	stress tensor (kg m^{-1} s^{-1}) $\bar{\bar{\tau}} = \mu\left[\left(\nabla\vec{v} + \nabla\vec{v}^T\right) - \frac{2}{3}\nabla \cdot \vec{v}I\right]$
ε	membrane porosity, %
γ_L	surface tension , N m^{-1}
$\wp$	dimensionless pressure, P/P_{ref}
λ	thermal conductivity of fluids/material, W m^{-1} K^{-1}

Suffix

i	location, *i = f or p*
f	feed
fm	feed-side membrane surface

g	gas
HL	heat loss
i, *o*	inlet and outlet of fluids
l	liquid
m	membrane
p	permeate
pm	permeate-side membrane surface
ref	reference pressure
s	solid
w	membrane wall

LIST OF FIGURES

LIST OF TABLES

CHAPTER 1

INTRODUCTION

1.1 Background

It was reported (Jury et al. 2007) that a young child will die every eight seconds because of water scarcity or waterborne diseases, and over one billion people cannot acquire clean drinking water all over the world. Due to the decrease in water resources and quality, this situation is continuously getting worse along with population growth, urbanization and increased domestic and industrial water uses. Therefore, the exploration of more efficient water treatment technologies has received increasing attention. As part of these tremendous efforts, people have tried to obtain drinking water through seawater desalination over the past decades. The techniques used cover a wide spectrum from conventional thermal distillation technology to membrane-based separation processes, such as reverse osmosis (RO) and nano-filtration (NF), etc. Nowadays, membrane distillation (MD) is considered to be a promising alternative to conventional distillation and RO, as it may be potentially cost effective by using low-grade waste heat or renewable green energy sources (Fane 1996).

MD is a thermally driven process which employs trans-membrane vapor pressure difference as the driving force and a hydrophobic porous-membrane as the support interface (El-Bourawi et al. 2006). Briefly, the separation mechanism of MD involves three steps. Firstly, water molecules vaporize from the hot feed solution;

secondly, water vapor transports through the membrane pores due to the vapor pressure difference resulting from the temperature difference between the hot feed and cold permeate. Finally, water vapor condenses at the permeate side (Smolders and Franken 1989). Thus the MD system involves a complicated combination of mass and heat transfer processes.

Compared with other separation technologies, MD offers many competitive advantages for seawater desalination (El-Bourawi et al. 2006):

- 100% theoretical solute rejection to different ions, big molecules, micro-particles, microorganisms and most non-volatiles;
- Modest operating temperatures;
- Dramatically smaller vapor space required than that of conventional distillation;
- Much lower operating pressures than those pressure-driven membrane separation processes such as RO and NF which have been commercialized in industry;
- Negligible chemical interaction between the membrane and process solutions;
- Undemanding requirement on mechanical strength for membrane itself which helps to reduce fabrication cost, etc.

In addition, MD is an evaporative process which can produce water with extremely high quality while potentially subject to less fouling than other membrane processes. It is feasible to make use of waste heat or employ renewably green energies such as solar heat and geothermal energy rather than primary electrical power to heat up the feed stream. Among the four types of MD configurations, direct contact membrane distillation (DCMD) is the simplest and most popular mode because no external condenser is required as compared to vacuum membrane distillation (VMD) and sweep gas membrane distillation (SGMD), and air gap membrane distillation (AGMD) which has lower permeate flux as the air gap presents an extra resistance (Lawson and Lloyd 1997; Khayet et al. 2000; Khayet et al. 2002; Phattaranawik et al. 2003).

1.2 Challenges for MD applications

The MD process has been proposed and investigated for over forty years, and the principles and benefits have been proved by lab-scale studies. Despite great efforts, MD has gained only little acceptance and is yet to be significantly implemented in industry, as it exhibits some potential disadvantages (El-Bourawi et al. 2006):

- Novel membranes are needed;
- Over an extended time, there may be flux decline and distillate contamination due to pore wetting;
- Permeate flux tends to be relatively low compared to other membrane filtration processes such as RO;
- Novel membrane module design is required to optimize performance;
- Energetic and economic costs are uncertain (for example, they depend on the availability of low grade heat and on the use of energy recovery).

1.3 Objectives of this thesis

Siemens Water Technologies (SWT) has developed novel fluoropolymer hollow fibers that are well-suited to MD applications. At the same time there is an unfulfilled market need for effective MD modules. As part of a collaboration between SWT and the Singapore Membrane technology Centre (SMTC), this thesis deals with the assessment and optimization of hollow fiber-based MD module design and operation with a focus on DCMD. The objectives of the thesis include the following:

- To characterize the commercially available hollow fibers (and other membranes including surface modified)) in standard MD tests to determine membrane mass transfer coefficient, water intrusion pressure, wettability, etc;
- To evaluate alternative MD module configurations, and hollow fiber dimensions, in terms of temperature polarization properties, energy efficiency, attainable fluxes, etc;
- To establish a mathematical model and verify the heat and mass transfer and fluid flow for selected MD configurations. Modeling tool is used as an aid for optimization and scale-up;
- To simulate the introduction of various turbulence promoters (spacers/baffles and/or microstructured fiber geometries) into a hollow fiber module for performance improvement.

To achieve the above-mentioned goals and explore the industrial potential in seawater desalination, a deep insight into the MD process in terms of membrane characteristics, module configuration, operating condition and fluid dynamics, etc, has to be acquired. Specifically, commercial hollow fibers and other membranes will be compared with respect to basic characterization (i.e. contact angle, porosity, liquid entry pressure of water (LEPw), mechanical strength and pore size/pore size distribution), MD flux and long-term performance. The factors that affect MD performance (such as operating conditions, fluid dynamics, module dimension effects, fiber arrangement/configurations, etc), will be evaluated based on mass and heat transfer analysis, which is anticipated to lead to an optimized module design. Additionally, a comprehensive mathematical model will be developed via conventional correlations and computational fluid dynamics (CFD) tools to reveal fundamentals of mass and heat transfer in an MD system. Finally, numerical simulations are conducted to evaluate the effectiveness of various hydrodynamic approaches for module performance enhancement.

1.4 Scope of this research

With the above mentioned objectives proposed, this thesis provides a comprehensive literature review on prior MD work, conducts both experimental studies and numerical simulation of hollow fiber module design for membrane distillation (MD) systems. A study of the performance improvement of direct contact membrane distillation (DCMD) process with one types of hydrophobic polyvinylidene fluoride (PVDF) hollow fiber membrane and its two modifications is carried out first, followed by the design, construction and evaluation of five types of modified hollow fiber module configurations. To further reveal the fundamentals of the heat-transfer process and module performance, a resistance-in-series model is used to analyze local heat-transfer resistances in DCMD and mathematical models are developed for computational fluid dynamics (CFD) simulations. Lastly, the connection of membrane fabrication and process engineering is investigated via the concept of microstructured hollow fiber designs, which could be introduced to implement MD applications.

1.5 Organization of this thesis

Chapter One includes a brief introduction to the background of membrane distillation as well as the description of research objectives and scope.

Chapter Two gives a comprehensive literature review, which outlines the basic concepts of MD and its historical background, and sheds light on those important aspects that are associated closely with the performance enhancement of MD systems. Specifically, the previous studies of the development of MD membranes, the module design concepts and energy considerations of hollow fiber modules involving passive enhancement aids (such as modified fiber configurations/arrangement) and active enhancement aids (such as vibrations/oscillation, bubbles and ultrasound etc), and process modeling are described in detail. It is expected that this review can provide inspiration for novel module development that serves for future MD industrialization.

Chapter Three presents chemical and plasma modification approaches to produce more hydrophobic grafting/coating layers on the newly developed polyvinylidene fluoride (PVDF) hollow fiber membranes. These modified membranes are expected to have better hydrophobicity while maintaining similar porosity and mechanical strength, and being less vulnerable to membrane pore wetting, thus resulting in higher salt rejection in long-term performance tests. In addition, to enhance the module performance, a preliminary evaluation of MD operating conditions and certain hollow fiber module characteristics, which include fiber length, packing density, fiber geometries and the effect of module diameter and flow rates, has been performed. It is expected that this study can help identify potential approaches to overcome the commonly encountered problem of membrane wetting and mitigate the concentration/temperature polarization effects to facilitate practical applications of the MD process.

Chapter Four studies five types of modified hollow fiber module configurations with structured-straight fibers, curly fibers, central-tubing for feeding, spacer-wrapped and spacer-knitted fibers. These modules have been designed and tested in a DCMD system. The module performance was evaluated based on permeation flux experiments, fluid dynamics studies, and tracer-response tests for flow distribution as well as process heat transfer analysis.

Chapter Five focuses on the exploration of process enhancing strategies in a MD hollow fiber module via computational fluid dynamic (CFD) modeling. Using a two dimensional CFD heat-transfer model, which was verified by experiments with less than 5% error, nine modified hollow fiber modules with various turbulence promoters were designed and modeled. Three scenarios are studied — MD systems with highly permeable membranes (large MD coefficient C), high operating temperatures and varying flow velocity. Investigations on their potential in improving heat transfer and module performance for a shell-side feed DCMD system were performed.

Chapter Six extends the concept of microstructured hollow fiber designs and explores their potential to enhance process performance in an MD system. A series of three dimensional module geometries were built computationally and CFD simulations were carried out to investigate the ability of improving water productivity and depolarizing the buildup of liquid boundary layers, by utilizing nine different modified fiber geometries in shell-feed DCMD modules. It is hoped to bring in a new perspective on the development of smart membranes for MD applications, and provide a foundation to guide the fabrication of microstructured hollow fiber membranes with an optimal design.

Chapter Seven summarizes the overall research, presents general conclusions and recommendations for future work.

CHAPTER 2

LITERATURE REVIEW

2.1 Introduction

This review provides a comprehensive introduction to the MD process, including basic mechanisms, configurational variations, and technical limitations or areas that need to be further strengthened. Most importantly, focus will be on the historical perspectives of MD study including membrane development, process modeling and hollow fiber module design. Since the process modeling and hollow fiber module design have been set as the targets for this thesis, prior modeling studies and a variety of process enhancement aids (passive/active techniques) to improve the mass/heat transfer in hollow fiber modules have been specifically summarized, followed by detailed analyses of corresponding applications in particular enhancement modes. The technical requirements together with the benefits and limitations will be addressed in terms of economic consideration and process engineering. It is expected that this review can provide inspiration for novel module development that serves for future MD industrialization.

2.1.1 Membrane distillation mechanisms

Membrane-based separation processes have found numerous applications in various fields such as water, energy, chemical, petro-chemical and pharmaceutical industries. This growth has been primarily due to two developments: firstly, the ability to produce high permeability and essentially defect-free membranes on a large scale; secondly, the ability to assemble these membranes into compact, efficient and economical membrane modules with a high membrane surface area (Porter 1990; Abetz et al. 2006).

The original concept of membrane distillation was initiated as direct contact membrane distillation (DCMD), where a hydrophobic micro-porous membrane acts as the interface between hot and cold aqueous streams. The hydrophobic property of the membrane helps to prevent the water penetrating into the membrane pores, while allowing the water vapor to pass through. The operation is simple and requires the least equipment. The vapor pressure gradient caused by temperature difference across the membrane drives the water vapor from the hot feed surface through the pores to the cold permeate side and condenses. The configuration of DCMD is illustrated in Fig. 2.1 (a), which is the main configuration employed throughout this thesis.

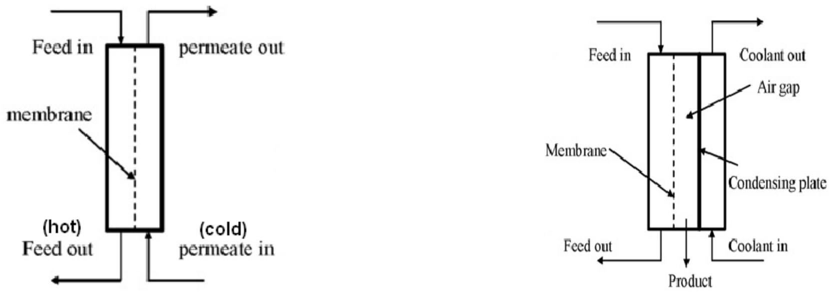

(a) DCMD (b) AGMD

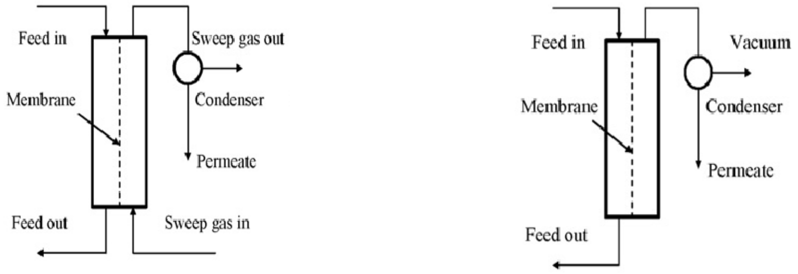

(c) SGMD (d) VMD

Fig. 2.1 Configurations of MD process (a) DCMD, (b) AGMD, (c) SGMD and (d) VMD (El-Bourawi et al. 2006)

2.1.2 Configurational variations

In DCMD system, both the feed and permeate are in direct contact with the membrane walls. There are three other configurations that have been developed along the way. They are known as: air gap membrane distillation (AGMD), sweep gas membrane distillation (SGMD), and vacuum membrane distillation (VMD), which are schematically shown in Fig. 2.1 (b)-(d), respectively.

As shown in Fig. 2.1 (b), in AGMD, the water vapor permeates through the membrane pores to the other side and diffuses through an air gap to a cold surface where it condenses. It introduces a heat insulating air gap between the membrane and the distillate water, so the conductive heat loss across the membrane is greatly reduced. However, the presence of air gap increases the mass/heat transfer resistance, thus results in lower permeate flux (Phattaranawik et al. 2001).

SGMD is similar to AGMD, both having permeate collected externally. The sweep gas in SGMD carries the vapor which is cooled down outside of the chamber (Fig. 2.1 (c)). The concept of VMD is to reduce the absolute pressure in the downstream side of the membrane by employing a vacuum, which establishes the vapor pressure difference, as shown in Fig. 2.1(d). VMD dominates the problem of air resistance to transfer.

2.1.3 Limitations of MD

The fundamental driving force for MD is the vapor pressure gradient across the membrane though different configurations use different ways to collect the distillate (Fig. 2.2). Similar to most membrane processes, MD is subject to solute concentration build-up adjacent to the membrane surface on the feed side, which is known as concentration polarization (CP). Although the concentration gradient has negligible impact on the driving force at a low concentration, it can still lead to consequent fouling problem. The fouling may result in membrane wetting or physical damage. In addition, there is one distinguished phenomenon called temperature polarization (TP) in the MD process. The presence of a temperature gradient in the liquid boundary layer adjacent to the membrane surface leads to reduction of vapor pressure difference across the membrane, thus resulting in lower permeate flux and thermal efficiency. The degree of TP is strongly dependent on the fluid dynamics adjacent to the membrane surface.

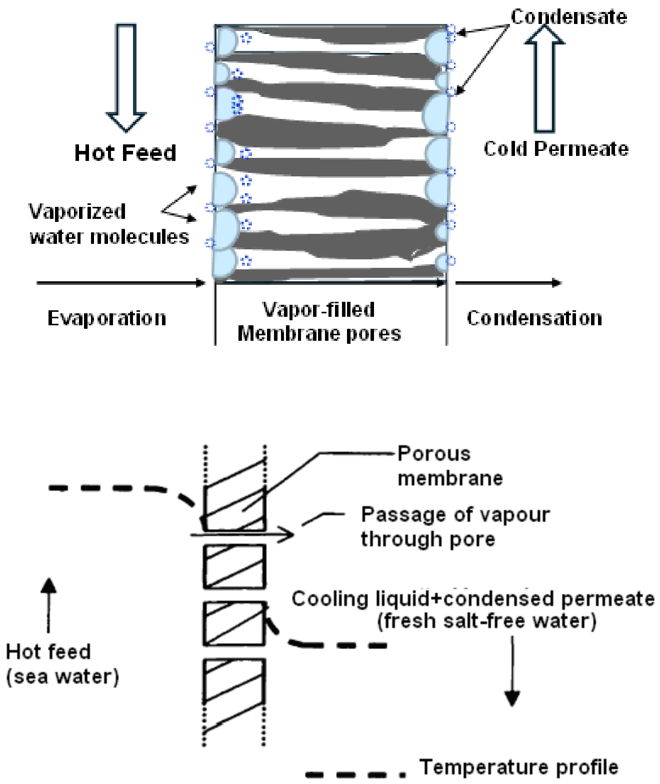

Fig. 2.2 Working principle of DCMD

Since the earliest publication on MD in the late 1960s (Bodell 1963; Findley 1967), numerous efforts have been made to develop new MD configurations to improve this technology. However, from the commercial point of view, MD has several limitations which have hindered its industrial implementation (Burgoyne and Vahdati 2000). The main barriers are:

1) Lack of specially designed and fabricated membranes for MD process;

2) The concentration and temperature polarization, which lead to the decrease of mass and heat transfer coefficients;

3) Pore wetting phenomenon caused by solute-membrane interactions and by hydrostatic pressure drop along the membrane surface;

4) Relatively low permeate flow rate (depending on temperature different and feed temperature);

5) Poor long-term performance (without an attainable flux).

Many approaches have been proposed to overcome these challenges and the critical parts involve developing novel membranes and designing efficient modules. It is worth pointing out that a well-designed module can improve the hydrodynamic conditions and enhance the mass/heat transfer tremendously. However, only a handful of experimental studies on this topic are available (Lawson and Lloyd 1996; Foster et al. 2001; Cath et al. 2004; Li and Sirkar 2004; Martínez and Rodríguez-Maroto 2007; Teoh et al. 2008). The module design for MD applications has not been studied systematically yet. Nevertheless, efforts have also been made to incorporate active techniques associated with external energy input such as ultrasound (Zhu et al. 1999; Zhu and Liu 2000) into the MD process in order to enhance the flux and reduce the TP and CP effects.

2.2 MD membrane development

As one of the characteristics of the MD process, MD membrane pores should be filled with water vapor or non-condensable gases and must not be wetted by the liquid. To avoid pore wetting, the membrane material has to be hydrophobic with a contact angle as high as possible and the membrane should have a relatively small maximum pore size. The hydrophobic micro-porous membranes such as those made from polytetrafluoroethylene (PTFE), polyvinylidene (PVDF), polyethylene (PE) or polypropylene (PP) can fulfill the basic requirement of hydrophobicity. However, since most of these membranes are fabricated for other processes such as microfiltration (MF), they suffered drawbacks such the presence of some large pore sizes when applied to MD processes. The pore sizes are ‘nominal’ mean sizes and there will be a distribution including larger pores. The presence of larger pores is a possible reason causing membrane wetting even though the membranes are highly hydrophobic (Phattaranawik et al. 2003).

Considering the characteristic wetting phenomenon and low permeation problem in MD applications, there is a need for new membranes designed and fabricated especially for MD applications as has been proposed by many researchers (Fujii et al. 1992; Zárate et al. 1995; Tomaszewska 1996; Lawson and Lloyd 1997; Khayet and Matsuura 2003; Li et al. 2003; Feng et al. 2004; Suk et al. 2006; Bonyadi and Chung 2009; Hendren et al. 2009; Qtaishat et al. 2009). With respect to hollow fiber fabrication, the optimization of process parameters using homogenous hydrophobic materials/dope solutions to achieve desired structures (Wang et al. 2008; Bonyadi and Chung 2009; García-Payo et al. 2010; Wang et al. 2011; Khayet et al. 2012) is of great interest. Nevertheless, the development of MD membranes is often constrained by the conventional spinning methods and the limitation of suitable material properties due to the MD process characteristics. Thus, the concept of composite membranes rises and greatly extends the possibility of producing better MD membranes. Briefly, there are two main strategies to modify the hydrophobic membrane surface and minimize membrane wetting: one is a hydrophobic coating or grafting which helps to minimize the pores size while maintaining similar porosity and higher contact angle; the other is a dense hydrophilic coating which can protect the effective membrane pores from wetting. This chapter mainly focuses on the surface modification methods for MD membranes.

2.2.1 Hydrophobic coating

To reduce the possibility of pore wetting and contamination, the outer surface of porous hydrophobic/hydrophilic membranes can be coated or grafted with an ultrathin porous/microporous layer which exhibits even higher hydrophobicity (Fig. 2.3a). A finely porous hydrophobic coating or grafting which helps to minimize the pores size can significantly increase the liquid entry pressure while maintaining suitable porosity (Li and Sirkar 2005; Song et al. 2007; Jin et al. 2008; Dumée et al. 2011; Fang et al. 2012; Wei et al. 2012). For example, Shi et al modified the Millipore PVDF membrane by chemically bonding a fluoro-compound via anchorage points, which are provided by resulting OH functions from the hydroxylation of PVDF films. By applying this method, the contact angle of the membrane was improved from 120° to 150° (Shi et al. 2009). It was also reported that plasma polymerized silicone fluoropolymer was coated on commercial PP membranes and achieved as high as 71 $\text{kg}\cdot\text{m}^{-2}\cdot\text{h}^{-1}$ permeate flux at 85 ℃ for seawater desalination by VMD (Li and Sirkar 2005). The same modification method was used to fabricate novel MD membrane for a large-scale DCMD desalination device (Song et al. 2007). Tested in a VMD system, the surface of the porous alumina hollow fiber was converted from hydrophilic to hydrophobic via grafting with fluoroalkylsilane (FAS) (Fang et al. 2012). Fluorine functional groups (CF4) have been introduced to improve the hydrophobicity of the polyethersulfone (PES) membrane using plasma modification method for DCMD applications (Wei et al. 2012).

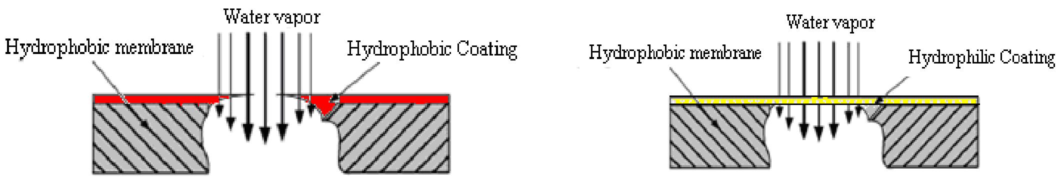

(a) (b)

Fig. 2.3 Schematic of membrane coating options

2.2.2 Hydrophilic coating

Another option for membrane surface modification is to coat the hydrophobic membrane with a thin relatively dense hydrophilic layer, which will cover the entire membrane surface and protect the mouths of pores (Fig. 2.3b). In the seawater desalination process, when brine concentration is high, crystallites may occur in the suspension, which tend to deposit on the membrane surface, leading to rapid membrane wetting. The purpose of coating a dense hydrophilic layer is to create an additional barrier between the substrate and the brine so that crystallites will deposit on the coating layer rather than the mouths of pores. The same approach will prevent wetting by surfactants and organics. Generally speaking, this approach can protect the effective membrane pores from wetting (Wu et al. 1992; Khayet et al. 2005; Bonyadi and Chung 2007; Qtaishat et al. 2009; Qtaishat et al. 2009; Chanachai et al. 2010; Lai et al. 2011). This approach was first applied for membrane distillation crystallization (MDC). In a similar osmotic distillation process, a thin layer of chitosan (a hydrophilic polymer) was crosslinked on the PVDF membrane surface (Chanachai et al. 2010). The plasma technology was used to modify the surface of a PTFE membrane to gain a hydrophilic layer (Lai et al. 2011). It was found that the modified membrane provided a much higher permeation rate, but with a loss in salt rejection.

These modified membranes are expected to have better performance, such as higher contact angle, porosity, Liquid entry pressure, smaller maximum pore size and narrower pore size distribution, mechanical strength, and longer lasting performance with high salt rejection.

2.3 MD modeling development

Based on the definition of transmembrane flux, the MD flux N can be calculated as the product of a transfer coefficient and the driving force:

$$N = C \cdot \Delta P = C \cdot (P_1 - P_2) \tag{2.1}$$

where C is the global membrane-distillation coefficient, kg m^{-2} h^{-1} kPa^{-1}. $\Delta P = (P_1 - P_2)$ is the driving force, which, for an average ‘module value’, is the logarithmic mean vapor pressure difference of the feed and permeate, kPa. If C is based on bulk temperature/vapor pressure values it is an ‘overall’ coefficient that includes the boundary layer effects and intrinsic membrane coefficient, C_i, which will be discussed in the later chapters. It is noted that the following modeling analyses are based on hollow fiber applications.

2.3.1 Heat transfer analysis

MD is a special process which involves both mass and heat transfer. The heat transfer in all configurations is essential and may be the rate controlling factor. It includes four steps: (i) heat transfer from the bulk feed to the membrane surface across the thermal boundary layer, which is related to the TP effect; (ii) heat transport by conduction across both the membrane matrix and the gas filled pores, that is considered as heat loss in MD; (iii) the latent heat of evaporation, which is the effective heat related to the vapor flux in MD; and (ⅳ) heat transfer from the membrane surface to the bulk permeate across the thermal boundary layer which is also associated to the TP effect.

Fig. 2.4 shows the combination of mass and heat transfers leading to two important phenomena in MD: concentration polarization (CP) and temperature polarization (TP). The CP refers to the build-up of the retained species at the membrane surface (here, salt is particularly studied as the main solute), and it exists in all membrane processes. TP refers to the thermal profiles developed near the membrane surface in the bulks. Both the CP and TP lead to smaller temperature differences than that of the bulk streams.

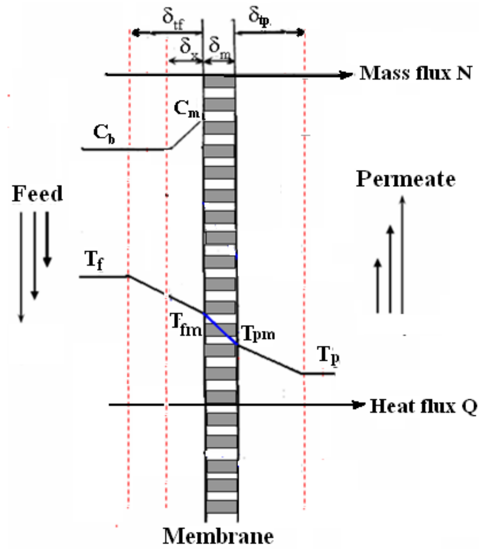

Fig. 2.4 Temperature and concentration profiles in MD

2.3.1.1 Heat transfer on the feed side & TP effect

Similar to any other thermal process, a bigger temperature difference will lead to a faster heat flow rate. The thermal boundary layer formed at each side of the membrane surface was reported to impose up to 80% reduction in the driving force due to the TP effect (Lawson and Lloyd 1997; Martinez-Diez and Vazquez-Gonzalez 1998; Martinez-Diez and Vazquez-Gonzalez 1999; Zhu and Liu 2000; Khayet et al. 2004). Thus, the temperature polarization coefficient (TPC) was defined as the fraction of transmembrane temperature difference to the bulk temperature difference (Schofield et al. 1987):

$$TPC = \frac{T_{fm} - T_{pm}}{T_f - T_p} \tag{2.2}$$

where T_{fm}, T_{pm}, T_f and T_p are membrane wall temperatures and fluid bulk temperatures at the feed and permeate side, respectively. All these related temperatures are schematically shown in Fig. 2.4. It is noted that both the feed and permeate thermal boundary layers are the function of fluid properties and operating parameters, as well as the hydrodynamic conditions. It is favorable to work under optimum mixing conditions to diminish the TP effect. Enhanced heat transfer can be achieved by improving the design of flow passage, membrane arrangement and fiber configuration or applying turbulence promotes like spacers/baffles (Teoh et al. 2008). Operating at a higher circulating flowrate is always seen as an option to achieve better mixing conditions and minimizing the TP effect. However, sometimes it will not be economically feasible under optimum conditions, and it is also necessary to ensure a low pressure drop along the fiber length in order to avoid membrane pore wetting, as the pressure drop along the fiber is a function of the second power of the fluid velocity (El-Bourawi et al. 2006).

Since MD relies on the phase change to perform the required separation, the latent heat for the evaporation must be continuously transferred from the bulk feed to the membrane surface. The total heat flux supplied, q_f (W•m^{-2}), depends on the film heat transfer coefficient of the feed, h_f, and the temperature difference between the feed bulk and membrane surface, as follows if the heat lost to the environment is not considered.

$$q_f = h_f (T_f - T_{fm}) \tag{2.3}$$

It was found that the TP effect increases with the feed temperature although a higher feed temperature usually results in an exponential increase in the transmembrane flux (Schofield et al. 1987; Martinez-Diez and Vazquez-Gonzalez 1999; Martinez-Diez and Vazquez-Gonzalez 2000; Khayet et al. 2003; Phattaranawik et al. 2003).

2.3.1.2 Heat transfer by conduction through the membrane

In MD, the heat transferred by conduction through both the membrane matrix and the gas-filled pores is considered heat loss and should be minimized in order to decrease the TP effect and increase the process efficiency. The heat flux transferred by conduction through the membrane can be expressed by (Schofield et al. 1987):

$$q_{HL} = h_{HL}(T_{fm} - T_{pm}) \tag{2.4}$$

where h_{HL} is the equivalent heat-transfer coefficient for conduction through the membrane, which is given by:

$$h_{HL} = \frac{\lambda_m}{\delta_m} \tag{2.5}$$

where λ_m is the average thermal conductivity of the membrane, which takes into account both thermal conductivity of the membrane matrix and thermal conductivity of the gas-filled pores.

$$\lambda_m = \varepsilon\lambda_s + (1-\varepsilon)\lambda_g \tag{2.6}$$

where ε is the membrane porosity, λ_s and λ_g are the thermal conductivities (W m^{-1} K^{-1}) of the membrane material and the gas in the pores, respectively.

It must be pointed out the thermal conductivity of air/gases is an order of magnitude lower than that of the membrane material. Thus the heat loss by conduction can be minimized by using membranes with high porosity.

2.3.1.3 Heat contributed to evaporation

Since MD relies on phase change to perform the required separation process, the amount of heat contributing to the evaporation step is considered as the efficient heat. The efficiency of the process will be maximized if the TP effect, the internal heat loss by conduction and the external heat loss to the environment are reduced. The corresponding heat flux can be estimated by the following equation:

$$q_{MD} = N\Delta H_T \tag{2.7}$$

where N is the MD permeation flux and ΔH_T is the latent heat of vaporization.

The total heat transferred through the membrane (including evaporation heat and heat loss by conduction) is written as follows:

$$q = q_{HL} + q_{MD} = h_{HL}(T_{fm} - T_{pm}) + N\Delta H_T \tag{2.8}$$

2.3.1.4 Heat transfer on the permeate side

The heat transfer from the membrane surface to the bulk permeate side, across the thermal boundary layer, is also associated to the TP effect. Due to the TP phenomenon, the temperature on the membrane surface of the permeate side is higher than in the bulk permeate. This part of heat flux is given as:

$$q_p = h_p(T_{pm} - T_p) \tag{2.9}$$

where h_p is the heat transfer coefficient of the thermal boundary layer at the permeate side. Under steady state conditions, the energy conservation equation is considered:

$$\frac{A_o}{A_i} q_f = q_p = q \tag{2.10}$$

where A_o and A_i are the outer and inner surface area, respectively. All the heat flux and heat transfer coefficients here are based on the internal surface of the fiber, and the permeate flows in the lumen of the fibers.

Due to the TP effect, the wall temperatures may be significantly different from the bulk temperatures. In order to estimate the actual driving force across the membrane and investigate the TP effect, the wall temperatures T_{fm} and T_{pm} can be determined from heat transfer relationships (Schofield et al. 1987; Bui et al. 2010):

$$T_{fm} = T_f - (T_f - T_p) \frac{1/h_f''}{1/h_f'' + 1/(h_{HL} + h_{MD}) + 1/h_p} \tag{2.11}$$

$$T_{pm} = T_p + (T_f - T_p)\frac{1/h_p}{1/h_f'' + 1/(h_{HL} + h_{MD}) + 1/h_p} \qquad (2.12)$$

where h_{MD} (W·m^{-2}·K^{-1}) is the equivalent heat-transfer coefficient associated with vapor flow, $h_f''(=\frac{A_o}{A_i}h_f)$ and h_p are the liquid film heat transfer coefficients on the feed and permeate sides, respectively. By assuming q_{MD} is constant at the average membrane temperature T_m, the vapor heat transfer coefficient h_{MD} is given by (Phattaranawik et al. 2003):

$$h_{MD} = \frac{NH_{Tm}}{\Delta T_m} = \frac{NH_{\frac{T_{fm}+T_{pm}}{2}}}{(T_{fm} - T_{pm})} \qquad (2.13)$$

Thus, the overall heat transfer coefficient can be expressed as:

$$U = \left(\frac{1}{h_f''} + \frac{1}{h_{HL} + h_{MD}} + \frac{1}{h_p}\right)^{-1} \qquad (2.14)$$

Here $R_{OV} = \frac{1}{U}$ is the overall transfer resistance, and $R_f = \frac{1}{h_f''}$, $R_p = \frac{1}{h_p}$ and $R_m = \frac{1}{h_{HL} + h_{MD}}$ are the individual resistances for the feed film, permeate film and the membrane, respectively. In the conventional MD modeling using semi-empirical equations, the film heat transfer coefficients h_f and h_p can be predicted in terms of the Nusselt number ($Nu_i = \frac{h_i d_h}{\lambda_i}$), which is correlated with Reynolds number ($Re = \frac{d_h v \rho}{\mu}$) and Prandtl number ($Pr = \frac{c_p \mu}{\lambda}$) through several correlations in ducts of various geometries. For the case of fully developed laminar conditions, the Graetz-Lévêque equation applies (Schofield et al. 1987; Tomaszewska et al. 1992):

$$Nu = 1.86(RePr\frac{d_h}{L})^{0.33} \qquad (2.15)$$

where L is the fiber length and d_h is the hydraulic diameter of the flow channel.

Based on Eq. (2.15), h_f and h_p can be estimated under given operating conditions, thus the local film resistance R_i can be obtained correspondingly. Additionally, the other alternative correlations for calculating the thermal coefficients and their agreements in different occasions can be found in the previous modeling work (Phattaranawik et al. 2003).

Moreover, another modeling tool namely Computational Fluid Dynamics (CFD), which has been rarely used in MD research and could be adopted to obtain the temperatures and velocity profiles for heat-transfer analysis in a flow channel, will be introduced in later sections.

2.3.2 Status and challenges of MD modeling

To properly understand the complicated combination of mass and heat transfers in the MD process, the temperature distributions adjacent to the membrane surfaces along the module length should be fully described. Unfortunately, it is impossible to attain temperature information via the most widely used non-intrusive experimental approaches such as the flow visualization with dye, Particle Image Velocimetry (PIV) and Direct Observation through the Membrane (DOTM), etc. These observational techniques are not able to provide sufficient flow and thermal field information in the boundary layers (Fimbres-Weihs and Wiley 2010). This review mainly introduces two approaches—semi-empirical equations and CFD modeling.

It should be noted that this section will mainly focus on mass transfer analysis for general liquid-liquid separations in hollow fiber modules, followed by a specific discussion (section 2.3.2.3) on MD mass transfer due to its uniqueness since the transport component of interest is the solvent (water).

For a general liquid-liquid membrane separation process, the overall flux J_s of the solute to be removed or retained can be expressed by film theory (Wickramasinghe et al. 1991):

$$J_s = k\Delta F = k\ln\frac{C_m}{C_b} \tag{2.16}$$

where k is the overall mass transfer coefficient and ΔF is the overall driving force, C_m and C_b are the solute concentration on the membrane surface and the bulk feed, respectively. If the feed is assumed to be in the shell side, based on the resistance-in-series model, the k can be written as (Cussler 1994):

$$\frac{1}{k} = \frac{1}{k_m} + \frac{1}{k_{tube}} + \frac{1}{k_{shell}}(\frac{d_i}{d_o}) \tag{2.17}$$

where k_m is the membrane mass transfer coefficient; k_{shell}, the mass transfer coefficient through the boundary layer in the feed side and k_{tube}, the mass transfer coefficient through the boundary layer in the permeate side. Here, k_m can be defined as (Kiani et al. 1984):

$$k_m = \frac{D\varepsilon}{\tau\delta_m} \tag{2.18}$$

where D is the diffusion coefficient of the solute through the membrane, which can be calculated by applying the Wilke and Chang method (Reid and Prausnitz 1987); ε is the membrane porosity and τ is the tortuosity. Thus, k_m is merely depending upon the solute diffusivity and the membrane structure regardless of the operating parameters (It should be noted that this solute transport mechanism across the membrane is not applicable in MD process); while k_{shell} and k_{tube} are the functions of flowing conditions and fiber/module geometries. k_{shell} and k_{tube} can be estimated by using mass transfer correlations in the form of (Gabelman and Hwang 1999):

$$Sh \propto Re^{\alpha_1} Sc^{\beta_1} f(geometry) \qquad (2.19)$$

where Sh, Re and Sc are the Sherwood number, Reynolds number and Schmidt number, respectively, and f is a function of module geometry. The applicable correlations for both tube and shell side flows have been provided by several investigators (Dahuron and Cussler 1988; Ho and Sirkar 1992; Wickramasinghe et al. 1992; Costello et al. 1993; Reed et al. 1995; Johnson et al. 1997).

2.3.2.1 Tube side flow

The fluid through the hollow fibers is generally treated as laminar flow, and the individual mass transfer coefficient k_{tube} is dependent on the flow velocity. Though there are several correlations available for the tube side flow calculation (Yang and Cussler 1986; Wickramasinghe et al. 1992), the Lévêque solution (Graetz Number, $Gz > 4$) has been widely accepted in the literature (Gabelman and Hwang 1999) to predict k_{tube} with a reasonable degree of accuracy:

$$Sh_{tube} = \frac{k_{tube} d_i}{D_t} = 1.62 Re_{tube}^{0.33} Sc^{0.33} (\frac{d_i}{L})^{0.33} \qquad (2.20)$$

$$k_{tube} = 1.62 \left(\frac{D_t^2 v}{L d_i} \right)^{0.33} \qquad (2.21)$$

where D_t is the diffusion coefficient of the solute in the tube side, v is the fluid velocity.

2.3.2.2 Shell side flow

The shell side mass transfer coefficients in the hollow fiber module can be similarly estimated by adopting the relationships between these dimensionless groups. In reality, in contrast to the tube side flow, the shell side flow still cannot be clearly illustrated. There are a number of semi-empirical correlations which have been proposed by different authors working on various systems and flowing conditions. However, most of the correlations can give similar results within certain ranges of operating conditions (Gabelman and Hwang 1999).

The following correlation by Prasad and Sirkar is widely used (Prasad et al. 1986; Prasad and Sirkar 1988):

$$Sh_{shell} = \frac{k_{shell} d_h}{D_s} = \beta(1-\phi) Re_{shell}^{0.6} Sc^{0.33} (\frac{d_h}{L}) \tag{2.22}$$

where ϕ is the packing density, the constant β is found to be 5.8 for hydrophobic membranes and 6.1 for hydrophilic membranes; the ranges of interest are $0 < Re < 500$ and $0.04 < \phi < 0.4$. In addition, another correlation was deduced using the analogy between heat transfer and mass transfer (Kreith and Black 1980):

$$Sh_{shell} = 0.39 Re_{shell}^{0.59} Sc^{0.33} \tag{2.23}$$

2.3.2.3 Mass transfer in MD process

As mentioned previously, the mass transfer in a general hollow fiber module for liquid separation process includes three steps: through the feed boundary layer, across the membrane and through the permeate boundary layer. while in the MD process, which produces highly purified distilled water, the mass transfer analysis will be given in another form because the transport component of interest is the solvent itself (water vapor). The transmembrane flux N is defined in Eq (2.1), which can be rewritten as:

$$N = K \frac{\Delta P}{\delta_m} \tag{2.24}$$

where K is the permeablity of the porous membrane, and is a function of pore geometry, pressure difference, operating temperature. etc.

A typical MD mass transfer process only involves two steps : the water molecules transport through the feed boundary layer and across the membrane. The mass transfer occurring in the feed boundary layer (here it is assumed in the shell-side) is described by the film theory and is strongly dependent on the fluid hydrodynamic (refer to Section 2.3.2.2). While the mass transfer across the membrane can be analyzed by the Dusty gas model, which elucidates the gas permeation through a porous membanre and comprises three submodels: Knudsen flow, Poiseuille flow, molecular diffusion and/or the transition between them. Knudsen diffusion model is suitable for a system where the mean free path of the molecule is much greater than the pore size (Nijdam et al. 2005):

$$N_K = \frac{2}{3}\frac{r\varepsilon}{\tau}\left\{\frac{8RT}{\pi M}\right\}^{1/2}\frac{M}{RT}\frac{\Delta P}{\delta_m} = K_K\frac{\Delta P}{\delta_m} \tag{2.25}$$

where $(8RT/\pi M)^{1/2}$ represents the mean molecular speed.

When the mean free path of the molecule is much less than the pore size, Poiseuille flow may apt for a simplified vapor permeation process (Schofield et al. 1987):

$$N_P = \frac{1}{8}\frac{r^2\varepsilon}{\tau}\frac{1}{\mu}\frac{MP}{RT}\frac{\Delta P}{\delta_m} \tag{2.26}$$

Nevertheless, a combination of these two models can be used for the transition region where both Knudsen diffusion and Poiseuille flow occur (Schofield et al. 1987):

$$N = a\wp^{b_v}\Delta P \tag{2.27}$$

where a is the membrane permeation constant, b_v ($0<b<1$) is the fraction of permeability arising from viscous effects (= 0, for Knudsen diffusion; = 1, for Poiseuille flow), and $\wp$ is the dimensionless pressure, P/P_{ref} .

Both the simplified models (Knudsen diffusion or Poiseuille flow) and transition model (Eq (2.27)) have been widely applied in many DCMD studies (Schofield et al. 1990; Lawson and Lloyd 1996; El-Bourawi et al. 2006).

2.3.3 Status and challenges of MD modeling

To properly understand the complicated combination of mass and heat transfers in the MD process, the temperature distributions adjacent to the membrane surfaces along the module length should be fully described. Unfortunately, it is impossible to attain temperature information via the most widely used non-intrusive experimental approaches such as the flow visualization with dye, Particle Image Velocimetry (PIV) and Direct Observation through the Membrane (DOTM), etc. These observational techniques are not able to provide sufficient flow and thermal field information in the boundary layers (Fimbres-Weihs and Wiley 2010). This review mainly introduces two approaches—semi-emperical equations and CFD modeling.

2.3.3.1 Semi-empirical correlations

As mentioned previously, to acquire heat transfer coefficients in the MD process, researchers (Phattaranawik et al. 2003) have replaced the membranes with aluminum film and others (Gryta et al. 1997; Lawson and Lloyd 1997; Gryta and Tomaszewska 1998; Aravinth 2000; Qtaishat et al. 2008) have conducted mathematical modeling using semi-empirical correlations and resistance-in-series model to predict the temperature distributions along the flow channel. By using this developed correlations, the primary purpose of modeling is to predict the theoretical permeation flux and its dependence on the membrane module design, membrane specifications and operating parameters, other than the estimation of the TP and CP coefficients (Drioli et al. 1986; Schofield et al. 1987; Schofield et al. 1990; Banat and Simandl 1994; Calabrò et al. 1994; Agashichev and Falalejev 1996; Godino et al. 1996; Lawson and Lloyd 1996; Gryta et al. 1997; Mengual and Peña 1997; Martinez-Diez and Vazquez-Gonzalez 1999; Martinez-Diez and Vazquez-Gonzalez 2000;

Phattaranawik et al. 2003; Cheng et al. 2008). Given this purpose, various theoretical models have been developed for each MD configuration (Lawson and Lloyd 1997). Here we mainly focus on the DCMD configuration. It is well known that both heat and mass transfer occur simultaneously in the MD process, thus both the TP and CP effects should be taken into consideration. The basic relationships among various parameters involved in MD modeling have been well reviewed (Lawson and Lloyd 1997). A more recent review concluded that more than 60% of the MD studies consider modeling as an essential part of their work (El-Bourawi et al. 2006).

Regardless their precision in prediction of permeation flux, numerous mathematical models have been developed and intensively studied by MD researchers. Nevertheless, these semi-emperical correlations used in these models were derived based on non-porous and rigid tube-shell heat exchangers which are not coupled with mass transfer (El-Bourawi et al. 2006). Also, the heat transfer coefficients, especially under low permeate flux, are strongly affected by the accuracy and applicability of these correlations. Although effort has been made to modify the model parameters to improve the accuracy of the empirical correlations (Bui et al. 2010), the following aspects are yet to be involved (Khayet 2011): the porous structure of the membrane, the interaction between the bulk solutions and membranes, the impact of mass transfer on the heat transfer rates, and temperature and concentration variations alongh the membrane module. The effect of fiber length and packing density also need to be considered.

2.3.3.2 CFD modeling

Since the empirical correlations and conservation equations used in earlier studies only provided simplified one-dimensional solutions, computational fluid dynamics (CFD) simulations involving Navier-Strokes equations in two dimensional (2D) and three dimensional (3D) domains have been employed to provide more reliable and comprehensive information on flow fields, which further improves model applicability and accuracy. For example, Charfi et al. (Charfi et al.) have used numerous submodels, such as the Ergun model, Knudsen-molecular diffusion model, momentum/energy and mass transport equations, in their CFD modeling to study the heat and mass transfer in the sweeping gas membrane distillation process. However, this model is rather complicated for industrial applications due to its high computational workload.

Commonly used simplifications for numerical simulation of the mass transfer process include estimating the mass transfer coefficients using empirical equations (Taha and Cui 2002), assuming a constant mass flux condition (Shakaib et al. 2009), or applying Henry’s law constant to describe the equilibrium state of the targeted compound partitioning between water and the membrane phases (Shakaib et al. 2009). Zhang et al (Zhang 2010; Zhang et al. 2010) suggested treat the transfer processes associated with the membrane and two surrounding fluids as a conjugate problem, and they have simulated the heat and mass transfer in membrane-based ventilators without considering phase changes. More widely used CFD models ignored the permeate flow and only focused on the mass/heat transfer in the bulk feed flow and /or simplify the transfer model across the membranes (Fimbres-Weihs and Wiley 2010). In summary, there has been no report on CFD modeling of all three simultaneous heat transfer steps taking place in the feed, permeate and membrane, respectively, in the DCMD process. Details of CFD model aplication and improvement in MD will be addressed in Chapter 5 and 6.

In a word, despite the lack of capability in obtaining accurate local temperature profiles, the method of using empirical equations has been helpful to provide general guidance for experimental results and process engineering purpose. Although have been rarely applied in an MD system, CFD modeling is anticipated to be a handier tool in terms of revealing the heat-transfer fundamentals by being able to present specific point values of temperature, pressure and velocity in a flow channel. Both methods will be discussed in this thesis.

2.4 Hollow fiber module design concepts

Industrial membrane separation requires large areas of membrane surface to be economically and effectively packaged. These packages are called membrane modules. Effective module design is one of the critical achievements that has led to the commercialization of membrane–based separation units (Baker 2004).

Compared to the other module configurations (plate and frame, spiral wound and tubular), hollow fiber modules have received the most attention because of their unique characteristics of self-support, high membrane packing density and high contact surface to volume ratio (7000–13000 m^2/m^3). They can be easily scaled up. Additionally, hollow fiber modules can be fabricated in different forms for various applications (Porter 1990). The most commonly used form is the conventional axially-parallel fiber arrangement, as shown in Fig. 2.5.

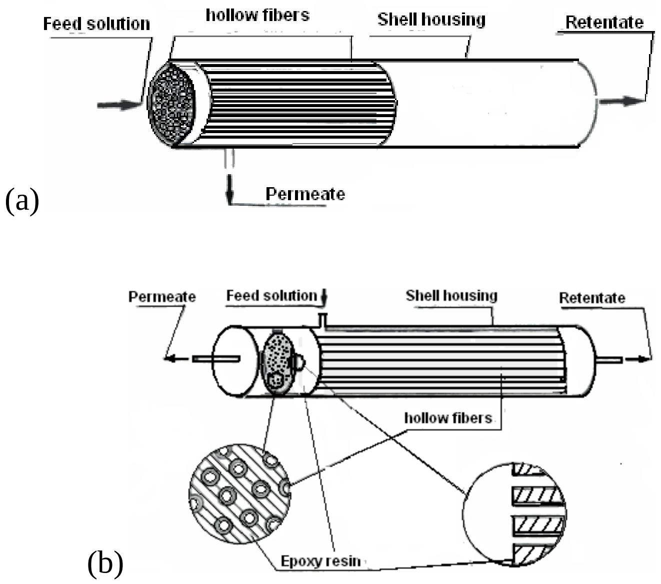

Fig. 2.5 A conventional parallel flow hollow fiber module

(a)bore-feed; (b) shell-feed with dead end (redrawn from (Porter 1990))

Hollow fiber modules typically operate using one of two flow patterns: tube-side feeding or shell-side feeding. The former is commonly used in biotechnology applications and the latter for water applications. In some cases, such as in membrane contactors, both tube and shell sides require controlled flows. Hydrodynamic challenges with the shell-side flow pattern of hollow fiber membrane modules include: bypassing, channeling and dead zones, which result in a loss in separation efficiency. While channeling may not be apparent in small scale bench tests, it becomes a serious concern in full scale applications (Porter 1990). This concern has led to major efforts in improving hydrodynamic conditions to overcome this problem, thus various enhancement techniques have emerged to fill this gap.

Generally, the enhancement aids to design better hollow fiber modules can be classified into two categories: passive enhancement techniques and active enhancement techniques. The commonly used passive techniques include: modifying membrane layout and introducing spacers into the membrane modules to alter the flow geometries. Both strategies serve to more evenly distribute the flow and create sufficient flow instabilities by inducing secondary flows or eddies adjacent to the membrane surface. The active techniques utilizes external energy to induce a high shear rate, which enhances the relative motion between the fluid and the membrane, facilitates mixing and reduces the thickness of the boundary layer at the membrane surface. There is considerable evidence to demonstrate that properly designed and fabricated membrane modules can improve the fluid hydrodynamic conditions and enhance overall system performance dramatically (Gabelman and Hwang 1999; Zhu and Liu 2000; Cui et al. 2003; Akoum et al. 2005; Teoh et al. 2008).

The basic principles to enhance heat/mass transfer in a membrane module are closely linked to the fluid hydrodynamics and membrane module structures/geometries. As discussed in Section 2.3, for general membrane contactors, though the heat/mass transfer through the membrane (h_m / k_m) merely depends on the fluid property and the membrane itself, the heat/mass transfer in the shell side and tube side (h_f / k_{shell} and h_p / k_{tube}) are functions of flow conditions and fiber/module geometries. These semi-empirical correlations shed some light on strategies to improve the heat/mass transfer by varying flow conditions and flow channels.

It is well understood that in the shell side, a high film heat transfer coefficient can reduce the temperature difference between the bulk stream~~s~~ and the membrane surface, thus maximizing the driving force across the membrane. As indicated by Eq. (2.15), the heat transfer coefficient h is related to the Nu and hydraulic diameter d_h. In the regime of fully developed flow, Nu is essentially a constant, thus a small hydraulic diameter would result in a high heat transfer coefficient. Assuming flow is well distributed, the value of the Nu constant depends on the duct geometry. Tightly packed fibers create ducts of a very small hydraulic diameter, leading to a high h. Normally, feed-side heat transfer coefficients are lower than those of the permeate, as the ducts on the shell side have a larger hydraulic diameter than the ducts on the lumen side.

On the tube side, Eqs. (2.20) and (2.21) are widely used to predict the mass transfer coefficient, where Sh_{tube} represents the transport conditions. However, the predictions by this model slightly overestimate the experimental data when the flow velocity is very low. It was found that the tube side mass transfer is not only related to the flow velocity (Reynolds number), but also related to the fiber length and inner diameter (Gabelman and Hwang 1999). As a certain degree of fiber uniformity is reached, the mass transfer coefficient k_{tube} can be predicted reliably. It increases with increasing Reynolds number (more turbulent) and the diffusivity of the solute of interest, but decreases with increasing inner diameter and fiber length. Under given conditions, the Reynolds number seems to be the dominant factor affecting k_{tube}.

On the other hand, the prediction of the shell-side mass transfer coefficient Sh_{shell} is more challenging, since the shell-side geometry and hydrodynamics are more complicated to correlate. Though there are numerous studies that focus on the shell-side, none are universally applicable due to the various parameters incorporated in the different models. However, the basic principles of mass transfer enhancement shown in these correlations are similar (Schofield et al. 1987; Gabelman and Hwang 1999; Gawronski and Wrzesinska 2000; Wu and Chen 2000; Lipnizki and Field 2001; Thanedgunbaworn et al. 2007). It can be concluded that the mass transfer depends on many factors and their combinations, such as the flow velocity (*Re*), states of hydrodynamic/concentration profiles, hydraulic shell diameter and effective length of the module, entrance effects, fiber polydispersity, packing density, and flow maldistribution. Furthermore, the mass transfer may also be influenced by the interaction between the surface properties of the membrane (i.e. hydrophobic/hydrophilic) and the diffusivity of the solute of interest (it affects the D value, which plays a role in calculating k value). For example, hydrophilic membranes may facilitate the transport of inorganic solutes, while hydrophobic membranes may transport the organic solutes preferentially (Gabelman and Hwang 1999; Yang et al. 2007).

Clearly, the main objective of improved membrane module design is to enhance the overall mass/heat transfers. The basic strategies include enhancing the module’s capabilities to create more eddies or turbulence between fibers, reduce the boundary layer thickness and provide better mixing. To achieve these goals, various methods and devices have been employed to enhance the mass transfer inside the module (e.g. the passive enhancement techniques, and active enhancement techniques). These strategies are reviewed in the following sections (refer to Section 2.4.1.1 and Section 2.4.2.2).

2.4.1 Process enhancement aids

2.4.1.1 Passive enhancement techniques

The majority of laboratory or industrial scale modules are designed for use with flat sheet membranes, because the membrane structure is simple and the membrane replacement is easy. From a commercial standpoint, however, hollow fiber modules are more productive as they have much larger surface area per volume. Despite the relatively high fabrication cost, hollow fiber modules can play an important role and gain better performance to minimize the cost per unit product volume (Wickramasinghe et al. 1991; Wickramasinghe et al. 1993; Chernyshov et al. 2005).

Most hollow fiber modules are designed for pressure-driven filtration processes rather than concentration-driven or thermally-driven contactor processes. However, from the process enhancement point of view, they can be adjusted to suit versatile applications to achieve different separation goals such as for MD applications.

(i) Fabric hollow fiber modules

In the early days, due to limited materials and fabrication methods, membranes themselves tended to be the controlling resistance in membrane-based separations. With the advancement of membrane fabrication techniques, it has been possible to produce thinner membranes with higher permeability. As a result, improving mass transfer of the process has shifted to alternative geometries that are able to offer better performance than the conventional parallel flows.

Some researchers have pointed out that flow mal-distribution in the membrane modules can lead to reduction of the average mass transfer coefficient (Cussler 1994). To overcome the problem~~s~~ of non-uniform fiber spacing in commercial modules, which often results in a flow mal-distribution, Wickramasinghe et al (Wickramasinghe et al. 1993) introduced fiber-woven fabric into hollow fiber modules to gain more uniform spacing. The results showed that the shell-side mass transfer coefficient was significantly higher than that of the commercial parallel modules. In order to make a comparison, they tested different configurations as shown in Fig. 2.6.

To compare the mass transfer coefficient per surface area of each module with that of a single fiber which represents the ideal situation, Wickramasinghe et al (Wickramasinghe et al. 1993) correlated *Re* (flow velocity) and *Sh* (mass transfer coefficient) under different flow regimes. The results showed that the fabric woven module (Fig. 2.6b) gained the highest mass transfer coefficient, which was more than 10 times higher than that of conventional modules at very low flow rates. It may be due to the multiple shell-side passages caused by a number of plugs and O-rings contained in this module. In other words, this type of module can achieve the same transfer rate as the conventional parallel module but with much less membrane area. These authors proposed the following shell-side mass transfer correlation, which is in good agreement with the experimental data (Wickramasinghe et al. 1993):

$$Sh = 0.82 Re^{0.49} Sc^{0.33} \tag{2.28}$$

Although their results were obtained based on the system of oxygen recovery from water, they also observed that these modules could be applied to both gas-liquid and liquid-liquid separations. Similar observations have been made by other authors (Chernyshov et al. 2005; Khayet et al. 2005).

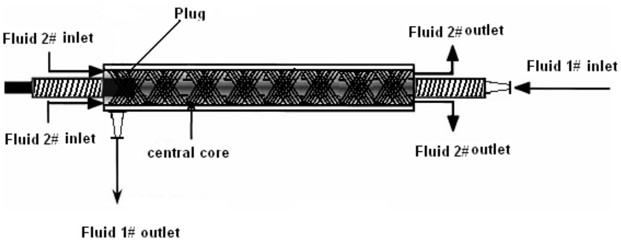

(a) Axial helically wound

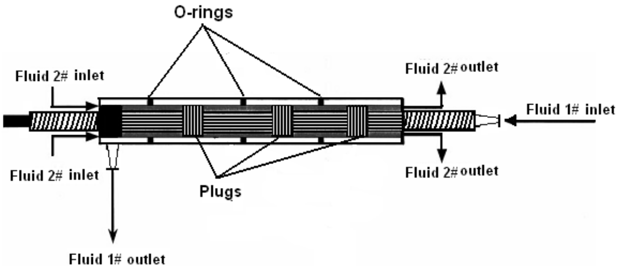

(b) Fabric woven with plugs and O-rings

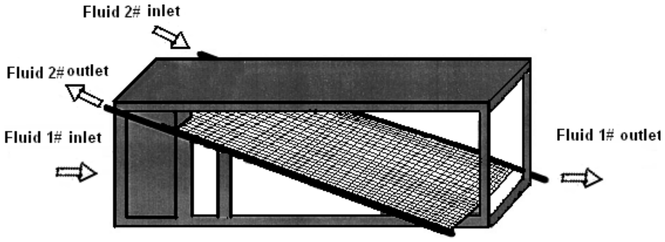

(c) Vane with fabric fibers

Fig. 2.6 Fabric hollow fiber modules:

(a) Axial wound module with fibers wound helically around a central core; (b) fabric module winds a hollow fiber fabric around a central core; (c) vane module with a vane of hollow fiber fabric mounted diagonally inside an open ended box (redrawn from (Wickramasinghe et al. 1993))

Another variant in module geometry is a fabric hollow fiber module with baffles. Wang et al (Chernyshov et al. 2005) reported that a baffled membrane module of hollow fiber fabric can supply both countercurrent contacting and perpendicular flow to the well spaced fibers. They tested and compared the baffled modules (shown in Fig. 2.7), unbaffled rectangular modules (not shown here) and conventional parallel flow module containing individual fibers. They also applied the same numerical model developed by Wickramasinghe et al (Wickramasinghe et al. 1993) to obtain the mass transfer coefficients. Surprisingly, it was found that the baffled rectangular modules (Fig. 2.7a) performed more poorly than the non-baffled ones, which was attributed to the stagnation of liquid in some corners of the shell side caused by the baffles, leading to the reduction of active contact area between adjacent fibers in each layer.

However, the baffles introduced to cylindrical modules (Fig. 2.7b) were able to achieve a better fluid mixing since the fluids tended to flow backwards and forwards between the spacers. As expected, the fully-baffled cylindrical module achieved the best performance per unit area, whereas a similar module with fewer baffles performed almost as well as the fully-baffled one. Moreover, the authors concluded that the counter-current flowing patterns had much higher mass transfer coefficients. The authors proposed that the following shell side mass transfer correlation was in good agreement with the experimental data:

$$Sh = 0.46Re^{0.46}Sc^{0.33} \tag{2.29}$$

This is similar to Eq (2.28) for the fabric module, but with a smaller coefficient of proportionality.

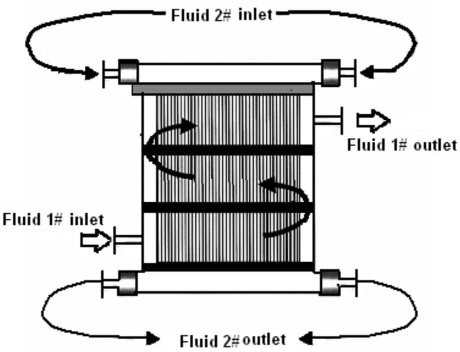

(a) Baffled rectangular module

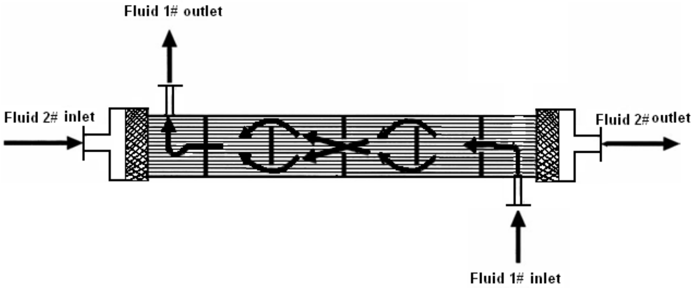

(b) Fully baffled cylindrical module

Fig. 2.7 two types of baffled hollow fiber modules (a) rectangular module with 2 baffles; (b) cylindrical module with fully baffled (redrawn from (Chernyshov et al. 2005))

From the examples mentioned above, it can be seen that baffles can constrain the hydrodynamic conditions in some cases (e.g., Fig. 2.7a). These previous studies suggest that turbulence promoters do not always enhance module efficiency. The effectiveness depends on how the promoters are arranged and how the flow channels are actually distributed. However, most of the mentioned configurations improve the fluid distribution and mixing to achieve much higher mass transfer coefficients in both gas and liquid separations (Wickramasinghe et al. 1993; Chernyshov et al. 2005).

(ii) Hollow fiber modules with transverse flow

Another geometry-based membrane module improvement technique is known as “transverse flow” or “radial cross-flow” (baffled module have some of this feature). With this technique, the membrane module has a central tube for shell-side feed distribution. The flow pattern in the module is radial cross-flow. The function of the central tube is to eliminate the concentration polarization and enhance the process in the upstream when scaling-up to a larger diameter (e.g. 0.3m). This configuration can also be achieved by forming a membrane bundle with knitted hollow fiber fabrics instead of individual hollow fibers, similarly to the modules discussed in the previous section.

One of the well-known commercial modules with a central tube is the Liqui-Cel®Extra-Flow module (as shown in Fig. 2.8), which was patented by CELGARD LLC (Sirkar 1995). This module contains Celgard® microporous polypropylene fibers that are woven into a fabric and wrapped around a central tube feeder that supplies the shell-side fluid. The woven fabric allows a more uniform fiber spacing, which leads to better flow distribution and higher mass transfer coefficients than those obtained with individual fibers. The fibers are potted into a solvent-resistant epoxy or polyethylene tube-sheet (Fig. 2.8).

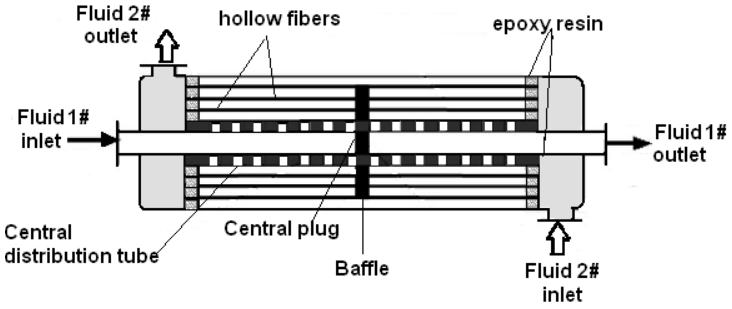

Fig. 2.8 The mechanism of Liqui-Cel®Extra-Flow module (redrawn from (Sirkar 1995))

The Extra-Flow module has a central shell-side baffle which improves the module efficiency by minimizing shell-side bypassing and provides a radial cross-flow to achieve a higher mass transfer coefficient than that of conventional parallel flows The largest module can handle liquid flow rates of thousands of liters per minute (Martínez-Díez et al. 1998).

Another transversal flow membrane module for liquid separation contains a number of hollow fibers which are arranged perpendicularly to the longitudinal axis of the module (Gronda et al. 2000). This type of module comprises many transverse-current flow segments formed by the seals between the main body and the shell. The channels in the fibers are connected to a space presented around the body which is further surrounded by a shell.

The concept of transversal flow in hollow fiber modules arose from the fabrication of similar flat sheet modules (Martinez-Diez and Vazquez-Gonzalez 2000; Phattaranawik and Jiraratananon 2001). It has recently been widely applied to gas-liquid absorption such as CO_2 removal from natural gas, pervaporation of ethanol from water, concentration of organic substances from aqueous solutions and dialysis in the artificial kidney (as shown in Fig. 2.9). Compared to the conventional contactors such as mixing towers or columns, the membrane contactors can avoid the constraints of flooding, loading, entrainment and foaming. In addition, the membrane module with a special fiber layout as shown in Fig. 2.9 exhibit better mixing, higher recovery and lower energy consumption than the hollow fiber module with a parallel layout. In spite of the complication in module assembly, one of the most competitive advantages of the transversally-arrayed hollow fiber module in liquid separation is the reduction of channeling and polarization (temperature/concentration) phenomena. Since this system can achieve well-mixing and better hydrodynamics at a relatively low velocity, it may also help to avoid the membrane wetting in a contactor due to the smaller hydrostatic pressure drop along the fiber (Wenten 2009). Hence, such configurations can be potentially applied to new processes like membrane-based extraction and membrane distillation (MD) which are subject to severe pore wetting.

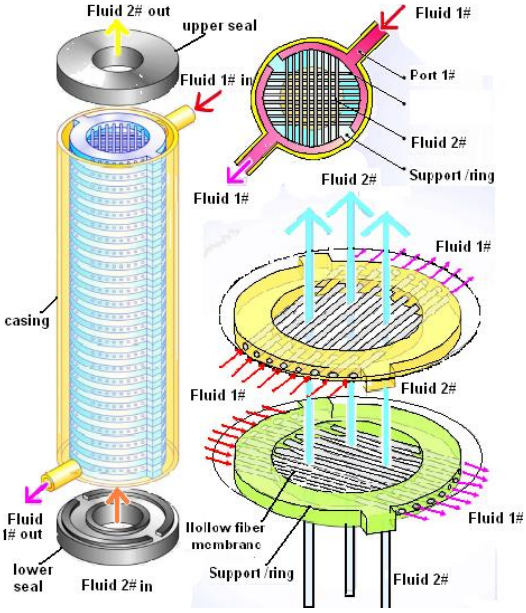

Fig. 2.9 The medical application of transversal membrane contactor (redrawn from (Gronda et al. 2000))

(iii) Dual hollow fiber modules/ U-shape modules

A dual hollow fiber module for CO_2 removal is shown in Fig. 2.10. This integrates the absorption and desorption processes in one module with different fluids flowing in the two bundles, respectively (Wenten 2009). It was observed in a CO_2 removal system, CO_2 was separated from the mixed gas flowing through bundle #1 and dissolved into the absorbent solution; while the desorbent flowing in bundle #2 will help to strip the CO_2 from the solution. Similar designs can be found from previous studies (Trimmer.Johnny.L 1992; Rijn et al. 2002). Compared to conventional linear modules, this type of module comprises one or more hollow fiber bundles which not only increases the contact area between fluids, but also crimp the flow channels to create better hydrodynamics. It was reported that this may favor both the gas and liquid separation due to the improved permeate flow characteristics and improved space/volume characteristics. The fiber bundles are very flexible and can be of any shape rather than being subject to mechanical stretching by the sealing epoxy. The possible configurations are shown in Fig. 2.11. To avoid or minimize liquid film transfer resistance, the liquid within the module needs to be agitated by circulating or other means (e.g. stirrer).

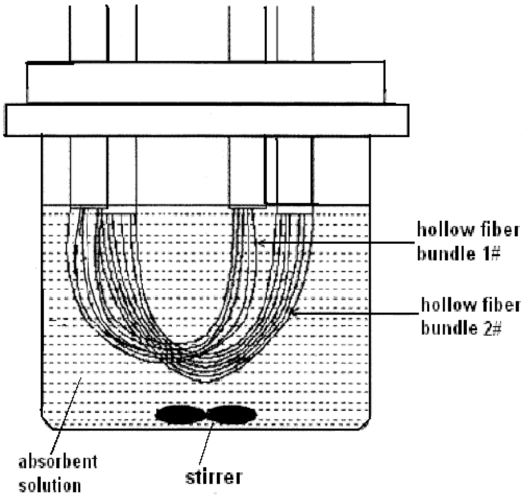

Fig. 2.10 dual hollow fiber module (redrawn from (Wenten 2009))

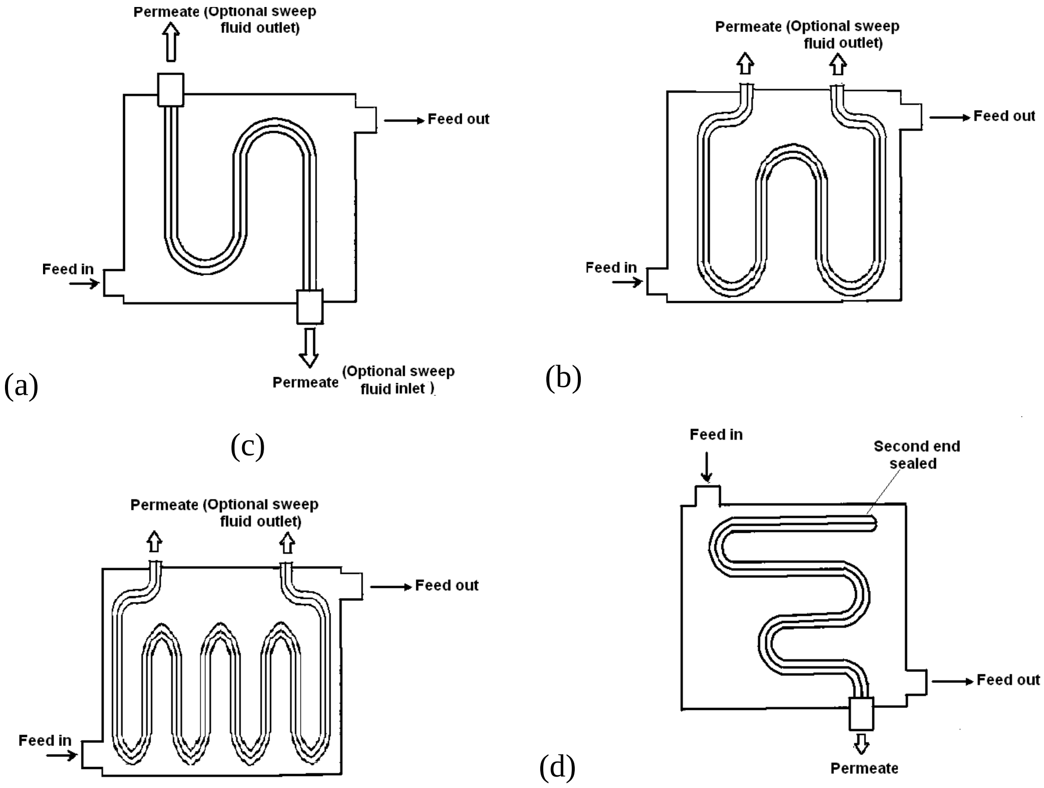

Fig. 2.11 flexible U-shape hollow fiber modules: (a) coiled; (b) French horn; (c) spiral; (d) one-ended U shape (redrawn from (Trimmer.Johnny.L 1992))

(iv) Hollow fiber module with modified fiber geometries

Most researchers focus on introducing channeled designs to enhance the flow passage, presenting various fiber layouts to even the flow distribution effectively, inserting turbulence promoters such as spacers, screens or baffles. Limited work (Ghogomu et al. 2001; Ding et al. 2003; Li et al. 2004; Teoh et al. 2008), however, has been done to investigate the enhancement effect of hollow fiber configurations with wavy geometries such as crimpled, braided and twisted fiber geometries, shown in Fig. 2.12.

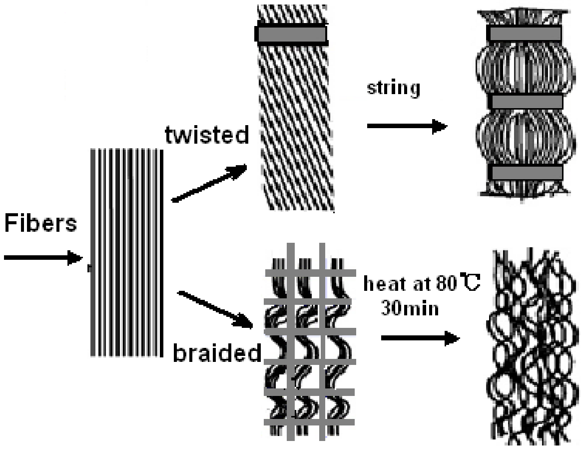

Fig. 2.12 hollow fiber configurations with wavy geometries (redrawn from (Teoh et al. 2008))

As reported by Teoh et al (Teoh et al. 2008), wavy geometries in the membrane distillation process led to flux enhancement by as much as 36% compared to that of a conventional straight-fiber module without inserting any external turbulence promoter. This seems to be more efficient than window or helical baffles assisted systems which correspond to 20~28% enhancements, respectively. Ghogomu et al (Ghogomu et al. 2001) studied MD using a hollow fiber module with coiled fibers. It was found that all the curved geometries, such as those that are helically coiled, twisted sinusoidal or meander-shaped, can induce dean vortices (secondary flows) which can significantly enhance the process as compared to conventional straight fibers. Li et al (Li et al. 2004) also reported the use of a commercial hollow fiber module Monsanto’s Prism® with crimpled fibers which was made by Monsato Company. It has been successfully used in H_2 recovery, and it may have the potential to be applied in liquid separation processes in the future.

Curved fibers as a geometry improvement can efficiently and easily be applied to increase the fluid-membrane contact area per unit volume, create better hydrodynamic conditions and enhance membrane flux. Moreover, this type of configuration can find its place in a broad range of industrial applications.

(v) Other hollow fiber modules

Some other passive, geometry-based membrane module improvements are described here. One hollow fiber module with a plurality of membrane units was designed to perform an attempted separation of one or more components from a multi-component feed (Fig. 2.13), each unit contains a number of elongated hollow fibers which are connected to the collecting manifolds. The axial movement of fibers is allowable due to unrestrained manifolds. This design solves a classical problem in hollow fiber modules that fibers should have a longer length than the shell in case of axial shrinking, and it alleviates the differential expansion between the membrane tubes and shell since the novel design allows the membrane tubes to expand independently. In order to meet different requirements of different separation processes, an integral two-stage (in parallel or series) module with two embodiments is also applicable (Li et al. 2004) (Fig. 2.14).

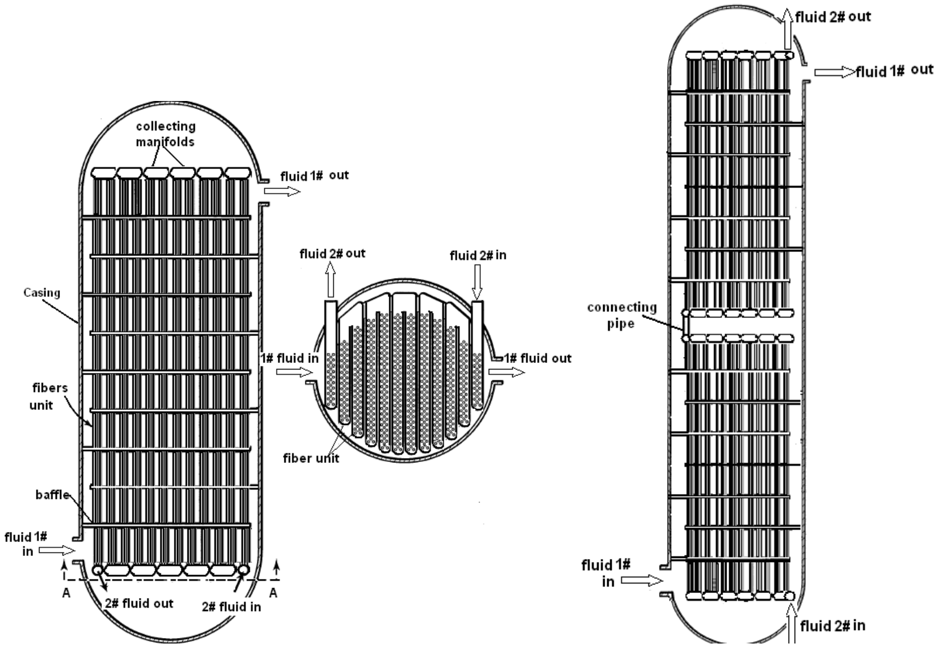

Fig. 2.13 Novel hollow fiber modules for fluid separation (redrawn from (Phattaranawik et al. 2003))

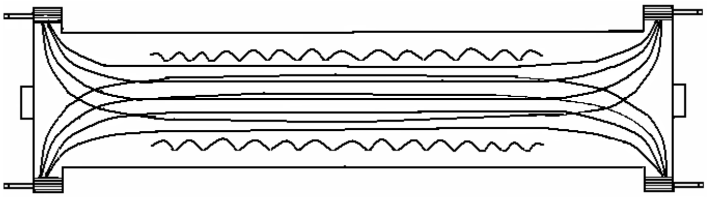

Fig. 2.14 Internal staged permeator for fluid separation (redrawn from (Generon 2000))

Submerged membrane modules are more versatile in aqueous separation processes; they are widely used in membrane bioreactor processes (Cath et al. 2004) (Fig. 2.15). In most cases, due to the severe fouling in biological wastewater treatment, the submerged module is operated with air sparging which can enhance the process effectively. This approach will be discussed in Section 2.4.3.2 in detail.

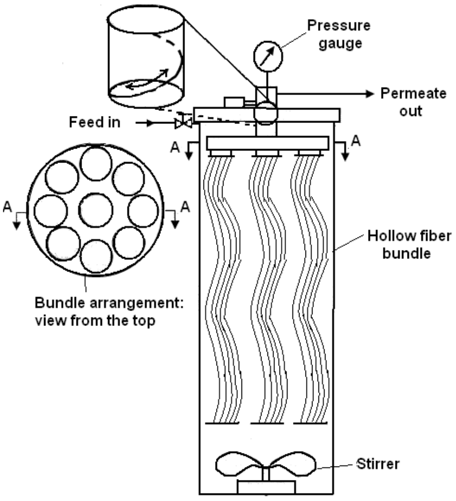

Fig. 2.15 Advanced submerged hollow fiber module (redrawn from (Cath et al. 2004))

Some of the membrane separation processes (such as membrane distillation or osmotic distillation) require extra cooling or heating devices for post treatment or to increase process driving force. Multi-functional modules, which serve separation as well as heat exchange purposes, have been developed (Herczeg 2004; Hanemaaijer et al. 2006). If the heat exchange operation is sufficient in a single module, then subsequent connected heat exchangers may be rendered unnecessary. For example, Memstill® technology developed by TNO institute and Kepple Seghers Company is now operated at the pilot scale in Singapore (Hanemaaijer et al. 2006). It combines a continuum of evaporation stages in countercurrent flow pattern which makes the heat recovery process simultaneously. A similar concept can be found from a European patent (Fig. 2.16).

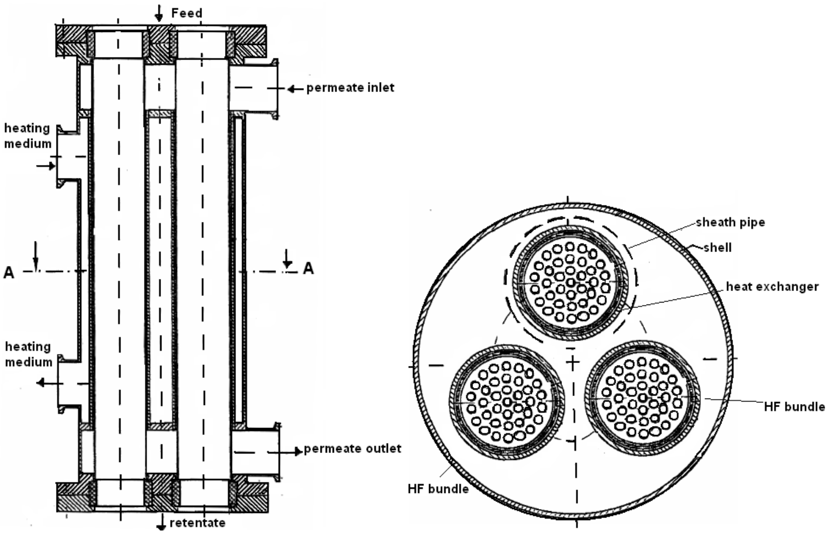

Fig. 2.16 Filter membrane module comprising an integrated heat exchanger (redrawn from (Herczeg 2004))

Most of these passive enhancement modules have been widely applied in gas/liquid contactors. They have the potential to be used for concentration-driven liquid/liquid mass transfer and temperature-driven MD processes, where their simplicity (and hence ease in manufacturing) would be an advantage. Furthermore, these configurations offer substantially higher mass transfer rates. Some of the commercially available filtration modules can also be applied to concentration-driven or thermally-driven processes such as membrane distillation, as they are able to provide good mixing conditions to enhance heat and mass transfer in both the bulk solution and the solution-membrane interface. It should be noted that most of these modules have only been studied in laboratory scale, except the Liqui-Cel®Extra-Flow module. There are some other commercial examples, which have not been categorized here due to the insufficient information. For example, the

DISSO3LVE^{TM} module, which is marketed by W.L. Gore & Associates (Wikol 1998), was primarily applied for the ozonation of semiconductor cleaning water. The Separel^{TM} EFM-530 module by Pall Corporation, was used in ultrapure water applications in a bubble-free gas/liquid manner (Krygier 1998). Similarly, Membrane Corporation provided modules designed for bubble-free gas/liquid mass transfer in applications such as oxygenation processes in bioremediation and aeration in wastewater treatment (Semmens 1998); In the late 1980s, Enka AG developed a commercial hollow fiber module for the membrane distillation process (Schneider et al. 1988). That was an axial-flow counter-current arrangement for DCMD.

2.4.1.2 Active enhancement techniques

Advancements in membrane materials and membrane fabrication techniques and broad applications of membrane-based processes have facilitated development of technologies for membrane module design and fabrication. There have been several generations of membrane modules to meet the demands of various applications. While the passive enhancement techniques described above can enhance membrane performance significantly by utilizing and distributing the energy of the fluid flow itself, there are still limitations that allow these techniques to only offer a moderate enhancement in mass transfer, and the improvement is limited for concentrated or viscous feed solutions.

In contrast, active enhancement techniques allow the introduction of various forms of external energy to improve membrane processes. Fane and Chang (Fane and Chang 2008) have briefly summarized various active enhancing strategies and reviewed their development up to early 2005. Those strategies include pulsed flow, high shear devices (rotating and vibratory systems), two-phase flow systems, electro-filtration, ultrasound-enhanced filtration, etc. The present review will focus on the mass transfer enhancing mechanisms and progress achieved in the past five years for the most commonly proposed techniques, such as bubbling, vibration waves and ultrasound. Additionally, the benefits and drawbacks of these active enhancement techniques will be highlighted in this section, and further compared in Section 2.4.4 with respect to energy consumption.

(i) Bubbling systems

The most widely used active approach to avoid membrane fouling in membrane-based processes, especially in membrane bioreactors, is air bubbles (Fane et al. 2002; Li et al. 2005; Psoch and Schiewer 2005; Kim and DiGiano 2006; Wicaksana et al. 2006) to induce surface shear and reduce membrane fouling. Especially, in a membrane bioreactor process, air sparging serves the double purpose of providing aeration and producing a two-phase flow to control fouling. As reviewed by Cui et al (Cui et al. 2003), the principles of process enhancement and fouling control by using bubbling systems (gas flow applied either inside or outside of the fiber) include:

(1) Bubble induced secondary flow;
(2) Displacement of the concentration polarization layer;
(3) Passing bubble induced pressure pulsing;
(4) Increase of superficial cross-flow velocity.

To correlate the bubble size/characteristics (effects of air flow rate, orifice size, fluid properties, submergence. etc) and bubble induced fiber movement into the module performance, it is essential to characterize the uniqueness of the bubbling system and distinguish the contribution from bubbles of different sizes. Many researchers (Chang et al. 2002; Wicaksana et al. 2006; Yeo et al. 2006; Lu et al. 2008; Zhang et al. 2009) have investigated the effect of bubble size on module performance in the submerged MBR systems. For example, to observe the relationship between bubbling and module performance via critical flux, trans-membrane pressure (TMP) and membrane fouling formation, Wicaksana et al (Wicaksana et al. 2006) studied the interaction between bubbling and fiber movement in submerged hollow fiber membranes. It was found that a lower fouling rate could be achieved by more fiber movement under certain conditions such as fiber looseness, smaller bubbles, higher air flow rate, lower feed viscosity and lower solid concentration. The authors also stated that the fiber movement was enhanced by using thinner and longer fibers, but it was insensitive to nozzle sizes (bubble sizes) used in the system. To study the fouling mechanism in submerged hollow fiber membrane modules with bubbling, Yeo et al (Yeo et al. 2006; Yeo et al. 2007) used the particle image velocimetry (PIV) to examine the bubble-induced phenomena by varying and correlating different operating parameters, they also stated that many small bubbles are better than few large bubbles.

Although Fane (Fane and Chang 2008) and Cui et al (Cui et al. 2003), have extensively documented the development of membrane processes associated with bubbling and demonstrated the benefits of bubbling systems that have caused an upsurge of interest in the use of air bubbles to enhance membrane process (e.g. submerged membrane bioreactors), there are some limitations in the applications of this coupled system. For instance, in most bio-separation processes using UF/MF hollow fiber modules (Cui et al. 2003), the fragmentation of protein or micro-organisms (Clarkson et al. 1999; Clarkson et al. 1999; Clarkson et al. 2000) will occur and aggregation could easily happen due to the high shear rate when bubbles burst. Therefore, bubble-flow induced bio-separation process can only perform well under relatively low air sparging rates. In high pressure membrane processes (NF and RO), the air can be dissolved into the feed at the high pressure side and released into the permeate side which may lead to back pressure build-up and lower the efficiency of the separation process. Additionally, a certain volume of gas must be injected into the modules at the operating pressure to achieve a higher critical flux. This could be energy intensive for high pressure applications.

Although the concept of gas sparging to enhance transport and reduce fouling formation can be very effectively applied to various membrane processes, a comprehensive study is deficient on the characteristic flow patterns (bubble flow, slug flow, churn flow and annular flow) in this gas-liquid two phase system, the dominant role of the slug flow regime, parameters contributing to pressure losses and fouling rate controlling factors. In hollow fiber modules, it is important to determine that the bubbles should be introduced through tube or shell sides, and to overcome the difficulty in ensuring even air distribution in a confined hollow fiber module.

(ii) Vibrating membranes

The original concept of dynamic filtration to improve membrane performance by applying vibration was initiated by Armando et al (Armando et al. 1992) from New Logic International Inc. The system was known as vibratory shear enhanced processing (VSEP), and contained a stack of membrane disks mounted in a circular casing connected to a torsion spring and a motor. The motor generates a vibrating force on the membrane elements. The vibration can help to disrupt the concentration and/or temperature polarization and fouling layer formation, which as described above are the major challenges in membrane-based processes. This concept has also been commercialized by Pall Filtration, US (PallSep 2004), their product was named as PALL-Sep Vibrating Membrane Filter..

Compared with the conventional cross-flow system, a vibrating membrane offers a lot of advantages. The conventional cross-flow system has a relatively low shear rate (less than 10,000~15,000/s), which restricts its application to low-concentration and low-viscosity feed solutions. Moreover, in spite of the high flow rate introduced into the system, membrane fouling and flux decline still easily occur due to an insufficient shear rate that cannot prevent the accumulation of retained particles on the membrane surface. In comparison, the vibrating system of the VSEP unit induces a much higher shear rate (100,000~150,000/s) that increases turbulence at the membrane surface and promotes the back diffusion of particles to the bulk solution effectively. Comparison of the working principles and wall velocity distributions in a conventional cross-flow and a VSEP system are shown in Fig. 2.17 and Fig. 2.18, respectively. It is clearly illustrated that in a VSEP system, the maximum flow velocity occurs near the membrane wall which will break down the boundary layer and keep particles suspended above the membrane surface (Culkin); while in a conventional cross-flow system, the flow adjacent to the membrane wall is stagnant, it can cause scaling or fouling formation easily.

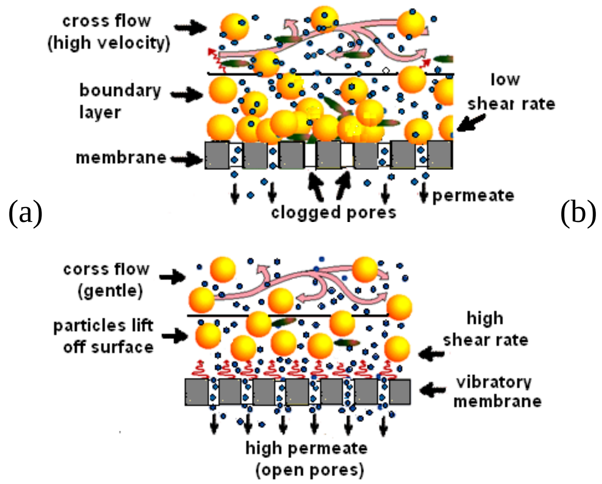

Fig. 2.17 The mechanism of particles removal due to shear in (a) conventional cross flow system and (b) VSEP unit (redrawn from (Culkin and Armando 1992))

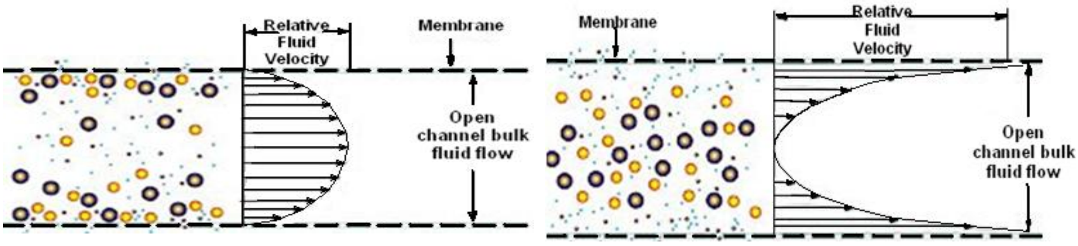

(a) (b)

Fig. 2.18 Comparison of velocity distribution profiles in: (a) cross-flow system; (b) VSEP system

Due to its benefits, the commercial VSEP module has been successfully used in treating concentrated feeds such as landfill leachate and high-salinity seawater (mainly reverse osmosis) in industry (Culkin). Recently, many researchers have tried to broaden its applications in the food industry (Akoum et al. 2002; Akoum et al. 2005) or pervaporation process (Vane et al. 1999), and extend this concept to hollow fiber modules such as submerged membrane bioreactors (Beier and Jonsson 2006; Genkin et al. 2006; Beier and Jonsson 2007; Beier and Jonsson 2009). Although the hollow fiber modules have higher potential for practical applications, there are only limited studies involving vibrating assisted hollow fiber modules (Krantz et al. 1997; Beier and Jonsson 2006; Beier and Jonsson 2007; Beier and Jonsson 2009) (a vibrating submerged hollow fiber module is shown in Fig. 2.19).

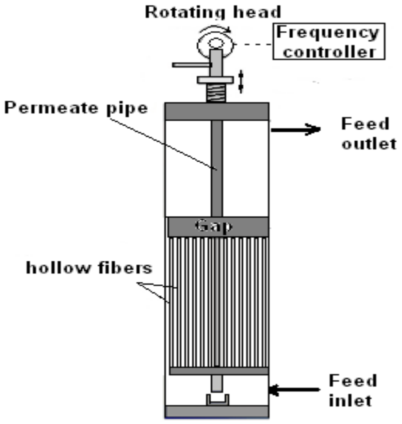

Fig. 2.19 hollow fiber vibrating membrane bio-reactor (VMBR) associated with vibrating device (redrawn from (Beier and Jonsson 2009))

To summarize the vibrating membrane techniques, vibrating the membrane itself, as opposed to vibrating the flow, can advantageously achieve the most relative motion on the membrane surface. This motion between bulk solution and membrane can greatly reduce the liquid boundary layers and the membrane fouling and polarization effects on both sides of the membrane. As a result, vibratory systems might have the potential to be coupled with other processes which suffer from low permeability or severe polarization, such as membrane distillation or membrane distillation bioreactors.

Thus, it is hoped that the vibrating concept can be implemented for various applications because it offers economically competitive advantages in treating high-salinity water and has the potential to greatly advance the use of membranes in desalination. However, there are also some limitations in this area, such as the potentially high demand of external energy input (detailed in Section 3.4.3) and the complexity of rotating devices, which lead to the relatively high operation maintenance and equipment costs in the system.

(iii) Ultrasonic system

Ultrasonic waves, as one of the active enhancement techniques in membrane separation, refers to acoustic waves of frequency between 20 kHz and 10 MHz accompanied by some concomitant physical effects, such as those to do with mechanics, thermotics and cavitations. The propagation of ultrasonic waves in various media is beneficial to many physical and chemical processes.

By introducing ultrasonic vibration, micro-streaming induced rapid fluid movement, acoustic heating and cavitations, ultrasonic technique has the practical capability to enhance filtration and membrane separation by mitigating membrane fouling, reducing concentration/temperature polarization effects and removing fine particles from the surface. It has been successfully applied to several membrane processes (Okahata and Noguchi 1983; Kost and Langer 1988.; Band et al. 1997; Li et al. 2002; Muthukumaran et al. 2005; Feng et al. 2006; Liu et al. 2007; Tran et al. 2007), such as MF, UF and dialysis which suffer from concentration polarization and subsequent fouling. It has also been reported that acoustic vibrations and induced heating could enhance thermally driven processes such as membrane distillation (Zhu et al. 1999; Zhu and Liu 2000), and improve their permeability, greatly reduce temperature polarization and membrane fouling. The mechanism of an ultrasonic irradiation system is illustrated in Fig. 2.20.

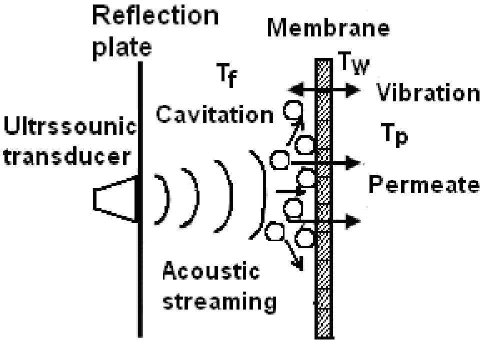

Fig. 2.20 Mechanism of ultrasonic irradiation system (redrawn from (Zhu and Liu 2000))

This concept was initiated by Madsen (Madsen 1977) who investigated the influence of ultrasound on hyper-ultra-filtration membrane separations. Later, Kobayashi et al (Chai et al. 1998; Kobayashi et al. 1999) observed for cross-flow UF of dextran that the high frequency vibration of the membrane surface resulted in the reduction of concentration polarization, thus increasing permeate rate as compared to the classical stirred system. The authors also stated that ultrasonically assisted dead-end UF system can be equally effective. It is also reported that the ultrasonic wave can induce convective currents and cavitations which are able to mitigate the concentration polarization (Simon et al. 2000). Other authors found that ultrasound was a promising technique to recover trans-membrane flux (Juang and Lin 2004; Muthukumaran et al. 2005). For example, 70~80% recovery can be achieved for a Cu–Polyethylenimine (Cu–PEI) solution. Detailed review on flux recovery can also be found in other literature (Fane and Chang 2008).

By combining the experimental data and mathematical modeling work, researchers found that process improvement increased with increasing intensity, and decreased with increasing acoustic frequency, solution temperature or even active membrane area. In an ultrasonic-assisted air gap membrane distillation system (Zhu and Liu 2000), the enhancement was up to 200% with 0 to 5 Wcm^{-2} intensity of the ultrasonic irradiation.

In previous studies, the ultrasonic enhancement technique was mainly applied to filtration using flat sheet membranes, and only few studies have been reported on other membrane processes involving hollow fiber modules. This may be due to the difficulty in identifying the appropriate position to place the reflection plate (refer to Fig. 2.20) and the transducer on the module; and the process enhancement factor can be affected. Thus, the enhancement potential of ultrasonic-assisted hollow fiber modules (membrane contactors) is yet to be exploited.

Notwithstanding the positive enhancement to several membrane processes, some authors have reported that ultrasonic radiation at inappropriate frequencies and intensities may damage the membrane. For instance, it has been observed via field emission scanning electron microscopy (FESEM) that some polymeric materials can be restructured by ultrasonic irradiation (Masselin et al. 2001; Juang and Lin 2004; Wang et al. 2005), such as polyethersulphone (PES), cellulose nitrate with cellulose acetate (CN–CA) or nylon6 (N6); on the other hand PVDF and Poly Acrylonitrile (PAN) showed no observable damage with long term exposure. Though some work has been done to examine the mechanism of membrane damage by ultrasound (Chen et al. 2006), caution must be taken to choose proper membrane materials, ultrasonic intensity and irradiation duration to avoid membrane damage.

(iv) Miscellaneous techniques

Beside vibration, bubbling and ultrasonic techniques which have been intensively reported, there are other techniques, such as magnetic stirring, ozonation (Huang 2008) and the use of electric fields (Chen 2007), that can create enhanced hydrodynamic conditions in membrane separation systems to enhance the permeation and reduce membrane fouling.

2.4.2 Energy consumption analyses

Most of the membrane-based separation processes involve lower energy consumption than conventional separation techniques due to the mild operating conditions and almost no chemical addition. However, as energy consumption is becoming a major concern worldwide, membrane users are also trying to minimize energy cost. For example, the specific energy consumption for RO desalination was 4.5 kWh m^{-3} in 1980, and it has been further reduced to less than 2.8 kWh m^{-3} recently (Baker 2008). As stated previously, module fabrication and design play important roles in the membrane process commercialization. The main objectives of module design should not only focus on maximization of the system performance through optimizing the flow geometries and external assistant devices, but also include minimization of the cost per amount of mass transferred (energy consumption and module production cost). According to the discussions in the previous section, both passive and active enhancement techniques have been employed in various systems to enhance the permeate flux and reduce membrane fouling for long-lasting performance. However, in these systems, energy consumption is always a significant concern, especially for active enhancement techniques which involves imposed energy such as aeration, oscillation or ultrasound. Therefore, this section will provide a preliminary energy analysis and energy consumption levels of various enhancement techniques.

Among the module configurations reviewed in this chapter, the energy consumption may come in the form of circulating energy and imposed energy (e.g. high pressure pumping, aeration, oscillation and ultrasound, etc.) The energy required for recirculating the feed is proportional to the head-loss across the membrane and the flow rate. The power consumption of the feed pump P_c is given by:

$$P_c = \frac{\Delta P Q_R}{\eta} \tag{2.30}$$

where V_R is the circulation flow rate (m^3 s^{-1}), and η is the efficiency of the pump (%). Normally the pump efficiency can be taken as 60% and no frictional loss is assumed (Gander et al. 2000). The specific energy consumption (*SEC*, kWh m^{-3} product) can be determined by:

$$SEC = \frac{P_c}{Q_P} \times 3.6 \tag{2.31}$$

Where V_p is the permeate flow rate (m^3 s^{-1}), which can also be expressed as the product of the permeate flux and membrane area. The imposed energy varies significantly from application to application.

The comparison of *SEC* in various membrane systems is presented in Table 2.1.

Table 2.1 Energy consumption levels of various membrane module systems

configuration	**Conventional module**	**Dynamic shear-induced system**				
	Spiral wound	Bubbling system (2-phase-flow, MBRs)	Vibratory system / VSEP	Vibratory system with coagulant addition	Ultrasonic system	Ultrasonic System
Process	Sea water RO	Submerged MBR	RO of dilute skim milk	Submerged MBR with 34ppm ACH	MD 1%NaCl solution	RO-WW
Membrane	Dow Filmtec™ SW30XLE-400i	Zenon, HF/ PE	FS/ Desal AG	HF/PVDF	PTFE, Millipore	ND
Area/m^2	37	31.5	100	0.0057	0.0160	0.0056
TMP/MPa	25	10(initial)	4	0.045	ND	0.1
Flow rate/ m3 h^{-1}	ND	ND		ND	0.011	0.0003
Shear rate/ s^{-1}	10,000~15,000 (Culkin and Armando 1992)	18,000~69,000 (Akoum et al. 2002)	135,000 (Culkin and Armando 1992)	2,000	ND	ND
Permeate flux/l m^{-2} h^{-1}	18	12.4	55	46	15	35
Circulation energy/ kWh m^{-3} product	1.05 (feed pump)	--	1.67	--	1.31	0.053
Frequency/ Hz	--	--	60.2	1.7	20	20,000
Imposed energy / kWh m^{-3} product	2.8 (min power required for high pressure pump)	--	1.63	0.29	351.6	800
SEC / kWh m^{-3} product	3.85	1.1-1.7	3.3	0.29	352.9	800
Calculation based on	(Zhu et al. 2009)	(Judd 2006)	(Frappart et al. 2008)	(Genkin et al. 2006)	(Zhu et al. 1999)	(Feng et al. 2006)

Key: FS, flat sheet; HF, hollow fiber; PE, polyethylene; ND, no data given;

As shown in Table 2.1, comparing the specific energy required for per m^3 permeate, the pressure-driven RO process with conventional spiral wound module is still relatively high due to the high pressure pumping, while in the submerged membrane system with air sparging the *SEC* is relatively low— but it has the lowest permeate flux. Therefore it is unwise to compare the high pressure and low pressure processes directly, the figures shown in Table 2.1 are to give an idea on the energy consumption of conventional membrane process and processes coupled with imposed energy forms. For example, the dynamic shear-induced system VSEP maintains much higher flux for a given amount of energy input. This advantage may become more apparent for difficult feed solutions (high concentration, high viscosity, etc.). The laboratory investigation of the ultrasonic system shows a significantly higher energy demand due to the high frequency ultrasound involved. Thus, compared to the other techniques, the ultrasonic system seems to be the least economic method. Nevertheless, since there is an offset relationship between the capital cost and energy demand in membrane processes, efforts still need to be made for higher flux and lower energy input.

Many energy-reduction strategies have been proposed by different researchers. For example, in submerged MBR systems, the main contribution of energy consumption is aeration. Thus, effective implementations of intermittent air-sparging and appropriate nozzle sizes can minimize the cost and suppress the low fouling rate (Cui et al. 2003; Sofia et al. 2004; Zheng and Liu 2004). In vibratory systems, the major energy consumption is rotation or vibration. For some applications, the VSEP system uses the resonant frequency to maximize the vibrating amplitude and presents a low *SEC* in industrial modules — only 9 kW with membrane area up to 150 m^2, while in this example the pumping energy for MF and RO varied from 5kW to 16kW. To treat wastewater by using 150 m^2 VSEP modules, the *SEC* is estimated as 4.1 kWh m^{-3} product in MF and 2.5 kWh m^{-3} product in RO and would be 22% less for the treatment of surface water (Culkin and Armando 1992). Genkin et al (Genkin et al. 2006) combined the vibration with submerged MBR system to achieve considerably high critical flux 130 L h^{-1} m^{-2} (normally around 20 L h^{-1} m^{-2}) by applying a combined axial-transversal oscillation at a low frequency of 10 Hz. Furthermore, with the addition of reasonable amount of coagulant 34 mgL^{-1}, the critical flux reached a maximum value 86L h^{-1} m^{-2} at low frequency (1.7 Hz) instead of high frequency when the floc will break up. (This low frequency operation requires a *SEC* of only 0.29 kWh m^{-3}, see Table 2.1). With the application of the ultrasound, researchers (Zhu et al. 1999; Feng et al. 2006) also found performance enhancement at certain frequency (lowest 20 kHz) and irradiation intensity, but the *SEC* is still relatively higher than other systems because of the high frequency imposed.

Above all, the approaches for energy reduction in membrane processes are focused on minimizing the fouling rate while maintaining an optimum performance, which are associated with reliable and economic operations to produce high quality products. This is the key factor that drives membrane technology to be more competitive than the conventional separation methods.

Membrane-based separation processes have found numerous applications in industries in recent decades. However, concentration and temperature polarization (in MD) and membrane fouling-induced high energy consumption, low productivity and short membrane lifespan present severe technical challenges to the commercialization of most membrane processes for liquid separation. Novel module technology is one of the key technologies to tackle the challenge.

2.5 Summary

In the commercialization of MD applications, the major concerns are the low permeation rate, concentration and temperature polarization and pore wetting phenomenon. To overcome these barriers, improved membrane module technology is one of the key strategies. As most of the hollow fiber module design concepts mentioned in Section 2.4 have not been implemented in industrial applications, and some commercialized applications have not yet reached their full potential, attempts to develop novel modules should begin with better understanding of the mass and heat transfer in the membrane modules. Fundamentally, for industrial applications, the general objectives of module design should include maximizing the system performance and minimizing the cost per unit of targeted product by means of optimizing the flow channels inside the modules (referred to as “passive enhancement techniques”) or inducing higher surface shear rate (referred to as “active enhancement techniques”). Moreover, constrains on scale-up, operating period, fouling control and membrane replacement should also be considered. Specifically for MD module design and optimization, the features in a conventional axial hollow fiber module including fiber characteristics (diameter, thickness, porosity, tortuosity and length), packing density, operating flow rate, flow direction and fluid properties, etc, need to be investigated systematically. In addition, some existing design concepts can be adopted and adjusted to MD applications, such as the baffled/spaced modules, transverse flow modules, Memstill concept, modified fiber geometries and modules associated with vibration, bubbling or ultrasound systems. It is anticipated that these concepts can be incorporated into novel MD module design and may provide significant enhancement.

Another effective way to tackle the pore wetting problem in MD is membrane development. Other than exploring highly hydrophobic materials, surface modification technologies provide more possibilities and easier solutions to improve those currently used membranes by grafting or crossliking an ultrathin hydrophobic or hydrophilic coating on the surface of a hydrophobic membrane.

To supplement the industrialization of MD, a practical modeling tool is needed to present and simulate this process. Though many investigators have worked on MD modeling and employed various semi-empirical correlations to illustrate the mass/heat transport mechanisms, CFD tools can be used to simulate the module performance and investigate the optimal parameters for improved process performance (enhanced the mass flux, alleviated TP effect and reduced energy consumption).

CHAPTER 3

PERFORMANCE IMPROVEMENT OF PVDF HOLLOW FIBER-BASED DCMD PROCESS

3.1 Introduction

As MD process can yield highly purified distillate and deal with concentrated salt solutions/brines under mild operating conditions (Lawson and Lloyd 1997; Karakulski et al. 2002), it has great potential to be applied in many applications, such as in desalination of seawater and brackish water and brine concentration. However, MD has some potential disadvantages, such as flux lowering due to poor hydrodynamics and inefficient module design (Lawson and Lloyd 1997) and distillate contamination due to membrane pore wetting (Banat and Simandl 1994; Lawson and Lloyd 1996), the latter is one of the main factors hindering the wider application of MD technology.

The maintenance of the vapor phase in dry membrane pores during MD is an essential condition for process function. To avoid pore wetting, the membrane material has to be hydrophobic with a contact angle as high as possible and the membrane should have a relatively small maximum pore size. However, since most of currently used membranes suffered drawbacks such as the presence of some large pore sizes which may cause membrane wetting even though the membranes are highly hydrophobic (Phattaranawik et al. 2003). As stated in the previous chapter, the suface modification can help to minimize wetting and improve the applicability of these membranes for the MD processes: Though the majority of modifications have been to apply a nonporous hydrophilic layer, this is likely to add more resistance than a porous hydrophobic coating. Our approach in this current study is to evaluate hydrophobic coatings.

Most of the reported MD studies have focused on flat sheet membranes due to their availability in hydrophobic materials. This is particularly so for PTFE which is processed in sheet form. However, in industrial applications, which require a large membrane surface area per unit volume without supporting structure, hollow fiber-based membrane modules are considered more favorably. Additionally, as a thermally driven process, MD can be significantly affected by the temperature polarization if the hydrodynamic conditions deteriorate (Schneider et al. 1988; Hogan et al. 1991; Lagana et al. 2000). It has been shown that the hollow fiber module could potentially have the least temperature polarization among various module configurations (Schofield et al. 1987). However, there are limited reports available on improving fluid dynamics and designing hollow fiber modules for MD applications in the open literature (Ding et al. 2002; El-Bourawi et al. 2006; Cheng et al. 2008). Some relevant studies have focused on the effect of packing density, flow maldistribution and hydrodynamic behavior in the shell side of hollow fiber modules, based on studies of various gas-liquid/ liquid-liquid contactors (Noda et al. 1979; Prasad and Sirkar 1988; Costello et al. 1993; Lemanski and Lipscomb 1995; Wu and Chen 2000; Zheng et al. 2003). It is widely accepted that non-ideal flow distribution leads to less active membrane area and insufficient mass transfer, and thus poor module performance. Generally, in order to increase membrane area and reduce module fabrication costs, larger module housings, higher packing density and/or longer fiber length are preferred in industry (Thanedgunbaworn et al. 2007). However, it has been observed in MD studies that the thermal efficiency can be impacted negatively by increasing packing density and fiber length because the distillate tends to be heated up along the fibers (Song et al. 2007; Cheng et al. 2008). In addition, the risk of membrane pore wetting increases with the increasing fiber length due to the imposed hydrostatic pressure drop along the module length (El-Bourawi et al. 2006).

A good flow geometry maintaining turbulence among the fibers can minimize the undesirable TP effect which leads to lower driving force across the membrane and consequently lower permeation flux. Therefore, several researchers have focused on introducing channel designs, presenting sufficient membrane arrangement to enhance mixing conditions, inserting turbulence promoters or utilizing active aids (ultrasonic devices) to enhance the flow passage and mixing conditions (Martínez-Díez et al.

1998; Zhu et al. 1999; Zhu and Liu 2000; Phattaranawik and Jiraratananon 2001; Li and Sirkar 2004). For example, a systematic study on applying spacers to increase flux were done by Phattaranawik et al, they verified that an increase of permeation flux as high as 60% was achieved from the investigation of 20 different spacers with different voidages and hydrodynamic angles. Although various baffles/spacers/turbulent promoters have been commonly employed for UF and MF applications (Gupta et al. 1995; B.J. Bellhouse and Costigan 2001), their application in MD process is only limited to flat sheet cases (Martínez-Díez et al. 1998; Zhu et al. 1999; Zhu and Liu 2000; Phattaranawik and Jiraratananon 2001; Li and Sirkar 2004). A study of modified baffles and spacers for hollow fiber modules has been reported by Teoh et al (Teoh et al. 2008) that the application of various hollow fiber configurations with wavy geometries led to flux enhancement as high as 36% without inserting any external turbulent promoter.

In this current study, we examine strategies to improve DCMD performance from two aspects: (1) modification of membrane surface properties; and (2) optimization of the hollow fiber module configuration. Specifically, we have enhanced membrane hydophobicity, reduced membrane pore sizes by two types of modification treatment, and then compared the modified and unmodified membranes in terms of sustainable flux and long-term performance. In addition, the fluid dynamics, effects of module diameter, effective fiber length, packing density and fiber geometries on the MD performance have been investigated based on heat transfer analysis. It is expected that this study can help identify potential approaches to overcome the commonly encountered problem of membrane wetting and mitigate the concentration/temperature polarization effects to facilitate practical applications of the MD process.

3.2 Experimental

3.2.1 Membrane material and modification methods

The unmodified membrane used in this chapter was newly developed polyvinylidene fluoride (PVDF) hollow fiber membranes supplied from Siemens Water Technology (SWT). To improve the membrane properties for better MD application, two surface modification methods were applied to modify the original PVDF hollow fiber membrane, as elaborated below.

3.2.1.1 Plasma modification

Plasma modification of the original PVDF hollow fiber membrane was conducted using a plasma device (model no P2i Ion Mask 40i) under a vacuum pressure of 20 mmHg. The plasma coating involved two subsequent processes: 1) surface activation, and 2) grafting of fluoroalkane. The monomers, which included 1H, 1H, 2H, 2H-perfluorodecyl acrylate, have different abilities to penetrate in to the membrane pores, as this is a diffusion controlled process. The degree of activation, the depth of the reactive layer into the membrane, and the thickness of the grafting layer on the very top of membrane was adjusted by power and time of the activation and polymerization steps, respectively.

3.2.1.2 Chemical modification

The chemical modification involved hydroxylation of the PVDF membrane by an aqueous lithium hydroxide (LiOH) solution and successive reduction with an organic sodium borohydride ($NaBH_4$) solution, followed by cross-linking with a fluoro-compound. The LiOH pretreatment resulted in HF elimination from the PVDF and the attachment of an oxygen element to the material. Subsequent reduction of the LiOH-treated PVDF membrane with $NaBH_4$ embodied the membrane with hydroxyl functions. Since the hydroxyl functional group (-OH) is reactive, cross-linking using a fluoro-compound with an ethoxysilane terminal group was performed, which was able to chemically bond to the -OH sites.

3.2.2 Membrane characterization

3.2.2.1 Measurements of hollow fiber membrane’s liquid entry pressure of water (LEPw), porosity and pore size distribution

The measurement of LEPw was conducted using dead-end hollow fiber modules containing 3–5 fibers. The detailed methodology can be found elsewhere (Smolders and Franken 1989). It should be noted that the pressure at which a continuous flow of water was observed on the permeate side was assumed to be the membrane LEPw. The Laplace equation provides the relationship between the maximum pore size, LEPw and the related operating conditions (Lawson and Lloyd 1997):

$$LEPw > \Delta P_{interface} = P_{liquid} - P_{vapor} = \frac{-2B\gamma_L \cos\theta}{r_{max}} \tag{3.1}$$

where B is a geometric factor determined by pore structure, γ_L is the liquid surface tension and θ is the liquid/solid contact angle. The membrane pores will be subject to wetting once the operating pressure exceeds the LEPw.

The membrane porosity is defined as the volume of the pores divided by the total volume of the membrane. It can be determined by comparing the density of the polymer material using isopropyl alcohol (IPA, analytical grade from VWR Co Ltd), which penetrates into the pores of the membrane, and the density of the membrane using pure water, which does not enter the pores. The detailed methodology was proposed by Smolders and Franken (Smolders and Franken 1989).

The pore size distribution were determined by a capillary flow porometer (model no CFP 1500A, from Porous Material. Inc (PMI)), whose working principle is based on the bubble-point and gas permeation tests (Khayet and Matsuura 2001). The hollow fiber samples were potted into the sample holder and soaked by the wetting fluid (Galwick, with surface tension 15.9 dynes/cm) till completely wet. During the test, the gas flow rate was increased stepwise and passed through the saturated sample until the applied pressure exceeded the capillary attraction of the fluid in the pores. By comparing the gas flow rates of a wet and dry sample at the same pressures, the percentage of flow passing through the pores larger than or equal to the specified size can be calculated from the pressure-size relationship.

3.2.2.2 Measurements of dynamic contact angle, mechanical strength and membrane morphology

Dynamic contact angle was measured by using a tensiometer (DCAT11 Dataphysics, Germany). A sample fiber glued to the holder was hung from the arm of an electro-balance, and then put through a cycle of immersions into DI water. The contact angle was calculated from the wetting force based on the Wihelmy method.

The mechanical strength of the fibers was measured using a Zwick 0.5kN Universal Testing Machine at room temperature. The sample was clamped at both ends and pulled under tension at a constant elongation velocity of 50 mm min^{-1}. Tensile modulus and tensile stress at the break point were measured to indicate the mechanical strength of the fibers and the degree of deformation under a given load.

To observe the morphologies of the original and modified PVDF hollow fiber membranes, dried membrane samples were fractured in liquid nitrogen and sputtered with a thin layer of gold. The cross-section and inner surface of the hollow fiber membranes were examined using a Zeiss EVO 50 Scanning Electron Microscope (SEM).

3.2.3 Membrane module fabrication

Lab-scale MD modules were fabricated by potting the unmodified and modified PVDF hollow fiber membranes into Teflon housings. The specifications of all modules are listed in Table 1. Two different sizes of Teflon housing (9.5 mm and 19 mm) were used in the investigations in this chapter. Regular modules, type #1 (9.5 mm housing) were packed with various types of membrane and were used for flux assessment. Modules #1 (9.5 mm housing) and #2 (19 mm housing) packed with unmodified fibers were compared in the investigation of module diameter**.** Single-fiber modules (#3), which contained only one straight fiber with various lengths ranging from 150 mm to 1020 mm were made to investigate the effect of fiber length. Module #4 (19 mm housing) of different lengths (450 mm and 650 mm, respectively) and different packing densities (3.5% – 71%) were used in the packing density study. Module #5 (9.5 mm housing) which contained two fibers with various geometries (straight, wry and spacer-wrapped) were made to observe and compare fiber configurations of better process performance.

Table 3.1 Module specifications for all performance tests

Module No	Housing diameter, d_s	Membrane Type	No of fibers, n	Effective fiber length L, mm	Packing density Φ, %	Membrane area A, m^2	Remark
#1	9.5 mm	Original /modified	20	225	50	0.022	Flux tests, circulating velocity and module size comparison
#2	19 mm	Original	80	360	50	0.135	Module size comparison
#3	9.5 mm	Original	1	150-1020	--	--	Single fiber tests
#4	19 mm	Original	--	450/650	3.5-71	--	Packing density tests
#5	9.5 mm	Original	2	225	--	--	Fiber geometries

3.2.4 MD performance tests

The MD experimental setup is shown in Fig. 3.1. Both the feed and permeate solutions were cycled through the hollow fiber module in countercurrent mode. On the shell side, the feed solution (synthetic seawater: 3.5 wt% sodium chloride (NaCl) with conductivity around 60 ms cm^{-1}), was heated (in range 313K – 343K) and circulated by a peristaltic pump (0–12 L min^{-1}). On the lumen side, the permeate (pure water, with conductivity around 0.5 μs cm^{-1}) was cooled down to 298K by a cooling circulator and cycled by another peristaltic pump (0–4 L min^{-1}). The distillate was collected in an overflow tank sitting on a balance (±0.1 g)).

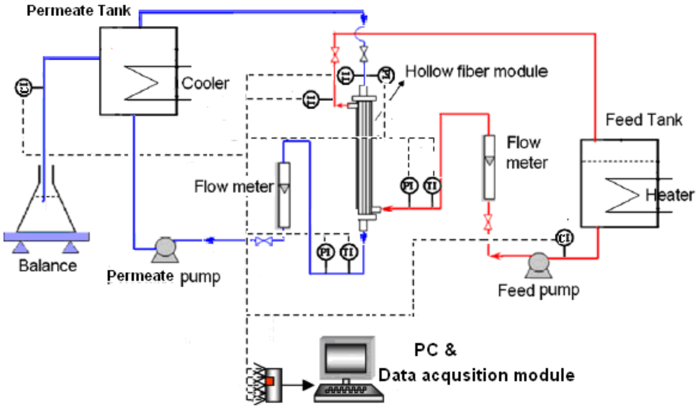

Fig. 3.1 DCMD experimental set-up

3.3 Results and discussion

3.3.1 Membrane Characterization

The SEM pictures, which show the morphologies of the outer and inner surfaces and the cross-section of the unmodified and modified PVDF membranes, are presented in Fig. 3.2. It was observed that the outer surface of the unmodified PVDF membrane was relatively smooth, while the surface became rougher after grafting with the fluoro-compounds, and the roughness tended to increase significantly after chemical modification (Fig. 3.2a). As for the inner surface morphology (Fig. 3.2b), both the pore size and the number of pores have been reduced visibly after the modifications. This is not surprising for the membrane treated by the chemical method, as the whole membrane was immersed into the chemical solution and the modification occurred throughout the entire membrane. For the plasma treated membrane, the results suggest that the poly-fluoro monomer has penetrated into the membrane pores during the plasma treatment. By observing the cross-section morphology (Fig. 3.2c), it can be seen that the sponge-like structure became tighter after the modifications.

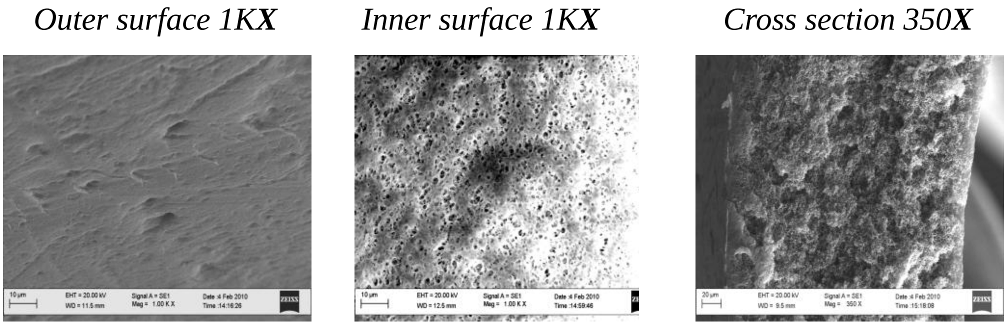

*Outer surface 1K**X*** *Inner surface 1K**X*** *Cross section 350**X***

(a) Original PVDF

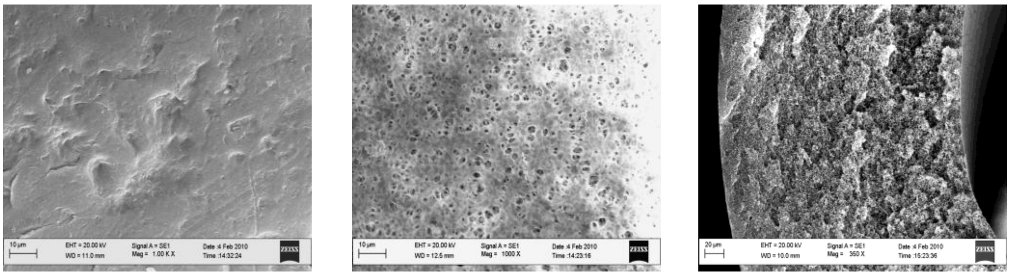

(b) Plasma modified

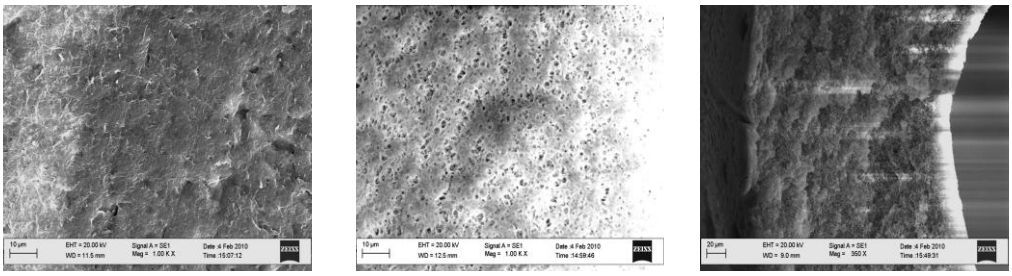

(c) Chemically modified

Fig. 3.2 SEM pictures of the original and modified PVDF membranes

Table 3.2 shows the basic characteristics of the original hollow fiber and two modified membranes, which include the fiber dimension~~s~~, contact angle, porosity, LEPw and mechanical strength. It can be seen that the original PVDF membrane has a very high porosity but relatively poor hydrophobic properties and low LEPw. After the plasma modification, the contact angle and LEPw increased by 20% and 180%, respectively. The chemical modification also improved the contact angle and LEPw of the original PVDF membrane by 30% and 164%, respectively. In addition, both of the modification methods helped to improve the mechanical strength of the fibers.

Table 3.2 Comparison of the original hollow fiber and two modified membranes

Membrane Type	Dimension	Contact angle (°)	Porosity ε (%)	LEPw (Bar)	Tensile modulus E_t ,MPa	Strain at break δ_b, %
Original PVDF	OD:1.47mm δ:275μm	88	85	1.38	44.60	98.60
Plasma Modified	OD:1.47mm δ:275μm	105	83	3.86	41.05	102.08
Chemically modified	OD:1.47mm δ:275μm	115	80	3.64	45.06	121.94

The membrane pore size and pore size distributions (number %) are illustrated in Fig. 3.3. The original PVDF membrane had a distinct bimodal distribution (Fig. 3.3a).Compared to the original membrane which has a maximum pore size of 0.421 μm and mean pore size of 0.064 μm, both modified membranes have much narrower pore size distributions and smaller maximum pore sizes (0.191 μm and 0.189 μm for the plasma and chemical methods respectively). This is due to the introduction of poly-fluoro monomers to the membrane surfaces that have restricted some of the big pores and blocked off some of the small pores in the plasma treatment. In the chemical modification process, the hydroxyl functionized PVDF molecules were cross-linked through fluoro-compound macromolecules, which formed a network on the membrane surface, leading to a reduction of the effective membrane pore size. Fig. 3.3c shows that the chemically modified membrane had the narrowest size distribution. These results are consistent with the change in the LEPw values. The smaller pore sizes of the modified membranes lead to much higher LEPw, as indicated in Table 3.2. Therefore, it is anticipated that the modified membranes would be less vulnerable to membrane pore-wetting but have correspondingly lower fluxes.

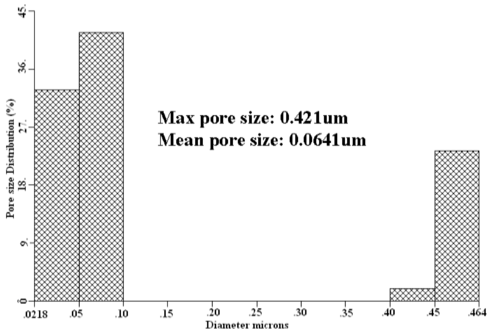

(a) Original PVDF

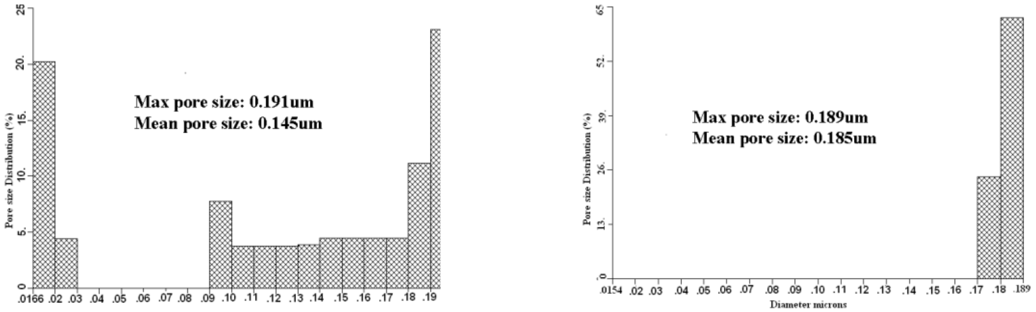

(b) Plasma modified

(c) Chemically modified

Fig. 3.3 Pore size/pore size distribution of the original and modified membranes

3.3.2 MD flux assessment of unmodified and modified membranes

Fig. 3.4 shows the permeation flux as a function of feed water temperature for the three membranes under the same operating conditions. The fluxes of the unmodified PVDF, plasma and chemically modified membranes all exhibited an exponential dependence on temperature, as anticipated by the vapor pressure of water versus temperature relationship given by the Antoine equation (Reid et al. 1977):

$$P = \exp(23.20 - \frac{3816.44}{T - 46.13}) \tag{3.2}$$

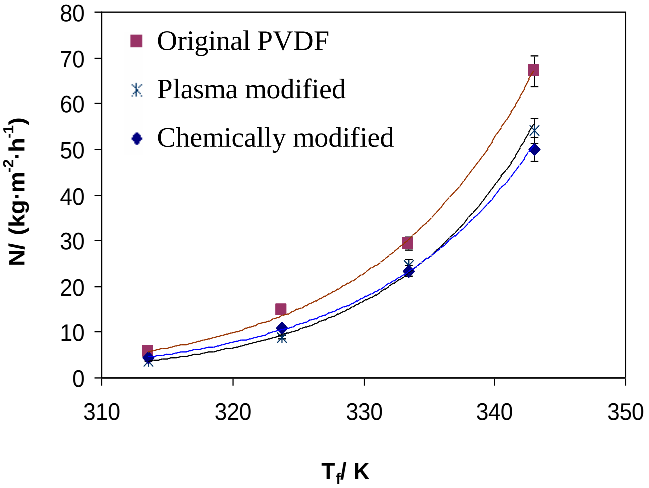

Fig. 3.4 Permeation flux vs. feed temperature (3.5 % NaCl solution as feed, V_f=2.5 L·min^{-1}, V_p=0.4 L·min^{-1}, T_p=298K. T_f=313–343K)

It can be seen that the modified membranes presented similar fluxes to the unmodified one at low operating temperatures, but about 20% flux reduction was found at the operating temperature of 70 ℃. The reasons for the flux reduction were the partial closure of pores, loss of large pores and overall decrease in the porosity after the modifications. In order to assess flux stability the original hollow fiber and two modified membranes were compared in long-term tests.

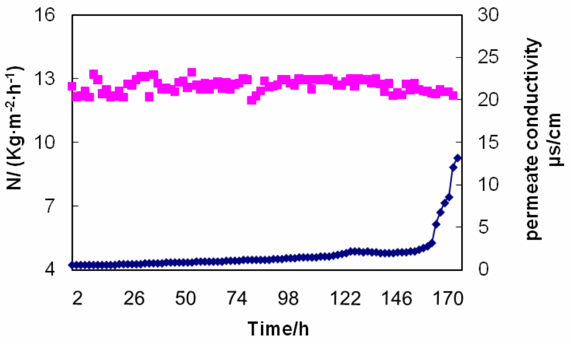

(a) Original PVDF

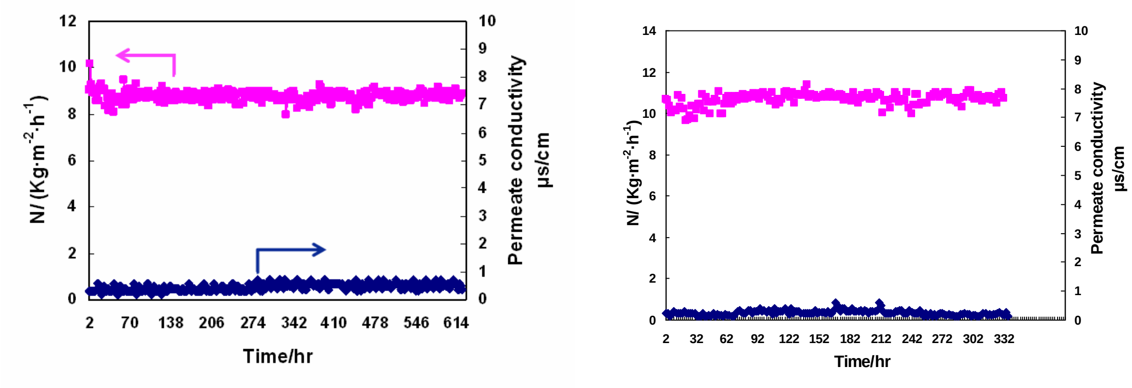

(b) Plasma modified

(c) Per-fluorination modified

Fig. 3.5 Long-term performance of the original and two modified PVDF membranes (3.5 % NaCl solution as feed, $V_f = 2.5$ L·min^{-1}, $V_p = 0.4$ L·min^{-1}, $T_p = 298$ K. $T_f = 323$ K)

Fig. 3.5 illustrates the flux and permeate conductivity of the three membranes over a long period of operation (200 to >600 hours). It can be seen that all of the membranes delivered sustainable fluxes for an extended period but, for the unmodified PVDF membrane, there was a slow and gradual conductivity build-up of the distillate followed by a sudden increase after about one-week (ca 170 hours). This indicates that this membrane was subject to pore wetting and further deterioration of the water quality was expected. In contrast the distillate conductivity obtained from the plasma modified membrane remained below 1.0 μs cm^{-1}, and the chemically modified membrane resulted in more stable performance and even better water quality (<0.5 μs cm^{-1}) over one-month of testing. Therefore, the advantage of the modified hollow fiber membranes over the unmodified is the greatly reduced membrane pore wetting, ensuring effectively 100% salt rejection. The chemically modified membrane achieved this non-wetting performance at a modest flux penalty (<20% lower).

3.3.3 Effects of fluid dynamics

One of the approaches to enhance the mass and heat transfer inside the hollow fiber modules is to improve the hydrodynamic conditions adjacent to the membrane surface, i.e. to optimize the flow velocity of the feed in the shell side. Fig. 3.6 shows the effect of the feed circulation velocity in terms of Reynolds number (Re_f) on the permeation flux. For the smaller module (9.5-mm housing) the MD flux remained unchanged when the flow rate was varied from 2 to 7.5 L·m^{-3} (corresponding to Re_f: 2500 to 9420). This may be due to the fact that the feed stream had reached turbulence (Re_f>2500) within this range and the shell-side was no longer the controlling transport resistance. For the bigger module #2 (19-mm housing), the permeation flux initially increased with increasing circulating velocity and then tended to an asymptotic value when entering the turbulent region (Re_f >2500) signifying a shift to lumen-side controlling resistance, However, the maximum flux obtained in the big module was lower than the small module under the same operating conditions. The difference was probably caused by the lower (lumen-side) Re_p in the larger module due to the similar permeate flow rates used in both modules. The greater fiber length in the larger module would have also contributed to the difference (see section 3.3.4).

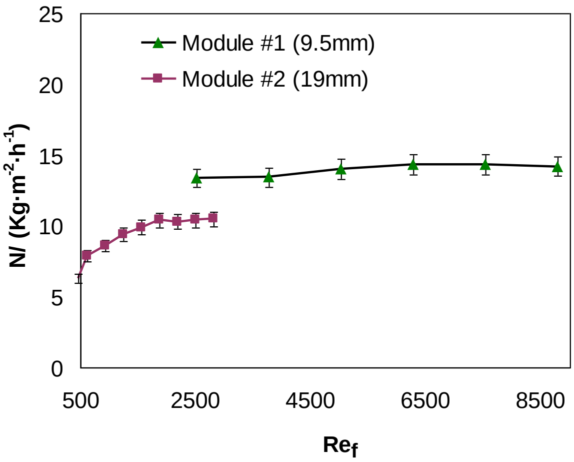

Fig. 3.6 Effect of feed circulating velocity on permeation flux (3.5 % NaCl solution as feed, v_f = 0.82~3.06 m·s^{-1} (module #1) and 0.17–1.05 m·s^{-1} (module #2), v_p = 0.17 m·s^{-1}, T_p = 298 K, T_f = 323 K)

It has been widely reported that a higher feed circulation velocity (i.e. higher mixing intensity) can help to reduce the thickness of the boundary layer adjacent to membrane surface (Banat and Simandl 1994; Bouguccha et al. 2002; Khayet et al. 2003), which is favorable for the mitigation of concentration and temperature polarization, and to maximize the driving force between the feed and permeate sides. However higher pumping energy is required to provide a higher feed circulation velocity. From this study, it was found that a moderate feed circulation velocity can be chosen based on the demand of satisfactory permeation flux and there is no added benefit in increasing flow rate once turbulence is reached.

On the other hand, the lumen-side permeate circulation velocity is also an important factor to be considered. Increase in the permeate circulation velocity can improve the heat transfer on the permeate side by reducing the temperature polarization effect (the effect of concentration polarization is negligible since the permeate fluid in this DCMD study is distilled water). By minimizing the thermal boundary layer on the permeate side, the temperature at the membrane surface approaches the temperature in the bulk permeate and consequently the driving force can be maximized. However it should be noted that temperature polarization on the permeate side is less important as vapour pressure is less sensitive to temperature at lower temperatures (Antoine equation). The greater effect would be the rise in the bulk temperature of the permeate at lower lumen flow. This effects the driving force at the permeate outlet region.

Fig. 3.7 shows the effect of permeate circulation velocity in terms of Re_p on the permeation flux. Since the permeate flowed through the lumen of the hollow fiber, a much low velocity in the lumen was used. It can be seen that the permeation flux firstly increased significantly at low Re range ($Re_p<300$), and then reached a steady asymptotic value when Re_p was higher than 300. The possible reason causing this early onset of the steady-state may be the increased transverse vapor flux that helped break down the laminar boundary layer, thus greatly enhancing the mixing on the membrane surface and facilitating the heat transfer at the permeate side. Consequently, the local film heat transfer (h_p) may not act as a controlling step even when the flow was still under laminar condition. Therefore, based on the study in this chapter, a reasonably low circulation velocity can be chosen to optimize the MD performance with relatively low energy consumption.

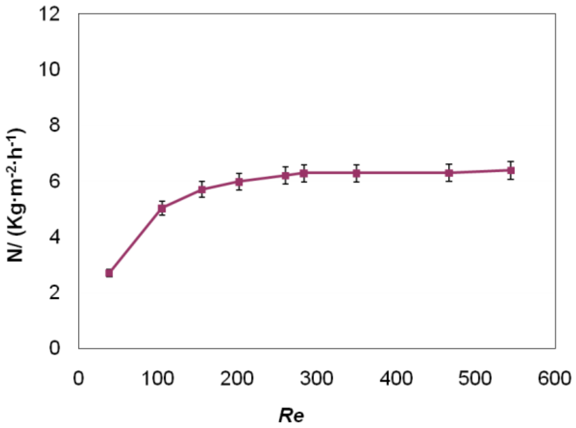

Fig. 3.7 Effect of permeate circulating velocity on permeation flux (3.5 % NaCl solution as feed $v_f = 0.2$ m·s^{-1} v_p= 0.04–0.61 m·s^{-1}, T_p = 298 K, T_f = 323 K)

3.3.4 Effects of membrane module configurations

Fig. 3.8 presents the MD fluxes of the small module and the big modules at different feed temperatures. The flow rates of the feed and permeate for the two modules were kept the same, hence their Reynolds numbers were different. The results showed that the permeation flux increased exponentially with increasing feed temperature from both modules. In evaluating the performance of the larger module #2, several factors should be considered. Firstly, since the large module #2 was operated at a much lower *Re*, which would result in a thicker boundary layer and hence more severe temperature polarization, the mass/heat transfer would be less efficient. This situation would be worse at a higher temperature, as observed. Secondly, the greater length should be taken into account, as performance decreased with increasing fiber length (further discussion is provided in this section). Thirdly, there would be greater tendency to flow maldistribution through the wider flow channel provided in the larger module. A comparison of the two modules can be made by correcting for the size effects in terms of *Re* and fiber length, based on the relationship between flux *N*, *Re* and *L* derived by fitting the experimental results. For example, the large module data in Fig. 3.6 can be correlated by,

$$N(big) = 2.86 + 5.15\left(\frac{Re}{Ld_h^{\,2}}\right)^{0.3} \qquad (R^2 = 0.992) \qquad (3.3)$$

Thus, in an ideal case with the same operating temperatures (T_f = 323K, T_p = 298K) and flow rates (V_f = 3 L·min^{-1}), for a small module of different *Re*, d_h and *L*, the predicted flux *N* would be 7.53 kg m^{-2} h^{-1} based on this equation. However, the actual flux of the small module reached 9.92 kg m^{-2} h^{-1} which was 30% higher than the predicted value. Having allowed for differences in *Re*, d_h and *L* the only significant difference between the small and large modules would be flow maldistribution which would worsen the transport processes in the larger module. To avoid these problems, improved mixing and appropriate fiber arrangement inside the housing are essential in scale-up to larger MD modules.

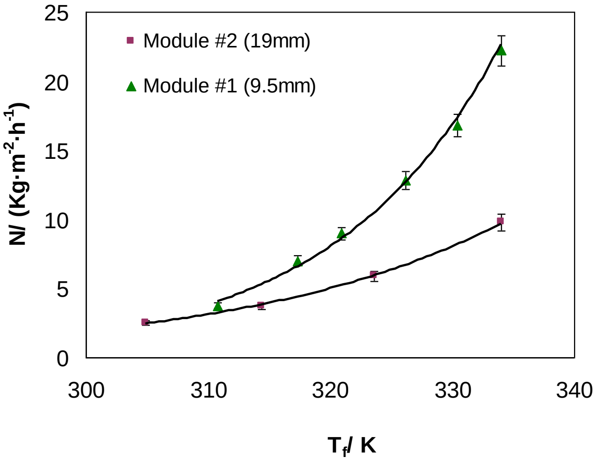

Fig. 3.8 Fluxes of small and big modules at different feed temperatures (3.5 % NaCl solution as feed, V_f = 3 L·min^{-1}, V_p = 0.4 L·min^{-1}, T_p = 298 K)

To investigate the fiber length effect, the relationships between MD coefficient, *C*, film transfer resistance R_i and fiber length, *L*, were plotted. In this case *C* is the overall experimental MD coefficient from equation (2.1) with the log-mean vapor pressures based on bulk temperatures. It is clearly shown in Fig. 3.9a that the MD coefficient decreased dramatically with increasing fiber length in the beginning, and then gradually reached a steady state after a certain length (840 mm). Though the feed side transfer resistances R_f played a dominant role in the mass transfer process over the range tested, all transfer resistances R_i increased with increasing fiber length and gradually reached asymptotic values at the same inflection point as the *C* curve. Hence, we defined a critical fiber length L_C which indicates the fiber length when the inflection point was reached. The corresponding temperature distributions along the fiber length can be seen from Fig. 9b. With an increase in fiber length, $T_{fm} = T_{pm}$ would be approached, eventually resulting in no contribution to the flux. The decrease in the driving force across the membrane with increasing fiber length can be viewed in Fig. 9c, which illustrates the development of thermal boundary layers along the fiber. Initially the MD coefficient decreased and local resistance increased dramatically with increasing length due to the rapid build-up of thermal boundary layers which reduced the temperature difference across the membrane and inhibited the mass and heat transfer. Also more conduction heat loss would be expected at lower wall temperatures when L <840 mm (Phattaranawik et al. 2003). However, with further increase in the fiber length (L >840 mm), the extremely low temperature gradient across the membrane at the end of the fiber would have had negligible differential contribution to the flux. Hence, the critical fiber length L_C is effectively the operational fiber length that contributes to the major portion of the mass transfer of vapor through the membrane. Although a longer module and thus a larger membrane area could result in higher water production, it is important to identify a critical fiber length to assure that the driving force along the fiber is sufficient to maintain a high efficiency. It is detrimental to make the module too long, as it involves compromise of capital and operating costs in industrial applications.

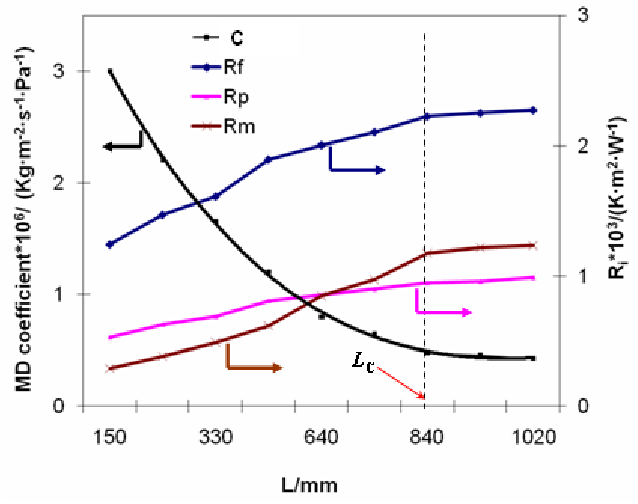

(a) *C* and *Ri* vs. fiber length *L*

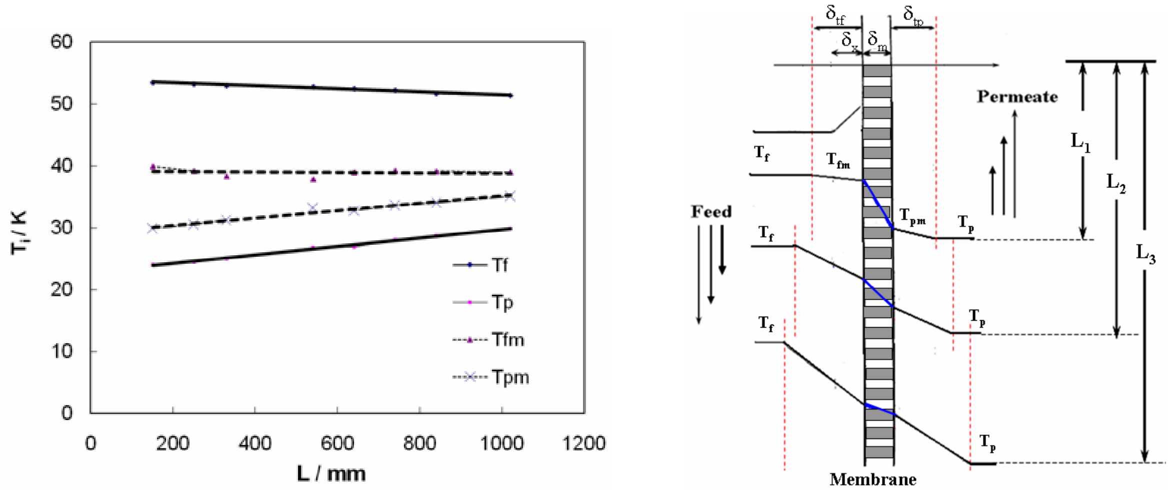

(b) The bulk and membrane wall temperature distributions along fiber length

(c) Thermal boundary layer build-ups along the fiber length

Fig. 3.9 Effect of fiber length (3.5 % NaCl solution as feed V_f = 0.25 L·min^{-1} (Re_f = 992), V_p = 0.017 L·min^{-1} (Re_p = 387), T_p = 298 K, T_f = 323 K): (a) C and R_i vs. fiber length L; (b) The bulk and membrane wall temperature distributions along fiber length; (c) Thermal boundary layer build-ups along the fiber length:

The MD coefficient as a function of the packing density Φ is shown in Fig. 3.10, to further explore the hydrodynamic behavior and the flow mal-distribution in a randomly packed hollow fiber module. The experimental results obtained from the 450 mm-long module and the 650 mm-long module reveal that the overall MD coefficient decreased with increasing packing density. A very high MD coefficient was obtained in the extremely low packing density (<5%), probably due to the local turbulence caused by the presence of transverse flow in a loosely packed module where each fiber had full contact with the two fluids. A dramatic decrease in the overall MD coefficient was observed when the packing density increased in the lower packing density range (5% – 40%). This may be due to the uneven flow distribution of flow around each fiber and the channeling problems in the module. In addition, it should be noted that these modules were tested under the same flow rate, thus both Re_f and Re_p decreased significantly with increasing packing density Φ. Based on hydraulic calculations, the Re_f ranged from 4700 (Φ = 3.5%) to 1100 (Φ = 40%) and the Re_p decreased accordingly because of the increasing number of fibers. Therefore, the hydrodynamic conditions at the membrane surface deteriorated from loosely packed to tightly packed modules. This would also worsen the mass and heat transfer processes. However, when the packing density further increased up to an extremely high value (40% – 71%), the MD coefficient only decreased marginally. This may be due to relatively minor changes in the fluid dynamics in the shell side (Re_f decreased gradually from 1100 to 674). It should be noticed that a similarly complex relationship between the packing density and module performance were observed in many studies involving shell-side flow distribution when using gas-liquid hollow fiber membrane contactors (Prasad and Sirkar 1988; Costello et al. 1993; Wu and Chen 2000; Lipnizki and Field 2001; Thanedgunbaworn et al. 2007).

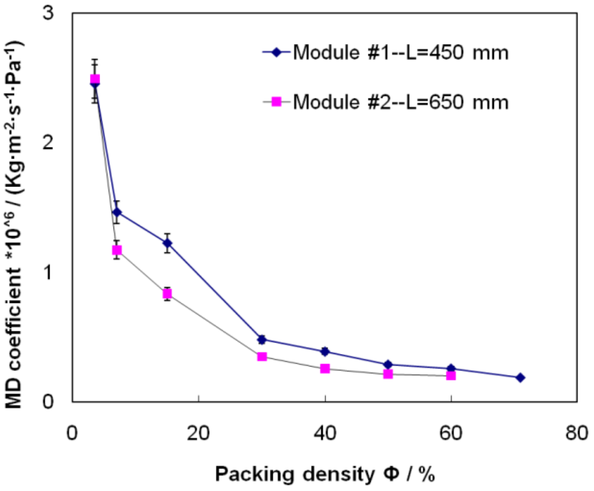

Fig. 3.10 Relationship between the MD coefficient and module packing density (3.5 % NaCl solution as feed V_f = 2.5 L·min^{-1}, V_p = 0.4 L·min^{-1}, T_p = 298 K, T_f = 323 K)

To investigate the variations on the fiber geometries, 2-fiber modules packed with the original PVDF fibers were made by twisting the fibers and baffling flow channel by various means and their fluxes were compared in terms of feed temperature (Fig. 3.11). It was found that the spacer-wrapped-fiber module gained the best enhancement, the enhancement was up to 70% at feed temperature 50 ℃ and 42% at 70 ℃ comparing to the straight-fiber module; while a 48% increase in the obtained flux at 50 ℃ and a 36% increase at 70 ℃ are observed from the module with wry fibers. This may be due to the cross flow induced over the spacer and wavy flow geometries that results in higher heat transfer efficiency compared to a parallel flow.

Therefore, both designs may improve the MD performance by increasing the feed side heat transfer which consequently suppresses the undesirable temperature polarization in the corresponding modules. In addition, similar trends can be observed from these two designs: the enhancement decreased with increasing feed temperature. It is indicating that the temperature polarization effect plays more negative role at higher temperature (El-Bourawi et al. 2006).

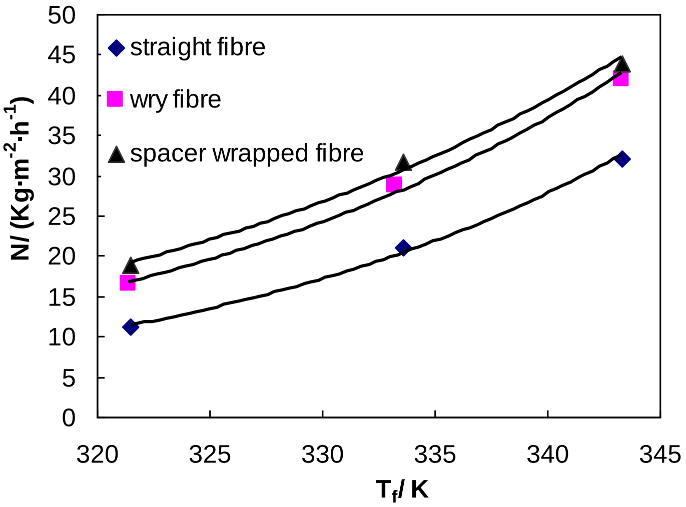

Fig. 3.11 Flux comparison of various fiber geometries (◆---straight fibers; ■---wry fibers; ▲---fiber wrapped with spacers, 3.5% NaCl solution as feed $V_f = 2.5$ L·min^{-1}, $V_p = 0.17$ L·min^{-1}, $T_p = 298$ K, $T_f = 323\sim343$ K)

3.4 Conclusions

In this chapter, two main strategies for MD process improvement have been executed. With respect to the membrane, one type of original hydrophobic hollow fiber and two modified membranes were evaluated for MD applications. It was found that a potential pore-wetting problem existed for the unmodified PVDF hollow fiber membrane due to its relatively low hydrophobicity and liquid entry pressure of water (LEPw). In contrast, both plasma and chemically modified PVDF hollow fiber membranes presented much higher contact angles, LEPw and mechanical strength, and smaller maximum pore sizes and narrower pore size distributions. The chemically modified membrane showed the best overall performance in terms of stable flux and permeate quality.

Due to the complex combination of mass and heat transfer in MD, the driving force and MD coefficient are closely related to the fluid dynamics and MD module configuration. It was found that, the MD flux increased till reaching an asymptotic value Re_f > 2500. Single fiber tests in combination with heat transfer analysis showed that a critical length existed that is the operational length to assure sufficient driving force along the fiber to maintain a high MD efficiency. It was also observed that the overall MD coefficient decreased with increasing packing density. In addition, initial module trials were commenced by comparing the performance of two-fiber-modules with various fiber geometries, it was verified that curved fibers or fibers with spacers aids performed better.

In summary, the study in this chapter suggests that more hydrophobic membranes with smaller maximum pore size and higher LEPw are favorable for MD applications, and optimized fluid dynamics and module configurations (module size, length, packing density and fiber geometries) should also be considered. Therefore, precautions must be taken during MD module scale-up.

CHAPTER 4

CONFIGURATION DESIGNS FOR IMPROVING THE PERFORMANCE OF HOLLOW FIBER MD MODULES

4.1 Introduction

As mentioned previously, despite many attractive characteristics and many lab-scale studies, MD has not been widely implemented in industry (El-Bourawi et al. 2006; Susanto 2011). Major challenges impeding its application include the following: developing appropriate MD membranes to avoid pore wetting; increasing the permeation rates; assessing the energy consumption; and mitigating flow maldistribution and/or poor hydrodynamics and severe temperature polarization (TP) that compromise module performance (Lawson and Lloyd 1996). In recent years a surge of studies have focused on membrane development (Chanachai et al. 2010; Su et al. 2010; Zhang et al. 2010; Khayet 2011; Yang et al. 2011) and energy analysis (Gander et al. 2000; Cabassud and Wirth 2003; Khayet et al. 2003; Zhu et al. 2009; Susanto 2011). However, there has not been a comprehensive investigation of MD module design. Yet the potential benefits of improved module design indicate that a more intensive effort is needed in this area.

Thus far most of the work on hydrodynamic improvement in MD studies has focused on flat sheet membrane modules that have small membrane areas and thus are limited to laboratory research (Martínez-Díez et al. 1998; Phattaranawik and Jiraratananon 2001; Phattaranawik et al. 2003; Chernyshov et al. 2005; Martínez-Díez and Rodríguez-Maroto 2006). In industry, hollow fiber-based membrane modules are preferable due to their larger membrane area per unit volume and reduced vulnerability to TP (Schofield et al. 1987). Although it has been often stated that poorly-designed hollow fiber modules will result in reduced productivity, increased energy consumption and shortened membrane lifespan (Yang et al. 2012), there are limited studies on improving fluid dynamics and designing hollow fiber modules for MD applications in the open literature (Schneider et al. 1988; Ding et al. 2003; El-Bourawi et al. 2006; Cheng et al. 2008; Teoh et al. 2008). It is well-recognized that by incorporating proper flow alteration aids or modifying fiber geometries to create secondary flows or eddies (such as novel fiber configurations or turbulence promoters, e.g. spacers or baffles), the permeation flux can be enhanced and TP can be mitigated. An early exploration on hollow fiber module design by Schneider *et al.* (Schneider et al. 1988) in 1988 investigated the effects of module size and modified fiber geometries on the transmembrane flux of the DCMD process. It showed that larger modules could achieve uniform flow more easily than smaller ones and certain capillary arrangements (twisted and braided geometries) could lead to much higher fluxes than those with straight woven fabric designs. In 2008 Teoh et al. (Teoh et al. 2008) studied different hollow fiber configurations in the DCMD process and found that the introduction of baffles could increase the feed-side heat-transfer coefficients leading to 20−28% flux enhancement. In addition, they also explored the concepts of wavy geometries (twisted and braided) of hollow fibers that were able to achieve as high as a 36% flux enhancement compared to the unaltered conventional modules. Recently, Yang et al. (Yang et al. 2011) described strategies to improve PVDF-based module performance in the DCMD process that included the investigations on the module size, packing density and critical fiber length combined with heat-transfer analysis. Although the existence of simultaneous concentration polarization (CP) and TP will lead to the reduction of mass and heat transfer driving forces, it is well-established that the effect of CP in the DCMD system is negligible in comparison to that of TP (Martinez-Diez and Vazquez-Gonzalez 1999; Khayet et al. 2004). Therefore, the quantification of the TP effect, which is used to assess the thermal efficiency, is essential for the implementation of an MD system (Schofield et al. 1987; Khayet et al. 2005; Khayet 2011). Yet, none of the above-mentioned MD module studies have addressed associated conductive heat loss or the mitigation of TP by altering the fiber geometries or introducing turbulence aids.

In spite of the absence of comprehensive module design work for MD applications, numerous prior studies have been done for general gas-liquid/ liquid-liquid contactors with focuses on the introduction of turbulence promoters (baffles/spacers/channel designs) or special housing configurations as well as on various aspects related to packing density, flow uniformity and shell-side hydrodynamics (Noda et al. 1979; Prasad and Sirkar 1988; Costello et al. 1993; Lemanski and Lipscomb 1995; Wu and Chen 2000; Zheng et al. 2003; Yang et al. 2012). These studies concluded that non-ideal flow distribution in a module will lead to less active membrane area, insufficient mixing and local loss of driving force, and hence low heat- or mass-transfer efficiencies. A recent review by Yang et al. (Yang et al. 2012) summarized the most practical membrane module design concepts and dynamic shear-inducing techniques to enhance liquid separation by hollow fiber modules. Unfortunately, very few of these design concepts have been adapted to MD applications.

Moreover, no report was found to correlate the flow distribution with MD process enhancement. In the DCMD process employing shell-side feed, the occurrence of significant channeling, bypassing, or dead zones can greatly reduce the local driving force and decrease the module performance. Hence, the detection of the flow distribution at the shell-side is important for module design. There are two main methods for characterizing the flow distribution: the experimental approach (tracer response technique) and mathematical modeling (Lemanski and Lipscomb 1995; Ding et al. 2003; Wang et al. 2003). The tracer technique is widely applied for the characterization of the flow distribution and the degree of mixing in membrane bioreactors as well as for the visualization of the shell-side flow distribution in randomly packed membrane contactors (Lemanski and Lipscomb 1995; Rector et al. 2006; Wang et al. 2009). It provides the residence-time distribution (RTD) for the fluid in a closed vessel (Levenspiel 1999). However, no comprehensive RTD study has been done to evaluate MD module performance.

Therefore, the objectives of this chapter are to develop particular hollow fiber module designs that can improve hydrodynamics and thus the MD module performance. The following issues will be addressed: (1) hollow fiber module design; (2) performance evaluation of various designs based on flux enhancement; (3) hydrodynamic studies of modified modules; (3) applications of tracer-response measurement for module flow distribution; (4) heat-transfer analysis to quantify the

TP effect and conductive heat loss of different design configurations.

4.2 Experimental

4.2.1 Hollow fiber module fabrication & assembly procedure

Polyvinylidene fluoride (PVDF) hollow fiber membranes developed by a commercial supplier were used to fabricate lab-scale MD modules. The fibers were potted into the housings that are made by transparent Acrylic material, which is provided by local supplier Acefund Pte Ltd., to facilitate direct observation of the flow conditions around the fiber bundles. Various module configurations were assembled in different ways with similar specifications (Table 4.1): inner diameter 19 mm and effective length 450 mm; packing density of 30%; and membrane area of 0.1−0.11 m^2. In this study a randomly packed module, which contained 51 randomly packed fibers, was fabricated and used as the conventional module benchmark. The fabrication procedure can be found in Chapter 3. In the module fabrication process, care must be taken to avoid damaging the membrane surface and no metal parts were inserted.

Five modified designs were compared. First, a special module with structured-straight fibers was fabricated by weaving all fibers into a fabric sheet that was subsequently rolled up and packed into the housing (Fig. 4.1a). This structured array is anticipated to avoid the clustering of hollow fibers and could possibly lead to more uniform flow distribution in the shell-side.

The second module contains curly fibers (Fig. 4.1b). To create a curly fiber geometry, an appropriate temperature and heat-treatment duration as well as a certain winding angle of the curl were selected. The fibers were first rolled up around stainless steel rods (diameter 1.6 mm) with a winding angle of 60 ° and then placed in an oven at 60 ℃ for 1hr until the curly shape was permanently established. This configuration is expected to create an undulating membrane surface that will help to change the flow geometry which might lead to enhanced hydrodynamics and surface renewal under laminar flow conditions. To characterize this configuration the major design variable is the winding angle.

To create transverse flow and more uniform fiber arrangement in a module, a central tube was inserted and surrounded by the woven fabric sheet in the third design; the feed inlet and outlet were still located at the shell-side via two drawtubes mounted on the central tube (see Fig. 4.1c). The gaps between the drawtubes and the feed entrance or exit on the housing were sealed using epoxy (Araldite®) ; in this case the feed would mostly flow through the holes on the central tube and the permeate would flow through the fiber lumen. Caution must be taken when designing the interval and number of holes on the central tube, because it is related to the uniformity of the flow distribution through the holes and the degree of transverse flow pattern. To investigate the potential variations of this configuration, the design of the central tube can be varied by adjusting the shapes of the flow distributing holes and the intervals between holes. In addition, the tube size, wall-thickness, size/shape of the holes and interval between the holes should be appropriately chosen.

The fourth design with spacer-wrapped fibers is shown in Fig. 4.1d. Here the woven fabric sheet was wrapped by spacers (with mesh size 1.6 mm) and rolled up. This is expected to create transverse flow across the membrane surface by evenly allocating layers of spacers between layers of fibers. However, it is possible that the inappropriate allocation of spacers or a tightly packed pattern might lead to liquid stagnation that instead would adversely affect the hydrodynamics.

In the fifth design that fibers were knitted into the mesh of the spacer (refer to the spacer-knitted module in Fig. 4.1e) to facilitate a meandering fluid flow. The inappropriate allocation of spacers or over-packed pattern can also lead to adverse effects on the hydrodynamics due to the liquid stagnation between the mesh and fibers as observed with the spacer-wrapped fibers.

Table 4.1 Module specifications and membrane properties

Module specifications

Membrane type	Housing diameter, d_s	No of fibers, n	Effective fiber length L, mm	Packing density ϕ, %	Membrane area A, m^2	Remark
PVDF	19 mm	51	450	30	0.1-0.12	The winding angle is taken into account to calculate membrane area of the curly-fiber module

Membrane properties

Dimension	Pore size (μm)	Contact angle (˚)	Porosity ε (%)	LEPw (Bar)	Tensile modulus E_t ,MPa	Strain at break δ_b, %
d_o: 1.45 mm δ_m: 235 μm	r_{max}: 0.125 r_{mean}:0.082	106–120	82–85	3.5	42.05	105.4

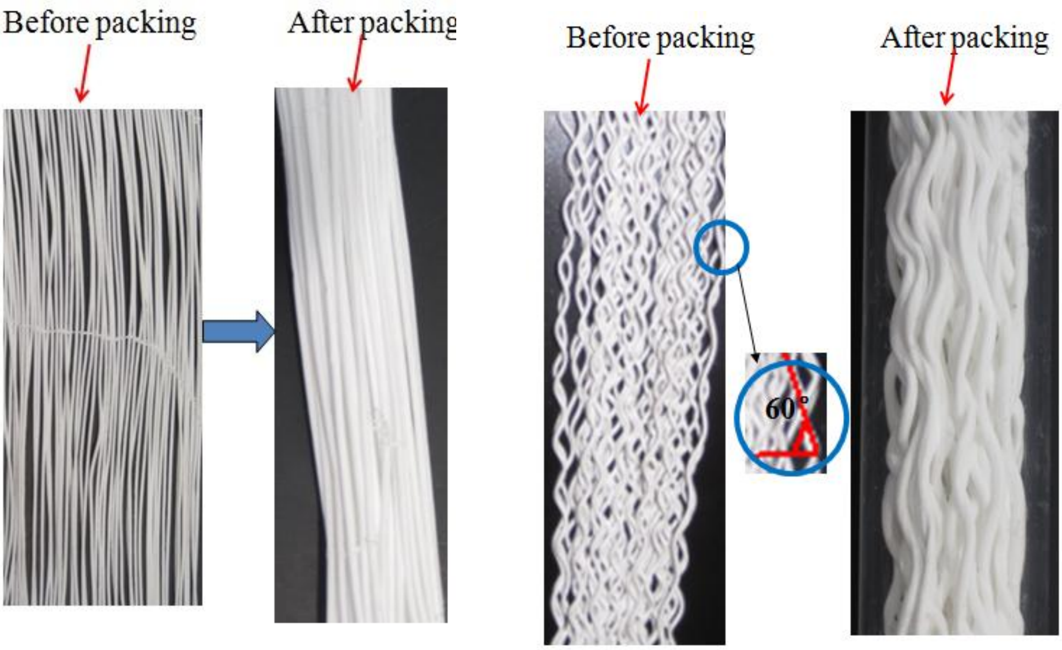

(a) structured-array module

(b) Curly-fiber module

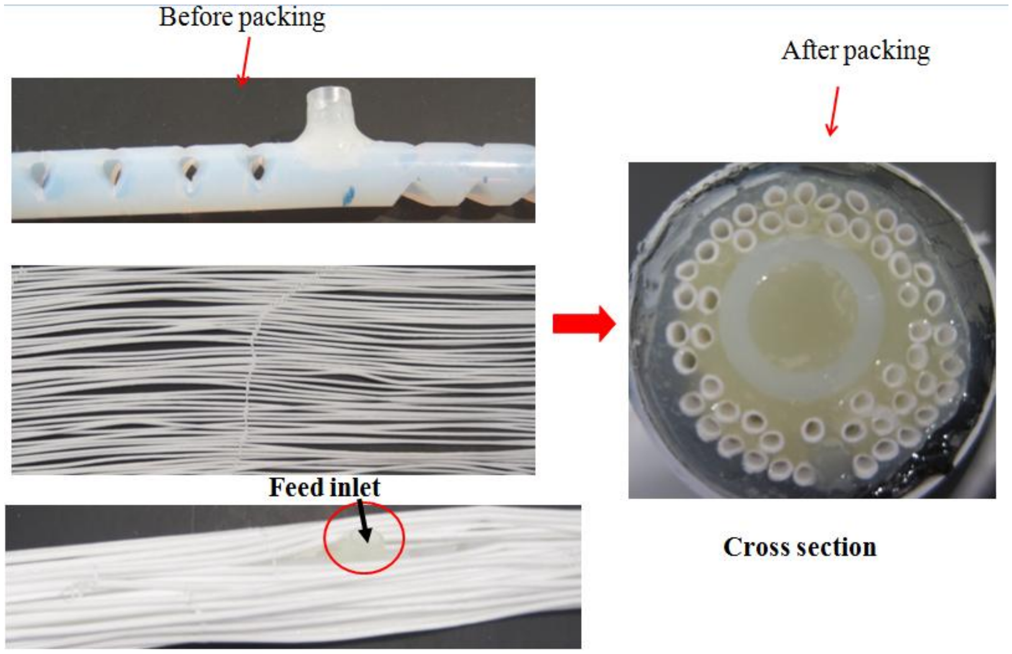

(c) Central-tubing module

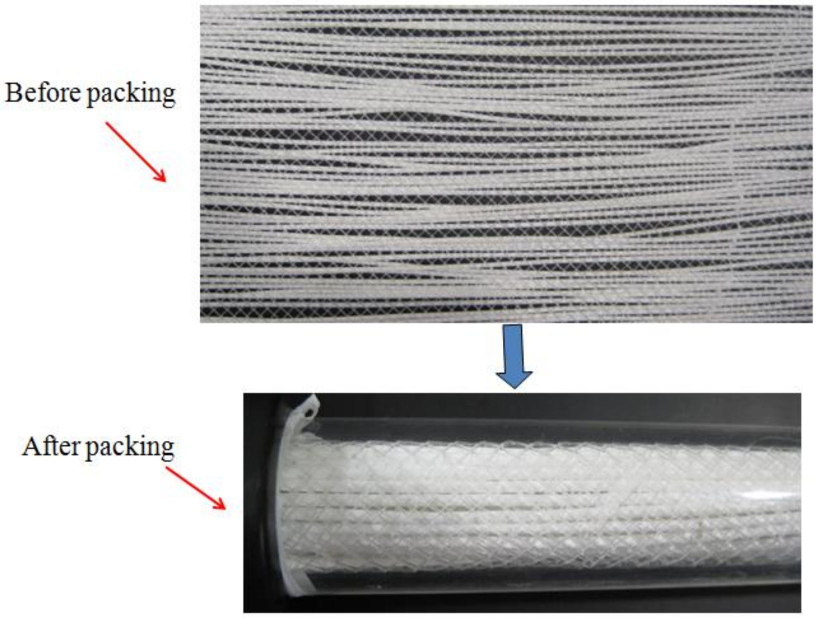

(d) Spacer-wrapped module

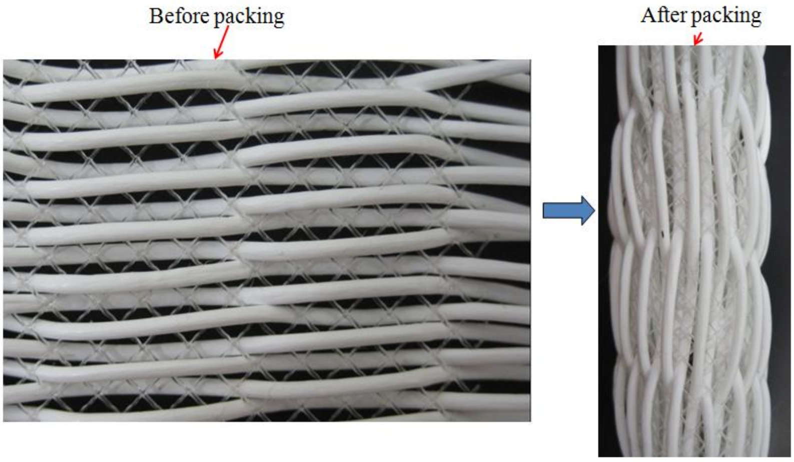

(e) Spacer-knitted module

Fig. 4.1 module design and fabrication:

(a) Structured-array module; (b) Curly-fiber module; (c) Central-tubing module; (d) Spacer-wrapped module; (e) Spacer-knitted module

4.2.2 Module performance evaluation and heat transfer analysis

To evaluate the module performance for various configurations, the following experiments were carried out: (i) attainable flux experiments in which the feed temperature was varied while holding the permeate temperature and other operating conditions constant; (ii) fluid dynamics experiments in which the recirculating feed or permeate velocity was varied while holding the other operating conditions constant. All the experiments were conducted using an established DCMD system, which was shown in Fig. 3.1, Chapter 3. Both the feed and permeate solutions were cycled through the hollow fiber module in countercurrent mode. For the performance tests using synthetic seawater (3.5 wt% sodium chloride solution), the operating details can be found in Section 3.2.4.

Deionized (DI) water was also used in the experiments to investigate the TP effect associated with the heat transfer analysis while excluding the CP effect. Both hot and cold DI water streams were circulated countercurrently through the shell and lumen sides. On the shell side the hot water was heated to between 308.15 K–343.15 K and circulated by a peristaltic pump (1–5.6 L min^{-1}). On the lumen side the cold permeate was cooled by a circulating bath (between 298.15 K–328.15 K) and cycled by another peristaltic pump (0.1-2.1 L min^{-1}). Two conductivity meters were installed to assess the water quality in the feed and permeate sides, respectively. The product was collected in an overflow tank placed on a balance (±0.1 g). The fluid dynamics experiments were performed with careful control of the temperature difference (<10 K) between the hot feed and cold permeate.

4.2.3 Tracer response protocol

The tracer-response studies were conducted using the same DCMD set-up to investigate the shell-side flow distribution in these modules. A schematic showing a module with the location of tracer injection and effluent concentration monitors is depicted in Fig. 4.2. At room temperature DI water was pumped into the shell-side of the modules as the feed stream (blank background solution) and a pulse input of sodium chloride solution was injected at the feed inlet. The tracer response signal was measured at the exit of the effluent stream. Since the salt rejection of this PVDF-based hollow fiber membrane is 100% (Yang et al. 2011), no leakage of the tracer was detected on the lumen side. The amount of tracer used was 1 mL with a concentration of 1 mol L^{-1}. The resulting concentration of tracer at different times was monitored by a conductivity meter (±0.1 μs cm^{-1}) installed at the exit of the effluent. The signals were monitored and recorded via a data-acquisition system. To determine the relationship between the concentration of sodium chloride solution and corresponding conductivity, samples of known concentrations were tested to obtain conductivity values using an external conductivity bridge.

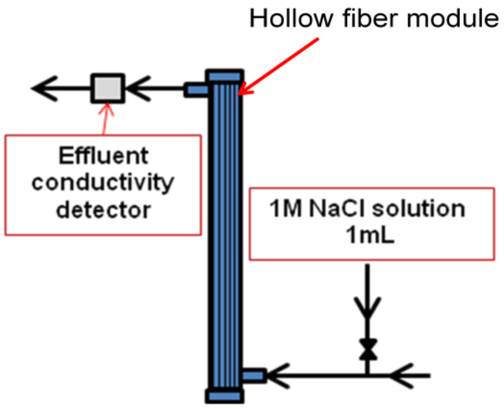

Fig. 4.2 Schematic of tracer-response experiment

In this experiment the proper selection and use of the tracer are essential to get correct *E(t)* curves that represent the age distribution of all components in the effluent stream. A physical, nonreactive and unabsorbable chemical must be used as a tracer. A sodium chloride solution meets these criteria and was therefore chosen for the study in this chapter. The concentration and dosage of the tracer solution also affect the results, and many attempts were made to determine the appropriate concentration and dosage to detect the shell-side flow distribution in the modules. In addition, the pumping speed had to be carefully chosen due to the relatively small size of the test modules. The feed solution (pure water) was pumped at 2.1−2.4 L min^{-1} into the shell-side until the effluent had no recorded tracer. To obtain reproducible and comparable results, the tracer tests for each module were repeated 8−10 times under constant operating conditions.

4.2.4 Error assessment

All the above-mentioned experiments were repeated and showed reproducible results. The results for the water-flux fluctuation were within ±5% (illustrated as error bars in the figures). The conductivity meters had accuracies of ±0.1 ms cm^{-1}(feed side) and ±0.1 μs cm^{-1} (permeate side), respectively. Two modules for each configuration were fabricated by following the same procedures and measured repeatedly under the same operating conditions. The temperature and flow rate variations were strictly controlled within ±0.4 ℃ and ±0.2 L min^{-1}, respectively. These would also result in less flux fluctuation.

4.3 Methodologies for data analysis

4.3.1 Pure water test

This chapter focuses on the application of an experimental approach to quantify the TP effect and acquire the temperature polarization coefficient (TPC) via pure water tests. The following modeling considerations (assumptions) are applied:

(a) Theoretically, the vapor flux N can be expressed in terms of the transmembrane temperature difference and pure water is used as feed (Schofield et al. 1987):

$$N_m = C\frac{dP}{dT}\Big|_{T_m}\left(T_{fm}-T_{pm}\right) \tag{4.1}$$

where C is the intrinsic mass-transfer coefficient, T_m is the membrane temperature, T_{fm} and T_{pm} are the membrane surface temperatures on the feed and the permeate sides, respectively. By assuming the temperature polarization effect is similar on both sides of the membrane, T_m can be estimated by $(T_f+T_p)/2$.

(b) The Clausius-Clapeyron equation is applicable to determine the vapor pressure gradient dP/dT across the membrane when assumption 1) is satisfied. Hence,

$$\frac{dP}{dT}\Big|_{Tm} = \frac{P\gamma M}{RT^2}\Big|_{Tm} \tag{4.2}$$

where γ (J•kg^{-1}) is the latent heat-of-vaporization, M is the molecular weight of water, R is the gas constant (8.314 J•K^{-1}), and P is obtained from the Antoine equation (T.K. Sherwood et al. 1975).

As analyzed previously in Section 2.3.1, the overall heat-transfer flux in MD, q, consists of the conductive heat flux q_{HL} across the membrane and the latent heat transfer q_{MD} accompanying the vapor flux N (Schofield et al. 1987):

$$q = q_{HL} + q_{MD} = \left(\frac{\lambda_m}{\delta_m}\right)\left(T_{fm}-T_{pm}\right) + N_m\gamma = \left(\frac{\lambda_m}{\delta_m} + \gamma\cdot C\frac{dP}{dT}\Big|_{Tm}\right)\left(T_{fm}-T_{pm}\right) = H\left(T_{fm}-T_{pm}\right) \tag{4.3}$$

where H is the effective heat-transfer coefficient based on the transmembrane temperature difference. The λ_m/δ_m value of the PVDF fiber used in this study is taken as 274 W•m^{-2}•K^{-1} based on the method provided by Sarti et al. (Sarti et al. 1985).

Combining Eq. (4.3) with the energy-conservation equation in Eq. (2.10), TP can be determined quantitatively using Eq. (4.4):

$$\left(T_{fm}-T_{pm}\right)=\left(T_f-T_p\right)\Big/\left[1+H\left(\frac{1}{h_f^{''}}+\frac{1}{h_p}\right)\right]=\tau\left(T_f-T_p\right) \tag{4.4}$$

Where $\tau = 1\Big/\left(1+H/h_f^{''}+H/h_p\right)$ is the *TPC*; The schematic of the temperature and the vapor-pressure profiles in the MD process is given in Fig. 2.4. Combining Eqs. (4.3) and (4.4) yields the following:

$$\frac{\Delta T}{N_m\gamma}=\frac{1}{dP/dT}\frac{1}{\gamma C}\left(1+\frac{k_m/\delta_m}{h}\right)+\frac{1}{h} \tag{4.5}$$

where $h \equiv 1\Big/\left(1/h_f^{''}+1/h_p\right)$ is the overall boundary layer heat-transfer coefficient and $\Delta T=\left(T_f-T_p\right)$. Therefore, with the measurable quantities λ_m/δ_m, T_f, T_p and N as well as the predetermined values o f dP/dT from Eq. (4.2), the only unknown parameters h and C can be calculated from the intercept and the slope by plotting $\frac{\Delta T}{N_m\gamma}$ versus $\frac{1}{dP/dT}$ as explained by Schofield *et al.* (Schofield et al. 1987).

4.3.2 Residence-time distribution (RTD)

In this chapter, the sodium chloride tracer-response technique (Levenspiel 1999) was used for investigating the flow distribution on the shell-side of these hollow fiber configurations. An example of an initial tracer concentration *c* (mol·m^{-3}) and its corresponding temporal values in the effluent stream known as *C(t)* curve for pulse injection is shown in Fig. 4.3. The RTD function *E(t)* (s^{-1}) can be used to further interpret the residence-time distribution (Levenspiel 1999):

$$E(t)=\frac{C(t)}{\int_0^\infty C(t)dt} \tag{4.6}$$

where the denominator represents the dosage of the tracer injected at the feed entrance; it is also the area under the *C(t)* curve.

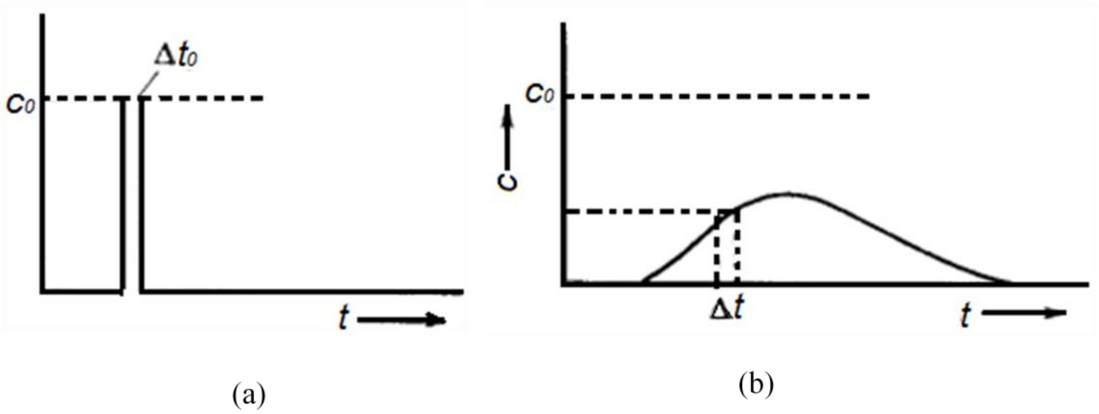

Fig. 4.3 The tracer-response concentration at different exit times for pulse tracer injection flowing through a vessel filled with liquid: (a) pulse injection of tracer with concentration of C_0 into the fluid entering the vessel at time Δt_0; (b) effluent concentration curve *C (t)* (no chemical reaction or adsorption occurred)

In the RTD approach many metrics can be used to evaluate the results. One of the main parameters is the mean residence time (t_m, s) that can be calculated based on the *E(t)* curve:

$$t_m = \int_0^\infty tE(t)dt \tag{4.7}$$

The theoretical (plug flow) residence time $\bar{t}$ (s), which is also known as hydraulic residence time, is equal to the actual vessel volume V_0 divided by the fluid flow rate V. In a hollow fiber MD module the difference between $\bar{t}$ and t_m shows the degree of mixing in the vessel (Levenspiel 1999), i.e., a larger deviation might indicate a longer contact time and hence more effective heat transferred across the membrane. However, the uniformity of the flow distribution is also crucial in the vessel design. Thus, another important parameter is used to represent the spread of the RTD curve − the variance σ^2; a larger value indicates a wider spread, or more deviation from the uniform flow pattern (Levenspiel 1999).

$$\sigma^2 = \int_0^\infty \left(t - t_m\right)^2 E(t)dt \tag{4.8}$$

In order to obtain comparable results for vessels of different size and mean residence time, the normalized *E(t)* function and dimensionless form of variance are more commonly used:

$$E_\theta(\theta) = t_m E(t) \tag{4.9}$$

$$\sigma_\theta{}^2 = \int_0^\infty (\theta - 1)^2 E_\theta(\theta) d\theta = \frac{\sigma^2}{t_m{}^2} \tag{4.10}$$

By applying the above RTD theory with the experimentally measured parameters (e.g., the tracer entrance concentration C_0 and dosage of tracer injected) and a responding concentration curve *C(t)* that can be obtained from the assessment of tracer concentration in the effluent stream, the RTD function curve *E(t)* can be determined based on Eq. (4.7). Thus, the mean residence time t_m and variance σ^2 (as well as the dimensionless variance) can be calculated based on Eqs. (4.7) − (4.10).

4.4 Results and discussion

4.4.1 Membrane properties

Similar to the membranes tested in Chapter 3, similar PVDF hollow fibers were used in the experiments of this chapter. Undergoing the same characterization procedures, the membrane properties are given in Table 4.1. It can be seen that this highly porous PVDF fiber showed reasonably large contact angles for water, high liquid-entry pressure for water (LEPw), good mechanical strength, small maximum pore size and a narrow pore-size distribution. More information on the methodologies for membrane characterization can be found in Chapter 3.

4.4.2 Attainable flux (feed-temperature tests)

Fig. 4.4 plots the permeation flux as a function of feed temperature for six module configurations. All five modified modules show improved performance over the conventional randomly packed module. The greatest enhancement is achieved by the modules with spacer-knitted and curly fibers for which the flux is increased more than 90% at T_f = 313.15 K and 70% at T_f = 333.15 K, respectively. The modules with curly fibers and spacer-wrapped fibers show similar performance, while those with central tubing and straight fibers are slightly lower, but still show significant improvement over the randomly packed module. Teoh et al. (Teoh et al. 2008) reported that the maximum flux enhancement achieved in modules with spacers/baffles or wavy geometries was only from 20 to 36% at feed temperature T_f = 348.15 K. In comparison, the 70 to 90% improvement under milder operating temperature in this study is encouraging, and may be due to more appropriate choice of flow rates.

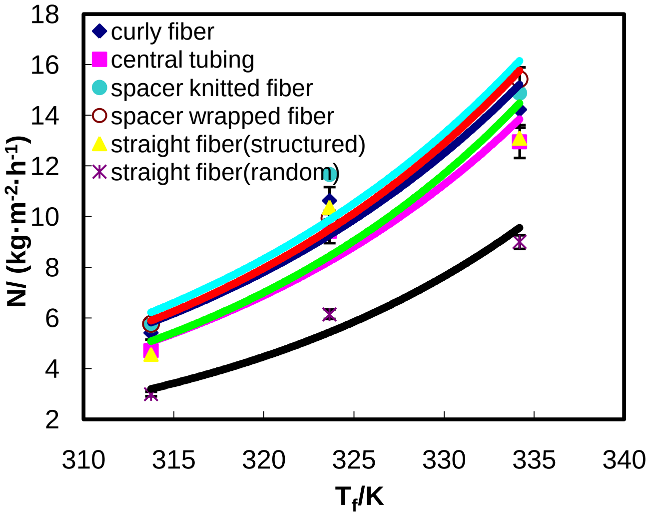

Fig. 4.4 Effect of feed temperature on the permeation flux for various hollow fiber module configurations [V_f = 3 L·min^{-1} (v_f = 0.33 m·s^{-1}), V_p = 0.4 L·min^{-1} (v_p = 0.08 m·s^{-1}), T_p = 298 K, T_f = 323 K]

The enhancement of permeation flux in the modified modules would be due to the improved hydrodynamic conditions achieved by the altered shell-side flow channels in the modified configurations. Hence, it is anticipated that the heat and mass transfer would increase and the TP effect would decrease in a well-designed module when compared to the conventional randomly packed configuration. The discussion in the following sections addresses these points. In addition, another important factor that could affect the heat- and mass-transfer processes is fluid channeling or bypassing (shell-side) that was characterized using the tracer-response technique and will be discussed later.

4.4.3 Fluid dynamics

Experiments were performed to study the effects of the recirculating flow velocities (characterized as Reynolds number, *Re*, of the feed and permeate) on the fluxes in different membrane modules. Fig. 4.5 shows the permeation flux as a function of the Re_f of the feed flow for six different modules. Four of these modified designs show relatively stable fluxes in the range of 10 to 12 kg m^{-2} h^{-1} from extremely low Re_f (laminar condition, e.g., $Re_f < 500$) to turbulent conditions ($Re_f > 2000$). This represents a significant improvement over the conventional randomly packed module as well as the structured-straight module, whose flux initially was rather low and increased with increasing Re_f until turbulent flow occurred. It is well understood that the steady flux across the Re range indicates a shift to the heat and mass transfer being controlled by the membrane and/or the lumen-side boundary layer. Normally, a higher recirculating velocity (i.e., higher mixing intensity) can help to reduce the thickness of the boundary layer adjacent to membrane surface and maximize the driving force between the feed and permeate sides (Banat and Simandl 1994; Bouguccha et al. 2002; Khayet et al. 2003), which is favorable for the mitigation of concentration and temperature polarizations. However, increased pumping energy is required to provide a higher velocity. From the results in Fig. 4.5, it can be seen that a much lower velocity can be chosen by employing modified configurations to reach the steady flux. Hence, there is no need to increase the flow rate.

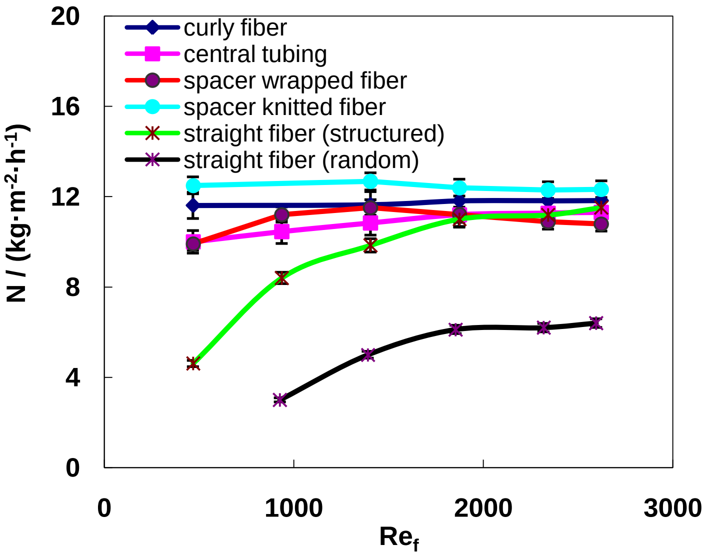

Fig. 4.5 Effect of recirculated feed velocity on permeation flux (3.5%NaCl solution as feed v_f = 0.08~0.47 m·s^{-1}, v_p = 0.08 m·s^{-1}, T_p = 298 K, T_f = 323 K)

From Fig. 4.5 it can also be observed that when compared with the randomly packed module, a one to three-fold flux enhancement could be obtained even at an extremely low flow velocity in four modified configurations. The highest flux enhancement (>300 %) was achieved by the modules with undulating membrane surface (spacer-knitted and curly fibers) under a low operating flow rate range. This might be due to a more even flow distribution in the modified module that improves the fluid dynamics. This finding will be corroborated by conducting residence-time distribution (RTD) tests in the later section (4.4.4). For example, the module with spacer-knitted fibers would facilitate a meandering fluid flow, thereby achieving a well-mixed condition. Moreover, secondary flows might be induced simultaneously to achieve more efficient heat and mass transfer.

Experiments were also conducted to investigate the effect of the lumen-side resistance by varying the recirculating permeate flow velocity (Re_p). Fig. 4.6 plots the permeation flux as a function of the permeate-side flow rate for six module configurations with Re_f = 1901.3. A similar response to the increase of the permeate flow rate as the randomly packed module presented was observed for the five modified modules. The experimental results in Section 3.3.3 indicated that the heat-transfer process could be enhanced by increasing the velocity to minimize the thermal boundary layer on the permeate side; i.e., when the temperature at the membrane surface approaches the temperature in the bulk permeate, the driving force for vapor transport through the membrane can be maximized. Moreover, an early onset of the steady state was observed at Re_p<200. The possible reason may be due to the increased transverse vapor flux that helped break down the laminar boundary layer, thus greatly enhancing the mixing on the membrane surface and facilitating the heat transfer at the permeate side. In addition, the four modified configurations show 28 to 39% flux enhancement compared to that of the with structured-straight module and a more significant improvement (110 to 127%) over the conventional randomly packed module after reaching a steady state (attainable fluxes). This is probably due to the enhanced heat transfer at the feed sides of those improved geometries, leading to a higher transmembrane vapor flux and consequently more efficient heat transfer at the permeate side.

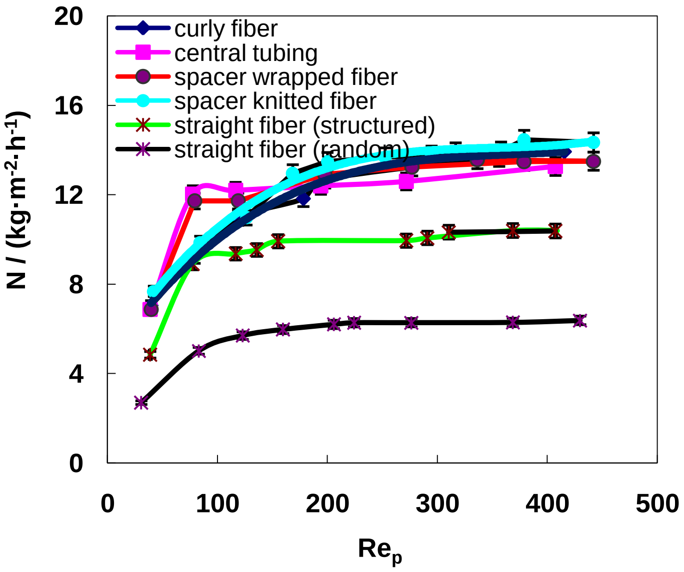

Fig. 4.6 Effects of recirculated permeate velocity for various hollow fiber module configurations [3.5% NaCl solution as feed V_f = 4 L•min^{-1}(v_f = 0.33 m•s^{-1}), V_p = 0.1-2.1 L•min^{-1} (v_p < 0.5 m•s^{-1}), T_p = 298 K, T_f = 323 K]

4.4.4 Residence-time distribution (RTD) tests

In the RTD tests, when the sodium chloride solution was injected into the module at the feed inlet, it took time to travel through the whole system before reaching and being detected by the conductivity analyzer located at the feed outlet. The theoretical residence time, based on a plug flow vessel of the same actual volume ($V_{housing}$-V_{fibers}), was calculated to be approximately 7.2 seconds from the injection point to the detector with a flowrate of 2.1–2.4 L·min^{-1} and a connecting tubing length of approximately 500 mm. The tracer responses for different modules are shown in Fig. 4.7, which plots the concentration of the tracer in the effluent stream as a function of time. To view the experimentally determined $C(t)$ curves more clearly, Fig. 4.7 depicts only the first 20 seconds of each module test. The solid lines and dots represent the experimental data, while the dashed lines are the Gaussian distribution curves (normalized distribution) that have symmetric shapes to simplify the probability prediction. For further comparison the average values of mean residence time t_m and the dimensionless variance σ_θ for each module are summarized in Table 4.2.

Table 4.2 Overall RTD results for various configurations

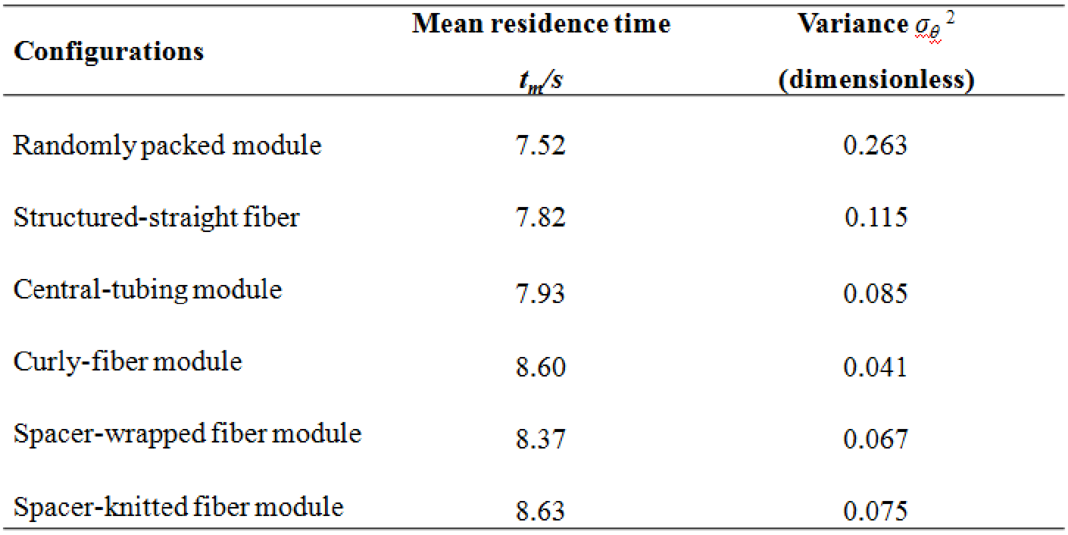

Configurations	**Mean residence time t_m/s**	**Variance σ_θ^2 (dimensionless)**
Randomly packed module	7.52	0.263
Structured-straight fiber	7.82	0.115
Central-tubing module	7.93	0.085
Curly-fiber module	8.60	0.041
Spacer-wrapped fiber module	8.37	0.067
Spacer-knitted fiber module	8.63	0.075

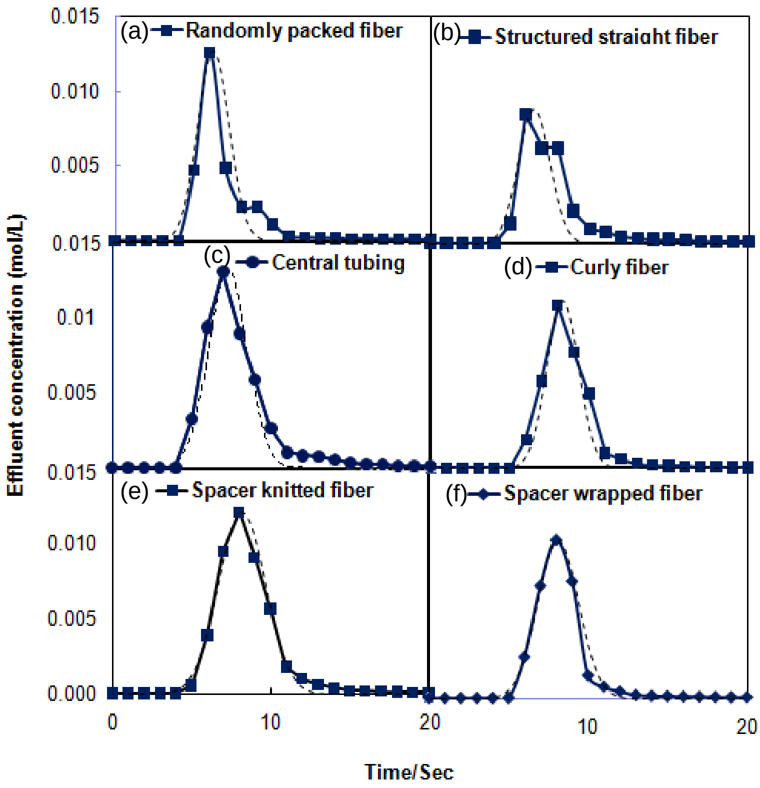

Fig.4.7 RTD concentration *C(t)* response curves for various configurations in tracer tests (Dash line represents the ideal Gaussian distribution. Background solution: pure water; tracer: sodium chloride solution, 1mol/L; amount: 1mL; $V_f = 2.5$ L•min^{-1}, $T_f = 298.15$ K)

It can be seen from Fig. 4.7 that the curves of the randomly packed and structured-straight modules have double peaks that imply the existence of parallel flow paths or channeling in the modules (Levenspiel 1999). Also, the relatively early peaks accompanied the occurrence of long tails on the right of the curves, implying that these two modules could be subjected to stagnant backwaters (local dead zone effects). The summary in Table 4.2 shows that their RTD curves have relatively wider dispersions (0.263 & 0.115) than the other modules.

Several researchers (Levenspiel 1999; Dindore VY et al. 2005; Rector et al. 2006; Shi et al. 2009) have stated that the variance is an important metric to evaluate the flow distribution. A smaller variance indicates a narrower RTD curve dispersion and a more ideal flow pattern. For example, the last three modules (Fig. 4.7) with curly, spacer-knitted and spacer-wrapped fibers show similar *C(t)* curves with a relatively spiked and asymmetric shape that indicate a reasonably uniform flow distribution, which is consistent with their small variances (lower than 10%, Table 4.2) indicating narrow curves. Although these three modules have relatively larger mean residence times t_m, which deviates from the plug flow behavior, they showed higher fluxes and enhanced performance in hydrodynamic investigations when compared to the other configurations. This may be due to their more complicated flow paths caused by the modified geometries that promote more even flow distribution and induce secondary flows to greatly enhance the mass/heat transfer between the hot feed and cold permeate. In addition, a direct comparison of the variance is illustrated in the histogram in Fig. 4.8 that shows a plot of dimensionless variance for the various module configurations. Interestingly, the overall RTD results correlate with the module performance.

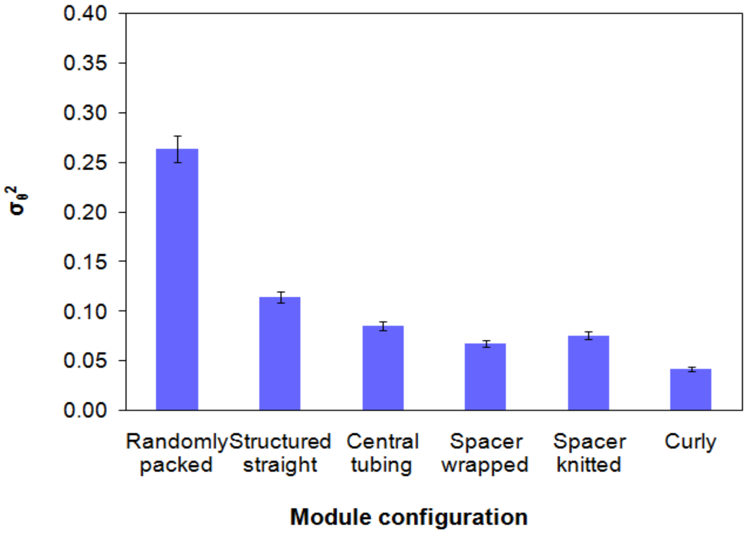

Fig. 4.8 Comparison of variance for various module configurations (Background solution: pure water; tracer: sodium chloride solution, 1mol/L; amount: 1mL; $V_f = 2.5$ L·min^{-1}, $T_f = 298.15$ K)

4.4.5 Temperature-Polarization coefficient (*TPC*) and heat-loss assessment

A series of pure water tests were performed in the laminar flow regime to determine the corresponding heat-transfer coefficients and *TPC* for the various module configurations. The unknown parameters h and C were obtained based on the known operating parameters and membrane properties by plotting $\frac{\Delta T}{N_m \gamma}$ vs. $\frac{1}{dP/dT}$, as shown in Fig. 4.9.

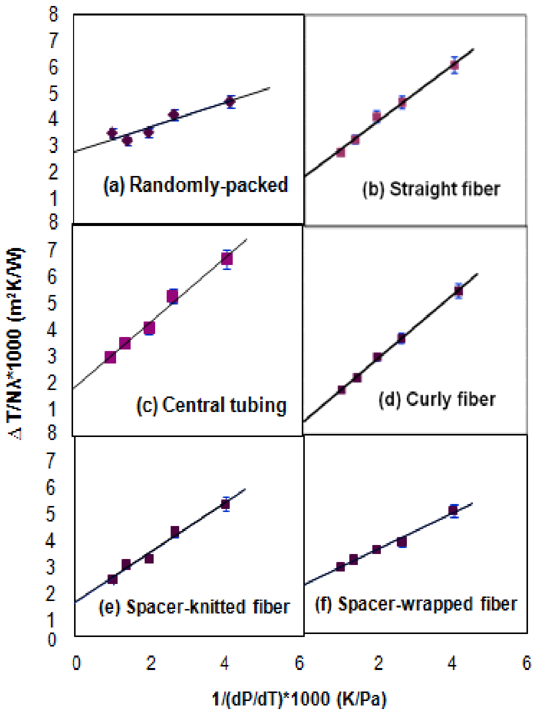

Fig. 4.9 Relationship between $\frac{\Delta T}{N_m \gamma}$ vs. $\frac{1}{dP/dT}$ [V_f = 4 L·min^{-1}(Re$_f$ =1800), V_p = 0.8 L·min^{-1} (Re$_p$= 180), T_m = 303~333 K]

Based on these plots, the heat transfer coefficient h was found to be from 943 W·m^{-2}·K^{-1} for the module with randomly packed fibers to 2300 W·m^{-2}·K^{-1} at T_m=333K for the module with curly fibers, which is consistent with its performance evaluation results. Also, the TPC and ratio of the conductive heat loss to the overall heat flux q_{HL}/q for each configuration are shown in Figs. 4.10 & 4.11 as functions of the membrane temperature T_m, respectively. It can be seen that both the *TPC* and q_{HL}/q decrease with increasing membrane temperature T_m. The *TPC* decreases because the higher fluxes generated by the higher vapor pressure gradient of dP/dT [(Eq. (4.2)] result in an increase in the effective membrane heat transfer coefficient H [(Eq. (4.3)]. Comparing the various designs (Fig. 4.10) the module with curly fibers shows the least temperature polarization under the same operating conditions (e.g., $TPC > 0.8$ at T_m=303K and 0.65 at 333K), followed by the module with central tubing and spacer-knitted fibers; while the modules with structured-straight and randomly packed fibers display higher vulnerability to the temperature-polarization effect. This again underscores the enhanced driving force and improved performance by the module with curly fibers. However, it is noted that the module with spacer-knitted module has a slightly lower *TPC*. This may be due to the more complicated layout and insertion of spacers leading to possibly lower thermal efficiency. Overall, compared to the *TPC* range (0.4−0.7) achieved by a typical MD system with satisfactory module performance (Khayet 2011), the current results are encouraging.

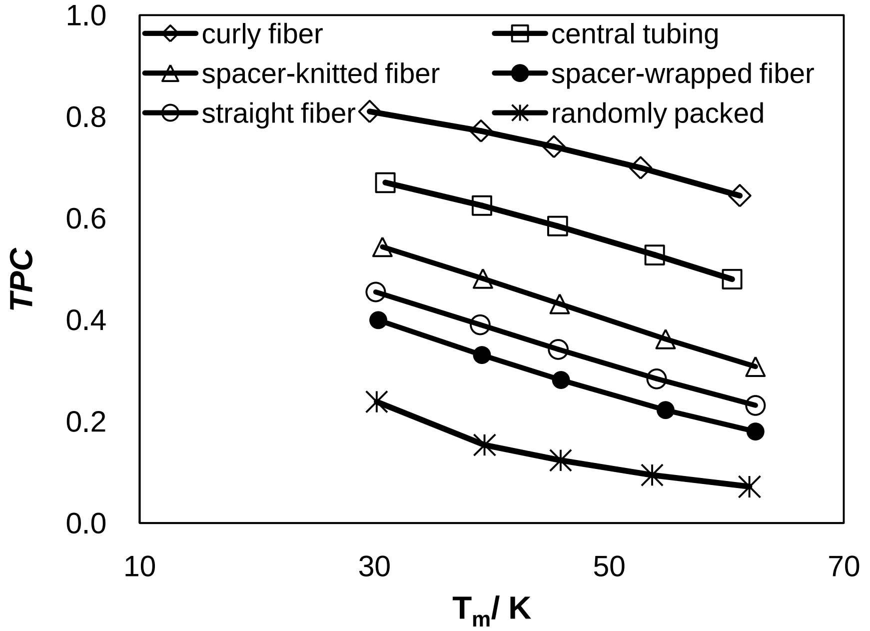

Fig. 4.10 Comparison of the TP effect for various module configurations in pure water tests [V_f = 4 L·min^{-1}(Re$_f$=1800), V_p = 0.8 L·min^{-1} (Re$_p$ = 180), T_m = 303~333 K]

The ratio of the conductive heat loss to total heat flux, q_{HL}/q, also decreases with increasing membrane temperature (Fig. 4.11), because q_{HL} has linear relationship with the temperature difference $\left(T_{fm} - T_{pm}\right)$ while the evaporation heat q_{MD} shows an exponentially increasing trend [Eq. (4.3)]. Interestingly, the module with curly fibers loses a larger portion of heat to conduction (e.g., 55% at T_m=30°C and 23% at 333.15 K), which is explained by a higher *TPC* and hence higher transmembrane temperature differences (driving force). Therefore, a trade-off exists between the TPC and the ratio of conductive heat loss to the total heat flux for module performance. However, it has been widely reported that the ratio of conductive heat loss to overall heat flux across the membrane is from 20% to 50% in a typical MD unit (Khayet 2011). Thus, the conductive heat-loss levels of the best performing modules are still acceptable for the range of operating temperatures studied here. For example, the module with curly fibers had a $\mathrm{TPC} = 0.65$ and $q_{HL}/q = 23\%$ at $T_m = 333\mathrm{K}$

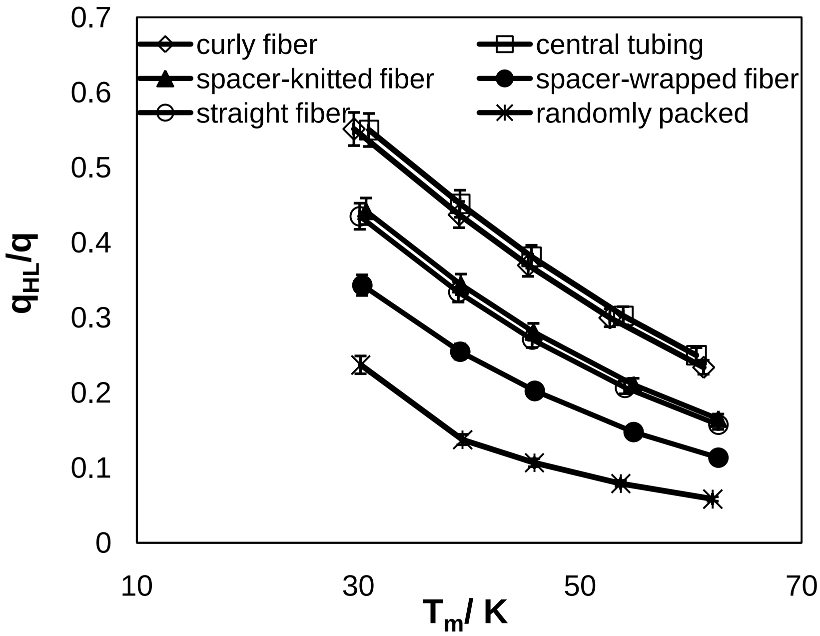

Fig. 4.11 Heat-loss assessment for various module configurations in pure water tests [V_f = 4 L·min^{-1} (Re$_f$ = 1800), V_p = 0.8 L·min^{-1} (Re_p = 180), T_m = 303~333 K]

Based on the above results, a summary is given in Table 4.3 to provide an overall comparison for all configurations. In general, the modules with undulating membrane surface (e.g., curly and spacer-knitted fibers) show advantages by achieving higher vapor permeability and mitigating TP effect with reasonably lower energy losses; this is mainly due to the enhanced shell-side hydrodynamics induced by altered fiber geometries and relatively uniform shell-side flow distribution.

Table 4.3 Overall comparison for various configurations

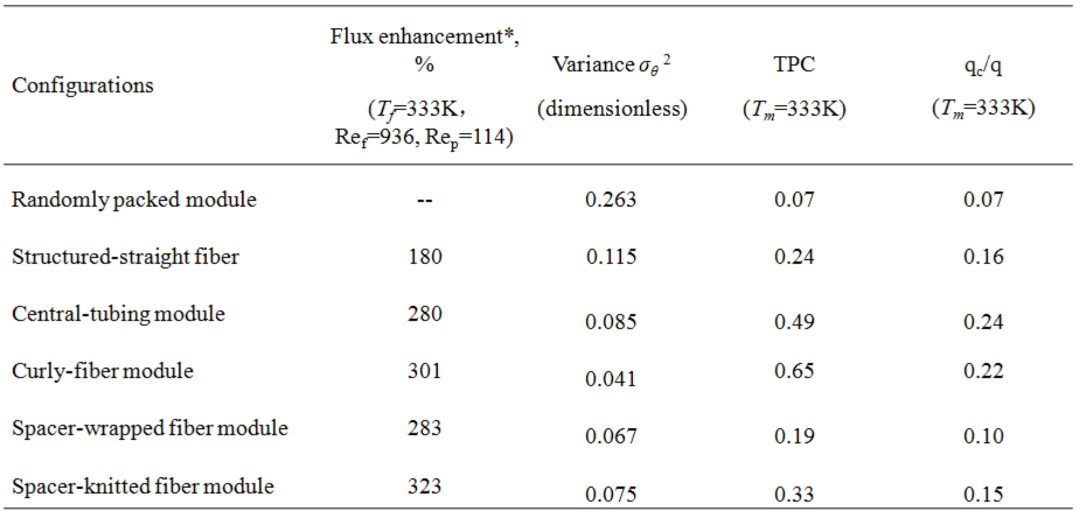

Configurations	Flux enhancement*, % (T_f=333K, Re_f=936, Re_p=114)	Variance $\sigma_\theta{}^2$ (dimensionless)	TPC (T_m=333K)	q_c/q (T_m=333K)
Randomly packed module	--	0.263	0.07	0.07
Structured-straight fiber	180	0.115	0.24	0.16
Central-tubing module	280	0.085	0.49	0.24
Curly-fiber module	301	0.041	0.65	0.22
Spacer-wrapped fiber module	283	0.067	0.19	0.10
Spacer-knitted fiber module	323	0.075	0.33	0.15

* The flux enhancement over the randomly packed module

4.5 Conclusions

In this chapter five types of modified hollow fiber module configurations were designed and constructed for the DCMD process. Their module performances were evaluated based on permeation flux experiments, fluid dynamics investigation, and tracer-response tests as well as process heat-transfer analysis.

- Experiments reveal that the modified module designs are able to enhance permeation flux up to 90% as compared to the conventional module, and the modules with curly and spacer-knitted fibers had the best performance.

- The fluid dynamic studies show that the performance of all modified configurations except the structured-straight module are independent to the feed flow velocity, and the modified fiber geometries with undulating membrane surface can achieve up to three-fold flux enhancement in the laminar flow regime.

- The sodium chloride tracer response technique is able to reveal the shell-side flow pattern and distribution for various designs. Improved fiber geometries or arrangements can provide a better flow distribution, thus much lower pumping energy cost and higher thermal efficiency could be accomplished.

The heat transfer analysis underscores the advantage of the modules with undulating membrane surface for mitigating TP. Although a trade-off exists between the TPC and conductive heat loss, all modified modules showed acceptable heat loss within the range of operating temperatures.

CHAPTER 5

ANALYSIS OF THE EFFECT OF TURBULENCE PROMOTERS IN HOLLOW FIBER MD MODULES BY CFD SIMULATIONS

5.1 Introduction

As the key concerns in MD industrialization, flux enhancement and module performance improvement have always been related to the development of novel membranes and module design concepts (Schofield et al. 1987; Lawson and Lloyd 1997). In recent years, intensive research has been done to develop better MD membranes, among which only a few highly permeable membranes with large MD coefficients are available (Khayet et al. 2005; Li and Sirkar 2005; Khayet et al. 2006; Song et al. 2007; Qtaishat et al. 2009; Su et al. 2010; Wang et al. 2011). In addition to the development of new membrane materials, many researchers have also investigated strategies to improve the MD process such as optimizing operation parameters (Lawson and Lloyd 1996; Cath et al. 2004; Li and Sirkar 2004; Martínez and Rodríguez-Maroto 2007; Teoh et al. 2008; Yang et al. 2011) and designing novel modules (Schofield et al. 1987; Martinez-Diez and Vazquez-Gonzalez 2000; Qtaishat et al. 2008) to alleviate the TP phenomenon and enhance permeation flux. However, to date, most of the investigations of MD module design have focused on flat sheet membrane modules (Martínez-Díez et al. 1998; Phattaranawik and Jiraratananon 2001; Phattaranawik et al. 2003; Chernyshov et al. 2005; Martinez-Díez and Rodriquez-Maroto 2006). On the other hand hollow fiber-based membrane modules have great potential for industrial applications due to their versatility, more compact structure and reduced vulnerability to TP effects (Schofield et al. 1987). It is well-recognized that by incorporating proper flow alteration aids (e.g. channel design, flow channel spacers or baffles) in flat sheet modules to create secondary flows or eddies, the MD flux can be enhanced and TP phenomenon can be mitigated (Phattaranawik et al. 2001; Cath et al. 2004; Li and Sirkar 2004; Martinez-Díez and Rodriquez-Maroto 2006; Martínez and Rodríguez-Maroto 2007). However, efforts are still needed for configuration designs and hydrodynamic improvements in hollow fiber MD processes (Schneider et al. 1988; Ding et al. 2003; El-Bourawi et al. 2006; Cheng et al. 2008; Teoh et al. 2008; Yang et al. 2011; Yang et al. 2011).

In addition to experimental research, computational fluid dynamics (CFD) modeling has been gradually adopted and has proved to be a useful tool in analyzing fluid dynamic behavior in membrane modules (Fimbres-Weihs and Wiley 2010; Yu et al. 2011). With the benefits of flow-field visualization (including velocity, pressure, temperature and concentration profiles) at any locations in a defined flow channel, CFD modeling can be used to correlate the fundamental mass- and heat-transfer performance with the hydrodynamic behavior and as a result provide guidance for scale-up and industrial applications. Nevertheless, due to the complex coupling of mass and/or heat transfer across bulk fluids and the membrane matrix, prior CFD models of membrane separation processes have adopted simplified methods (Fimbres-Weihs and Wiley 2010). For instance, in a membrane-based ventilator system (Zhang 2010; Zhang et al. 2010), the mass and heat transfer through a membrane and two fluids was treated as a conjugate problem by ignoring phase changes. In a study of an MD system (Hwang et al. 2011), the feed, permeate and membrane were incorporated into the simulation to obtain velocity and temperature fields, but the concentration transport and latent heat induced by evaporation were ignored. Another CFD study of MD flat sheet membrane module design suggested that spacer orientations should have great impact on the heat and mass transfer (Shakaib et al. 2012). However, the heat-transfer model developed in this study was over-simplified being based on non-porous and rigid shell and tube heat exchangers, which are not coupled with the mass transfer and phase changes. Moreover, these prior simulation studies only focused on mass- and/or heat-transfer improvement by designing better flow channels or incorporating spacers for both non-MD and MD flat sheet or spiral wound membrane modules (Koutsou et al. 2004; Fimbres-Weihs et al. 2006; Shakaib et al. 2009; Xu et al. 2009; Shakaib et al. 2012). Thus far, CFD analysis for process modeling in hollow fiber MD modules has been limited to our previous work (Yu et al. 2011; Yu et al. 2012).

A recent review of the development of CFD modeling stated that most MD researchers tended to simplify the transmembrane transfer models by ignoring the permeate flow and focusing on the bulk feed flow (Fimbres-Weihs and Wiley 2010). Nevertheless, our recent CFD study has proposed an improved heat-transfer model, which couples the latent heat to the energy conservation equation and combines it with the Navier-Stokes equations, to address the transport correlation between the fluids (feed and permeate) and the membrane in a single fiber MD module (Yu et al. 2011). Using the same heat-transfer model, a series of numerical simulations were conducted to analyze the effectiveness of different process enhancement strategies by identifying the controlling local resistances in mass- and hear-transfer processes under laminar flow (Yu et al. 2012). It was found that hydrodynamic means showed a significant effect on improving the heat transfer in a hollow fiber module system when the heat-transfer controlling resistance is in the liquid boundary layers, i.e., where highly permeable membranes (with high C values) or high operating temperatures were employed.

As an extension of the previous work (Yu et al. 2012), this Chapter focuses on a MD system, in which the liquid-boundary layers play dominant roles in determining the overall heat-transfer resistance, to investigate the potential of incorporating different turbulence promoters into the shell-side flow to enhance hydrodynamic conditions. This analysis has been motivated by our experimental observations on hollow fiber MD (Yang et al. 2011). To simulate the effect of turbulence promoters on enhancing process performance, a series of single fiber MD modules with attached annular quad/round spacers, floating spacers and baffles have been structured and modeled under the following conditions: (1) low operating temperatures and large MD coefficient (C) values at constant flow velocity; (2) high operating temperatures and varying C values at constant flow velocity; (3) varying feed velocity at low operating temperatures. Conditions (1) and (2) are chosen to investigate the effectiveness of various turbulence promoters employed in the modified modules; while condition (3) is to study the effect of feed flow velocity on enhancing the heat transfer in an ‘original’ (unmodified) module. In these simulations, various performance metrics, including heat transfer coefficients, TP coefficient (*TPC*), mass flux and thermal efficiency, are examined as functions of membrane properties (*C* values) and/or operating temperatures. Finally, a comparison is provided of hydraulic energy consumption (*HEC*) caused by the introduction of various turbulence aids with the original module design.

5.2 Model development for numerical simulations

5.2.1 Geometric structure, governing transport equations and boundary conditions in CFD modeling

Two dimensional double precision models were developed using the commercial software Fluent v6.3 to study the hydrodynamic behavior and the heat transfer process of an original MD hollow fiber module and modified configurations equipped with turbulence promoters of various specifications.

Before conducting CFD simulations, geometric structures of all modules were built via Gambit® v2.4.6. The novel designs, which were adapted from the original single fiber module, all have the same cylindrical housings with regularly distanced annular spacers attached to the membrane outer surface, and/or baffles attached to shell walls, and/or floating spacers in the shell-side chambers. The assumed dimensions of these single fiber modules are 0.25 m length and 0.0095 m housing diameter. For the convenience of CFD modeling, their geometries were assumed to be ideal axially-symmetric structures. Hence, a series of geometric structures for the 2D computing domains were built for half of the actual modules, whose local geometric structures (within a length range of 0−0.06 m with respect to the overall length of 0.25 m) are shown Fig. 5.1 (a)-(b) and (d)-(e); while Fig. 5.1 (c) shows a local domain amplification to specify the dimensions of the turbulence promoters inserted in a modified module, in which R_{mi} and R_{mo} are the inner and outer radii of the fiber, Δx and Δy are the cross-sectional dimensions of the regularly shaped internals in x and r directions, Lx is the interval between two internals and Ly is the vertical distance between an internal and the membrane outer surface. In these novel configurations, insertions with regular shapes are periodically distributed on the shell sides, through which the feed stream flows (Fig. 5.1). In this chapter ten different designs of the insertions have been investigated and their respective specifications are listed in Table 5.1.

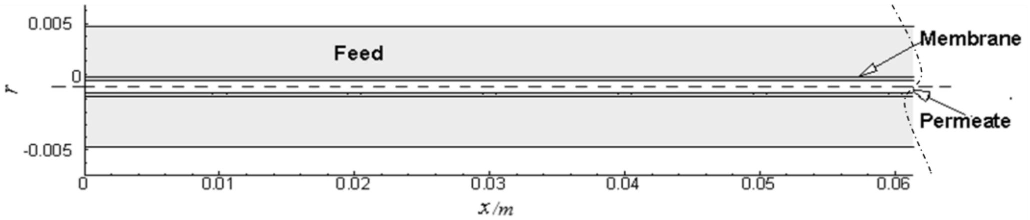

(a)Original module

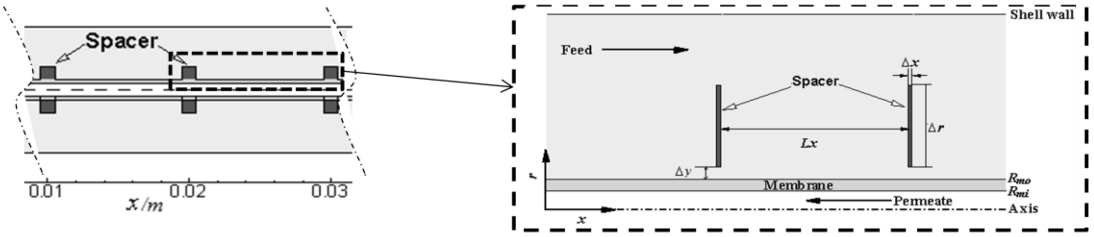

(b) Module with spacers

(c) Amplified local domains for dimension specification

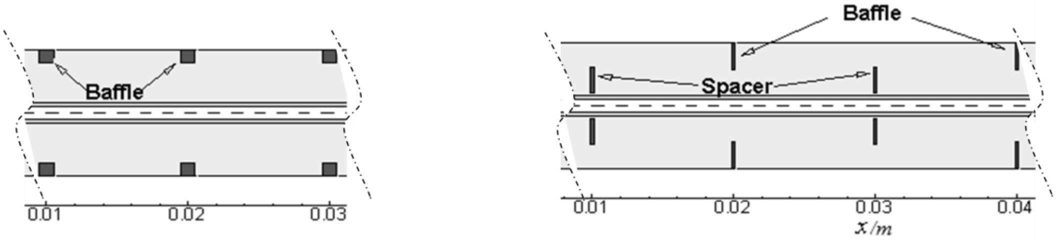

(d) Module with baffles

(e) Module with alternate spacers and baffles

Fig. 5.1 Schematic of axially-symmetry single fiber modules in CFD simulating domains

With the geometries of these modules built, CFD simulations were carried out in Fluent using a newly-established heat-transfer model, which couples the latent heat induced by evaporation/condensation on the membrane surfaces into the MD process. It is noted that the influence of the normal mass flow across the membrane matrix was ignored. This is because the MD mass flux has a negligible contribution to either the feed or permeate bulk flow when compared to the operating feed flow rate in a single fiber module. For example, the typical transmembrane mass flow rate in the current study is around 7.50×10^{-6} kg s^{-1} in a single fiber module, which is three orders of magnitude lower than the feed flow rate $V_f = 4.22\times10^{-3}$ kg·s^{-1}. Thus, in this chapter, a heat-transfer model was established for the DCMD process by ignoring the influence of the transmembrane mass flux in the conservation equations, but combining the characteristic latent heat incurred by evaporation/condensation into the heat-transfer process.

Table. 5.1 Specifications of various turbulence promoters

Insertion type			Spacer				Baffle		
			Δx / mm	Δy / mm	Lx / mm	Ly / mm	Δx / mm	Δy / mm	Lx / mm
1	No spacer	Original	-	-	-	-	-	-	-
2	Round spacer	Attached round spacer 0.5	r=0.5	-	10	-			
3		Floating round spacer 0.75	r=0.75	-	10	0.5			
4	Quad spacer	Quad spacer 0.5×0.5×10	0.5	0.5	10				
5		Quad spacer 0.5×1.0×10	0.5	1.0	10				
6		Quad spacer 0.2×2.0×30	0.2	2.0	30				
7		Quad spacer 0.2×2.0×20	0.2	2.0	20				
8		Quad spacer 0.2×2.0×10	0.2	2.0	10				
9		Floating quad spacer 0.2×2.0×10×1.5	0.2	2.0	10	1.5	-	-	-
10	Baffle	Baffle 0.2×2.0×10	-	-	-	-	0.2	2	10
11		Alternate spacer + baffle 0.2×2.0×10	0.2	2	10		0.2	2	10

Note:

1. quad spacer indicates an annular spacers with quad cross section; while a round spacer means an annular spacer with circular cross section; For instance, a modified module named "quad spacer 0.2×1.0×10" indicates a total number of 24 regularly distanced quad spacers, *Δx* is 0.2 mm, *Δy* is 1.0 mm, the interval *Lx* is 10 mm and *Ly* 0 mm (attached spacer)

2. Δ*x* and Δy are the dimensions of the annular baffle in *x* and *r* directions, respectively; *Lx* is the interval between two spacers or baffles, *Ly* is the vertical gap between the spacers and the membrane outer surface.

In a steady-state heat transfer-process, the overall governing transport equations for the feed, permeate and membrane are as follows:

The continuity equation:

$$\nabla \cdot (\rho \vec{v}) = 0 \tag{5.1}$$

The momentum transport equation:

$$\nabla \cdot (\rho \vec{v}\vec{v}) = -\nabla p + \nabla \cdot (\bar{\bar{\tau}}) + \rho \vec{g} \tag{5.2}$$

where $\bar{\bar{\tau}}$ is the stress tensor, which can be expressed as:

$$\bar{\bar{\tau}} = \mu \left[\left(\nabla \vec{v} + \nabla \vec{v}^T \right) - \frac{2}{3} \nabla \cdot \vec{v} I \right] \tag{5.3}$$

The energy conservation equation:

$$\nabla \cdot (\vec{v} \rho c_p T) = \nabla \cdot (k \nabla T) + S_h \tag{5.4}$$

where k is the heat conductivity (W·m^{-1}·K^{-1}), S_h (W·m^{-3}) is the boundary condition which serves as a heat-source term for the feed or permeate on the membrane surface, and indicates the amount of latent heat generated by evaporation at the hot-side membrane surface and subsequently released through condensation at the cold-side membrane surface. It can be written as:

$$S_h = \begin{cases} \dfrac{q_{MD}}{\delta r} \cdot \dfrac{R_{mo}}{R_{mi}} & \text{for } r = R_{mi} \\ -\dfrac{q_{MD}}{\delta r} & \text{for } r = R_{mo} \\ 0 & \text{otherwise} \end{cases} \tag{5.5}$$

where q_{MD} is the latent heat flux on the feed side membrane surface, r is the radial direction, δr is the chosen grid thickness in the r direction. The temperature profile and heat-transfer mechanism of MD was given in Fig. 2.4.

For the MD modules with the same length L (0.25 m), other boundary conditions are applied:

- Entrances of the feed and permeate: uniform velocities and temperatures are employed, u_{fi}= 0.06 m s^{-1}–0.283 m s^{-1} with Re_f=836–4000 for the original module, u_{pi}= 0.417 m s^{-1} (Re_p= 460), T_{fi} = 327.15 to 360.15 K, T_{pi} = 293.85 to 327.15 K (note: these are typical experimental values).

- Outlet of feed and permeate: outlet pressure is 0.0 Pa (gauge pressure)

- Membrane wall: no-slip condition, conjugate heat conduction:

$$q_f\Big|_{r=R_{mo}} = q_m\Big|_{r=R_{mo}},\ q_m\Big|_{r=Rmi} = q_p\Big|_{r=R_{mi}}$$

$$T_f\Big|_{r=R_{mo}} = T_m\Big|_{r=R_{mo}},\ T_f\Big|_{r=R_{mi}} = T_m\Big|_{r=R_{mi}} \tag{5.6}$$

where Re_f, Re_p, T_{fi}, T_{pi} are Reynolds number and inlet bulk temperature of feed and permeate respectively.

- No molecular transport across the membrane is applied in this model.

In this chapter, a laminar model is used to simulate the unaltered module operated under laminar operating conditions (Re<2000); and a realizable k-ε method (Shih et al. 1995) with enhanced wall treatment is applied to the unaltered module under turbulent conditions (Re>2000) or the modified configurations with insertions.

5.2.1 Computational domain and grid scheme

By assuming the single-fiber modules have a cylindrical structure, a series of 2D axial-symmetric single-fiber domains were built. The quad mesh was adopted for grid generation of most of modules except the configuration with round spacers, whose feed chamber is scaled by triangular meshes due to the irregular domain. In the r direction, a grid scale of 5×10^{-6} m was chosen for the bulk permeate (lumen), the membrane and bulk feed (shell); while in the x direction, a grid scale of 1×10^{-4}m was employed. As an example, the grid configuration for a 0.25 m long module is shown in Fig. 5.2, which illustrates the whole geometry and locally amplified regions in the 2D domain. The effect of the hollow fiber membrane surface roughness on the wall boundary conditions was ignored due to its much smaller scale than that of a mesh element. The computational accuracy for convergence is 10^{-5} in Fluent.

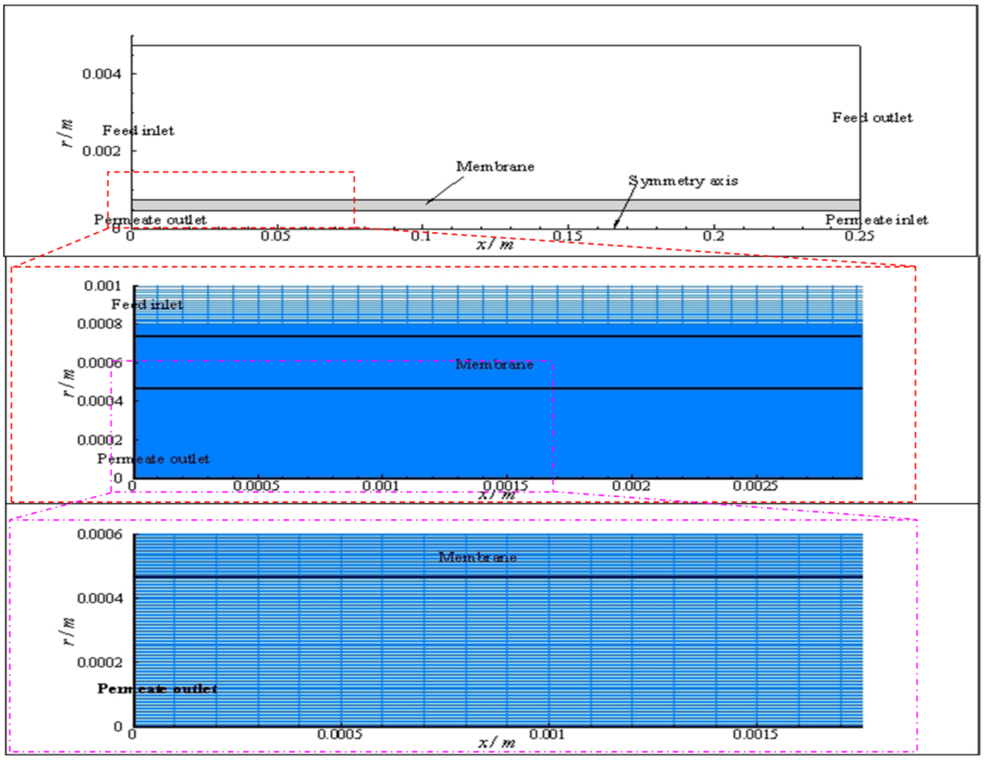

Fig. 5.2 CFD domain & meshes of the single-fiber module in a 2D model

5.2.2 Analysis of heat-transfer resistance in MD

5.2.2.1 Overall heat-transfer coefficient and heat-transfer coefficient across the membrane

As the influence of the normal mass transferred across the membrane matrix was ignored due to the negligible amount, the corresponding induced latent heat was treated as MD characteristics and coupled into the heat-transfer model during the simulations.

In general, the heat-transfer mechanism in MD involves three steps in series: firstly, heat is transferred from the bulk liquid feed to the hot membrane surface, water molecules evaporate at the surface (at the mouth of the pores); secondly, water vapor carries the heat through the membrane matrix from the hot surface to the cold side, accompanied by latent heat generation and conductive heat loss; finally, the heat is released at the cold membrane surface by condensation and then reaches the bulk permeate (Schofield et al. 1987; Schofield et al. 1987). A schematic showing this heat-transfer process is given in Fig. 5.3, in which h_f and h_p are the heat-transfer coefficients for the feed and permeate, respectively; h_{MD} and h_{HL} are defined as equivalent heat-transfer coefficients for the heat transfer associated with evaporation and conduction, respectively.

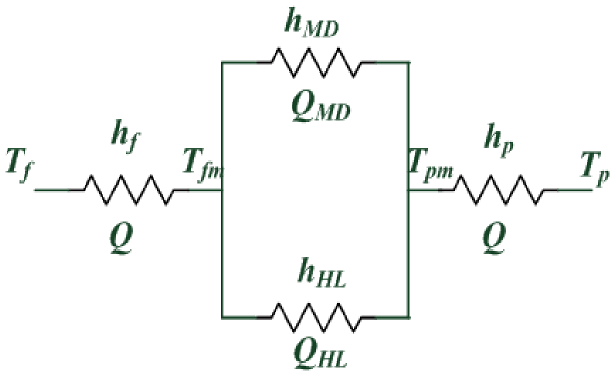

Fig. 5.3 Schematic of heat-transfer process in MD

The overall heat-transfer rate (W) across the membrane Q is written as:

$$Q = Q_f = Q_p = Q_{MD} + Q_{HL} \tag{5.7}$$

In CFD modeling, the bulk temperature T_f or T_p of a particular location in the flow channel are calculated by:

$$T_b = \frac{\int_S \rho u T \mathrm{d}S}{\int_S \rho u \mathrm{d}S} \tag{5.8}$$

where ρ and S are density, and cross-sectional area of feed-side or permeate-side, respectively and u is the velocity which normalizes to S. The overall heat-transfer coefficient, K, for a hollow fiber module can be expressed as (Thomas 1980):

$$\frac{1}{K} = \frac{1}{h_f} + \frac{1}{h_m} + \frac{1}{h_p} \cdot \frac{R_{mo}}{R_{mi}} \tag{5.9}$$

where

$$h_m = h_{MD} + h_{HL} \cdot \frac{R_{lm}}{R_{mo}} \tag{5.10}$$

and R_{lm} is the log mean radius of the hollow fiber; the coefficients K_{mo}, h_f, h_m and h_{MD} are calculated based on the outside wall surface of the hollow fiber. The reciprocals of heat-transfer coefficients $1/h$ represent the corresponding local resistances. h_m is the equivalent heat-transfer coefficient of the membrane, where the heat flux across the membrane q_m was defined in Eq. (2.5) as $q_m = h_m\left(T_{fm} - T_{pm}\right)$:

5.2.2.2 Heat-transfer coefficient of the bulk fluids (feed/permeate)

In an MD system the heat transfer across the liquid films–the feed side q_f and permeate side q_p were expressed in Eqs. (2.3) and (2.9), respectively. Thus, the corresponding heat-transfer coefficients h_f and h_p can be calculated:

$$h_f = \frac{q_f}{(T_f - T_{fm})} \tag{5.11}$$

$$h_p = \frac{q_p}{(T_{pm} - T_p)} \tag{5.12}$$

where the wall temperatures T_{fm} and T_{pm} are obtained from the temperature field in CFD simulations.

5.2.2.3 Equivalent heat-transfer coefficients due to evaporation and conduction

As the mass and heat transfer are closely related in MD, the latent heat flux q_{MD} is described in Eq. (2.7) as $N_m \cdot \Delta H_{T_{fm}}$, where $\Delta H_{T_{fm}}$ is the latent heat of evaporation occurring at the membrane surface on the feed side (T_{fm}). Different from Eq. (2.1), the mass flux N_m, kg m^{-2} s^{-1}, can also be defined using the transmembrane vapor pressure difference:

$$N_m = C\left(P_{fm} - P_{pm}\right) \tag{5.13}$$

or $N_m = C \frac{dP}{dT}\Big|_{T_m}\left(T_{fm} - T_{pm}\right)$ in Eq. (4.1) based on the vapor pressure gradient (Schofield et al. 1987). The saturated vapor pressures P_{fm} and P_{pm} are obtained from Antoine equation (T.K. Sherwood et al. 1975) at the membrane wall temperatures T_{fm} and T_{pm}, respectively. Here, the C is the intrinsic mass-transfer coefficient of the membrane, which is dependent on the membrane pore geometries and the operating temperature based on the mass transfer models (Phattaranawik et al. 2003).

To obtain the C value for the heat-transfer simulations in MD, various approaches such as the combined Knudsen diffusion, molecular diffusion and Poiseuille flow transition model (Ding et al. 2003), Knudsen diffusion model (Qtaishat et al. 2008; Bui et al. 2010) and Monte Carlo simulation method (Imdakm and Matsuura 2005) have been reported. Although C could change slightly with varied membrane temperatures, it can be taken as a constant with fixed membrane properties under certain operating conditions (Schofield et al. 1990). Therefore, in this chapter a similar simplified model has been adopted to assume a constant C equal to 2.0×10^{-7} kg m^{-2} s^{-1} Pa^{-1}, calculated from a series of single-fiber module tests presented in Chapter 3.

The combination of Eqs. (4.1) and (5.13) yields the following:

$$q_{MD} = C \frac{dP}{dT}\Big|_{T_m} \Delta H_{T_m} \left(T_{fm} - T_{pm}\right) \tag{5.14}$$

It can be simplified based on Newton’s law of cooling (Rohsenow and Hartnett 1973):

$$q_{MD} = h_{MD} \cdot \left(T_{fm} - T \right) \tag{5.15}$$

Thus, the h_{MD} is expressed as:

$$h_{MD} = C \frac{dP}{dT}\Big|_{T_m} \Delta H_{T_m} \tag{5.16}$$

Similarly, as given in Eq. (2.4), the equivalent heat-transfer coefficient for conduction is $h_{HL} = \frac{\lambda_m}{\delta_m}$, which is a constant for fixed membrane properties.

5.2.2.4 Thermal efficiency and characteristic temperature

Since energy is a major concern in MD, and the energy consumption can be assessed via three thermally related metrics namely the thermal efficiency (η_h), temperature-polarization coefficient (*TPC*) and hydraulic energy consumption (*HEC*). Firstly, as the total heat flux transferred through the membrane is split into two parts: the latent heat of evaporation (the effective portion that generates a certain amount of vapor) and the conduction across the membrane matrix (considered as heat loss), the MD thermal efficiency η_h is defined as the fraction of the evaporation heat:

$$\eta_h = \frac{Q_{MD}}{Q_{MD} + Q_{HL}} = \frac{h_{MD} \cdot A_o \cdot \left(T_{fm} - T_{pm}\right)}{\left(h_{MD} + h_{HL} \cdot \frac{R_{lm}}{R_{mo}}\right) A_o \cdot \left(T_{fm} - T_{pm}\right)} = \frac{h_{MD}}{h_{MD} + h_{HL} \cdot \frac{R_{lm}}{R_{mo}}} \tag{5.17}$$

In order to maximize the thermal efficiency η_h, the conductive heat loss should be minimized. It is mainly determined by the intrinsic MD coefficient C and operating temperatures. According to a previous study (Yu et al. 2011), η_h increases with increasing membrane temperature.

Secondly, *TPC* characterizes the actual driving force of the system (Schofield et al. 1987). It is expressed as in Eq. (2.2) as $TPC = \frac{T_{fm} - T_{pm}}{T_f - T_p}$.

Thirdly, the *HEC* describes the hydraulic pressure loss per kg distillate generated when waste heat is available:

$$HEC = \frac{\Delta P_{fluid} \cdot V}{N_m \cdot A} \tag{5.18}$$

In this chapter, the *HEC* is used to assess the advantages of applying different strategies to enhance the mass flux and mitigate the TP effect in terms of the pumping electricity cost.

5.3 Experimental settings

This section describes measurements and experiments used to validate the CFD simulation model.

5.3.1 Materials

In this chapter, similar polyvinylidene fluoride (PVDF) membrane (characterized experimentally in Chapter 4) was used. Briefly, the thermal properties of the PVDF hollow fibers and testing fluids were presented in Tables 5.2 and 5.3.

Table 5.2 Properties of the PVDF membrane

Material	Density kg/m^3	Specific heat J/(kg ·K)	Thermal conductivity W/(m ·K)
PVDF[23]	1775	1325	0.2622
Vapor*	0.554	2014	0.0261
Membrane	302.2	1896.9	0.0662

Table 5.3 Properties of the tested fluids

Material	Density kg/m^3	Specific heat J/(kg ·K)	Thermal conductivity w/(m ·K)	Viscosity ×10^{-4} Pa s
3.5% synthetic seawater (~323K) (Sparrow 2003)	1013.2	4064.8	0.642	5.86
Pure water (~303K) (Yaws 1999)	995.2	4182.1	0.613	8.38

5.3.2 DCMD experiment

To confirm the validity of the heat-transfer model for varied operating conditions and modified configurations, both the original (base line) and modified (with attached annular quad spacers 0.2 mm×2 mm of Ly = 10 and 30 mm, respectively) single-fiber modules were fabricated and tested. Similar to the fabrication procedures and materials in Chapter 4, these lab-scale MD modules with an effective fiber length of

0.25 m and a membrane area of 0.0011 m^2 were made by potting the PVDF hollow fiber membranes into Teflon housings.

The experimental data for these modules was obtained via a DCMD setup, which was described in Chapter 3. However, the operating conditions are different. Briefly, in a hollow fiber module operated in a countercurrent mode, the feed solution (synthetic seawater: 3.5 wt% sodium chloride (NaCl)) was heated (T_{fi} = 327.2 – 360.2 K) and circulated through the shell side (u_{fi} = 0.060 – 0.285 m s^{-1}, Reynolds number Re_f = 836 – 4000 for the original module). On the lumen side, the permeate (DI water) was cooled (T_{pi} = 293.85 – 327.15 K) and cycled through the lumen (u_{pi} = 0.417 m s^{-1}, Re_p = 460). The inlet and outlet pressure for the feed side were monitored by pressure transmitters (±0.01 Pa).

Hence, based on the operating conditions, laminar conditions were applied to the conservation equations on the permeate side during the simulations; while either laminar or turbulent models were used for the feed flow.

5.4 Results and discussion

5.4.1 CFD heat-transfer model verification

The heat-transfer model for the original MD module without promoters presented in Section 5.2.1 has been verified in our previous study (Yu et al. 2012). To further verify its applicability for altered configurations and varied flow velocities, an original and two modified 0.25 m modules (with annular quad spacers inserted) have been tested for the studies in the chapter. The comparison between the CFD simulation results and experimental data of mass flux and pressure drop is shown in Table 5.4, in which both the inlet temperatures (T_{fi} and T_{pi}) of selected systems (varied feed flow velocities and module configurations) and pressure drop (ΔP_f) along the module on the feed sides of modified modules are listed. It can be seen that the simulation results agree very well with the experimental data. The relative errors are within ±5% for both temperature and pressure drop results, which further verify the applicability of this currently-used heat-transfer model for various experimental settings.

Table. 5.4 Heat-transfer model verification--comparison of experimental data and simulation results (C = 2. 0 ×10^{-7}kg m^{-2} s^{-1} Pa^{-1}, L = 0.25m, T_{fi} = 327.15K, T_{pi} = 293.85K)

Temperature verification

Conditions		**T_{fi} (K)**	**T_{pi} (9)**	***Mass flux* (kg m^{-2} s^{-1})**		**Error (%)**
				Exp.	Sim.	
Original module (u_{pi} = 0.417 m s^{-1})	u_{fi}=0.107m s^{-1}	327.5	294.1	0.00190	0.00199	4.46
	u_{fi}=0.178m s^{-1}	327.1	293.8	0.00208	0.00201	-3.47
Modified modules (u_{fi} = 0.06m s^{-1}, u_{pi}= 0.417m s^{-1})	Q0.2*2*10	327.2	294.2	0.00211	0.00209	-0.93
	Q0.2*2*30	327.3	294.5	0.00195	0.00189	-2.99

Pressure-drop verification (shell side)

Conditions		**ΔP_f (Pa)**		**Error (%)**
		Exp.	Sim.	
Modified modules (u_{fi} = 0.06m s^{-1}, u_{pi} = 0.417m s^{-1})	Q0.2*2*10	66.2	66.7	0.656
	Q0.2*2*30	33.5	33.3	-0.585

5.4.2 Shift of dominant resistance in MD heat transfer

For scale up and industrial implementation, a qualitative evaluation of the overall/local heat-transfer resistances in a specific MD system is essential in prioritizing the key design parameters that would most affect the process performance. Fig. 5.4 shows the distributions of local heat-transfer coefficients for the original (base line) module as functions of the fiber length L for selected MD systems with various membrane properties (MD coefficient C) and operating conditions (temperatures T_{fi} and T_{pi}).

The first system in Fig. 5.4 (a) (small C = 2.0 ×10^{-7} kg m^{-2} s^{-1} Pa^{-1}, low temperatures T_{fi} = 327.15K, T_{pi} = 293.85K) shows an absolute dominance from the membrane itself in this heat-transfer process, which was the reference case studied previously (Yu et al. 2012). With the same operating temperatures but different membrane properties, the second system [Fig. 5.4 (b), large C = 8.0 ×10^{-7} kg m^{-2} s^{-1} Pa^{-1}, low temperature T_{fi} = 327.15K, T_{pi} = 293.85K] indicates that both membrane and feed flow play equally dominant roles; the third system [Fig. 5.4 (c), small $C = 2.0\times10^{-7}$ kg m^{-2} s^{-1} Pa^{-1}, high temperatures T_{fi} = 360.15K, T_{pi} = 326.85K] shows the main heat-transfer resistance partially shifts from the membrane to the liquid-boundary layer at the feed side along the module length; while the fourth case [Fig. 5.4 (d), large C value, high temperature T] indicates that the heat transfer through the feed liquid-boundary layer is the controlling step in heat transfer. Therefore, as an extended exploration of the effectiveness of hydrodynamic enhancement on the shell-side when the liquid-boundary layer controls the heat-transfer process, cases (b), (c) and (d) were chosen as the simulated conditions in this chapter. Approaches such as the insertion of turbulence promoters and increase of flow velocity to alter flow geometries, reduce the TP effect and enhance permeation flux will be discussed in the later sections.

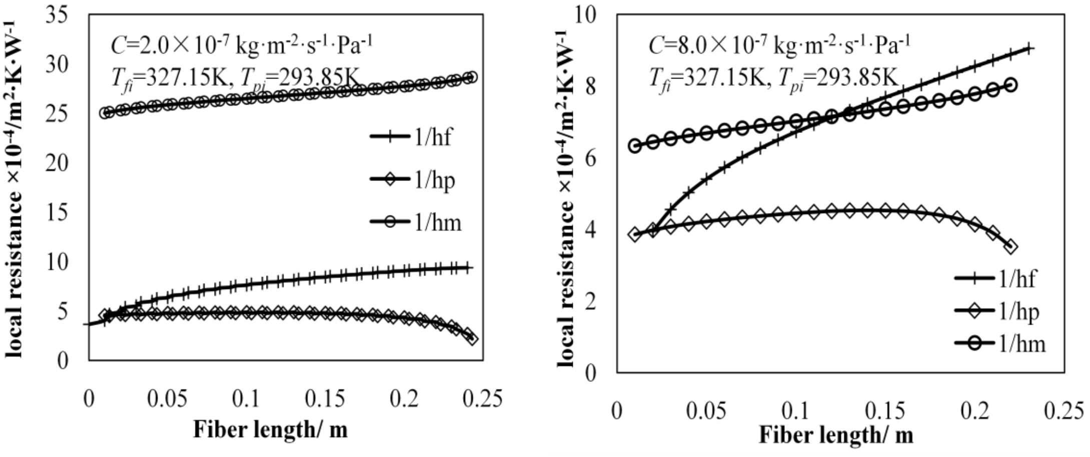

(a) Small C, low temperature T

(b) Large C, low temperature T

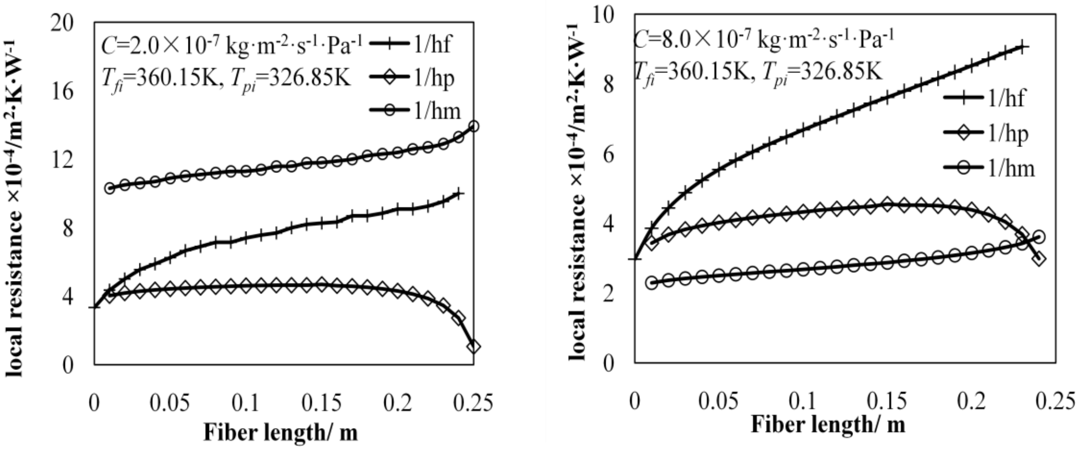

(c) Small C, high temperature T

(d) Large C, high temperature T

Fig. 5.4 Local heat-transfer coefficients distributions along the module length under various operating conditions (T_{fi}= 327.15 &360.85 K, T_{pi}= 293.85 & 326.85 K, u_{fi}= 0.06 m s^{-1}, u_{pi}= 0.417m s^{-1}, C= 2.0& 8.0×10^{-7} kg m^{-2} s^{-1} Pa^{-1})

5.4.3 Effect of turbulence promoters at large C & low temperatures

5.4.3.2 Improvement on heat transfer coefficients

As discussed previously, in an MD system with a highly permeable membrane of C = 8.0×10^{-7} kg m^{-2} s^{-1} Pa^{-1} and low operating temperatures T_f = 327.15 K, T_p = 293.85 K [Fig. 5.4 (b)] the heat transfer coefficient of the liquid-boundary layer on the feed-side, h_f, plays an important role in determining the overall resistance. Fig. 5.5 shows the simulated distributions of heat transfer coefficients h_f and h_p along the module length, respectively, for the original and modified modules with different turbulence promoters.

In Fig. 5.5 (a) the h_f distribution curves for all configurations show a decreasing trend along the module length, except the slight changes at the entrances and exits. This is due to the build-up of thermal boundary layers along the flow direction. For the original module, the highest value appears at the entrance of the feed side and then decreases along the flow direction until it reaches a plateau when the flow is fully developed. In contrast, the modified modules generally show a convex decreasing trend along the module length, i.e., starting with a relatively small value at the entrance region before hitting the first barrier (attached/floating spacer or baffle), rising to a higher value when the flow crosses this barrier and starting a slight decrease after reaching the second one.

Overall, the original module has the lowest h_f distribution curve, which indicates an average value of 1495 W m^{-2} K^{-1}; while the configuration with baffles 0.2×2×10 shows the highest value of 10057 W m^{-2} K^{-1}, which is 6.7 times of the original module, followed by the configurations with attached quad spacers 0.2×2×20 and floating round spacers 0.75. It is of interest that the module with attached quad spacers of a smaller interval Lx = 10mm (i.e., more spacers) even shows a lower curve compared to that with Lx = 20mm. Generally, the h_f curves for the modified modules decrease more slowly than that of the original. This may be because the flow disturbance has greatly delayed the flow development and build-up of thermal boundary layers along the flow directions. The significant enhancement of heat-transfer coefficients by incorporating turbulence promoters has confirmed the controlling effect of the liquid-boundary layers in this MD system with a large C &

low temperatures. More discussions on the flow-field distribution associated with intensified radial mixing, reduced TP and enhanced permeation flux will be presented in a later section.

In Fig. 5.5(b), the distribution curves of the heat-transfer coefficients on the permeate side h_p shows a similar trend to the h_f of the original module, i.e., the highest values appear at the entrances of the permeate side (L = 0.25) and then decrease along the flow directions until a plateau reached. However, the difference between the original and modified modules is negligible, due to similar hydrodynamics. This observation is consistent with the explanation for Fig. 5.4(b), which shows that the heat transfer on the permeate side is not a controlling step.

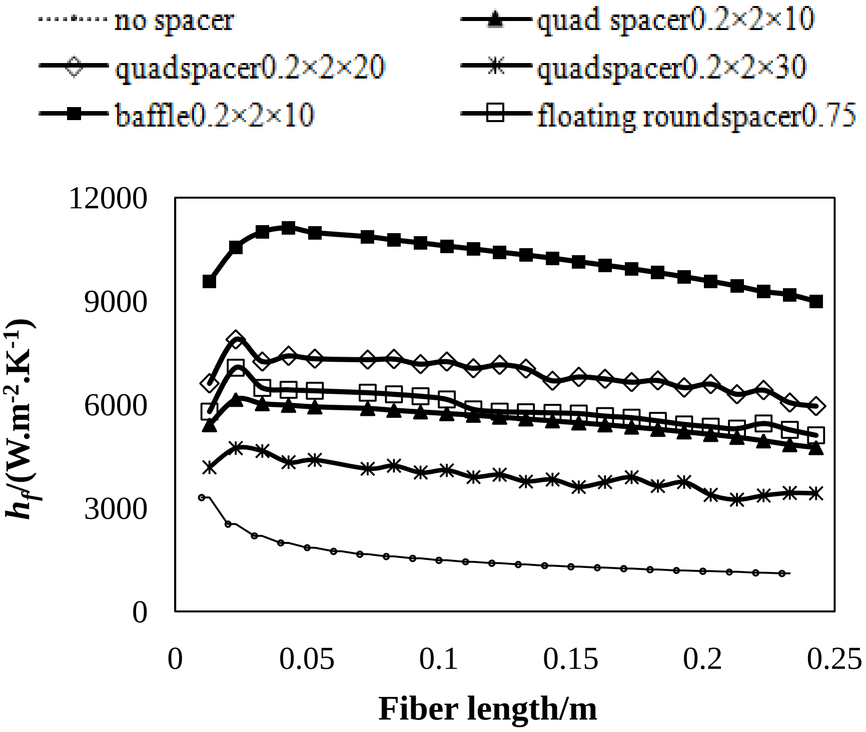

(a) h_f distributions vs. module length L

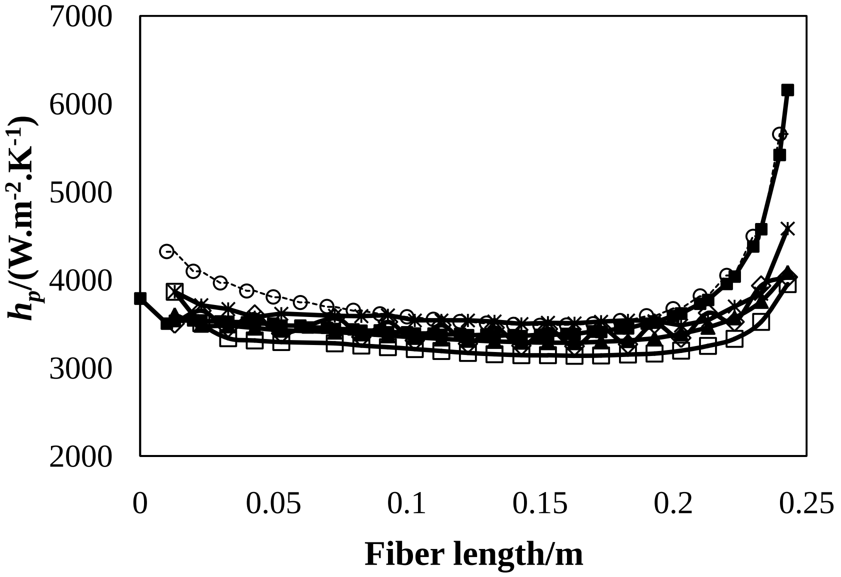

(b) h_p distributions vs. module length L

Fig. 5.5 h_f & h_p distributions along the fiber length for various turbulence promoters (a) h_f distributions vs. module length L; (b) h_p distributions vs. module length L (C = 8.0×10^{-7} kg m^{-2} s^{-1} Pa^{-1}, L = 0.25m, u_{fi} = 0.06 m s^{-1}, u_{pi} = 0.417m s^{-1}, T_{fi} = 327.15 K, T_{pi} = 293.85 K)

5.4.3.3 Temperature-polarization mitigation and flow-field visualization

Since the introduction of certain turbulence promoters made a significant improvement in heat transfer coefficient h_f, it is anticipated that the TP effect would be reduced due to the enhanced heat transfer. To explore the ability of TP prevention of various turbulence promoters in the same MD system (Fig. 5.4 (b)), Fig.5.6 shows the simulated *TPC* distribution curves along the module length L for both original and ten different modified single fiber modules (i.e., listed in Table 5.1).

It can be seen from Fig. 5.6 that the original module presents a downward U shape profile with the maximum value at the entrance and the lowest at the midpoint of the module then a slow increase towards the exit. This is because the transmembrane temperature difference (T_{fm} – T_{pm}) first decreases and then increases due to the opposite thermal boundary-layer build-ups on the feed and the permeate sides: the T_{fm} continues to decrease along its flow direction (x) and T_{pm} first increases and then decreases along the *x* direction. On the other hand, the *TPC* curves of the modified configurations show a U shape with an upward trend—only a slight decrease when the flow hits the first barrier and then a continuous increasing trend along the module length. The maximum values appear at the exits of the modules. A possible reason is that the insertion of different turbulence promoters has caused secondary flows in between barriers and a degree of radial mixing in the entire flow channel. The formation of vortices has greatly disturbed the thermal boundary layer build-up on the membrane surface and reduced the temperature difference between the bulk and membrane wall. Therefore, the temperature polarization phenomenon in MD is greatly mitigated due to the effective flow alteration that results in an increased effective driving force.

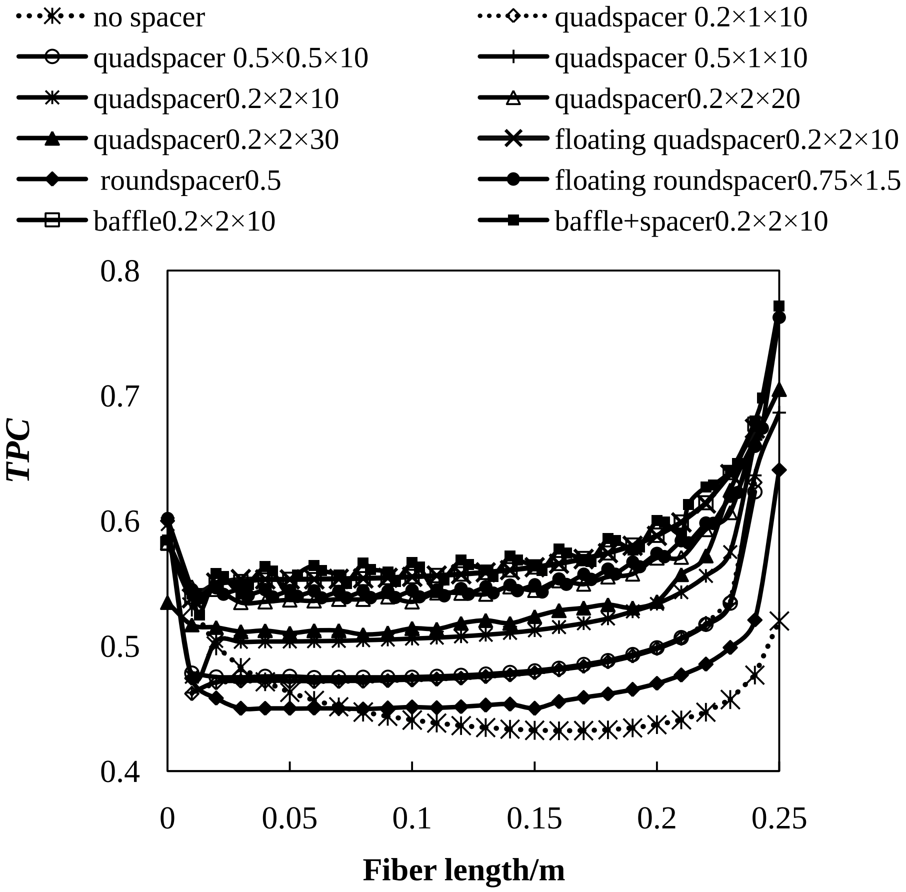

Fig. 5.6 *TPC* distribution along the fiber length for modules with turbulence aids of various specification ($C = 8.0\times10^{-7}$ kg m^{-2} s^{-1} Pa^{-1}, L = 0.25m, u_{fi} = 0.06 m s^{-1}, u_{pi} = 0.417m s^{-1}, T_{fi} = 327.15 K, T_{pi} = 293.85 K)

Overall, the original module has the lowest *TPC* curve; while the design with alternate arrangements of quad spacers and baffles (r = 0.75 mm, Ly = 0.5mm) shows the highest, which is up to a 45% increase compared to the original module, closely followed by the configurations with baffles, floating round spacers and floating quad spacers 0.2×2×10. Interestingly, the results of quad spacers with the same specifications (Δx = 0.2 mm, Δy = 2 mm) but different intervals Lx (from 10 to 30 mm) indicate that the configuration with the most spacers inserted (smallest interval of 10 mm) is not necessarily a better design. For example, a configuration with Lx of 10 mm shows similar results to that with less spacers (Lx= 20 mm) in terms of TP mitigation; while its h_f curve was even slightly lower as shown in Fig. 5.5(a). This is probably because the over-frequent arrangement has instead caused more liquid stagnant zones that compromise the module performance. However, a further decrease in the number of spacers (Lx= 30 mm) might result in insufficient disturbance and mixing, and there may be an optimum spacing.

Moreover, for modules with quad spacers of the same interval Lx =10 mm, the longer spacers (e.g., Δy = 2 mm) are less vulnerable to the TP phenomenon than shorter ones (e.g., Δy =1 mm); while wider spacers (e.g., Δx = 0.5 mm) are more vulnerable than narrower ones (e.g., Δx = 0.2 mm). This indicates that the shorter and wider spacers are less likely to promote secondary flows in the flow channels. It has negligible contributions to disturb the flow or enhance the heat transfer when the spacers have small dimensions ($\Delta y \leq 2$ mm) on the shell side. Interestingly, a design with attached round spacers (r = 0.5 mm) shows negligible improvement in terms of TP alleviation, due to its small diameter and the particular cross-sectional shape that possibly causes stagnation of the passing liquid. Therefore, it gives almost the same average *TPC* result as the original module. Nevertheless, it still shows an upward U shape, which evidently implies its potential in creating stronger secondary flows with an increased diameter (e.g., floating round spacer 0.75).

To relate the enhanced module performance with the hydrodynamic improvement by employing turbulence promoters of various specifications, Fig. 5.7 shows the local flow fields and temperature distribution in the modified modules. Since all turbulence promoters are inserted with regular intervals, the velocity profiles along the module length can be seen periodically between every two barriers. Therefore, only local flow fields within a certain range of fiber length (0.105−0.125 m) for modified modules are presented in Fig. 5.7. The velocity profiles (flow fields) are described by the stream traces and temperature distribution by band colors. These results are consistent with the trends of the heat-transfer coefficients curves shown in Fig. 5.5 and *TPC* distributions in Fig. 5.6 for these modified modules. Clearly, in Fig. 5.7 (a) the attached round spacers (r = 0.5 mm) do not show effective disturbance in the bulk flow. As those round spacers are raised (Ly = 1.5 mm) and have a larger diameter, stronger secondary flows form in between the barriers and vortices appear near the membrane surface to reduce the thickness of liquid-boundary layers. Similarly, there is no visible altering effect from those short and wide quad spacers (e.g., $\Delta x \times \Delta y \times Lx$ = 0.5mm×0.5mm×10mm). The secondary flows between spacers become more intense with an increasing Δy [from 0.5 mm to 2 mm in Fig. 5.7 (b)]. As the gap between membrane surface and spacers Ly increases from 0 to 1.5 mm till the spacers reach the shell wall (i.e., baffles), more vortices form along the x direction and more intense radial mixing is observed from the schemes of flow fields. The flow tends to be more homogenous when an alternate arrangement of attached spacers and baffles 0.2×2×10 is employed. Combined with the simulation results shown in Figs. 5.3 and 5.4, in a liquid-film controlled heat-transfer system, the more intense secondary flows and radial mixing will result in reduced thermal boundary layers, alleviated TP effect and hence enhanced heat transfer.

(a) Round spacers—annular spacers with circular cross-section

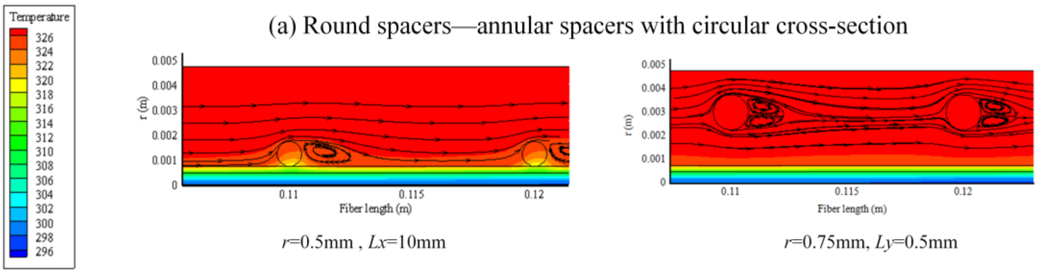

r=0.5mm , Lx=10mm

r=0.75mm, Ly=0.5mm

(b) Quad spacers—annular spacers with square cross-section

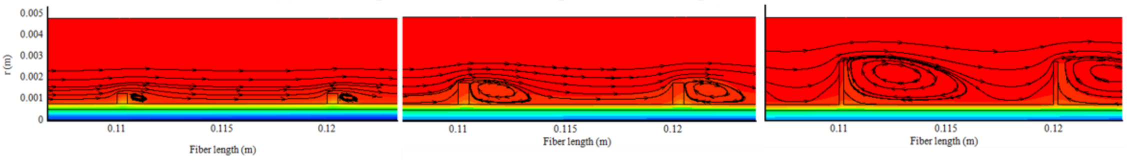

$\Delta x\times\Delta y\times Lx\times Ly$=0.5×0.5×10×0mm

$\Delta x\times\Delta y\times Lx\times Ly$=0.5×1.0×10×0mm

$\Delta x\times\Delta y\times Lx\times Ly$=0.2×2.0×10×0mm

(c) Floating quad spacers and/or baffles

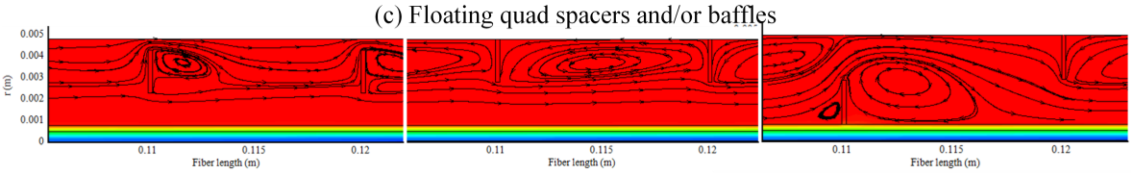

$\Delta x\times\Delta y\times Lx\times Ly$=0.2×2.0×10×1.5mm

$\Delta x\times\Delta y\times Lx$=0.2×2×10mm, baffles

$\Delta x\times\Delta y\times Lx$=0.2×2×10mm, baffles+spacers

Fig. 5.7 Local flow field visualization for modules with various turbulence promoters (C = 8.0×10^{-7} kg m^{-2} s^{-1} Pa^{-1}, L = 0.25 m, u_{fi}= 0.06 m s^{-1}, u_{pi}= 0.417m s^{-1}, T_{fi}= 327.15 K, T_{pi}= 293.85 K)

5.4.3.4 Enhancement of permeation flux

Fig. 5.8 gives the distributions of mass fluxes N_m along the module length for modules with various turbulence promoters. For the original module, the N_m curve has a similar trend to its *TPC* distribution shown in Fig. 5.6 — first decreasing and then slowly increasing until the exit. This trend can also be explained by the countercurrent build-ups of the thermal boundary layers on the feed and permeate sides, where the thinnest boundary layers occur at the respective entrances. Consistent with the upward trend of *TPC* curves in Fig. 5.6, the modified modules show dramatically increasing N_m distributions along the module length.

Overall, the original module has the lowest N_m curve; while the modified modules with alternate arrangements of attached spacers & baffles, baffles and floating quad spacers (0.2×2×10, Ly=1.5mm) achieve the best N_m results, closely followed by the designs with floating round spacers (r = 0.75mm, Ly=1.5mm) and attached quad spacers (0.2×2×20); the highest average flux improvement is up to 58% when compared to the original configuration. The modules with shorter and wider quad/ smaller round attached spacers show relatively lower fluxes. This may be due to the insufficient disturbance of the fluid from the radial direction, as displayed in Fig. 5.7, which shows that the intensity of the secondary flows induced by turbulence promoters of different specifications is consistent with their temperature-polarization mitigating performance (Fig. 5.6) and permeation flux increment (Fig. 5.8). Additionally, based on the above discussions of Figs. 5.5−5.8, the interval of the quad spacers does not necessarily make a significant difference for enhancing module performance. e.g., both modules with intervals of *Lx* = 10 mm and 20 mm show similar results. In this case selection of the most appropriate design should be based on the least complex fabrication and on hydraulic energy consumption (see section 5.4.6).

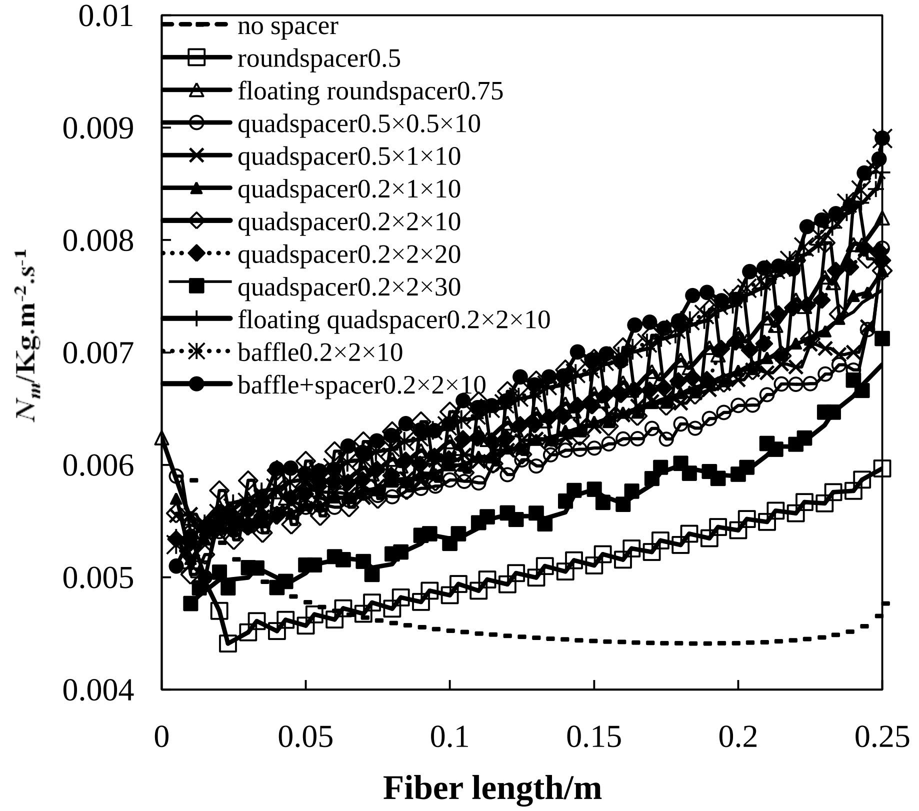

Fig. 5.8 Mass flux N_m distribution along the fiber length for modules with turbulence aids of various specification (C = 8.0×10^{-7} kg m^{-2} s^{-1} Pa^{-1}, L = 0.25 m, u_{fi} = 0.06 m s^{-1}, u_{pi} = 0.417 m s^{-1}, T_{fi}= 327.15 K, T_{pi} = 293.85 K)

5.4.3.5 Effect of turbulence promoters on thermal efficiency

Fig. 5.9 depicts the thermal efficiency η_h distribution along the module length for the original and modified modules with a membrane of large C (i.e., $C = 8.0\times10^{-7}$ kg m^{-2} s^{-1} Pa^{-1}) and lower operating temperatures (i.e., $T_f = 327.15$ K, $T_p = 293.85$ K). It is observed that the insertion of turbulence promoters (e.g., baffles or floating round spacers) can only achieve up to 5% improvement on the thermal efficiency compared to the original configuration. These results show that the magnitude of thermal efficiency is not sensitive to the introduction of turbulence aids; this is because the permeability of the membrane (C value) is a determinant factor for the fraction of effective heat in an MD system.

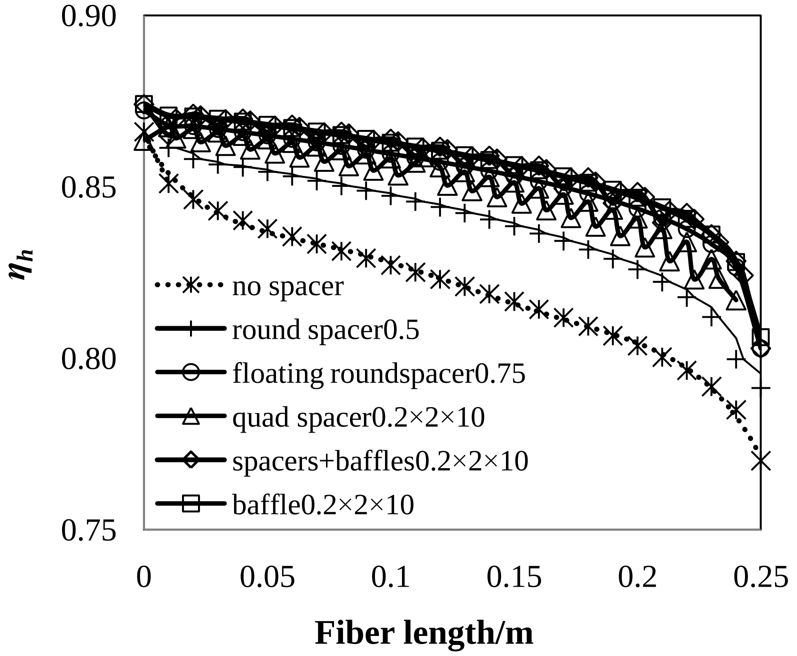

Fig. 5.9 η_h distribution along the module length for modules with various turbulence promoters ($C = 8.0\times10^{-7}$ kg m^{-2} s^{-1} Pa^{-1}, $L = 0.25$m, $u_{fi} = 0.06$ m s^{-1}, $u_{pi} = 0.417$ m s^{-1}, $T_{fi} = 327.15$ K, $Re_p = 460$, $T_{pi} = 293.85$ K)

5.4.4 Effect of turbulence promoters at high operating temperatures

Based on the discussions of the prior selected MD system [Fig. 5.4 (b)], an appropriate insertion of turbulence promoters in the feed flow could greatly enhance the module performance when the heat-transfer process is controlled by the liquid boundary layer. The other two selected MD systems [Fig. 5.4 (c) & (d)], which are operated at high feed/permeate temperatures; also indicate a dominant effect of the heat transferred through the feed-side flow. To further explore the effectiveness of turbulence promoters under different operating conditions, a series of simulations were conducted for these two systems [Fig. 5.4 (c) & (d). The results are shown in Figs. 5.8–5.10, which depict the effects of turbulence promoters (floating round and quad spacers) on the distributions of h_f, *TPC* and N_m along the module length at high operating temperatures (i.e., $T_f = 360.15$ K, $T_p = 326.85$ K), respectively. These two membrane systems with different C values of 2.0 and 8.0×10^{-7} kg m^{-2} s^{-1} Pa^{-1} are simulated and compared.

In Fig. 5.10 (a), when C is small (i.e., 2.0×10^{-7} kg m^{-2} s^{-1} Pa^{-1}) the heat-transfer coefficient h_f of the modified module with regularly-distanced baffles on the feed side gains a 5.8-fold improvement over the original configuration, closely followed by the module with floating round spacers; while the one with attached quad spacers ($0.2\times2\times10$) has a 2.3-fold increase. Similarly, when C increases to 8.0×10^{-7} kg m^{-2} s^{-1} Pa^{-1} [(Fig. 5.10 (b)] the enhancement of the modified modules is as significant as 6- and 3-fold with the same designs of baffles (or floating round spacers) and attached-quad spacers, respectively. In Fig. 5.11 (a), the most significant increase of *TPC* is achieved by the design with floating-round spacers— 30% enhancement compared to the original module, closely followed by a design with baffles; while the same configuration (floating-round spacers) shows a much higher increment of 57% when C increases to 8.0×10^{-7} kg m^{-2} s^{-1} Pa^{-1} [Fig. 5.11 (b)]. This is consistent with the results of mass fluxes N_m shown in Fig. 5.12— the percentages of flux enhancement by modified modules with floating-round spacers are 42% and 74% for the membranes with small and large C values, respectively.

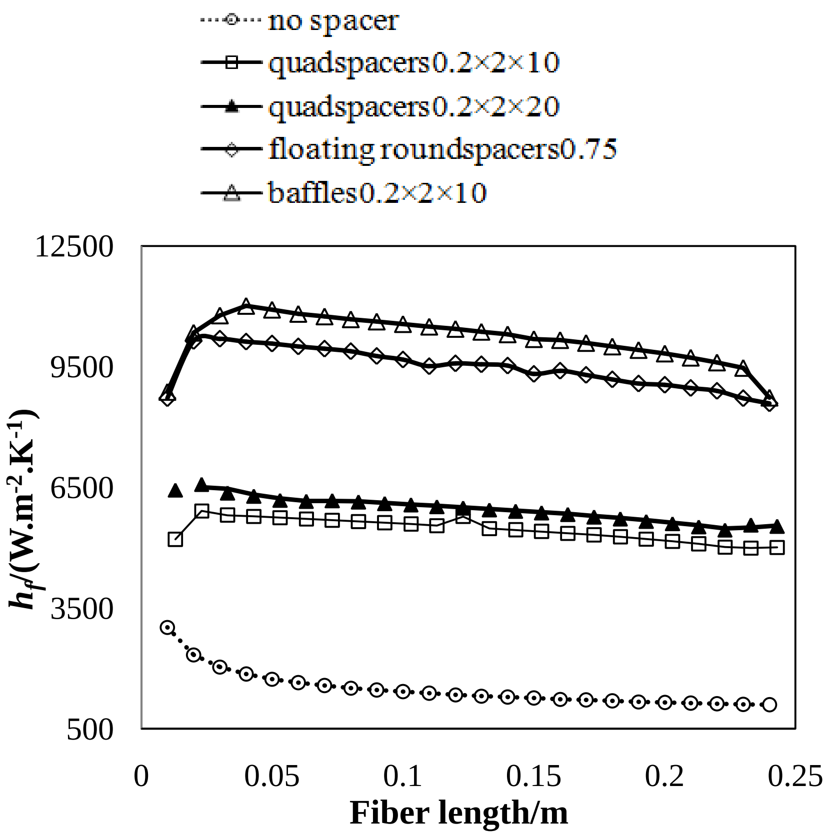

(a) C=2.0×10^{-7} kg m^{-2} s^{-1} Pa^{-1}

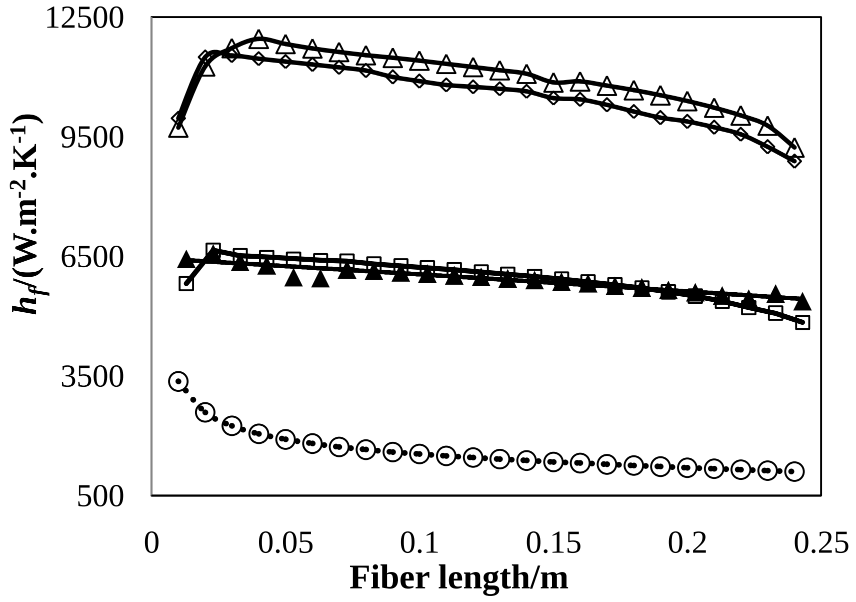

(b) C=8.0×10^{-7} kg m^{-2} s^{-1} Pa^{-1}

Fig. 5.10 Effects of turbulence promoters on h_f distributions along the fiber length at high temperatures for membranes with different C values (L = 0.25 m, u_{fi} = 0.06 m s^{-1}, u_{pi} = 0.417m s^{-1}, T_{fi} = 360.15 K, T_{pi} = 326.85 K)

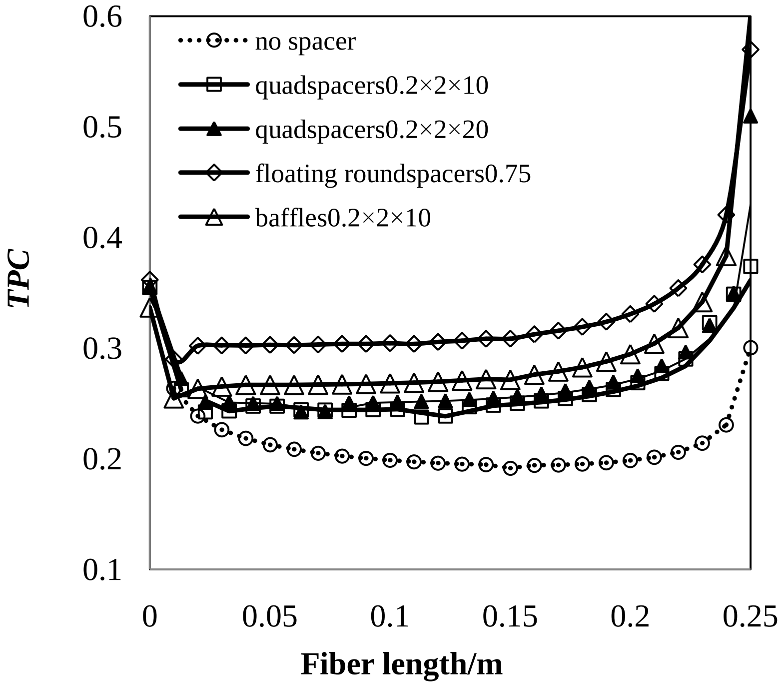

(a) $C = 2.0 \times 10^{-7}$ kg m^{-2} s^{-1} Pa^{-1}

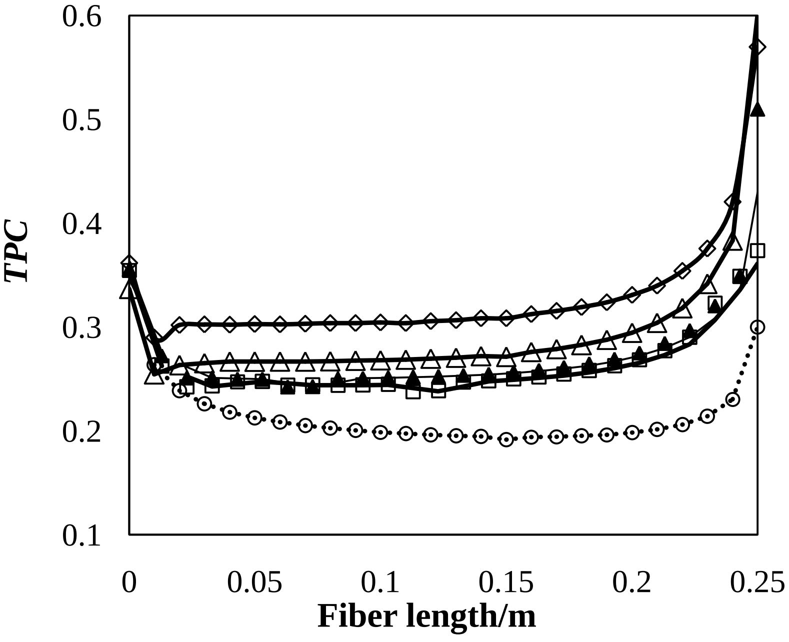

(b) $C = 8.0 \times 10^{-7}$ kg m^{-2} s^{-1} Pa^{-1}

Fig. 5.11 Effects of turbulence promoters on *TPC* distributions along the fiber length at high temperatures for membranes with different *C* values ($u_{pi} = 0.417$m s^{-1}, $T_{fi} =$ 360.15 K, $T_{pi} = 326.85$ K)

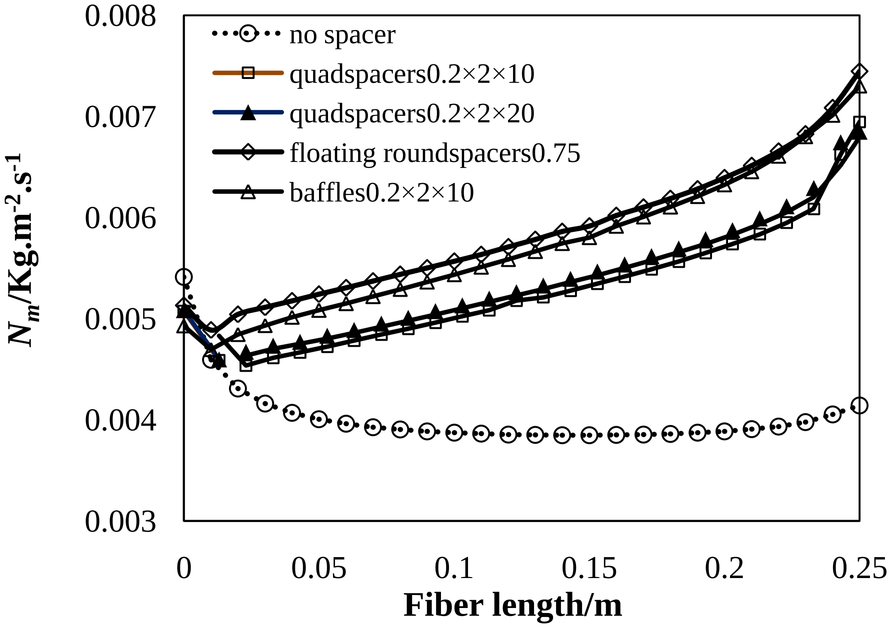

(a) $C = 2.0\times10^{-7}$ kg m^{-2} s^{-1} Pa^{-1}

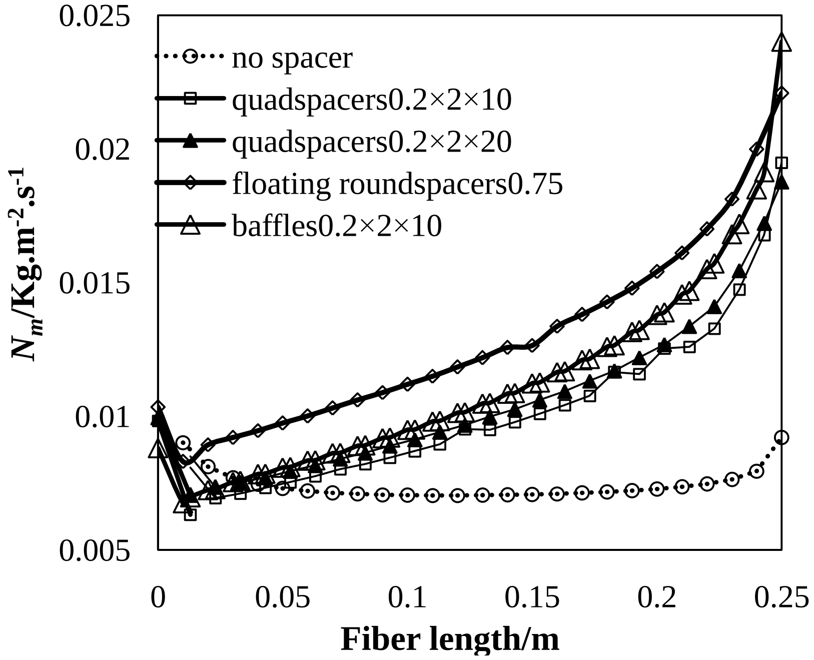

(b) $C = 8.0\times10^{-7}$ kg m^{-2} s^{-1} Pa^{-1}

Fig. 5.12 Effects of turbulence promoters on N_m distributions along the fiber length at high temperatures for membranes with different C values ($u_{pi} = 0.417$ m s^{-1}, $T_{fi} = 360.15$ K, $T_{pi} = 326.85$ K)

These simulation results for an MD system operated at high operating temperatures shows an absolute control of heat transferred through the liquid boundary layers, regardless of the membrane permeability. Therefore, the module design plays an essential role in achieving a higher water production and better performance. Nevertheless, with a more highly permeable membrane, the heat transfer resistance in the liquid boundary layer is more dominant and hence the enhancement of hydrodynamics with the aid of turbulence promoters would be more effective. Thus, it is important to identify the dominant factors when designing novel module configurations for an MD system.

Based on the above discussions, two three-dimensional charts are given in Fig. 5.13 to present the relationships between the MD coefficient *C* and operating temperatures *T* vs. *TPC* and thermal efficiency. In Fig. 5.13 (a) the *TPC* is shown decreasing as *C* and the operating temperatures increase; while in Fig. 5.13 (b) the thermal efficiency increases dramatically with increasing *C* and operating temperatures. Obviously, to predict the module performance and assess the process efficiency, considerations should be taken for selecting process parameters based on the membrane properties and available heat sources. For example, a potentially selected MD system (as shown in Fig. 5.13), which has a medium MD coefficient $C = 3 - 6$ kg m^{-2} s^{-1} Pa^{-1} and relatively mild operating feed temperature of 340 K, can achieved an overall *TPC* of 0.55 and thermal efficiency up to 70%.

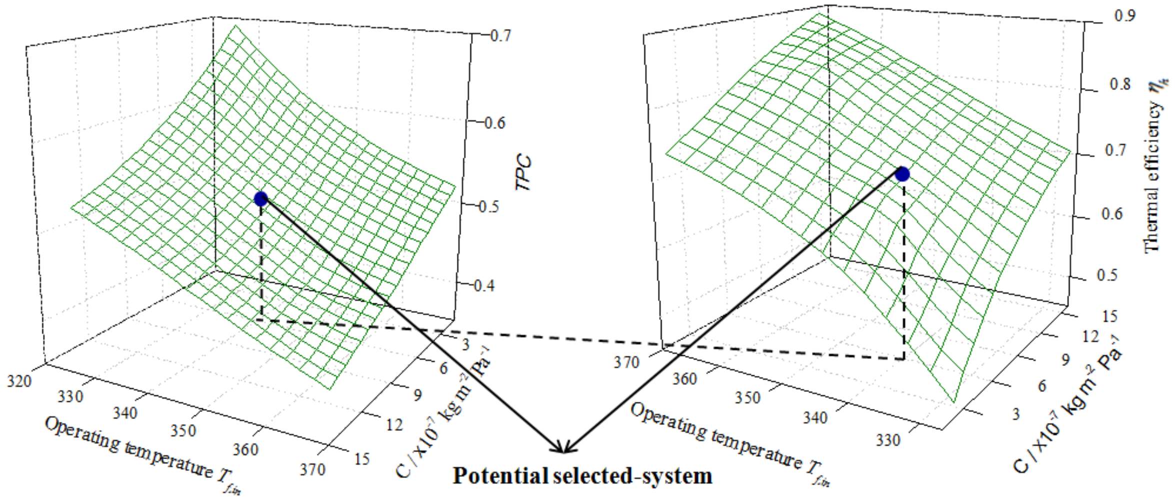

Fig. 5.13 Effects of *C* values and operating temperatures on the *TPC* and thermal efficiency for the original module ($C = 2.0 \times 10^{-7}$ kg m^{-2} s^{-1} Pa^{-1}, $L = 0.25$m, $u_{fi} = 0.06$ m s^{-1}, $u_{pi} = 0.417$ m s^{-1}, $T_{fi} = 327.15$ K, $T_{pi} = 293.85$ K)

5.4.5 Effect of feed flow velocity for non-spacer original module

As a conventional strategy to improve hydrodynamic conditions, an increase of flow velocity to reach turbulence is found to be effective. However, similar to other approaches, its effectiveness may differ from system to system. Fig. 5.14 shows the effects of feed-flow velocity on the *TPC* and mass flux N_m distributions for the original module with membranes of different C values under operating temperatures of $T_{fi} = 327.15$ K and $T_{pi} = 293.85$ K. Similar to the distributing trends of modified modules with turbulence promoters, in Fig. 5.14 (a) the *TPC* distributions for both membranes under laminar condition (i.e., $u_{fi} = 0.006$ m s^{-1}, $Re_f = 836$ for the original module) show a typical U shape; while the curves for the turbulence conditions [i.e., $u_{fi} = 0.178$ m s^{-1} ($Re_f = 2500$) and 0.285 m s^{-1} ($Re_f = 4000$)] present an increasing trend. It is also noted that a further increase of turbulent intensity (i.e., Re_f) does not contribute to better module performance.

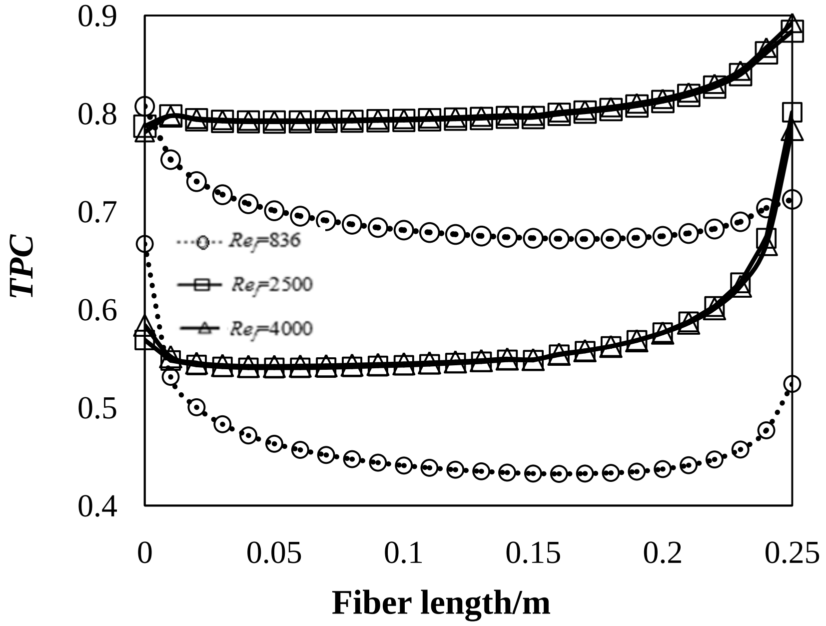

(a) *TPC* distributions vs. module length L

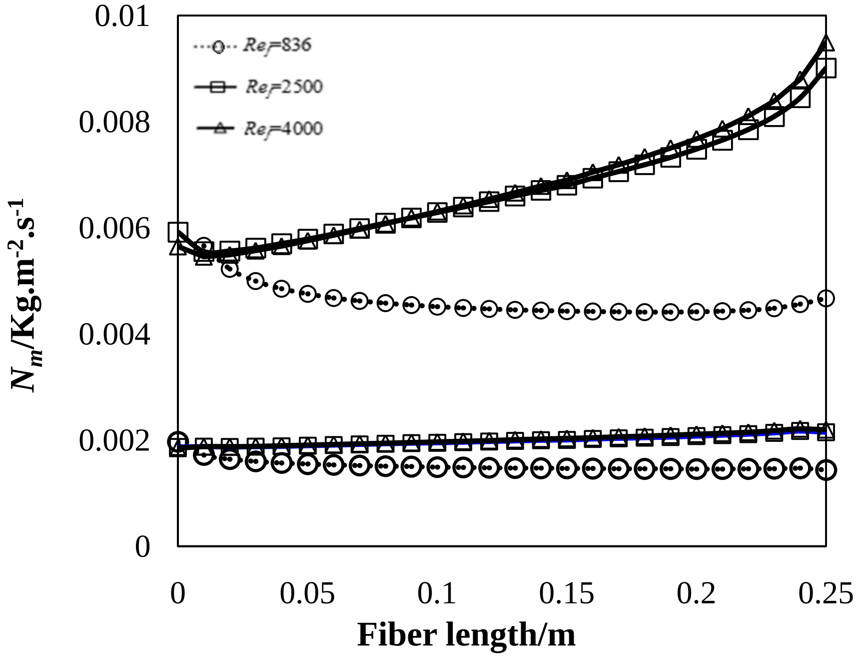

(b) N_m distributions vs. module length L

Fig. 5.14 Effects of flow velocity on *TPC* and N_m distributions along the fiber length for unaltered modules with different C values (a) *TPC* distributions; (b) N_m distributions (C = 2 & 8.0×10^{-7} kg m^{-2} s^{-1} Pa^{-1}, L = 0.25m, Re_f=836, 2500 & 4000, Re_p = 460, T_{fi} = 327.15 K, T_{pi} = 293.85 K)

In general, the MD system with a smaller C (2.0×10^{-7} kg m^{-2} s^{-1} Pa^{-1}, upper curves) has a higher *TPC* but is less sensitive to the velocity change compared to that with a larger C (8.0×10^{-7} kg m^{-2} s^{-1} Pa^{-1}, lower curves) as shown in Fig. 5.14 (a). In the former system the turbulence condition brings 15% *TPC* increase while the latter 25%. This is because the controlling heat-transfer resistance shifts from the membrane itself to the liquid-boundary layers on the feed-side with an increased C value under the same operating conditions. Interestingly, at a higher flow velocity u_{fi} = 0.178 m s^{-1}, the original module with a membrane of a smaller C (i.e., 2.0×10^{-7} kg m^{-2} s^{-1} Pa^{-1} at T_f = 327.15K and T_p = 293.85K) gains similar enhancement (i.e., 15%) to that of the modified module with annular baffles investigated at a lower velocity (u_{fi} = 0.006 m s^{-1}) in our previous work (Yu et al. 2012). However, compared to the 25% increase by employing a high velocity (u_{fi} = 0.178 m s^{-1}), the *TPC* of the same modified design (i.e., 8.0×10^{-7} kg m^{-2} s^{-1} Pa^{-1} at T_f = 327.15 K and T_p = 293.85 K) increased by 42% at the same temperature conditions but a low velocity (u_{fi} =

0.006 m s^{-1}) (Fig. 5.6). This may be due to the more intense radial mixing and surface renewal effect induced by the turbulence promoters than merely increasing the flow velocity. Thus, the membrane wall temperatures tend to be closer to that of the bulk fluids in a properly modified module.

Similar to the N_m curves shown in Fig. 5.8, the mass flux distributions in Fig. 5.14 (b) for the same systems under laminar condition initially decrease and then slightly increase towards the exit of the feed flow; while under turbulent conditions, it shows an increasing trend due to better local mixing and surface renewal effect that led to an increase of driving force at a higher flow velocity. However, the system with a larger C (upper curves) has a more dramatic flux increment 47% compared to that with a smaller one (lower curves), which achieves 30% enhancement with the same velocity increase. Yet, it was 32% and 53% for a modified module with baffles for respective C values (Fig. 5.8). Hence, given the more dominant role that liquid boundary layers play in the heat-transfer system, the appropriate selection of turbulence promoters could bring more significant enhancement in improving the module performance. However, for a more comprehensive evaluation of the different enhancement strategies, the hydraulic energy consumption (*HEC*) is another metric that will be compared.

5.4.6 Analysis of hydraulic energy consumption (*HEC*)

As discussed in the previous sections, an appropriate selection and arrangement of turbulence aids (e.g., floating spacers, baffles, high velocity, etc.) would greatly reduce the heat-transfer resistance and enhance the module performance, when the heat transferred through the liquid boundary layer is dominant. Nevertheless, with available waste heat sources, the hydraulic loss caused by the insertion of turbulence promoters or increase of circulating velocity becomes a major concern of energy consumption in MD. Fig. 5.15 shows the average permeation flux and hydraulic loss as a function of turbulence aids, including all turbulence promoters listed in Table. 5.1 and varied feed-flow velocity. The original module has a low *HEC* of 6.5 J kg^{-1} when u_{fi} = 0.06 m s^{-1} (Re_f = 836, laminar flow) and it dramatically rises to 100.7 J kg^{-1} when entering the turbulence regime with u_{fi} = 0.178m s^{-1} (Re_f = 2500). Among these modified modules operated under the same low feed flow velocity u_{fi} =

0.06 m s^{-1}, the alternate arrangement of attached quad spacers and baffles (i.e., Q+B) show the highest *HEC* of 191.5 $J{\cdot}kg^{-1}$, followed by the baffles (B0.2×2×10) and floating quad spacers (FQ0.2×2×10), which cause drastic pressure rises compared to the attached quad (Q0.2×2×10) and floating round spacers (FR0.2×2×10) with fairly insignificant hydraulic pressure losses (<40 $J{\cdot}kg^{-1}$).

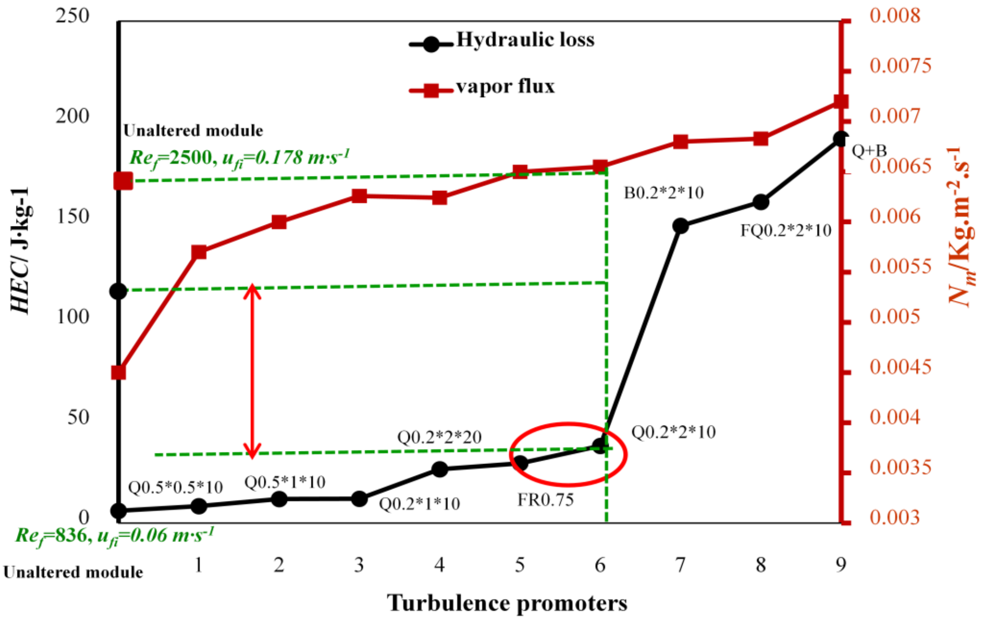

Fig. 5.15 Hydraulic loss and vapor flux comparisons for various turbulence promoters ($C = 8.0\times10^{-7}$ kg m^{-2} s^{-1} Pa^{-1}, $L = 0.25$m, $u_{fi} = 0.06$ m s^{-1} for all modified modules, $u_{fi} = 0.06$ & 0.178 m s^{-1} with respective Re_f=836 & 2500 for the original module, u_{pi}=0.417 m s^{-1} (Re_p= 460), T_{fi} = 327.15 K, T_{pi} = 293.85 K, Q = quad spacer, FR = floating round spacer, B = baffle, FQ = floating quad spacer, Q+B = quad spacer + baffle)

Although the design with alternate spacers and baffles (Q+B) shows the highest flux increase of 58% over the original module, it has the highest *HEC* result, followed by those with floating quad spacers (FQ0.2×2×10) and baffles (B0.2×2×10). Clearly, the configurations with attached quad (Q0.2×2×10) and floating round spacers (FR0.75) show a good compromise for achieving enhanced vapor fluxes with relatively low *HECs* of 28.9 and 38.4 $J{\cdot}kg^{-1}$, respectively. Presumably, they have reached the same turbulent conditions by achieving the same flux as the original module with a higher velocity (Re_f = 2500), which causes an approximately 3-fold higher hydraulic loss of 100.7 $J{\cdot}kg^{-1}$. Therefore, a compromise must be made for an enhanced permeation flux as well as a relatively lower *HEC* in evaluating the module performance.

5.5 Conclusions

In this chapter a series of CFD simulations were conducted to investigate the effectiveness of nine different turbulence aids in single fiber DCMD modules using a two dimensional heat-transfer model. Three scenarios were studied — MD systems with highly permeable membranes (large MD coefficient C), high operating temperatures and varying flow velocity.

It was found that the enhancement of overall heat-transfer coefficients, h_f, was up to 6-fold with annular baffles and floating round spacers. Consistent with the h_f results, their *TPC* and mass flux N_m distribution curves presented increasing trends and gained respective improvement of 57% and 74%. The improved performance was attributed to the secondary flow and radial mixing of different intensities in the entire flow channel, visualized by the local flow fields and temperature profiles in CFD simulations. In addition, an increase of flow velocity was used as a conventional strategy to compare its effectiveness in improving hydrodynamics. The results showed that a well-designed configuration with an appropriate selection of turbulence promoters could bring more significant enhancement for a liquid-boundary layer dominant heat-transfer system.

Moreover, the hydraulic energy consumption (*HEC*) caused by the insertion of turbulence promoters or increase of circulating velocity was compared. The configurations with appropriate quad spacers or floating round spacers show a good compromise for achieving an enhanced permeation flux with rather low *HEC*, compared to other novel designs or the original module with a high velocity. Overall, in an MD system the *TPC* decreases with increasing C values and operating temperatures; while the thermal efficiency increases dramatically with increasing C and operating temperatures. To predict module performance and assess the process energy efficiency, considerations should be taken for selecting enhancement strategies based on the membrane properties, process parameters and availability of waste heat sources.

CHAPTER 6

A CFD MODELING STUDY ON MICROSTRACTURED FIRBER DESIGNS FOR MD APPLICATIONS

6.1 Introduction

Having been studied for over decades, MD is of great interest credited to many attractive features such as a theoretical 100% rejection for non-volatile impurities, a low operating temperature, no requirement for applied hydraulic pressure and a relatively low capital cost. However, industrial applications of MD remain limited due to the difficulties in fabricating suitable MD membranes for high water permeation flux and pore wetting prevention, relatively high energy consumption, and poor flow hydrodynamics and/or severe temperature polarization (TP) effects (Schofield et al. 1987; Lawson and Lloyd 1997).

In MD, the membrane structure and material properties contribute to the permeation rate, wetting resistance as well as the TP effect. Therefore, a surge of studies in recent years have focused on membrane development (Chanachai et al. 2010; Su et al. 2010; Zhang et al. 2010; Khayet 2011; Yang et al. 2011), with special interest in hollow fibers due to their high surface area and modular versatility (Schofield et al. 1987). Although a few highly permeable hollow fiber membranes with large MD coefficients are available (Khayet et al. 2005; Li and Sirkar 2005; Khayet et al. 2006; Song et al. 2007; Qtaishat et al. 2009; Su et al. 2010; Wang et al. 2011), the development of MD membranes are still constrained by the conventional spinning methods and the limitation of suitable material properties. Also, the advantages of highly permeable fibers are often compromised by the morphological defects, weak mechanical strength and unsustainable long-term performance (Wang et al. 2011).

On the other hand, many studies have also focused on strategies to improve the MD performance through optimizing operation parameters (Lawson and Lloyd 1996; Cath et al. 2004; Li and Sirkar 2004; Martínez and Rodríguez-Maroto 2007; Teoh et al. 2008; Yang et al. 2011) and designing novel membrane modules (Schofield et al. 1987; Martinez-Diez and Vazquez-Gonzalez 2000; Qtaishat et al. 2008) to alleviate the TP phenomenon and enhance permeation flux. It is shown that by incorporating proper flow alteration aids such as channeled design, external spacers or baffles into module designs, secondary flows or eddies are created. As a result, the MD flux can be greatly enhanced and the TP phenomenon can be mitigated (Schneider et al. 1988; Phattaranawik et al. 2001; Ding et al. 2003; Cath et al. 2004; Li and Sirkar 2004; Martínez and Rodríguez-Maroto 2007; Cheng et al. 2008; Teoh et al. 2008; Yang et al. 2011; Yang et al. 2011).

Another area that has been investigated for improved module performance is the microstructured surface design of the hollow fiber membranes. Inspired by the concept of corrugated surface adopted in heat-exchangers to enhance flow hydrodynamics, novel hollow fibers with modified surface geometries have been fabricated using specially designed spinnerets (Rijn et al. 2002; Herczeg 2004). It was reported that hollow fibers with modified surface geometries such as gear or flower shapes in cross-section have greatly improved membrane filtration performance by not only allowing a 5 or 6-fold increase of surface area and hence significant water flux enhancement, but also acting as turbulence promoters and improving anti-fouling performance for submerged membrane bioreactors (MBR) and ultrafiltration modules (Nijdam et al. 2005; Çulfaza et al. 2010; Çulfaza et al. 2011; Hashino et al. 2011; Çulfaza et al. 2011). In spite of the potential benefits for creating similar improvement in a combined mass- and heat-transfer process, no related work has been done for MD applications.

In parallel with extensive experimental studies to investigate the hydrodynamics in membrane modules, computational fluid dynamics (CFD) modeling has also been widely adopted to simulate and analyze fluid dynamic behaviors in membrane processes (Fimbres-Weihs and Wiley 2010; Yu et al. 2011). With the visualization of the flow-field (including velocity, pressure, temperature and concentration profiles) at any locations in a defined flow channel, CFD modeling can be used to correlate the fundamental mass- and heat-transfer performance with flow hydrodynamics. Therefore, it has become a valuable evaluation tool for industrial applications. Nevertheless, the CFD simulations of the MD process have been greatly limited due to the complex coupling of mass and heat transfer across bulk fluids and the membrane matrix. Mostly, simplified mathematical models were used in prior MD modeling work (Fimbres-Weihs and Wiley 2010). To date, the CFD work on hollow fiber MD modules is sparsely reported (Yu et al. 2011; Yu et al. 2012). Our previous work has proposed to use an improved heat-transfer model, which was discussed in Chapter 5, to analyze the effectiveness of different process enhancement strategies by identifying the controlling local resistances in MD under various circumstances (Yang et al. 2012; Yu et al. 2012).

In a word, CFD simulations are useful in evaluating process performance and providing guidance for flow enhancement approaches and module design studies. Also, with the thought of microstructured membrane surface designs raised, numerical simulation will be a handy tool to predict experimental outcomes to provide valuable guidance for membrane makers.

Chapter 6 aims to evaluate the performance of a shell-side feed DCMD system with nine different types of fiber geometries via three dimensional (3D) CFD modeling. Since the gear- or flower-shaped fibers were comprehensively studied experimentally by others (Rijn et al. 2002; Herczeg 2004), the current chapter mainly discusses the wavy microstructure and only one specific gear-shaped design. The following aspects have been investigated computationally: (1) optimization of fiber geometric structures in terms of main MD process metrics and flow field and temperature distributions; (2) investigations of the length effect of modules with original straight, optimized wavy and gear-shaped fibers; (3) effect of flow conditions on the performance of the modules with original straight and modified fibers; (4) comparison of membrane area, water production and hydraulic energy consumption (*HEC*) among modules with various micro-structured fibers using the original design as a benchmark.

6.2 Modeling methodologies

6.2.1 Geometric structures and modeling methods in CFD

In this chapter, three dimensional (3D) models were developed using the commercial software Fluent 6.3 to study the hydrodynamic behaviors and the heat transfer fundamentals of a series of modules, including nine single-fiber modules with original straight and modified fibers of various surface geometries.

Similar to the simulated modules studied in Chapter 5, all modified configurations packed with fibers of respective novel geometries have the same cylindrical housings as the original one. Instead of being a uniform cylindrical shape, these modified fibers were designed to have regularly distanced waves with constant wall thickness or gear-like (cross-section) structure on the outer surface. The assumed dimensions of these single-fiber modules are 0.25−0.84 m in length and 0.0095 m in shell diameter. For the convenience of CFD modeling, the geometries were assumed to be ideal axially-symmetric structures. Hence, a series of geometric structure for 3D computing domains were built using Gambit® v2.4.6 for half of the actual modules, whose mirrored images of cross-sectional structures (within a length range of 0.015 m with respect to the overall length of 0.25 m) are shown in Fig. 6.1 (a); while Fig. 6.1 (b) shows a local domain amplification to specify the dimensional parameters of these wavy microstructures, in which R_{mi} and R_{mo} are the inner and outer radii of the fiber, Δx and Δy are the cross-sectional dimensions of a wave in x and r (from the baseline to the conic peak) directions; Lx is the interval between two waves; b is the shape parameter, which represents the shape of the conic wave. To clearly show the structures of these configurations, Fig. 6.2 depicts the 3D schematics of single-fiber modules containing fibers of a representative wavy design and gear-shaped, respectively. In all modules, the feed and permeate streams flow through the shell and lumen of the fiber, respectively, in a counter-current mode. The dimensional specifications and respective actual outer surface area A_s (taking into account the surface corrugation) of these modified fiber geometries are given in Table 6.1, which shows that both wavy designs 02 and 03 have a 3.6-fold area increase compared to the original fiber; while the gear-shaped fiber gains 1.9-fold increase.

Table 6.1 Specification of various fiber geometric designs

Geometric pattern			Wavy geometry				Gear structure		Surface area
			Δx /mm	Δy /mm	Lx /mm	b	α /°	L_b /mm	$A_s \times 10^{-4}$ m^2
1	Unmodified	Original	-	-	-	-	-	-	11.54
4	Wavy designs	Wavy 01 5.0/1.0	5.0	2.0	0	0.8			21.11
5		Wavy 02 2.5/2.0	2.5	2.0	0	0.5			41.39
6		Wavy 03 2.5/2.0	2.5	2.0	0	0.8			41.39
7		Wavy 04 1.25/1.0	1.25	1.0	0	0.7			27.30
8		Wavy 05 2.5/1.0	2.5	1.0	0	0.5			22.51
9		Wavy 06 alternate 5.0/1.0	5.0	2.0	5.0	0.8			16.34
		Wavy 07 alternate 1.25/1.0	1.25	1.0	1.25	0.7			19.42
		Wavy 08 alternate 2.5/1.0	2.5	1.0	2.5	0.5			17.03
10	Gear design	Gear-shaped	-	-	-	-	45	0.25	21.60

Note:

1. Δ*x* and Δy are the dimensions of the wavy arch in *x* and *r* directions, respectively; *Lx* is the interval between two waves, *b* is the shape parameter representing the angle between the tangent of the circle and baseline. For example, a wavy design 2.5/1.0 indicates a conic arch of 2.5mm in *x* direction, 1.0mm in *r* direction from the baseline to the conic peak.
2. α is the interval angle between gears on the fiber, L_b is the dimension of a gear with square shape.

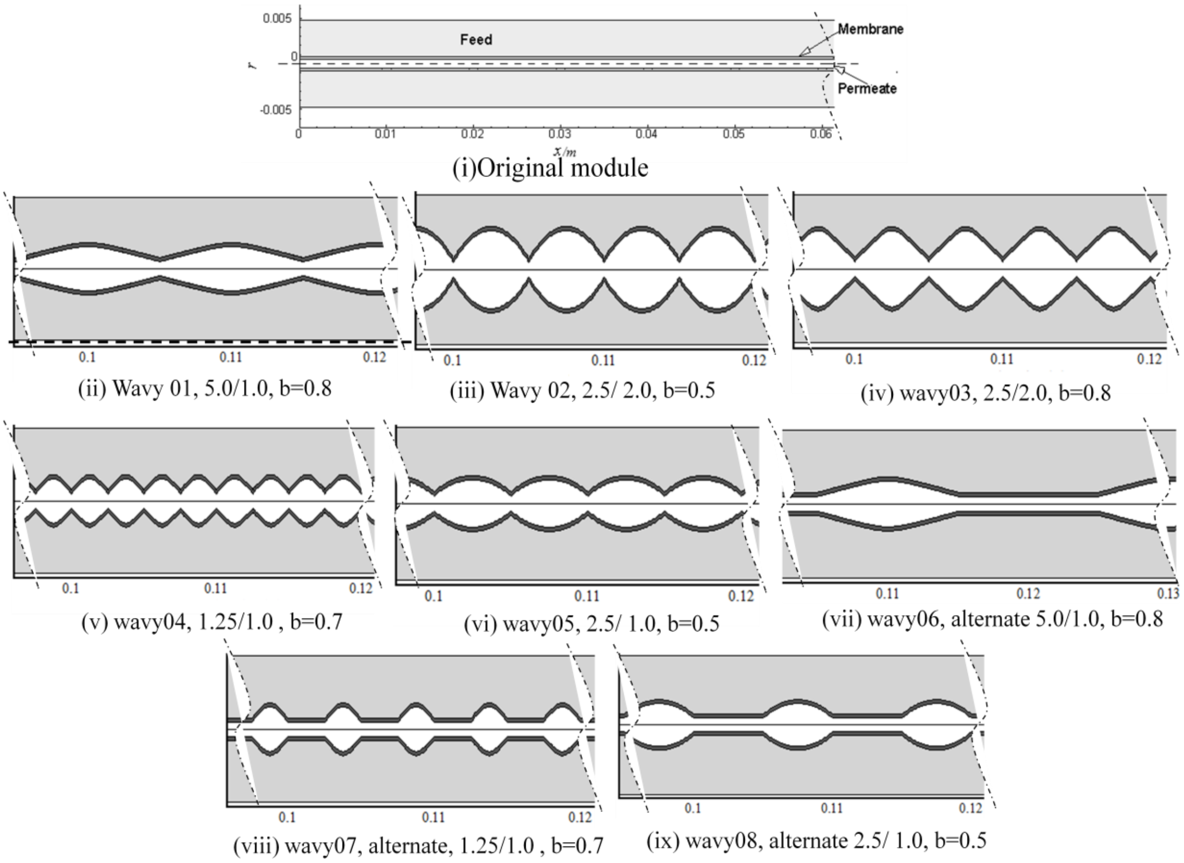

(i)Original module

(ii) Wavy 01, 5.0/1.0, b=0.8

(iii) Wavy 02, 2.5/ 2.0, b=0.5

(iv) wavy03, 2.5/2.0, b=0.8

(v) wavy04, 1.25/1.0 , b=0.7

(vi) wavy05, 2.5/ 1.0, b=0.5

(vii) wavy06, alternate 5.0/1.0, b=0.8

(viii) wavy07, alternate, 1.25/1.0 , b=0.7

(ix) wavy08, alternate 2.5/ 1.0, b=0.5

Fig. 6.1 (a) Schematic of axially-symmetry single fiber modules in CFD simulating domains

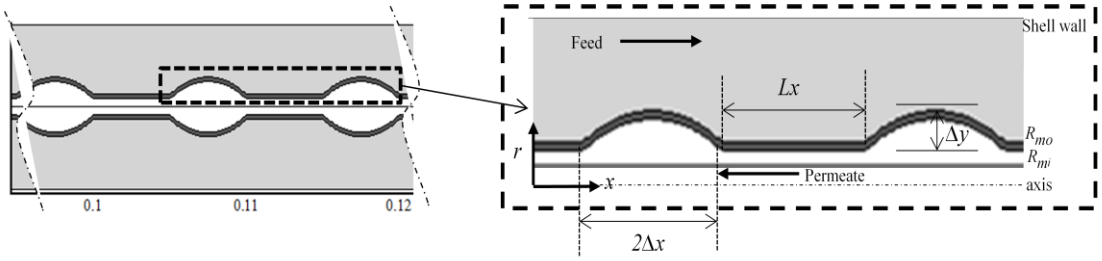

Fig. 6.1 (b) local domain amplification of an axially-symmetry wavy single-fiber module in CFD simulations

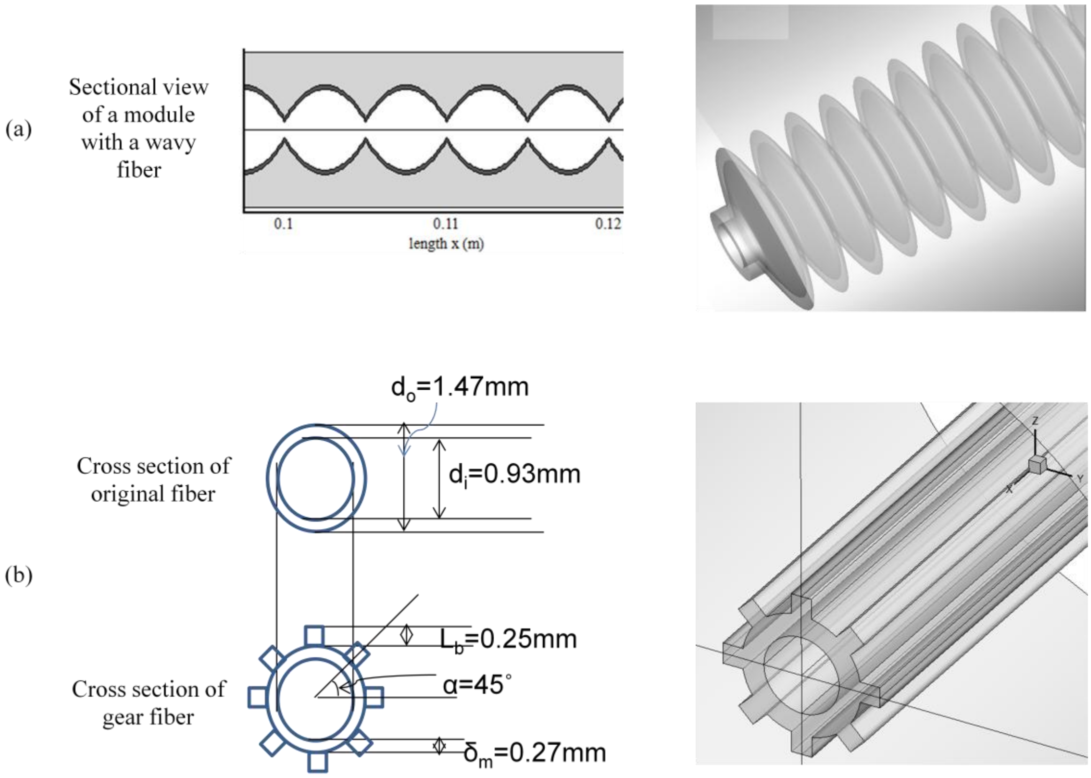

Fig. 6.2. 3D geometric structures of modules with (a) wavy fiber; (b) gear-shaped fiber

With the geometries structured, CFD simulations were carried out using Fluent. The same heat-transfer model, which was developed in Section 5.2.1, was employed for the investigations in this chapter. Therefore, the same governing transport equations, boundary conditions and modeling algorithms were used. Similarly, a laminar model is used for simulating the original module operated under laminar operating conditions (Re<2000); while a realizable k-ε method is applied for the original module under turbulent conditions (Re>2000) or configurations with modified fibers.

In addition, it is assumed that all nine modified fibers have the similar membrane characteristics (i.e., wall thickness, porosity, and pore size/pore size distribution, etc) as the original fiber but with different surface geometries. The properties of the original membranes, the module specifications and the opterating conditions are the same as used previously in Chapter 5 (Tables 5.1 and 5.2). The heat-transfer model has also been verified in Chapter 5 and a co-authored publication (Yu et al. 2011; Yang et al. 2012; Yu et al. 2012), in which the model has been validated based on the same DCMD system for a series of experimental settings, including various feed inlet temperatures, fiber lengths and flow velocities, and modified module configurations with externals. Comparisons between the CFD simulation results and experimental data of mass flux (N_m) and feed pressure drop (ΔP_f) showed good agreement with small relative errors of ±5%.

For the simulating data post-processing, the main heat-transfer equations and definitions and equations involved in a characteristic heat-transfer process as MD are the same as those given in Section 5.2.2. Based on the prior studies, the C is an intrinsic mass-transfer coefficient of the membrane (Schofield et al. 1990) and is calculated based on a combination of structural parameters (thickness, porosity, pore size and pore size distribution) (Yang et al. 2012). Therefore, in the current study a general C value for the selected original straight and wavy designs is determined as 8.0×10^{-7} kg m^{-2} s^{-1} Pa^{-1}; while due to the slight variation of thickness, the gear-shaped fiber has a modified value C^* of 6.4×10^{-7} kg m^{-2} s^{-1} Pa^{-1} with fixed membrane matrix structure (where $C^* = (0.6+0.4\ (\delta_m/\delta_m^*))C$, with the original δ_m = 0.27 mm and modified δ_m^* = 0.52 mm, as shown in Fig. 6.2(b)). Other than commonly evaluated parameters such as heat transfer coefficients, *TPC* and mass flux, the hydraulic energy consumption (*HEC*) and water production (kg day^{-1}) are also used to assess the performance of these microstructured fibers.

6.2.2 Computational domain and grid structures

As mentioned previously, the geometric structures of ten single-fiber modules with original straight and modified fibers were created via Gambit for the simulations in this chapter. A combination of tetrahedral and hexahedral girds was adopted to generate meshes within the calculating domains for all configurations. In the radial r direction, a grid scale of 5×10^{-6} m was chosen for the bulk permeate and membrane, and progressively increasing scales from 5×10^{-6} to 2×10^{-4} m were set for the bulk feed (shell-side); while in the axial x direction, a grid scale of 1×10^{-4}m was employed. A local mesh structure of a module with straight fibers is shown in Fig. 6.3. As mentioned in Chapter 5, the effect of the hollow fiber membrane surface roughness on the wall boundary conditions was ignored and the computational accuracy for convergence is 10^{-5} in Fluent.

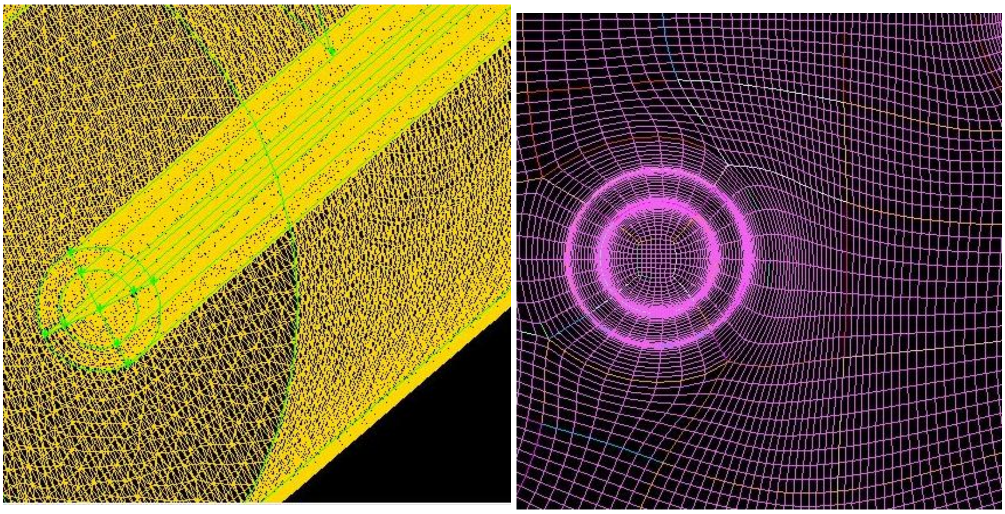

Fig. 6.3 Local mesh schemes of a module with the original straight fiber

6.3 Results and discussion

6.3.1 Optimization of fiber geometric designs in DCMD

6.3.1.1 Improvement of heat transfer coefficients

Based on an analysis of the controlling heat-transfer resistance in different MD systems, external hydrodynamic aids can be employed to achieve a significant enhancement when the heat transfer through the liquid-boundary layers plays a dominant role (Yang et al. 2012). Hence, in this study, the same DCMD system [highly permeable membrane with membrane coefficient $C = 8.0\times10^{-7}$ kg m^{-2} s^{-1} Pa^{-1} and C^{*}(gear) = 6.4×10^{-7} kg m^{-2} s^{-1} Pa^{-1}, and relatively low operating temperatures T_f = 327.15 K, T_p = 293.85 K] was selected to investigate the effectiveness of hydrodynamic improvement by incorporating modified fibers with various surface microstructures. To optimize the fiber geometry particularly for MD applications, nine different microstructures listed in Table 6.1 were simulated, and Fig. 6.4 shows the distributions of the simulated heat transfer coefficients at the feed and permeate sides, h_f and h_p, along the fiber length L, respectively, for single-fiber modules with the original and nine modified fibers.

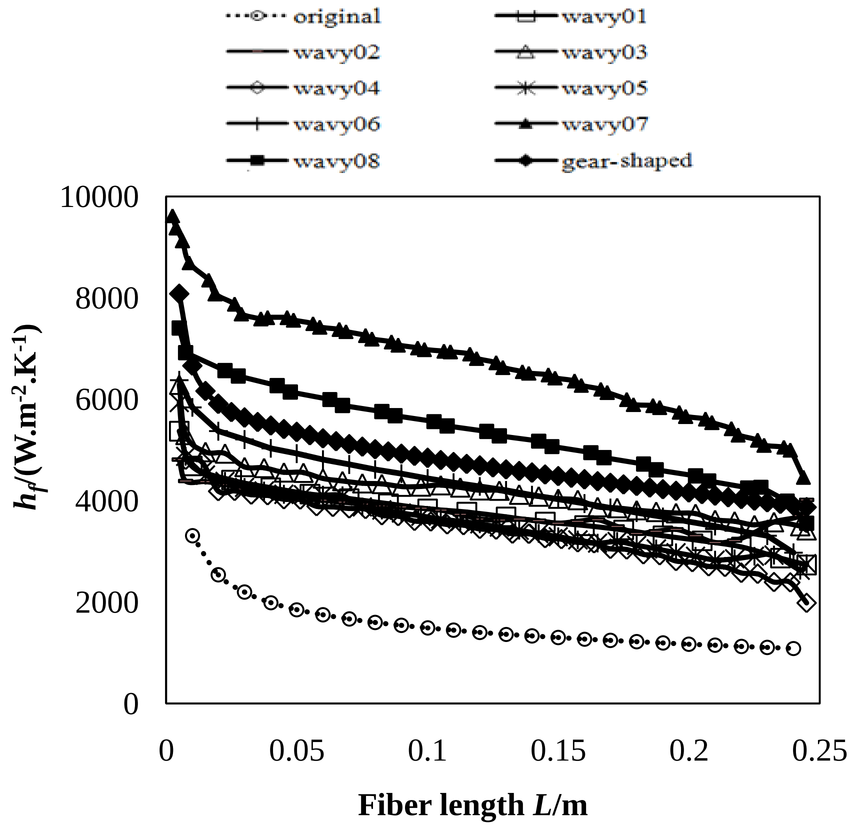

(a) h_f distributions vs. module length L

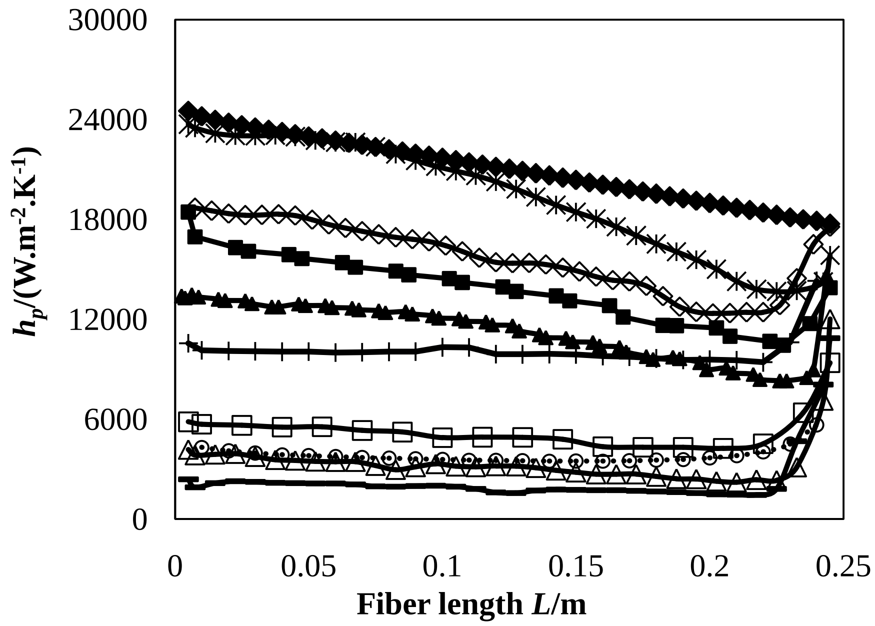

(b) h_p distributions vs. module length L

.

Fig. 6.4 h_f & h_p distributions along the fiber length for single-fiber modules with fiber of various geometries ($C = 8.0\times10^{-7}$ kg m^{-2} s^{-1} Pa^{-1} and C^*(gear) = 6.4×10^{-7}

g m^{-2} s^{-1} Pa^{-1}, L = 0.25m, T_{fi} = 327.15 K, T_{pi} = 293.85 K, u_{fi} = 0.06 m s^{-1}, u_{pi} = 0.417m s^{-1})

In Fig. 6.4 (a) the h_f distribution curves for all fiber geometries show a general decreasing trend along the fiber length L. For the original module, the highest h_f appears at the entrance of the feed side and then decreases along the flow direction until reaching a plateau when the flow is fully developed; while for the rest of the modules, the curves continuously decrease towards the exits. This is due to the slower build-up of the liquid boundary layer along the feed flow direction credited to the disturbance by the surface corrugations. Overall, the curves of modules with microstructured fibers are much higher than that of the original one, which shows the lowest average h_f of 1495 W m^{-2} K^{-1}. The configuration with an alternate wavy design 07 (1.25/1.0 mm, Lx = 1.25 m) shows the highest h_f of 6823.9 W m^{-2} K^{-1}, which is 4.6-fold higher than the original fiber, followed by another alternate wavy design 08 (2.5/1.0 mm, Lx = 2.5 m) and the gear-shaped fiber. The results indicate that these new microstructured geometries have successfully introduced flow disturbance to disrupt the temperature polarization layer on the membrane surface and hence enhance the heat transfer. Also, the significant improvement of heat-transfer coefficients by introducing the corrugated surfaces has confirmed the controlling role of the liquid-boundary layers in this MD system with a large membrane coefficient C & low operating temperatures. More discussion of the flow-field distribution associated with intensified local mixing, reduced TP and enhanced permeation flux is presented in a later section.

In Fig. 6.4 (b) the curve of the heat-transfer coefficients on the permeate side h_p of the original module shows a similar trend to its h_f distribution − a continuous decrease appears after entering the inlet of the permeate side (L = 0.25) and then reaches a plateau. The modified designs wavy 01, 02, 03 and 06 follow the same trend. Surprisingly, wavy 02 (5.0/2.0 mm, b = 0.5) and 03 (5.0/2.0 mm, b = 0.8) even have lower h_p curves than the original fiber. The possible reason is that the presence of deeper waves (Δy = 2.0 mm) has created strong vortices in the valley zones on the permeate side, which caused liquid stagnation. However, the rest of the designs present an increasing h_p trend. It is observed that the gear-shaped design has the highest average h_p of a 5.5-fold increase compared to the original fiber, followed by a wavy geometry 05. For all the wavy configurations, the significant h_p enhancement is mainly due to the appropriate size of the corrugations that have greatly improved the hydrodynamic conditions and heat transfer at the permeate side, by increasing the surface shear-rate of the flow and hence reducing the thickness of liquid boundary layers; while for the gear-shaped design, the improved heat transfer at the permeate side was credited to the better hydrodynamic conditions on the corrugated outer membrane surface (i.e., feed side), which has much higher wall temperatures and hence a more efficient thermal diffusion across the thermal boundary layers at both sides.

It should be pointed out that different from the conclusions of our previous work on the introduction of external turbulence promoters into MD modules (Yang et al. 2012), the current h_p results showed that microstructured designs on the membrane surface are able to improve the heat transfer not only at the feed but also at the permeate side.

6.3.1.2 Temperature-polarization effect and flow-filed visualization

It was observed in Fig. 6.4 that most of the modules with modified fiber geometries have shown significant enhancement in heat transfer coefficients h_f and h_p, which are closely related to the TP phenomenon—one of the critical barriers in MD practice. Thus, the corresponding results on TP effect are investigated and shown in Fig. 6.5, which gives the simulated *TPC* distributions along the module length *L* for all modules (i.e., listed in Table 6.1).

It can be seen seen from Fig. 6.5 that all modules present a similar U shape – the maximum *TPC* value occurs at the entrance and the lowest at the midpoint of the module then a slow increase towards the exit. The reason is that the transmembrane temperature difference ($T_{fm} - T_{pm}$) first decreases and then increases due to the opposite build-ups of thermal boundary layers on the feed and the permeate sides: the T_{fm} continues to decrease along its flow direction (x) and T_{pm} first increases and then decreases along -x direction. It is not surprising to see that the modules with wavy designs 02 and 03 (5.0/2.0 mm, b = 0.5 and 0.8) show even lower *TPC* curves than the original straight one, which are consistent with those of the heat-transfer coefficients in Fig. 6.4, i.e., the continuous wavy designs 02 and 03 had lower h_p curves than the original straight fiber. The reason responsible for this result may be that a fiber surface with deep and over-frequent corrugations (waves) might result in intense local secondary flows, which are possibly trapped between the valleys of two neighboring projections and subsequently compromise the module performance. Hence, liquid stagnation would instead lead to a lower heat-transfer efficiency and more severe TP phenomenon.

On the other hand, the alternate wavy designs 07, 08 and gear structured modules present relatively higher *TPC* curves, which are also consistent with their high h_f and h_p distributions in Fig. 6.4. Compared to the original design, a *TPC* increase of 70% is achieved by the gear-fiber module. This might be due to the intensified secondary flows induced by gear-shaped corrugations on the membrane surface that has reduced the thickness of thermal boundary layer and facilitated the heat transfer. For the alternate wavy designs 07 and 08, the reason for improvement may include two factors: firstly, these alternate wavy projections with an appropriate height have increased the surface roughness to create flow eddies and improve the hydrodynamic conditions on both sides; secondly, the presence of wavy corrugations have broadened the flow channel at the permeate side, which allows more cooling water to flow through and achieve better heat exchanging performance. Therefore, the temperature polarization phenomenon is greatly mitigated due to the effective flow alteration caused by modified flow channels. As a result, the overall driving force is increased.

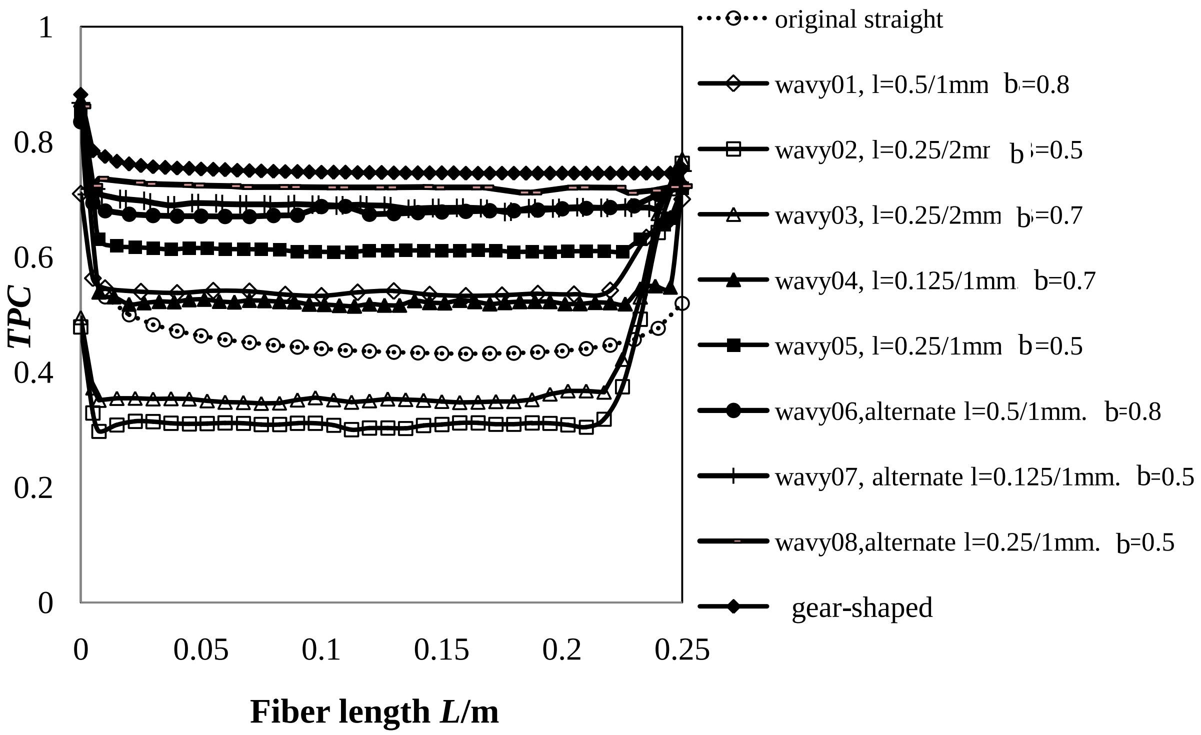

Fig. 6.5 *TPC* distributions along the fiber length for single-fiber modules with fiber of various geometries ($C = 8.0\times10^{-7}$ kg m^{-2} s^{-1} Pa^{-1} and C^{*}(gear) = 6.4×10^{-7} kg m^{-2} s^{-1} Pa^{-1}, L = 0.25m, T_{fi} = 327.15 K, T_{pi} = 293.85 K, u_{fi} = 0.06 m s^{-1}, u_{pi} = 0.417 m s^{-1})

To further reveal the fundamentals of the heat-transfer enhancement by employing microstructured fibers in MD modules, Fig. 6.6a shows the local flow fields and temperature distribution in modules with various fiber geometries (within a length range of 0.105−0.125 m with respect to the overall length 0.25 m). The velocity profiles are described by stream traces and temperature distribution in band colors. These results are consistent with the trends of the heat-transfer coefficients curves shown in Fig. 6.4 and *TPC* distributions in Fig. 6.5 for these modified designs. Clearly, the intensity of secondary flows induced by the wavy corrugations increases with increasing wave depth and decreases with increasing the arching width. Nevertheless, it is shown that a microstructure of deeper and more frequent corrugations is not necessarily a superior choice for achieving improved module performance. For example, the wavy design 02 with continuous waves Δx of 2.5 mm and depth Δy of 2.0 mm showed a negative effect in terms of TP mitigation; while another lower wavy design 05 with continuous waves (Δx=2.5 mm and Δy=1.0 mm) performed much better. Interestingly, the alternative design 08 with less and low waves (Δx = 2.5 mm, Δy =1.0 mm and Lx = 2.5 mm) achieved the best results among these three configurations. However, a further decrease in the number of turbulence aids might result in insufficient flow disturbance and mixing instead, which was presented in Chapter 5. Due to the difficulty in presenting via a cross-sectional flow field, the flow conditions of the gear-fiber module is analyzed using the local temperature and pressure contours (slicing planes at x = 0.01, 0.10 and 0.20 m) in band colors, as shown in Fig. 6.6b. Compared to the module with an original straight fiber, the presence of a gear-shaped geometry successfully disrupts the liquid boundary layers on the feed side and simultaneously enhances the permeate flow. Hence, the TP effect is greatly reduced and heat transfer enhanced as indicated in Figs. 6.4 and 6.5.

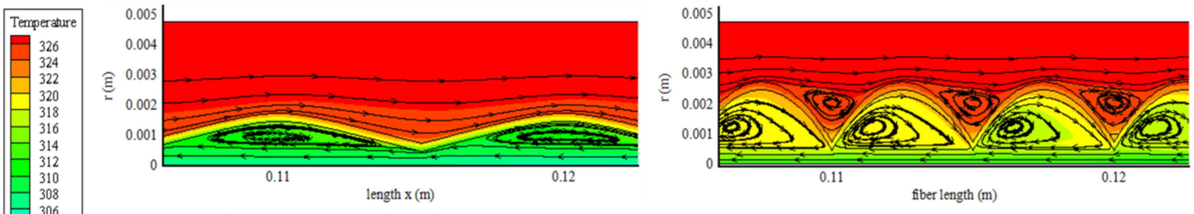

(b) Wavy 01, 5.0/1.0, b=0.8

(c) Wavy 02, 2.5/ 2.0, b=0.5

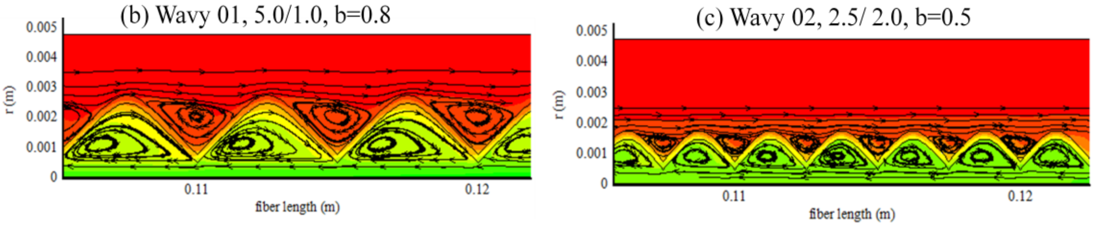

(d) wavy03, 2.5/2.0, b=0.8

(e) wavy04, 1.25/1.0 , b=0.7

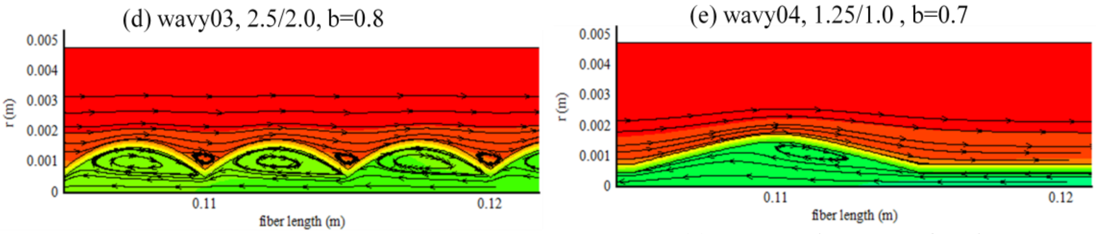

(f) wavy05, 2.5/ 1.0, b=0.5

(g) wavy06, alternate 5.0/1.0, b=0.8

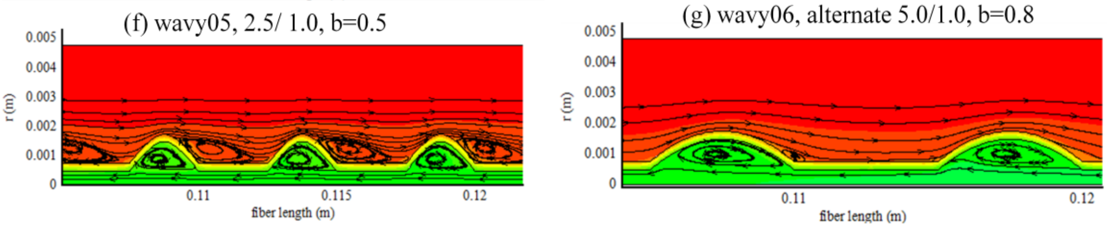

(h) wavy07, alternate, 1.25/1.0 , b=0.7

(i) wavy08, alternate 2.5/ 1.0, b=0.5

Fig. 6.6 (a) Local flow field visualization for modules with fibers of various wavy designs ($C = 8.0\times10^{-7}$ kg m^{-2} s^{-1} Pa^{-1}, L = 0.25m, T_{fi} = 327.15 K, T_{pi} = 293.85 K, u_{fi} = 0.06 m s^{-1}, u_{pi} = 0.417 m s^{-1})

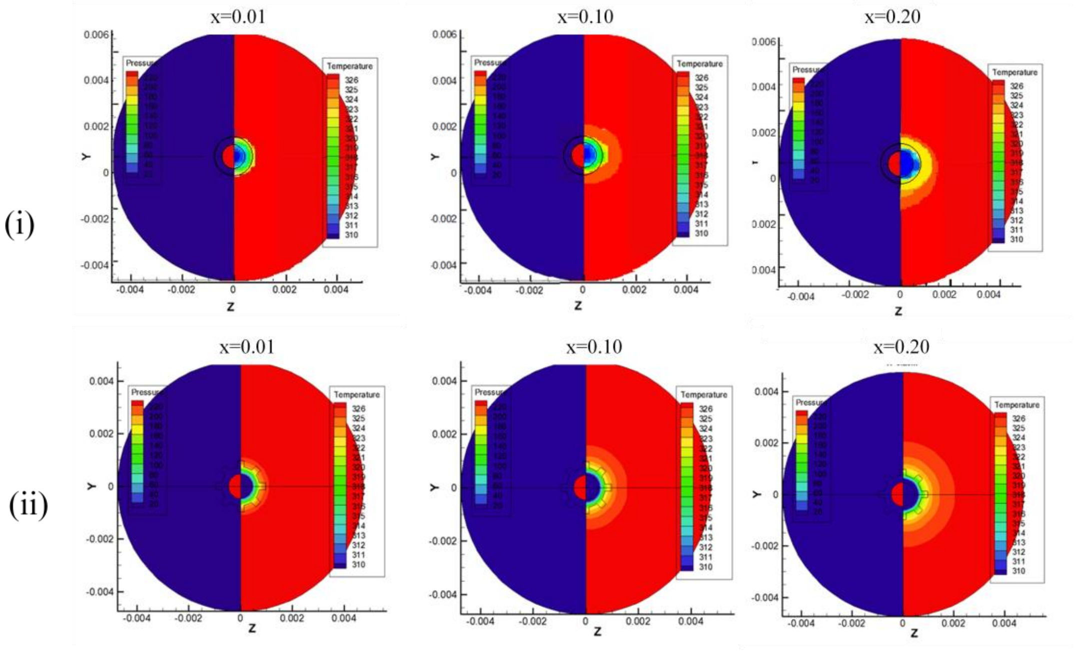

Fig. 6.6 (b) Comparison of local temperature and pressure distributions for single-fiber modules with (i) original straight fiber; (ii) gear fiber ($C = 8.0\times10^{-7}$ kg m^{-2} s^{-1} Pa^{-1} and C^{*}(gear)=6.4×10^{-7} kg m^{-2} s^{-1} Pa^{-1}, $L = 0.25$ m, $T_{fi} = 327.15$ K, T_{pi}= 293.85 K, $u_{fi} = 0.06$ m s^{-1}, $u_{pi} = 0.417$ m s^{-1})

Thus, combined with the simulation results shown in Figs. 6.4 and 6.5, it is concluded that an appropriate design of the membrane surface geometry can lead to reduced thermal boundary layers, alleviated TP phenomenon and hence enhanced heat transfer in a liquid-film controlled MD system.

6.3.1.3 Enhancement of permeation flux

Fig. 6.7 gives the distributions of mass fluxes N_m along the fiber length L for modules packed with fibers of various microstructural designs, under the same operating conditions. It is noted that N_m is defined based on the outer membrane area of the fiber. For the original module, the N_m curve has a similar trend as its TPC distribution (shown in Fig. 6.5), which firstly decreased and then slightly increased due to the countercurrent build-ups of the thermal boundary layers on the feed and permeate sides. However, the modules with modified fibers show dramatic flux increase along the feed flow direction. This is due to the slower flow development and hence boundary layer buildup along a channel with corrugated surface.

Similar to the *TPC* results in Fig. 6.5, few configurations with modified fiber geometries show negative results compared to the original straight fiber — wavy 02, 03 and 04, which gain even lower average mass fluxes; while wavy 05 slightly outscores the original configuration. The highest flux enhancement of 60% is achieved by the module with gear fibers, followed by the alternate wavy designs 07 and 08 with approximate improvement of 38%. These results again imply the advantages of a gear-shaped structure and alternate wavy geometries for achieving better module performance. However, the relatively lower fluxes per unit area of the continuous wavy designs 02−05 do not necessarily result in lower water production per day, due to the enhanced contact area generated by the corrugated geometry (a comparison of actual membrane areas A_s is given in Table 6.1). Therefore, a fair comparison will be provided in terms of water production (kg day^{-1}) in a later section.

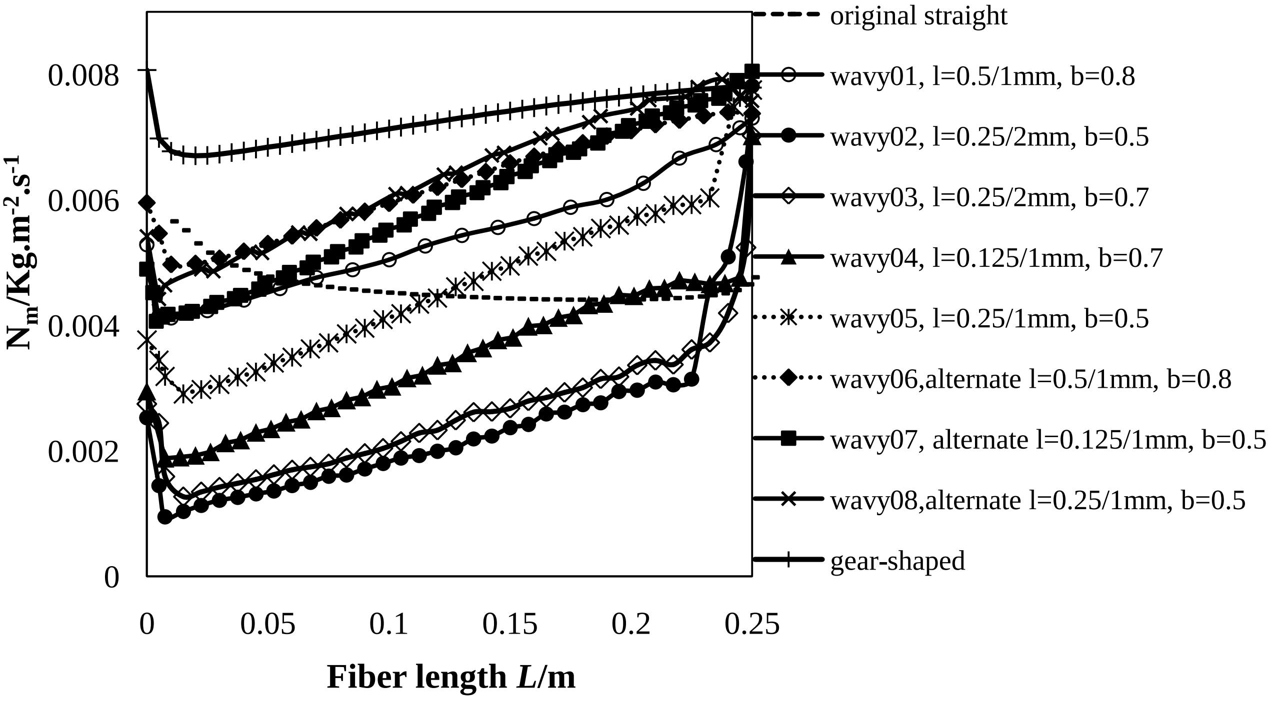

Fig. 6.7 Mass flux N_m distribution along the fiber length for single-fiber modules with fiber of various geometries (C= 8.0×10^{-7} kg m^{-2} s^{-1} Pa^{-1} and C^*(gear) = 6.4×10^{-7}

kg m^{-2} s^{-1} Pa^{-1}, L = 0.25m, T_{fi} = 327.15 K, T_{pi} = 293.85 K, u_{fi} =0.06 m s^{-1}, u_{pi} = 0.417 m s^{-1})

6.3.2 Effect of fiber length for modules with various fiber geometries

Based on the previous discussions of the selected MD system (high *C* value and low operating temperatures), an appropriate modification of fiber geometry could greatly enhance the module performance. Thus, the most promising were selected to further explore their potential for industrial applications. A series of simulations were conducted to compare the length effect among single-fiber modules with original straight, wavy 08 and gear-shaped fibers. The results are shown in Figs. 6.8 and 6.9, which depict the effects of module length (*L*= 0.25, 0.54 and 0.84 m respectively) on the distributions of *TPC* and N_m along the dimensionless module length *x/L* under given operating conditions.

In Fig. 6.8 all *TPC* curves for different modules show U shapes with different curvatures. Regardless of fiber geometries, the average *TPC* values of these configurations decrease with increasing module length. i.e., shorter modules are less vulnerable to the TP effect and hence show higher *TPCs*. Overall, the modules with original straight fibers have the lowest curves among all configurations with the same lengths; while the ones with gear-shaped and wavy 08 fibers show similarly high *TPC*s. For the module with the original fiber, an increase of length from 0.25 m to 0.54 m causes 20% *TPC* decrease; a further increase of length to 0.84 m results in an approximate 50% decrease in the average *TPC*. Moreover, the shorter module (*L*= 0.25 m) presents a rather flat U shape compared to the longer ones with much slower flow development along the dimensionless length *x/L*. Yet, the module with a wavy design 08 presents 17% decrease with a length increase from 0.25 m to 0.54 m and 21% deterioration with a further increase to *L* = 0.84 m. The modules with gear-shaped fibers show a similar percentage of *TPC* decrease with increasing fiber length. Apparently, a much slower decrease with increasing fiber length is observed for modified fibers, due to a slower buildup of boundary layers at the same location (but a smaller *x/L* as the module gets longer). Although it was reported that longer modules tend to be subject to more severe TP effect (Yang et al. 2011), the simulated result in Fig. 6.8 show that fibers with modified geometries are advantageous for scale-up modules.

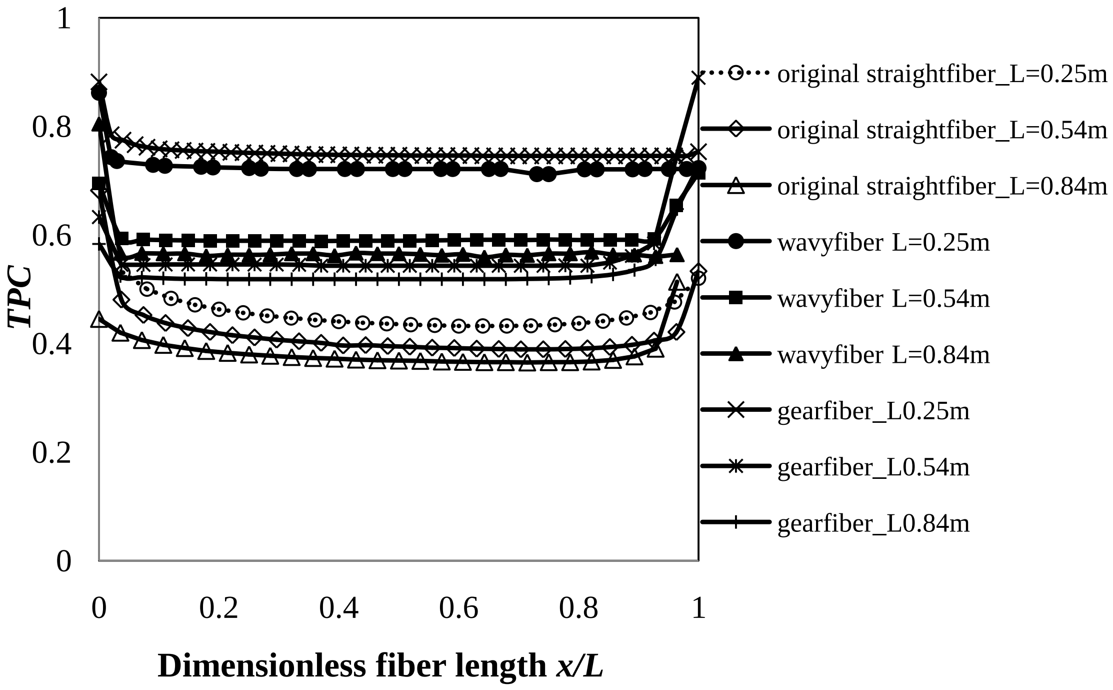

Fig. 6.8 Effect of fiber length I: *TPC* distributions for single-fiber modules with fiber of various geometries ($C = 8.0\times10^{-7}$ kg m^{-2} s^{-1} Pa^{-1} and C^*(gear) = 6.4×10^{-7} kg m^{-2} s^{-1} Pa^{-1}, L = 0.25, 0.54 and 0.84 m, T_{fi} = 327.15 K, T_{pi} = 293.85 K, u_{fi} = 0.06 m s^{-1}, u_{pi} = 0.417 m s^{-1})

Fig. 6.9 shows the distributions of mass flux N_m for these three fiber geometries (straight, wavy 08 and gear-shaped) along the dimensionless module length *x/L*. In general, for the same configuration the local mass flux decreases with increasing module length at the same *x/L*, which is consistent with both our previous experimental data and simulation results (Yang et al. 2011; Yu et al. 2011). This is mainly due to the decrease in the local driving forces and the build-up of thermal boundary layers as the flow channel length increases. Except for a downward U shape for the module with a short straight fiber (0.25 m), the rest of the N_m curves show an upward U shape — a slight decrease at the entrance region, where the thinnest boundary layer of the feed side appears, and then an increase as the transmembrane temperature difference increases with increasing dimensionless length *x*/*L*. This is a result of the counter-current buildup of liquid boundary layers. Although longer modules with larger membrane areas will result in a higher water production, an optimized length should be chosen for industrial applications based on an acceptable magnitude of the local driving force and a more even distribution of N_m.

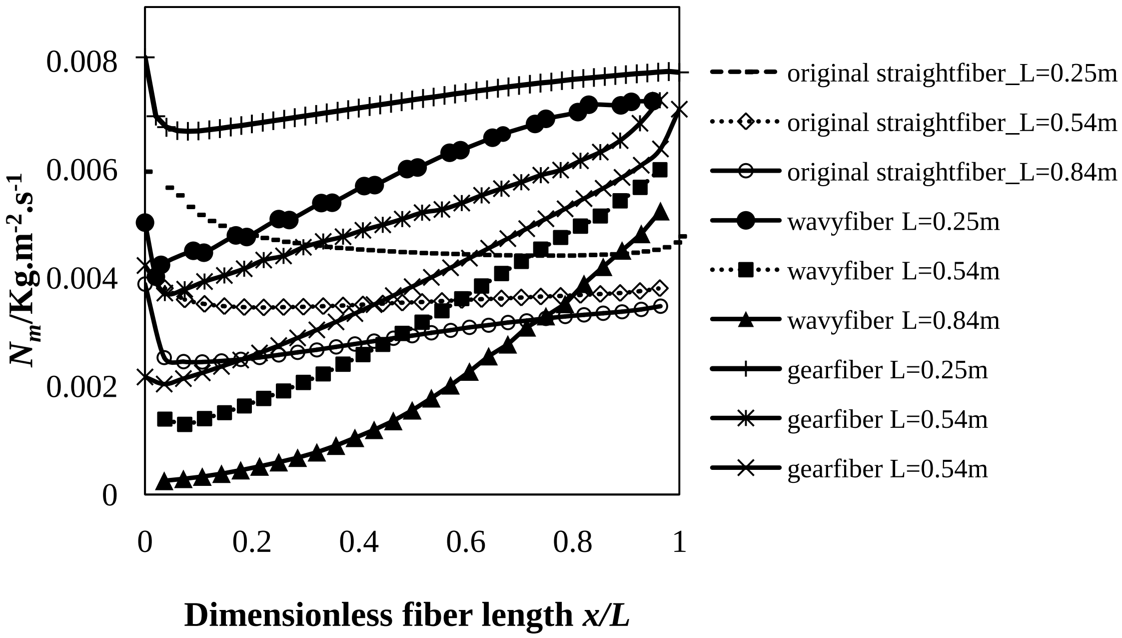

Fig. 6.9 Effect of fiber length II: mass flux N_m distributions for single-fiber modules with fiber of various geometries (C = 8.0×10^{-7} kg m^{-2} s^{-1} Pa^{-1} and C^*(gear) = 6.4×10^{-7} kg m^{-2} s^{-1} Pa^{-1}, L= 0.25, 0.54 and 0.84 m, T_{fi} = 327.15 K, T_{pi} = 293.85 K, u_{fi} = 0.06 m s^{-1}, u_{pi} = 0.417 m s^{-1})

It is also observed in Fig. 6.9 that the N_m of the modified designs (wavy and gear-shaped) increases more significantly along the dimensionless module length *x/L* than the original module. This is mainly attributed to the increase of driving force as a result of disruptive boundary layers by surface corrugation. Overall, the modules with gear-shaped fibers gain the highest flux enhancement ratios among all configurations with the same length. Interestingly, compared to original modules, the gear-fiber configuration gains a slight increase of enhancement from 57% to 65% with increasing length from 0.25 m to 0.84 m. Therefore, it is meaningful to employ a modified fiber geometry like a gear-shaped, which performs more advantageously when longer modules are desired for a higher water production in industry.

6.3.3 Effect of flow conditions for modules with various fiber geometries

6.3.3.1 Reynolds number of the feed, Re_f

As a conventional strategy to improve hydrodynamic conditions in MD systems, an increase of flow velocity to create turbulence is found to be effective. However, similar to other hydrodynamic approaches (Yang et al. 2012), its effectiveness may differ in MD modules of different configurations. Based on the previous results of geometric optimization, the gear-shaped design was selected and simulated to investigate the effect of flow conditions with modified surface geometry. With other operating conditions kept constant, Fig. 6.10 and 6.11 show the effects of flow conditions (in terms of Reynolds number, *Re*) on the *TPC* and mass flux N_m distributions for 0.25 m-long modules with single straight and gear fibers, respectively. In Fig. 6.10 (a) the average *TPC* increases with increasing Re_f for either configuration due to the improved fluid dynamics at a higher flow velocity. For the original module, all *TPC* distributions for varied feed flow conditions from laminar to turbulence (i.e., $Re_f = 420 – 2500$) show a similar U shape—initially decreasing after entering the module and then slowly increasing towards the exit; while the curves of the gear-fiber modules present a rather flat trend after leaving the entrance region. It is noted that the Re_f for the gear-fiber module was calculated based on the modified hydraulic diameter characterized by its gear-shaped surface.

Compared to the gear-fiber configuration, in Fig. 6.10 (a) the original module generally shows lower average *TPC* values and a negligible change with a velocity increase under laminar flow ($Re_f \leq 1500$). The *TPC* of the original module only fluctuates within 6% with Re_f increasing from 420 to 1500; while the turbulence condition ($Re_f = 2500$) brings 30% *TPC* increase compared to that of $Re_f = 420$. The dramatic enhancement is credited to the reduced thickness of liquid boundary layer and hence improved heat transfer under turbulent flow conditions. In contrast, the gear-fiber module shows fairly significant changes with the corresponding Re_f adjustment. This is probably because of the ups and downs of the gear-shaped surface, which could facilitate the occurrence of cross flow and hence enhanced fluid dynamics even at an extremely low Re_f. For instance, the gear-fiber module shows an encouraging average *TPC* of 0.7, which is 1.6 times higher than the original configuration, at the same low Re_f of 420.

In Fig. 6.10 (b) the mass flux N_m increases with increasing Re_f for both configurations. Similar to the *TPC* distributions, the N_m curves of the original module show a downward U shape along the fiber length *L* and have a rather insignificant response to a Re_f increase under laminar conditions ($Re_f \leq 1500$); its N_m distribution presents a dramatic increase along the feed flow direction once the turbulent condition is reached ($Re_f = 2500$). The maximum flux increase is up to 50% compared to that of $Re_f = 420$. On the other hand, the gear-fiber module shows an initial decrease at the entrance and subsequent increase along the fiber length for each flow condition. Although a relatively flat curve is obtained at an extremely low Re_f of 420, the slope of the N_m curve for the gear-fiber configuration increases significantly with increasing Re_f. This indicates that the flow disturbance induced by the gear microstructure becomes more intense as the flow develops along the flow channel, especially at a higher flow velocity.

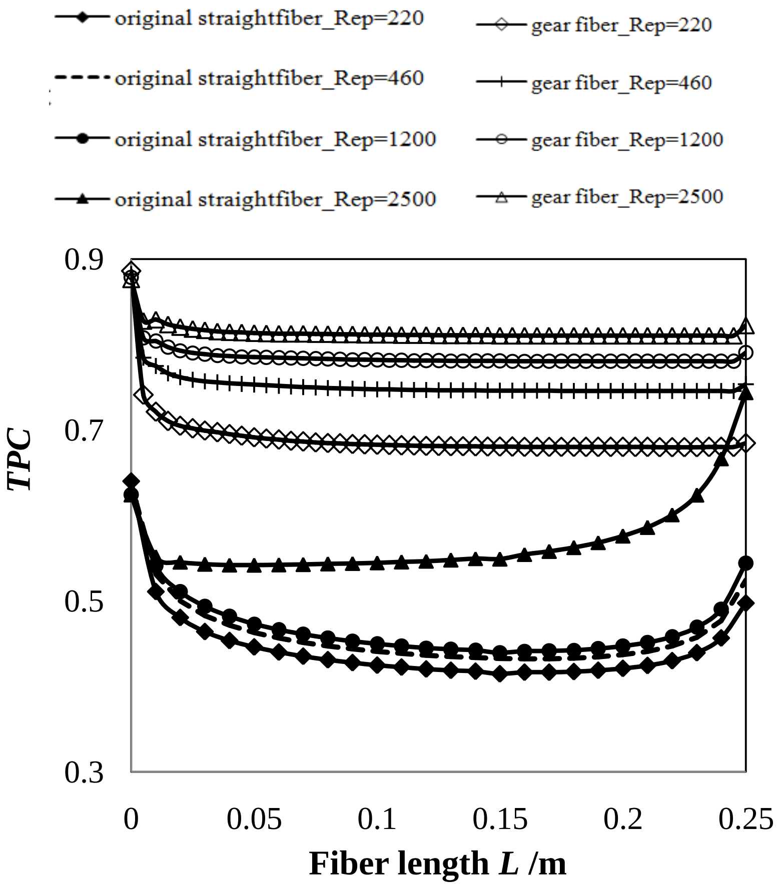

(a) *TPC* distributions

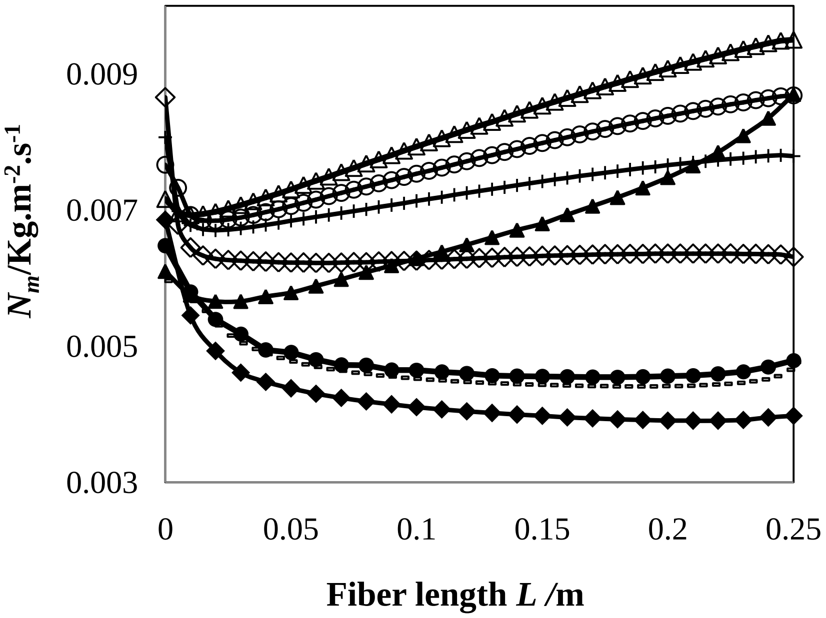

(b) N_m distributions

Fig. 6.10 Effect of feed flow conditions (Re_f) for fibers of single-fiber modules with original straight and gear-shaped fibers (a) TPC distributions; (b) N_m distributions (C = 8.0×10^{-7} kg m^{-2} s^{-1} Pa^{-1} and C^*(gear) = 6.4×10^{-7} kg m^{-2} s^{-1} Pa^{-1}, L = 0.25 m, T_{fi} = 327.15 K, T_{pi} = 293.85 K, Re_f = 420–2500, Re_p = 460)

6.3.3.2 Reynolds number of the permeate, Re_p

Similarly, with the Re_f kept constant, the permeate flow conditions (Re_p) was varied to simulate the module performance in terms of TP alleviation and flux enhancement. Fig. 6.11 presents the TPC and N_m distributions along the fiber length L for both the original and gear-fiber modules with increasing Re_p from 220 to 2500. Similar to Fig. 10, the original module shows much lower TPC and N_m curves compared to the modified configuration at the same Re_p.

In Fig. 6.11 (a) the average TPC increases with increasing Re_p for both configurations. The reason is that a change in the heat-exchange rate at a higher Re_p leads to a decrease of permeate bulk temperature and hence a higher transmembrane temperature difference (driving force) occurs at the same fiber length. However, different from the influence of the feed flow conditions, a major increase of Re_p from laminar to turbulence only brings a modest change in their respective TPC results—an increase of 19% occurs for the original module and 10% for the gear-fiber one.

It is shown in Fig. 6.11(b) that the average N_m increases with increasing Re_p for both modules. Generally, at a relative higher Re_p (≥1500) the N_m curves of both modules show an increasing trend along the permeate flow direction. This is because of a decrease of flow temperature on the permeate side, which results in an increasing transmembrane temperature difference towards the feed inlet (L = 0) at under-developed flow conditions. However, at an extremely low Re_p of 220 when the flow tends to be fully developed, the N_m curves of the original module shows a decreasing trend; while the gear-fiber module show a more dramatic decrease after the permeate flow enters the module. This is probably due to its particular corrugated gear structure that might regionally retain some liquid at low Re_p and hence result in a reduced local driving force due to a more rapid flow development and buildup of liquid boundary layer along the permeate flow direction. Nevertheless, compared to the original module, the gear-fiber module still gains 47% flux enhancement at such a low Re_p of 220. Overall, a change in the flow conditions from laminar (Re_p = 220) to turbulence (Re_p = 2500) has brought significant influence on the permeation flux—32.5% flux enhancement for the original module and 46% for the gear-shaped fiber.

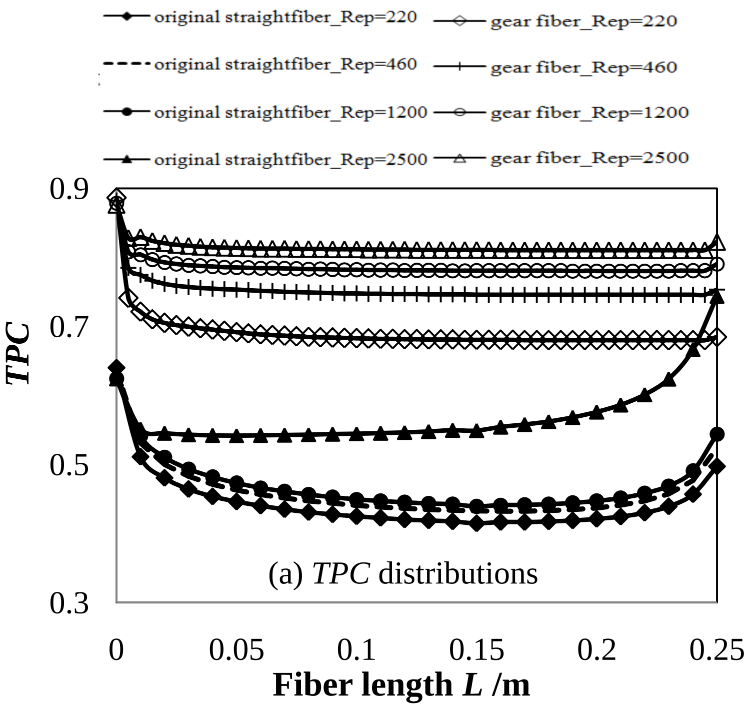

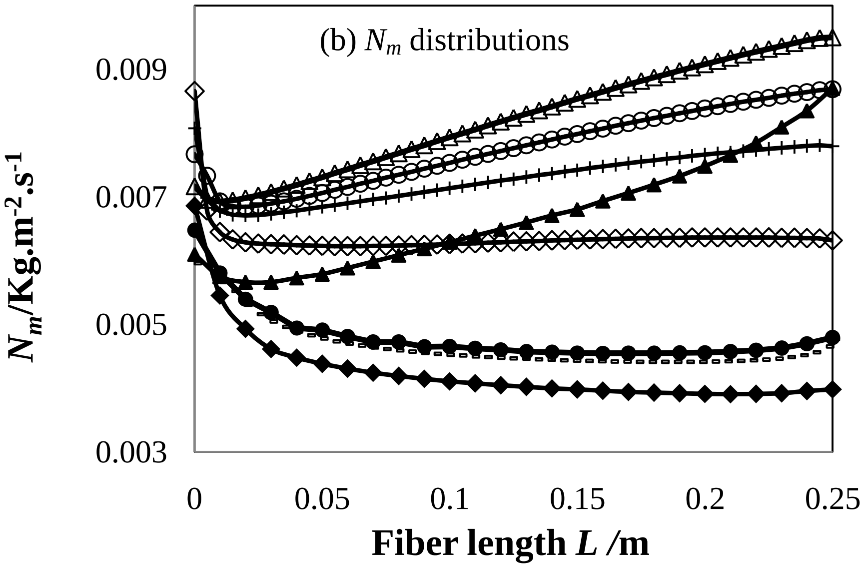

Fig. 6.11 Effect of permeate flow conditions (Re_p) for fibers of original straight and gear-shaped fibers ($C = 8.0\times10^{-7}$ kg m^{-2} s^{-1} Pa^{-1} and C^*(gear) = 6.4×10^{-7} kg m^{-2} s^{-1} Pa^{-1}, L = 0.25 m, T_{fi} = 327.15 K, T_{pi} = 293.85 K, Re_f = 836, Re_p = 220−2500)

However, it should be pointed out that instead of employing high flow velocity to create turbulence, a major achievement of TP mitigation and flux enhancement could be accomplished by utilizing fibers with smarter microstructured designs under laminar conditions.

6.3.4 Comparison of water production and hydraulic loss for modules with various fiber geometries

As discussed in the previous sections, an appropriate geometric modification on the membrane surface (e.g., alternate wavy or geared shapes) would greatly reduce the heat-transfer resistance and improve the module performance, when the heat transferred through the liquid-boundary layers presents a dominant resistance. To fully evaluate these fibers of various geometries, two important process metrics—water production (kg day^{-1}) and hydraulic energy consumption (*HEC*) were calculated and compared among various modules (geometric specifications listed in Table 6.1), as shown in Fig. 6.12. Assuming that each ideal module contains one-hundred pieces of fiber with different geometric designs (i.e., total membrane area A = 100A_s), the configuration with original straight fibers has a *HEC* of 6.5 J kg^{-1} and water production of 46 kg day^{-1}; while the module with gear fibers shows the highest water production of 136 kg day^{-1} but the lowest *HEC* of 3.5 J kg^{-1}, followed by the alternate wavy designs 01, 07 and 08. Although the continuous wavy designs 02 and 03 also gain reasonably high water production, they tend to be subject to high hydraulic loss (>20 J·kg^{-1}).

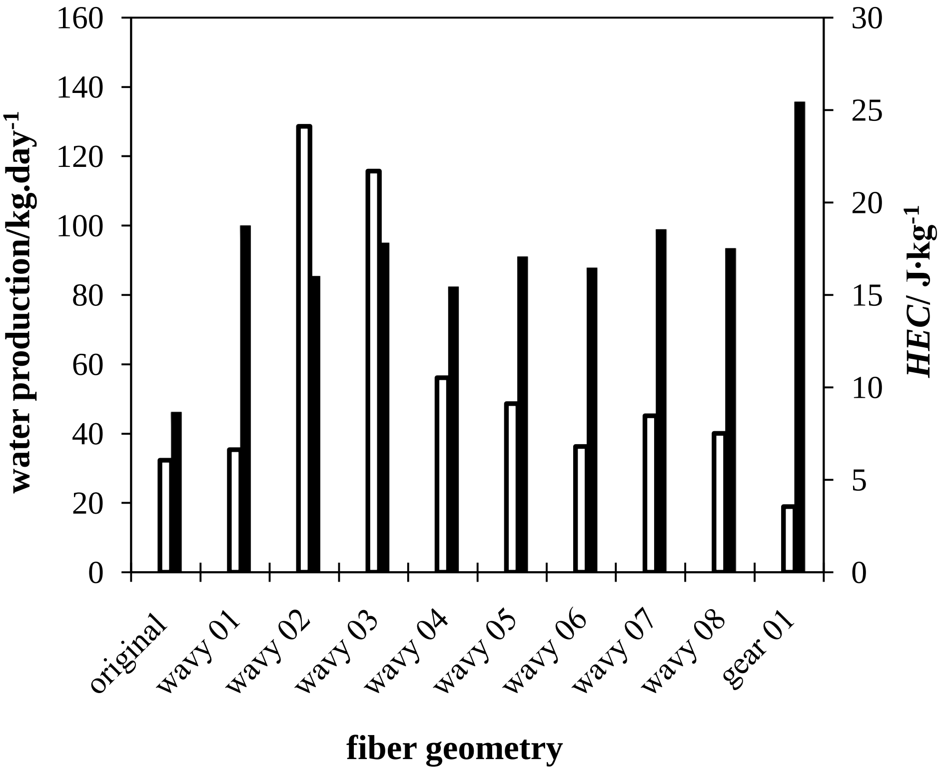

Fig. 6.12 Comparison of water production in multi-fiber modules with various fiber geometries (each module contains100 fibers, A = 100A_s, C = 8.0×10^{-7} kg m^{-2} s^{-1} Pa^{-1} and C^*(gear) = 6.4×10^{-7} kg m^{-2} s^{-1} Pa^{-1}, L = 0.25m, u_{fi} = 0.06 m s^{-1}, u_{pi} = 0.417 m s^{-1}, T_{fi} = 327.15 K, T_{pi} = 293.85 K)

Overall, the gear-fiber module shows the most promising features for achieving approximately 3-fold water production enhancement with only half of the hydraulic loss, compared to the original design.

6.4 Conclusions

In this chapter a series of CFD simulations were carried out to explore the potential benefits of employing microstructured hollow fiber membranes used in a DCMD system.

It is found that the module with fibers of gear-shaped structure achieves the highest average TPC and mass flux N_m values compared to the original straight design, followed by the alternate wavy fibers. The enhanced performance of modified modules can be attributed to the improved hydrodynamics caused by intense secondary flows and improved surface renewal with the presence of corrugations on the membrane surface, which is confirmed by the observation of the flow field and temperature profiles from the CFD simulations. The investigations on fiber length effect show that the gear-shaped fiber modules provide the highest flux enhancement ratios with equivalent effective lengths, followed by the modules with alternate wavy fibers. Interestingly, the advantages of the smart fiber designs are further amplified for longer modules, which is attractive for scale-up to a higher total water production in industrial applications.

Investigations of the flow conditions shows that the gear- shaped fiber module has a promising enhancement at an extremely low Re. Although a flow transition from laminar to turbulent conditions would bring a significant improvement in a conventional MD module, introducing a smart microstructured design into the membrane surface would be a cost-effective option under adverse flow conditions. Also, the computed water production and hydraulic energy consumption (HEC) of different modules with various fiber geometries have been compared. The configuration with gear-shaped fibers has the highest water production but the lowest HEC. In addition, a high water production can be obtained using modules with wavy fibers, due to their greatly increased membrane area by surface corrugations. However, these geometries might possibly cause higher HEC. It is hoped that this study can bring a new perspective on the development of smart membranes for MD applications, and provide a foundation to guide the fabrication of microstructured hollow fiber membranes with an optimal design.

CHAPTER 7

CONCLUSIONS AND RECOMMENDATIONS

7.1 Overall conclusions

This thesis focuses on both experimental study and numerical simulation on hollow fiber module design for membrane distillation (MD) systems, which are commonly subjected to low permeation rate, concentration and temperature polarizations and pore wetting phenomenon. Therefore, attempts have been made to develop novel modules to enhance module performance for desalination based on deep understanding of the mass and heat transfer in the MD process.

Experimentally, the features in a conventional axial hollow fiber module, which include membrane properties (hydrophobicity, pore size/pore size distribution, porosity and cross-sectional morphology), module characteristics (fiber length, packing density, and module diameter), and fluid hydrodynamics, etc, were investigated systematically. Membrane surface modification and optimization of process parameters were executed. In addition, new design concepts, such as the baffled/spaced modules, transverse flow modules and modules with modified fiber geometries, were proposed for direct contact MD (DCMD) applications. The current studies have showed that an appropriate module design can improve the mass and heat transfer in the MD module, leading to a significant performance enhancement.

Numerically, an improved heat-transfer model which couples the latent heat into the energy conservation equation was developed and combined with the Navies-Stokes equations to study the heat-transfer fundamentals and evaluate the potential of various performance-enhancement strategies in a hollow fiber module using computational fluid dynamics (CFD) tools. CFD modeling can be used to correlate the mass- and heat-transfer performance with flow hydrodynamics in a shell-feed

DCMD module. A series of two and three dimensional CFD simulations were carried out to investigate the capability of depolarizing the buildup of liquid boundary layers and thus improving water productivity, by utilizing turbulence promoters (spacers and baffles) and modified fiber geometries (wavy- and gear-shaped). The optimization of module configurations was based on the results of heat- and mass-transfer analysis, flow field distribution, water production and hydraulic loss.

The major findings and conclusions are summarized as follows:

- Compared to the original fluoride (PVDF) hollow fiber membrane, the modified membranes (plasma modified and chemically modified) showed higher contact angles, LEPw and mechanical strength, and smaller maximum pore sizes and narrower pore size distributions. Also, they were less vulnerable to pore-wetting and able to maintain reasonably high MD flux in long-term operation. The chemically modified membrane had the narrowest pore size distribution and the best overall performance, in terms of sustainable flux and permeate quality.
- The MD flux increased to an asymptotic value when turbulence was reached, while the stream on the permeate/lumen side showed a flatten curve of mass flux at a much lower Re_p. By comparing the performance of the modules with different housing sizes, a higher Re was needed to maintain adequate mixing in a larger module.
- Single fiber tests in combination with heat transfer analysis showed that a critical length existed that is the operational length to assure sufficient driving force along the fiber to maintain a high MD efficiency. In addition, the over MD coefficient decreased with increasing packing density.
- Among all modified configurations studied, the modules with curly and spacer-knitted fibers had the best performance. The permeation flux was greatly enhanced up to 90% as compared to the conventional module under the same operating temperatures.
- The fluid dynamic studies show that the performance of all modified configurations except the structured-straight module showed fairly insignificant response to the feed flow velocity, and the modified fiber geometries with

undulating membrane surface can achieve up to three-fold flux enhancement in the laminar flow regime.

- The sodium chloride tracer response technique is able to reveal the shell-side flow pattern and distribution for various designs. Improved fiber geometries or arrangements can provide a better flow distribution, thus much lower pumping energy cost and higher thermal efficiency could be accomplished.
- The heat transfer analysis emphasizes the advantage of the modules with undulating membrane surface for mitigating TP. Although a trade-off exists between the TPC and conductive heat loss, all modified modules showed acceptable heat loss within the range of operating temperatures.
- A CFD heat-transfer model, which couples the latent heat into the energy conservation equation and combines this with the Navies-Stokes equations to address the transport between the fluids (feed and permeate) and the membrane, was developed and applied to study the hydrodynamics in single hollow fiber modules. The numerical simulations have been verified by experiments with less than 5% error in predicted permeation flux and pressure drop along the shell side of the module.
- In the two dimensional CFD modeling of various baffled and spacered single fiber modules, the feed heat-transfer coefficient h_e of the modified modules generally showed much slower decreasing trends along the fiber length compared to the original (unmodified) module. Among all, modified modules with annular baffles and floating round spacers presented the highest results. Consistently, their temperature polarization coefficient (*TPC*) and mass flux distribution curves also presented increasing trends and gained an optimal improvement.
- With the local flow fields and temperature profiles visualized in CFD simulations, it was confirmed that an appropriate selection of turbulence promoters could promote intense secondary flows and radial mixing to improve the shell-side hydrodynamics and enhance heat transfer. Moreover, an increase of flow velocity was employed and compared as a conventional approach to improve hydrodynamics. It was found that a well-designed module could bring

more significant enhancement for a liquid-boundary layer dominant heat-transfer process.

- Modified configurations with attached quad spacers or floating round spacers achieved a good compromise between enhanced permeation fluxes and modest hydraulic energy consumption (*HECs*). Overall, the *TPC* decreases with increasing MD coefficient (*C*) values and operating temperatures; while the thermal efficiency increases dramatically with increasing *C* and operating temperatures in a MD system.
- With three dimensional module structures and simulated domains built in CFD modeling, nine modified fiber geometries were found to have different capabilities of enhancing the permeation rate and depolarizing the buildup of liquid boundary layers. The results of heat-transfer coefficients, average *TPC* and mass flux N_m showed that the gear-shaped fiber module had the most encouraging improvement over the original design, followed by the wavy designs 07 and 08.
- The investigations on fiber length effect showed that the gear-shaped fiber modules gained the highest flux enhancement with an equivalent effective length, followed by the modules with alternate wavy fibers. Interestingly, the advantages of the smart fiber designs were further amplified for longer modules, which are desired for a higher total water production in industrial applications.
- Under various flow conditions, the gear-shaped fiber module showed encouraging response to a velocity change at an extremely low Reynolds number; while the original configuration only responded when turbulence was reached. Hence, a smart microstructured design on the membrane surface would possibly bring remarkable improvement under adverse flow conditions.
- With 1.9-fold surface area increase per unit volume, the gear-shaped fiber configuration had the highest water production but the lowest *HEC*, followed by wavy designs 07 and 08. A high water production could be obtained using modules with wavy fibers, due to their greatly increased membrane area by surface corrugations. However, these geometries might possibly cause high *HEC*.

7.2 Recommendations for future research

For the lab-scale hollow fiber module design, more variations could be explored such as a module with helically wound fibers. The major design variable would be the winding angle. Also, two-phase systems in MD are yet to be extensively studied. The use of bubbles in the shell could enhance heat and mass transfer in the boundary layers around the fibers. This will be examined, with the mode and degree of bubbling being parameters of interest. It should be noted that air bubbling could also have a detrimental effect as dissolved air will tend to transfer into the pores creating a diffusion resistance. It has been observed (Schofield et al. 1987; Schofield et al. 1990) that de-aeration of feed in MD can increase flux. The encouraging computational results for the gear-shaped fibers need to be verified by producing and experimentally testing such fibers.

For the CFD modeling, the currently established heat-transfer model could be further improved by incorporating the normal mass flow across the membrane matrix to achieve more accurate simulation results. Moreover, since the current studies are mostly on the simulations of single fiber modules, more complicated computational domains of triple- and multi-fiber modules are yet to be built to investigate the flow interaction between fibers as well as the effect of packing density in an ideal hollow fiber module. The purpose of computer modeling is to serve the design optimization in an industrial scale.

With respect to energy consumption in MD, integrated systems could include a heat exchanger for energy recovery (from permeate) and a second exchanger for solar or waste heat input. In previous work (Hogan et al. 1991), it has been shown that there are trade-offs of membrane area and heat exchanger areas. The optimal arrangements will be established for various scenarios.

Lastly, industrial demonstration of MD modules applied to water production from various types of feed water could be carried out, including potentially fouling feeds, brine concentrate (from RO desalination plant) and NeWater concentrate (from NeWater plant). The performance will be assessed in terms of attainable fluxes, rates of fouling, rates of wetting, response to cleaning and regeneration etc.

REFRENCES

Abetz, Brinkmann, et al. (2006). "Developments in Membrane Research: from Material via Process Design to Industrial Application." Advanced Engineering Materials **8**(5): 328-358.

Agashichev and Falalejev (1996). "Modeling temperature polarization phenomena for longitudinal shell-side flow in membrane distillation process." Desalination **108**( ): 99-103.

Akoum, Jaffrin, et al. (2005). "Concentration of total milk proteins by high shear ultrafiltration in a vibrating membrane module." Journal of Membrane Science **247**(1-2): 211-220.

Akoum, Jaffrin, et al. (2002). "An hydrodynamic investigation of microfiltration and ultrafiltration in a vibrating membrane module." Journal of Membrane Science **197**(1-2): 37-52.

Aravinth (2000). "Prediction of heat and mass transfer for fully developed turbulent fluid flow through tubes." International Journal of Heat and Mass Transfer **43**(8): 1399-1408.

Armando, Culkin, et al. (1992). New separation system extends the use of membranes. Proceedings of the Euromembrane.

B.J. Bellhouse and Costigan (2001). "The performance of helical screw-thread inserts in tubular Membranes." Separation and Purification Technology: 22-23.

Baker (2004). Membrane Technology and Applications, John Wiley and Sons.

Baker (2008). Advanced Membrane Technology and Applications Wiley-Interscience.

Banat and Simandl (1994). "Theoretical and experimental study in membrane distillation." Desalination **95**
39-52.

Band, Gutman, et al. (1997). "Influence of specially modulated ultrasound on the water desalination process with ion-exchange hollow fibers." Desalination **109**(3): 303-313.

Beier and Jonsson (2006). "Dynamic microfiltration with a vibrating hollow fiber membrane module." Desalination **199**(1-3): 499-500.

Beier and Jonsson (2007). "Separation of enzymes and yeast cells with a vibrating hollow fiber membrane module." Separation and Purification Technology **53**(1): 111-118.

Beier and Jonsson (2009). "A vibrating membrane bioreactor (VMBR): Macromolecular transmission--influence of extracellular polymeric substances." Chemical Engineering Science **64**(7): 1436-1444.

Bodell (1963). Silicone rubber vapor diffusion in saline water distillation, U.S Patent 285 032. United State. **285 032**.

Bonyadi and Chung (2007). "Flux enhancement in membrane distillation by fabrication of dual layer hydrophilic-hydrophobic hollow fiber membranes." Journal of Membrane Science **306**(1-2): 134-146.

Bonyadi and Chung (2009). "Highly porous and macrovoid-free PVDF hollow fiber membranes for membrane distillation by a solvent-dope solution co-extrusion approach." Journal of Membrane Science **331**(1–2): 66-74.

Bouguccha, Chouilkh, et al. (2002). "Numerical study of the coupled heat and mass transfer in membrane distillation." Desalination **152**: 245-252.

Bui, Vu, et al. (2010). "Modelling the simultaneous heat and mass transfer of direct contact membrane distillation in hollow fibre modules." Journal of Membrane Science **353**(1-2): 85-93.

Burgoyne and Vahdati (2000). "Direct Contact Membrane Distillation." Separation Science and Technology **35**(8): 1257 - 1284

Cabassud and Wirth (2003). "Membrane distillation for water desalination: How to chose an appropriate membrane?" Desalination **157**(1-3): 307-314.

Calabrò, Jiao, et al. (1994). "Theoretical and experimental study on membrane distillation in the concentration of orange juice." Industrial & Engineering Chemistry Research **33**(71): 1803-1808.

Cath, Adams, et al. (2004). "Experimental study of desalination using direct contact membrane distillation: a new approach to flux enhancement." Journal of Membrane Science **228**(1): 5-16.

Chai, Kobayashi, et al. (1998). "Ultrasound effect on cross-flow filtration of polyacrylonitrile ultrafiltration membranes." Journal of Membrane Science **148**(1): 129-135.

Chanachai, Meksup, et al. (2010). "Coating of hydrophobic hollow fiber PVDF membrane with chitosan for protection against wetting and flavor loss in osmotic distillation process." Separation and Purification Technology **72**(2): 217-224.

Chang, Fane, et al. (2002). "Modeling and optimizing submerged hollow fiber membrane modules." AIChE Journal **48**(10): 2203-2212.

Charfi, Khayet, et al. "Numerical simulation and experimental studies on heat and mass transfer using sweeping gas membrane distillation." Desalination **259**(1-3):

84-96.

Chen (2007). "Study of the influence of the electric field on membrane flux of a new typeof membrane bioreactor." Journal of Chemical Engineering **128**: 177-180.

Chen, Weavers, et al. (2006). "Ultrasonic control of ceramic membrane fouling by particles: Effect of ultrasonic factors." Ultrasonics Sonochemistry **13**(5): 379-387.

Cheng, Wu, et al. (2008). "Modeling and optimization of hollow fiber DCMD module for desalination." Journal of Membrane Science **318**: 154–166.

Chernyshov, Meindersma, et al. (2005). "Comparison of spacers for temperature polarization reduction in air gap membrane distillation." Desalination **183**: 363.

Clarkson, Cui, et al. (1999). "Protein Denaturation in Foam: I. Mechanism Study." Journal of Colloid and Interface Science **215**(2): 323-332.

Clarkson, Cui, et al. (1999). "Protein Denaturation in Foam: II. Surface Activity and Conformational Change." Journal of Colloid and Interface Science **215**(2): 333-338.

Clarkson, Cui, et al. (2000). "Effect of solution conditions on protein damage in foam." Biochemical Engineering Journal **4**(2): 107-114.

Costello, Fane, et al. (1993). "The effect of shell side hydrodynamics on the performance of axial flowhollowfibre modules." Journal of Membrane Science **80**: 1-11.

Cui, Chang, et al. (2003). "The use of gas bubbling to enhance membrane processes." Journal of Membrane Science **221**(1-2): 1-35.

Çulfaza, Haddad, et al. (2011). "Fouling behavior of microstructured hollow fibers in cross-flow filtrations: Critical flux determination and direct visual observation of particle deposition." Journal of Membrane Science **372**: 210-218.

Çulfaza, Rolevink, et al. (2010). "Microstructured hollow fibers for ultrafiltration." Journal of Membrane Science(347): 32-41.

Çulfaza, Wessling, et al. (2011). "Fouling behavior of microstructured hollow fiber membranes in submerged and aerated filtrations." Water Research(45): 1865-1871.

Culkin Concentrating RO Reject Streams with VSEP (guest article), New Logic Research, Inc**:** http://www.waterandwastewater.com/www_services/ask_tom_archive/concentrating_ro_reject_streams_with_vsep.htm.

Culkin and Armando (1992). "New separation system extends the use of membranes." Filtration & Separation **29**(5): 376-378.

Cussler (1994). Hollow fiber contactors. Membrane Processes in Separation and

Purification. J.G. Crespo and K. W. B. (Eds.). Dordrecht, Kluwer Academic Publishers.

Dahuron and Cussler (1988). "Protein extractions with hollow fibers." AIChE Journal **34**(1): 130-136.

Dindore VY, Cents AHG, et al. (2005). "Shell-side dispersion coefficients in a rectangular cross-flow hollow fibre membranre module." Chemical Engineering Research and Design **83**(A3): 317-325.

Ding, Liu, et al. (2003). "Study on the effect of flow maldistribution on the performance of the hollow fiber modules used in membrane distillation." Journal of Membrane Science **215**: 11-23.

Ding, Ma, et al. (2002). "A new model for mass transfer in direct contact membrane distillation." Desalination **151**: 217-227.

Drioli, Calabrò, et al. (1986). "Microporous membranes in membrane distillation." Pure and Applied Chemistry **58**(12): 1657-1662.

Dumée, Campbell, et al. (2011). "The impact of hydrophobic coating on the performance of carbon nanotube bucky-paper membranes in membrane distillation." Desalination **283**(0): 64-67.

El-Bourawi, Ding, et al. (2006). "A framework for better understanding membrane distillation separation process." Journal of Membrane Science **285**(1-2): 4-29.

Fane (1996). "Membranes for water production and wastewater reuse." Desalination **106**(1): 1-9.

Fane and Chang (2008). Techniques to Enhance Performance of Membrane Processes. Handbook of Membrane Separations, CRC Press.

Fane, Chang, et al. (2002). "Submerged hollow fibre membrane module -- design options and operational considerations." Desalination **146**(1-3): 231-236.

Fang, Gao, et al. (2012). "Hydrophobic porous alumina hollow fiber for water desalination via membrane distillation process." Journal of Membrane Science **403–404**(0): 41-46.

Feng, Shi, et al. (2004). "Preparation and properties of microporous membrane from poly(vinylidene fluoride-co-tetrafluoroethylene) (F2.4) for membrane distillation." Journal of Membrane Science **237**(1-2): 15-24.

Feng, van Deventer, et al. (2006). "Ultrasonic defouling of reverse osmosis membranes used to treat wastewater effluents." Separation and Purification Technology **50**(3): 318-323.

Fimbres-Weihs and Wiley (2010). "Review of 3D CFD modeling of flow and mass transfer in narrow spacer-filled channels in membrane modules." Chem. Eng. Process. **49**(7): 759-781.

Fimbres-Weihs, Wiley, et al. (2006). "Unsteady flows with mass transfer in narrow zigzag spacer-filled channels: a numerical study." Ind. Eng. Chem. Res. **45**: 6594-6603.

Findley (1967). "Vaporization through porous membranes." Industrial & Engineering Chemistry Research **6**: 226–230.

Foster, Burgoyne, et al. (2001). "Improved process topology for membrane distillation." Separation and Purification Technology **21**(3): 205-217.

Frappart, Jaffrin, et al. (2008). "Reverse osmosis of diluted skim milk: Comparison of results obtained from vibratory and rotating disk modules." Separation and Purification Technology **60**(3): 321-329.

Fujii, Kigoshi, et al. (1992). "Selectivity and characteristics of direct contact membrane distillation type experiment. I. Permeability and selectivity through dried hydrophobic fine porous membranes." Journal of Membrane Science **72**(1): 53-72.

Gabelman and Hwang (1999). "Hollow fiber membrane contactors." Journal of Membrane Science **159**(1-2): 61-106.

Gander, Jefferson, et al. (2000). "Aerobic MBRs for domestic wastewater treatment: a review with cost considerations." Separation and Purification Technology **18**(2): 119-130.

García-Payo, Essalhi, et al. (2010). "Effects of PVDF-HFP concentration on membrane distillation performance and structural morphology of hollow fiber membranes." Journal of Membrane Science **347**: 209-219.

Gawronski and Wrzesinska (2000). "Kinetics of solvent extraction in hollow fibre contactors." Journal of Membrane Science **168**.

Generon (2000). "Internal staged permeator for fluid separation, patent no: PCT WO 00/71234 A1(US)."

Genkin, Waite, et al. (2006). "The effect of vibration and coagulant addition on the filtration performance of submerged hollow fibre membranes." Journal of Membrane Science **281**(1-2): 726-734.

Ghogomu, Guigui, et al. (2001). "Hollow-fibre membrane module design: comparison of different curved geometries with Dean vortices." Journal of Membrane Science **181**(1): 71-80.

Godino, Peña, et al. (1996). "Membrane distillation: theory and experiments." Journal of Membrane Science **121**: 83-93.

Gronda, Buechel, et al. (2000). "Mass transfer in corrugated membranes." Journal of Membrane Science(165): 177-187.

Gryta and Tomaszewska (1998). "Heat transport in the membrane distillation process." Journal of Membrane Science **144**(1-2): 211-222.

Gryta, Tomaszewska, et al. (1997). "Membrane distillation with laminar flow." Separation and Purification Technology **11**(2): 93-101.

Gupta, Howell, et al. (1995). "A helical baffle for cross-flow microfiltration." Journal of Membrane Science **102**: 31-42.

Hanemaaijer, van Medevoort, et al. (2006). "Memstill membrane distillation - a future desalination technology." Desalination **199**(1-3): 175-176.

Hashino, Katagiri, et al. (2011). "Effect of surface roughness of hollow fiber membranes with gear-shaped structure on membrane fouling by sodium alginate." Journal of Membrane Science(366): 389–397.

Hendren, Brant, et al. (2009). "Surface modification of nanostructured ceramic membranes for direct contact membrane distillation." Journal of Membrane Science **331**(1-2): 1-10.

Herczeg (2004). Convoluted surface hollow fiber membranes.

Ho and Sirkar (1992). Membrane Handbook, Van Nostrand Reinhold.

Hogan, Sudjito, et al. (1991). "Desalination by solar heated membrane distillation." Desalination **81**: 81-90.

Huang (2008). "Improvement of membrane filterability of the mixed liquor in a membrane bioreactor by ozonation." Journal of Membrane Science **318** (1-2): 210-216.

Hwang, He, et al. (2011). "Direct contact membrane distillation (DCMD): Experimental study on the commercial PTFE membrane and modeling." Journal of Membrane Science **371**(1-2): 90-98.

Imdakm and Matsuura (2005). "Simulation of heat and mass transfer in direct contact membrane distillation (MD): The effect of membrane physical properties." Journal of Membrane Science **262**(1-2): 117-128.

Jin, Yang, et al. (2008). "Hydrophobic modification of poly(phthalazinone ether sulfone ketone) hollow fiber membrane for vacuum membrane distillation." Journal of Membrane Science **310**(1-2): 20-27.

Johnson, Semmens, et al. (1997). "Diffusive transport across unconfined hollow fiber membranes." Journal of Membrane Science **128**(1): 67-81.

Juang and Lin (2004). "Flux recovery in the ultrafiltration of suspended solutions with ultrasound." Journal of Membrane Science **243**(1-2): 115-124.

Judd (2006). The MBR book: principles and applications of membrane bioreactors in water and wastewater treatment. Amsterdam, Elsevier.

Jury, Vaux Jr, et al. (2007). The Emerging Global Water Crisis: Managing Scarcity and Conflict Between Water Users. Advances in Agronomy, Academic Press. **95:** 1-76.

Karakulski, Gryta, et al. (2002). "Membrane processes for portable water quality improvement." Desalination **145**: 315-319.

Khayet (2011). "Membranes and theoretical modeling of membrane distillation: A review." Advances in Colloid and Interface Science **164**(1–2): 56-88.

Khayet, Cojocaru, et al. (2012). "Hollow fiber spinning experimental design and analysis of defects for fabrication of optimized membranes for membrane distillation." Desalination **287**: 146-158.

Khayet, Godino, et al. (2003). "Possibility of nuclear desalination through various membrane distillation configurations: a comparative study: Khayet, M. et al. International Journal of Nuclear Desalination." Fuel and Energy Abstracts **44**(6): 372-372.

Khayet, Godino, et al. (2000). "Theory and experiments on sweeping gas membrane distillation." Journal of Membrane Science **165**: 261-272.

Khayet, Godino, et al. (2002). "Thermal boundary layers in sweeping gas membrane distillation processes." AIChE Journal **48**(7): 1488-1497.

Khayet, Godino, et al. (2004). "Study of asymmetric polarization in direct contact membrane distillation." Separation and Purification Technology **39**(1): 125-147.

Khayet and Matsuura (2001). "Preparation and Characterization of Polyvinylidene Fluoride Membranes for Membrane Distillation." Industrial & Engineering Chemistry Research **40**(24): 5710-5718.

Khayet and Matsuura (2003). "Application of surface modifying macromolecules for the preparation of membranes for membrane distillation." Desalination **158**(1-3): 51-56.

Khayet, Matsuura, et al. (2005). "Porous hydrophobic/hydrophilic composite membranes: estimation of the hydrophobic layer thickness." Journal of Membrane Science **266**: 68-79.

Khayet, Matsuura, et al. (2006). "Design of novel direct contact membrane distillation membranes." Desalination **192**(1-3): 105-111.

Khayet, Mengual, et al. (2005). "Porous hydrophobic/hydrophilic composite membranes: Application in desalination using direct contact membrane distillation." Journal of Membrane Science **252**(1-2): 101-113.

Kiani, Bhave, et al. (1984). "Solvent extraction with immobilised interfaces in a microporous hydrophobic membrane." Journal of Membrane Science **20**: 125.

Kim and DiGiano (2006). "Defining critical flux in submerged membranes: Influence of length-distributed flux." Journal of Membrane Science **280**(1-2): 752-761.

Kobayashi, Chai, et al. (1999). "Ultrasound enhanced cross-flow membrane filtration." Separation and Purification Technology **17**(1): 31-40.

Kost and Langer (1988.). Ultrasonic enhancement of membrane permeability, U.S Patent 4,780,212. M.I.T. M.I.T. US.

Koutsou, Yiantsios, et al. (2004). "Numerical simulation of the flow in plane channel containing a periodic array of cylindrical turbulence promoters." Journal of Membrane Science **231**: 81-90.

Krantz, Bilodeau, et al. (1997). "Use of axial membrane vibrations to enhance mass transfer in a hollow tube oxygenator." Journal of Membrane Science **124**(2): 283-299.

Kreith and Black (1980). Basic Heat Transfer, Harper & Row, New York.

Krygier (1998). personal communication, 25 November, Pall Corporation.

Lagana, Barbieri, et al. (2000). "Direct contact membrane distillation: modelling and concentration experiments." Journal of Membrane Science **166**: 1-11.

Lai, Liou, et al. (2011). "Preparation and characterization of plasma-modified PTFE membrane and its application in direct contact membrane distillation." Desalination **267**(2–3): 184-192.

Lawson and Lloyd (1996). "Membrane distillation. I. Module design and performance evaluation using vacuum membrane distillation." Journal of Membrane Science **120**(1): 111-121.

Lawson and Lloyd (1996). "Membrane distillation. II. Direct contact MD." Journal of Membrane Science **120**(1): 123-133.

Lawson and Lloyd (1997). "Membrane distillation." Journal of Membrane Science **124**(1): 1-25.

Lemanski and Lipscomb (1995). "Effect of shell-side flows on hollow fiber membrane device performance." AIChE Journal **41**: 2322-2326.

Levenspiel (1999). Chemical Reaction Engineering, John Wiley & Sons, Inc.

Li, He, et al. (2005). "Comparison of the filtration characteristics between biological powdered activated carbon sludge and activated sludge in submerged membrane bioreactors." Desalination **174**(3): 305-314.

Li, Sanderson, et al. (2002). "Ultrasonic cleaning of nylon microfiltration membranes fouled by Kraft paper mill effluent." Journal of Membrane Science **205**(1-2): 247-257.

Li and Sirkar (2004). "Novel Membrane and Device for Direct Contact Membrane Distillation-Based Desalination Process." Ind. Eng. Chem. Res. **43**(17): 5300-5309.

Li and Sirkar (2005). "Novel membrane and device for vacuum membrane distillation-based desalination process." Journal of Membrane Science **257**(1-2): 60-75.

Li, Wang, et al. (2004). "Fabrication of lab-scale hollow fiber membrane modules with high packing density." Separation and Purification Technology **40**(1): 15-30.

Li, Xu, et al. (2003). "Microporous polypropylene and polyethylene hollow fiber membranes. Part 3. Experimental studies on membrane distillation for desalination." Desalination **155**(2): 153-156.

Lipnizki and Field (2001). "Mass transfer performance for hollow fiber modules with shell-side axial feed flow: using an engineering approach to develop a framework." Journal of Membrane Science **193**: 195-208.

Liu, Ding, et al. (2007). "Ultrasonic enhancement of membrane-based deoxygenation and simultaneous influence on polymeric hollow fiber membrane." Separation and Purification Technology **56**(2): 133-142.

Lu, Ding, et al. (2008). "The influence of bubble characteristics on the performance of submerged hollow fiber membrane module used in microfiltration." Separation and Purification Technology **61**(1): 89-95.

Madsen (1977). Hyperfiltration and Ultrafiltration in Plate-and-Frame systems. Amsterdam, Elsevier.

Martinez-Díez and Rodriquez-Maroto (2006). "Characterization of membrane distillation modules and analysis of mass flux enhancement by channel spacers." Journal of Membrane Science **274**(1-2): 123-137.

Martinez-Diez and Vazquez-Gonzalez (1998). "Effect of polarization on mass transport through hydrophobic porous membranes." Industrial & Engineering Chemistry Research **37**: 4128-4135.

Martinez-Diez and Vazquez-Gonzalez (1999). "Temperature and concentration polarization in membrane distillation of aqueous salt solutions." Journal of Membrane Science **156**: 265-273.

Martinez-Diez and Vazquez-Gonzalez (2000). "A method to evaluate coefficients affecting flux in membrane distillation." Journal of Membrane Science **173**(2): 225-234.

Martínez-Díez, Vázquez-González, et al. (1998). "Study of membrane distillation using channel spacers." Journal of Membrane Science **144**(1-2): 45-56.

Martínez and Rodríguez-Maroto (2007). "Effects of membrane and module design improvements on flux in direct contact membrane distillation." Desalination **205**(1-3): 97-103.

Masselin, Chasseray, et al. (2001). "Effect of sonication on polymeric membranes." Journal of Membrane Science **181**(2): 213-220.

Mengual and Peña (1997). "Membrane distillation." Journal of Colloid and Interface Science **1**: 17-29.

Muthukumaran, Kentish, et al. (2005). "Mechanisms for the ultrasonic enhancement of dairy whey ultrafiltration." Journal of Membrane Science **258**(1-2): 106-114.

Muthukumaran, Kentish, et al. (2005). "The optimisation of ultrasonic cleaning procedures for dairy fouled ultrafiltration membranes." Ultrasonics Sonochemistry **12**(1-2): 29-35.

Nijdam, Jong, et al. (2005). "High performance micro-engineered hollow fiber membranes by smart spinneret design." Journal of Membrane Science(256): 209-215.

Noda, Brown-West, et al. (1979). "Effect of flow maldistribution on hollow fibre dialysis-experimental studies." Journal of Membrane Science **5**: 209-225.

Okahata and Noguchi (1983). "Ultrasound-responsive permeability control of bilayer-coated capsule membranes." Chemistry Letters: 1517-1520.

PallSep (2004). "http://www.pall.com."

Phattaranawik and Jiraratananon (2001). "Direct contact membrane distillation: effect of mass transfer on heat transfer,." Journal of Membrane Science **188**: 137-143.

Phattaranawik, Jiraratananon, et al. (2003). "Effect of pore size distribution and air flux on mass transport in direct contact membrane distillation." Journal of Membrane Science **215**: 75-85.

Phattaranawik, Jiraratananon, et al. (2003). "Heat transport and membrane distillation coefficients in direct contact membrane distillation." Journal of Membrane Science **212**: 177-193.

Phattaranawik, Jiraratananon, et al. (2001). "Mass flux enhancement using spacer filled channels in direct contact membrane distillation." Journal of Membrane Science **187**(1-2): 193-201.

Porter (1990). Handbook of Industrial Membrane Technology, William Andrew Inc.

Prasad, Kiani, et al. (1986). "Further studies on solvent extraction with immobilized interfaces in a microporous hydrophobic membrane." Journal of Membrane Science **26**: 79.

Prasad and Sirkar (1988). "Dispersion-free solvent extraction with microporous hollow-fiber modules." AIChE Journal **34**(2): 177.

Psoch and Schiewer (2005). "Critical flux aspect of air sparging and backflushing on membrane bioreactors." Desalination **175**(1): 61-71.

Qtaishat, Khayet, et al. (2009). "Guidelines for preparation of higher flux hydrophobic/hydrophilic composite membranes for membrane distillation." Journal of Membrane Science **329**(1-2): 193-200.

Qtaishat, Matsuura, et al. (2008). "Heat and mass transfer analysis in direct contact membrane distillation." Desalination **219**(1-3): 272-292.

Qtaishat, Rana, et al. (2009). "Preparation and characterization of novel hydrophobic/hydrophilic polyetherimide composite membranes for desalination by direct contact membrane distillation." Journal of Membrane Science **327**(1-2): 264-273.

Rector, J.L. Garland, et al. (2006). "Dispersion characteristics of a rotating hollow fiber membrane bioreactor: effects of module packing density and rotational frequency." Journal of Membrane Science **278**: 144-150.

Reed, Semmens, et al. (1995). Membrane contactors. in: R.D. Noble, S.A. Stern (Eds.), Membrane Separations Technology. Principles and Applications. Amsterdam, Elsevier**:** 474.

Reid and Prausnitz (1987). C.R. Wilke and P. Chang method (1955). The Properties of Gases and Liquids, McGraw-Hill Inc.

Reid, Prausnitz, et al. (1977). The Properties of Gases and Liquids. New York, McGraw-Hill.

Rijn, Vogelaar, et al. (2002). Method of making a product with a micro or nano sized structure and product.

Rohsenow and Hartnett (1973). Handbook of heat transfer, McGraw-Hill, Inc.

Sarti, Gostoli, et al. (1985). "Low energy cost desalination processes using hydrophobic membranes." Desalination **56**: 277-286.

Schneider, Hölz, et al. (1988). "Membranes and modules for transmembrane distillation." Journal of Membrane Science **39**(1): 25-42.

Schofield, Fane, et al. (1990). "Factors affecting flux in membrane distillation." Desalination **77**: 279-294.

Schofield, Fane, et al. (1987). "The efficient use of energy in membrane distillation." Desalination **64**: 231-243.

Schofield, Fane, et al. (1987). "Heat and mass transfer in membrane distillation." Journal of Membrane Science **33**(3): 299-313.

Schofield, Fane, et al. (1990). "Gas and vapour transport through microporous membranes. I. Knudsen-Poiseuille transition." Journal of Membrane Science **53**(1): 159-171.

Semmens (1998). personal communication, 25 August.

Shakaib, Hasani, et al. (2012). "A CFD study on the effect of spacer orientation on temperature polarization in membrane distillation modules." Desalination **284**: 332-340.

Shakaib, Hasani, et al. (2009). "CFD modeling for flow and mass transfer in spacer-obstructed membrane feed channels." Journal of Membrane Science **326**(2): 270-284.

Shi, Wang, et al. (2009). "Modification of PVDF membrane surface to enhance its hydrophobicity (unpublish work)."

Shih, Liou, et al. (1995). "A new k-ε eddy viscosity model for high reynolds number turbulent flows." Computers & Fluids **24**(3): 227-238.

Simon, Penpenic, et al. (2000). "A comparative study between classical stirred and ultrasonically-assisted dead-end ultrafiltration." Ultrasonics Sonochemistry **7**(4): 183-186.

Sirkar (1995). Newer concepts and applications for the food industry, in Bioseparation Processes in Foods. Membrane separations. New York, CRC Press**:** 353-356.

Smolders and Franken (1989). "Terminology for membrane distillation." Desalination **72**: 249-262.

Sofia, Ng, et al. (2004). "Engineering design approaches for minimum fouling in submerged MBR." Desalination **160**(1): 67-74.

Song, Li, et al. (2007). "Direct contact membrane distillation-based desalination: novel membranes, devices, larger-scale studies, and a model." Industrial &

Engineering Chemistry Research **46**: 2307-2323.

Sparrow (2003). "Empirical equations for the thermodynamic properties of aqueous sodium chloride." Desalination **159**(2): 161-170.

Su, Teoh, et al. (2010). "Effect of inner-layer thermal conductivity on flux enhancement of dual-layer hollow fiber membranes in direct contact membrane distillation." Journal of Membrane Science **364**(1-2): 278-289.

Suk, Matsuura, et al. (2006). "Synthesis of a new type of surface modifying macromolecules (nSMM) and characterization and testing of nSMM blended membranes for membrane distillation." Journal of Membrane Science **277**(1-2): 177-185.

Susanto (2011). "Towards practical implementations of membrane distillation." Chem. Eng. Process. **50**: 139-150.

T.K. Sherwood, R.L. Pigford, et al. (1975). Mass Transfer. New York, McGraw-Hill.

Taha and Cui (2002). "CFD modelling of gas-sparged ultrafiltration in tubular membranes." Journal of Membrane Science **210**(1): 13-27.

Teoh, Bonyadi, et al. (2008). "Investigation of different hollow fiber module designs for flux enhancement in the membrane distillation process." Journal of Membrane Science **311**(1-2): 371-379.

Thanedgunbaworn, Jiraratananon, et al. (2007). "Shell-side mass transfer of hollow fibre modules in osmotic distillation process." Journal of Membrane Science **290**: 105-113.

Thomas (1980). Fundamentals of heat transfer, Prentice-Hall, Inc., Englewood Cliffs, N.J.

Tomaszewska (1996). "Preparation and properties of flat-sheet membranes from poly(vinylidene fluoride) for membrane distillation." Desalination **104**(1): 1-11.

Tomaszewska, Gryta, et al. (1992). "Study on the concentration of acids by membrane distillation." Journal of Membrane Science **102** 113-122.

Tran, Gray, et al. (2007). "Ultrasound enhancement of microfiltration performance for natural organic matter removal." Organic Geochemistry **38**(7): 1091-1096.

Trimmer.Johnny.L (1992). Flexible hollow fiber fluid separation module, PCT WO Patent 93/12866. US.

Vane, Alvarez, et al. (1999). "Reduction of concentration polarization in pervaporation using vibrating membrane module." Journal of Membrane Science **153**(2): 233-241.

Wang, Chen, et al. (2003). "Effect of random packing on shell-side flow and mass transfer in hollow fiber module described by normal distribution function." J. Membr. Sci. **216**: 81-93.

Wang, Chung, et al. (2008). "Hydrophobic PVDF hollow fiber membranes with narrow pore size distribution and ultra-skin for the fresh water production through membrane distillation." Chemical Engineering Science **63**: 2587-2594.

Wang, Li, et al. (2005). "Effect of ultrasound irradiation on polymeric microfiltration membranes." Desalination **175**(2): 187-196.

Wang, Sanly, et al. (2009). "Diagnosis of membrane bioreactor performance through residence time distribution measurements - a preliminary study." Desalination **236**: 120-126.

Wang, Teoh, et al. (2011). "Morphological architecture of dual-layer hollow fiber for membrane distillation with higher desalination performance." Water Research **45**(17): 5489-5500.

Wei, Zhao, et al. (2012). "CF4 plasma surface modification of asymmetric hydrophilic polyethersulfone membranes for direct contact membrane distillation." Journal of Membrane Science **407–408**: 164-175.

Wenten (2009). Novel large scale applications of membrane technology (unpublished work).

Wicaksana, Fane, et al. (2006). "Fibre movement induced by bubbling using submerged hollow fibre membranes." Journal of Membrane Science **271**(1-2): 186-195.

Wickramasinghe, Semmens, et al. (1991). "Better hollow fiber contactors." Journal of Membrane Science **62**(3): 371-388.

Wickramasinghe, Semmens, et al. (1992). "Mass transfer in various hollow fiber geometries." Journal of Membrane Science **69**(3): 235-250.

Wickramasinghe, Semmens, et al. (1993). "Hollow fiber modules made with hollow fiber fabric." Journal of Membrane Science **84**(1): 1-14.

Wikol (1998). "W.L.Gore & Associates, personal communication,25 November."

Wu and Chen (2000). "Shell-side mass transfer performance of randomly packed hollow fiber modules." Journal of Membrane Science **172**: 59-74.

Wu, Kong, et al. (1992). "Surface-modified hydrophilic membranes in membrane distillation." Journal of Membrane Science **72**(2): 189-196.

Xu, Pan, et al. (2009). "CFD simulation on membrane distillation of NaCl solution." Front. Chem. Eng. Chin. **3**: 293-297.

Yang, Cao, et al. (2007). "Study on highly hydrophilic cellulose hollow fiber membrane contactors for thiol sulfur removal." Journal of Membrane Science **305**(1-2): 247-256.

Yang and Cussler (1986). "Designing hollow-fiber contactors." AIChE Journal **32**: 1910-1915.

Yang, Wang, et al. (2011). "Novel designs for improving the performance of hollow fiber membrane distillation modules." Journal of Membrane Science **384**(1-2): 52-62.

Yang, Wang, et al. (2012). "Membrane module design and dynamic shear-induced techniques to enhance liquid separation by hollow fiber modules: a review." Desalination and Water Treatment **submitted**.

Yang, Wang, et al. (2011). "Performance improvement of PVDF hollow fiber-based membrane distillation process." Journal of Membrane Science **369**(1-2): 437-447.

Yang, Yu, et al. (2012). "Analysis on the effect of turbulence promoters in hollow fiber membrane distillation module via computational fluid dynamic (CFD) simulations." Journal of Membrane Science **415–416** (2012), 758-769.

Yaws (1999). Chemical Properties Handbook, McGraw-Hill.

Yeo, Law, et al. (2006). "Factors affecting the performance of a submerged hollow fiber bundle." Journal of Membrane Science **280**(1-2): 969-982.

Yeo, Law, et al. (2007). "The relationship between performance of submerged hollow fibers and bubble-induced phenomena examined by particle image velocimetry." Journal of Membrane Science **304**(1-2): 125-137.

Yu, Yang, et al. (2011). "Numerical simulation of heat and mass transfer in direct membrane distillation in a hollow fiber module with laminar flow." Journal of Membrane Science **384**(1-2): 107-116.

Yu, Yang, et al. (2012). "Analysis of heat and mass transfer by CFD for performance enhancement in direct contact membrane distillation." Journal of Membrane Science **405- 406**: 38- 47.

Zárate, Pena, et al. (1995). "Characterization of membrane distillation membranes prepared by phase inversion." Desalination **100**(1): 139-148.

Zhang (2010). "Heat and mass transfer in a quasi-counter flow membrane-based total heat exchanger." Int. J. Heat Mass Transfer **53**(23-24): 5478-5486.

Zhang, Cui, et al. (2009). "Effect of bubble size and frequency on mass transfer in flat sheet MBR." Journal of Membrane Science **332**(1-2): 30-37.

Zhang, Li, et al. (2010). "Performance of asymmetric hollow fibre membranes in membrane distillation under various configurations and vacuum enhancement." Journal of Membrane Science **362**(1-2): 517-528.

Zhang, Liang, et al. (2010). "Conjugate heat and mass transfer in membrane-formed channels in all entry regions." Int. J. Heat Mass Transfer **53**(5-6): 815-824.

Zheng and Liu (2004). Development and cost analysis of MBR for wastewater treatment and reuse in China, Oral presentation World Engineers' Convention, Shanghai.

Zheng, Xu, et al. (2003). "Flow distribution in a randomly packed hollow fiber membrane module." Journal of Membrane Science **211**: 263-269.

Zhu, Christofides, et al. (2009). "Minimization of Energy Consumption for a Two-Pass Membrane Desalination: Effect of Energy Recovery, Membrane Rejection and Retentate Recycling." Journal of Membrane Science **339**(1-2): 126-137.

Zhu and Liu (2000). "Modeling of ultrasonic enhancement on membrane distillation." Journal of Membrane Science **176**(1): 31-41.

Zhu, Liu, et al. (1999). "Ultrasonic stimulation on enhancement of air gap membrane distillation." Journal of Membrane Science **161**(1-2): 85-93.